UNIVERSITÀ DI PARMA

# UNIVERSITA' DEGLI STUDI DI PARMA

DOTTORATO DI RICERCA IN

"*Scienze Chimiche*"

CICLO XXXV

## *Bioinorganic strategies for the development of metal-enzymes inhibitors and compounds with antitumor activity*

Coordinatrice:

Chiar.ma Prof.ssa Alessia Bacchi

Tutore:

Chiar.mo Prof. Mauro Carcelli

Dottoranda: Francesca Miglioli

Anni Accademici 2019/2020 – 2021/2022

**ABSTRACT**

This PhD thesis is centred on two main research areas within the bioinorganic strategies for the development of bioactive compounds.

The first one regards the synthesis and characterization of water-soluble thiosemicarbazones (TSCs) copper complexes as compounds with anticancer activity. Promising results were previously obtained in this research group with salicylaldehyde TSCs Cu(II) complexes that, nevertheless, showed that their application could be improved enhancing their water solubility. Therefore, the first project focused on the synthesis of some sulfonated salicylaldehyde TSC ligands and of their copper(II) complexes. The synthesis of structurally modified ligands and complexes was carried out to have insights on the structure-activity relationship in this class of compounds. Another way to improve solubility brought to the synthesis of a panel of glyco-conjugate TSCs ligands and their copper(II) complexes.

The second subject concerns the synthesis and characterization of chelating compounds as inhibitors of viral metal-dependent enzymes, by using the validated strategy of the metal chelation of the ion cofactors within the active site of the target enzymes. The synthesis of different chelating compounds targeting the metal-dependent RNA-dependent RNA polymerase in viruses of the *Bunyavirales* order was undertaken. Several bunyaviruses represent emerging zoonotic pathogens and the therapeutic options for the treatment of these infections are very limited, thus the identification of effective antiviral compounds is of vital importance. Finally, due to the arrival of the COVID-19 pandemic, an in-house library of chelating compounds and metal complexes has been completed to be used in a screening targeting PLpro, a specific zinc-dependent enzyme of SARS-COV-2.

**Abbreviations**

| | |
|---|---|
| δ | chemical shift |
| ACE | angiotensin converting enzyme |
| AIDS | acquired immunodeficiency syndrome |
| ANDV | Andes virus |
| APH | acid phosphatase |
| AT-IR | attenuated total reflection infrared spectroscopy |
| ATOX | antioxidant protein |
| ATP | adenosine triphosphate |
| ATP7A/B | ATPase 7A/B |
| BUNV | Bunyamwera virus |
| BXA | Baloxavir acid |
| BXM | Baloxavir Marboxil |
| CA | carbonic anhydrases |
| CASV | California Academy of Sciences virus |
| CCHFV | Crimean-Congo haemorrhagic fever virus |
| CCS | copper chaperone for SOD1 |
| CDDP | *cis*-diamminedichloroplatinum(II), cis-platin |
| cDNA | Complementary DNA |
| COX | cytochrome C Oxidase Chaperone |
| CTR | copper transporter |
| CYP51 | cytochrome P450 14α-sterol demethylase |
| DCM | Dichloromethane |
| Dept | distortionless enhancement by polarization transfer |
| DKA | diketo acids |
| DMSO | dimethyl sulfoxide |
| DMT | divalent metal transporter |
| DNA | deoxyribonucleic acid |
| DNP | Dinitrophenol |
| DPBA | 2,4-dioxo-4-phenylbutanoic acid |
| D-Pen | D-penicillamine |
| EA | elemental analysis |
| $EC_{50}$ | half maximal effective concentration |
| EGCG | Epigallocatechin gallate |
| EMT | epithelial to mesenchymal transition |
| Eqv | Equivalents |
| ESI-MS | Electrospray ionization mass spectrometry |
| EtOAc | ethyl acetate |
| EtOH | Ethanol |
| FDA | Food and Drug Administration |
| FRET | Fluorescence resonance energy transfer |
| FT-IR | Fourier-transform infrared spectroscopy |
| GLUT | glucose transporters |
| GSH | Glutathione |
| HAART | highly active antiretroviral therapy |
| HDAC | histone deacetylase |
| HIV | human immunodeficiency virus |
| HSAB | hard soft acid base |
| HTNV | Hantaan virus |
| IAV | Influenza A virus |

| | |
|---|---|
| $IC_{50}$ | half-maximal inhibitory concentration |
| ICP-AES | inductively coupled plasma – atomic emission spectroscopy |
| IN | Integrase |
| LACV | La Crosse encephalitis virus |
| LASV | Lassa virus |
| LCMV | Lymphocytic choriomeningitis virus |
| LLC | Lewis lung carcinoma |
| LOX | lysine oxidase |
| MEMO | Mediator of ErbB2-driven cell Motility |
| MeOH | Methanol |
| MRI | Magnetic Resonance Imaging |
| MT | Metallothionein |
| MTT | 3-(4,5-dimethylthiazol-2-yl)-2,5-diphenyltetrazolium bromide |
| ND | non-detectable |
| NRM | nuclear magnetic resonance |
| NTP | nucleoside triphosphate |
| OT | organic cations transporter |
| PDI | protein disulfide isomerase |
| PET | positron emission tomography |
| PFV | prototype foamy virus |
| PICV | Pichinde virus |
| RdRP | RNA-dependent RNA polymerase |
| RNA | ribonucleic acid |
| ROS | reactive oxygen species |
| RVFV | Rift Valley Fever virus |
| SARS-CoV | severe acute respiratory syndrome coronavirus |
| SC-XRD | single-crystal X-ray diffraction |
| SD | standard deviation |
| SFSV | Sandfly fever Sicilian virus |
| $S_N2$ | substitution nucleophilic $2^{nd}$ order |
| sNSV | segmented negative-strand RNA virus |
| SOD | superoxide dismutase |
| ssRNA | single strand RNA |
| STEAP | six-transmembrane epithelial antigen of prostate protein |
| TETA | Triethylenetetramine |
| THC | bis-thiocarbohydrazone |
| TME | tumor microenvironment |
| Topo | Topoisomerase |
| TOSV | Toscana virus |
| TS | transition state |
| TSC | Thiosemicarbazone |
| TTM | Tetrathiomolibdate |
| UPLC | Ultra High Performance Liquid Chromatography |
| VEGF | Vascular-Endothelial Growth Factor |
| WHO | World Health Organisation |
| WT | wild type |
| XIAP | X-linked inhibitor of Apoptosis Protein |

INDEX

## 0. Premise

A considerable number of chemical elements are vital for the living systems. Of the 21 elements essential for the humans, 11 are metals.[1] These metals take part in a variety of biological processes in the human body. Just to make some examples, iron in haemoglobin binds to oxygen and carries it to the tissues; zinc ions are present in insulin, a hormone that regulates sugar metabolism; many metal ions (such as copper, manganese, magnesium, zinc) are present as co-factors in metalloenzymes, that catalyse a wide range of chemical reactions.[2]

Given the extensive and important role metals play in the biological systems, they have been used in medicine for almost five millennia, even without knowing the exact mechanisms of action involved.[3] The use of copper and zinc dates to Egypt in 3000 BC, when copper was utilised as a water sanitizer and zinc in wounds treatments. Gold was present in various traditional remedies in China and Arabia around 3500 years ago.[4] Paracelsus, a famous Swiss alchemist and doctor, around 1500 AD recommended the use of mixtures, containing iron, cadmium, mercury, antimony and arsenic in the treatment of many human diseases, including cancer.

The importance of metal-based compounds in the medicinal field has grown since the beginning of 20$^{th}$ century. Ehrlich, in 1909, discovered the activity of an arsenic compound against syphilis, later commercialized under the name Salvarsan (**Scheme 0.1**).[5] In the same period, Koch was working with gold cyanide (**Scheme 0.1**) as a therapy for tuberculosis. In 1912, an antimony-based compound was discovered to be useful against leishmaniosis, and from 1929 several gold complexes were employed in the treatment of rheumatoid arthritis.[4]

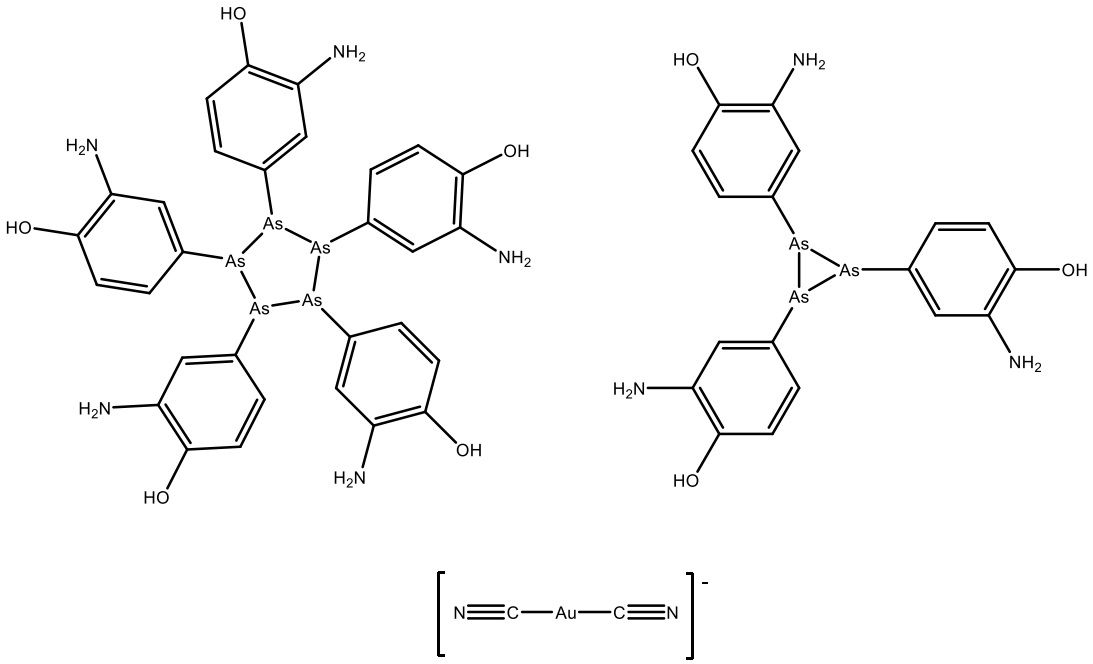


**Scheme 0.1** Chemical structures of Salvarsan (mixture of two different cyclic compounds, top) and gold cyanide (bottom).

Nowadays, there is a more accurate understanding of the role of metals in human physiology and the branch of bio-inorganic medicinal chemistry comprises the use of both metal-based compounds and metal chelators. To cite a few, one of the most famous metal complex used in medicine is *cis*-platin, whose

cytotoxic activity was discovered by Rosemberg in the sixties[6] and is still currently used in different anticancer therapy regimes. The polymeric compound silver sulfadiazine (**Scheme 0.2**), having antibacterial properties, is employed in the treatment of burn wounds[7]. Metal-based compounds are also extensively used as MRI (Magnetic Resonance Imaging) contrast agents, a vast number of which are Gd(III)-based, such as gadoteric acid, also known as Dotarem[8] (**Scheme 0.2**).

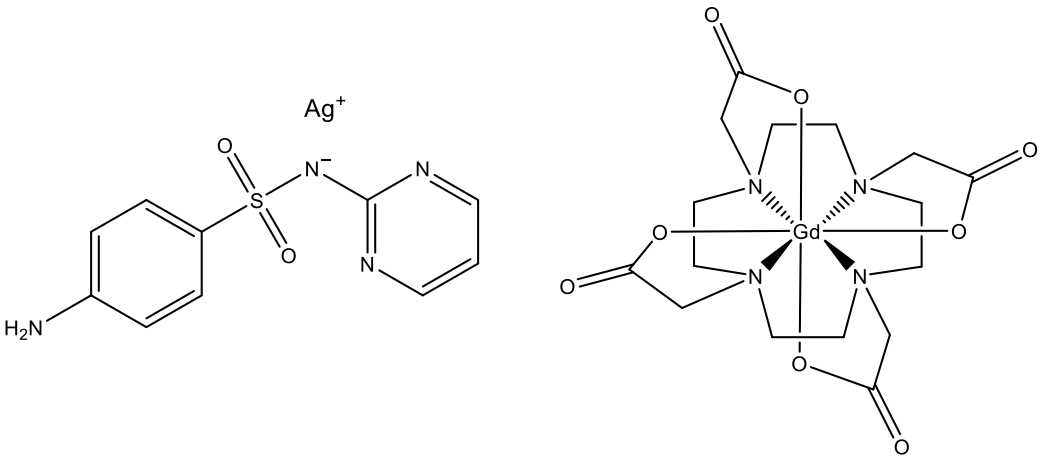


**Scheme 0.2** Chemical structures of silver sulfadiazine (left) and gadoteric acid Gd(III) complex, Dotarem (right).

Chelating compounds are extensively used in the treatment of heavy metal poisoning. Likewise, they are used to regulate the homeostasis of certain essential metal ions, such as tetrathiomolybdate (**Scheme 0.3**) employed in the treatment of Wilson's disease[9], a pathology charactherized by abnormal copper accumulation. Raltegravir[10] (**Scheme 0.3**) and several other derivatives of this drug,[11] metal chelators derived from the family of diketoacids, are used to treat HIV/AIDS infections targeting HIV integrase, a $Mg^{2+}$ dependent viral enzyme.

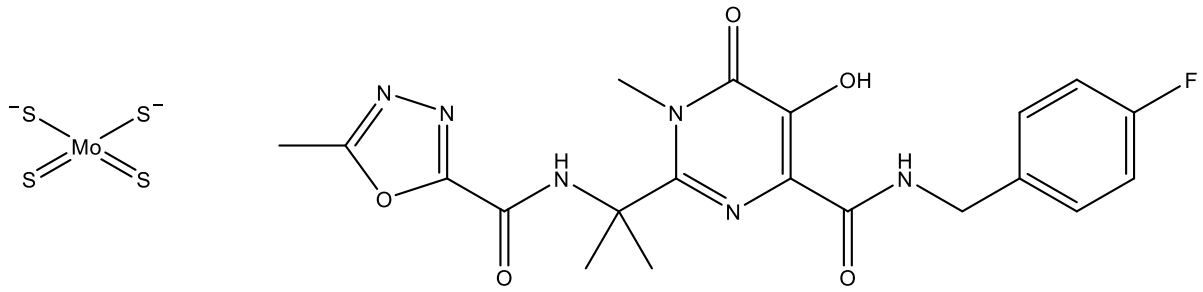


**Scheme 0.3** Chemical structures of tetrathiomolibdate (left) and Raltegravir (right).

This PhD thesis is centred on the development of bioactive compounds in two different research areas, within the context of bio-inorganic chemistry. The first one focuses on the synthesis of water soluble thiosemicarbazone scaffolds and their copper(II) complexes as compounds endowed with anticancer activity. The second one regards the synthesis of chelating compounds as inhibitors of metal-dependent viral enzymes, by using the strategy of the metal chelation of ion cofactors within the active site of the target enzymes.

# Part 1:
# Water soluble thiosemicarbazones Cu(II) complexes as anticancer agents

# Chapter 1: **Introduction to Part 1**

## 1.1 Metal-based anticancer compounds

The importance of metal-based compounds as anticancer is critical, as testified by the presence of cis-platin and its derivatives Carboplatin and Oxaliplatin in the World Health Organization Model List of Essential Medicines.[12]

The history of these metal-based compounds in cancer treatment begins in 1965 when Rosemberg discovered that *E. Coli* cell proliferation was blocked by cis-platin, *cis*-diamminedichloroplatinum(II) (CDDP), a compound previously known as Peyrone's salt. After this discovery, further studies were conducted on the cytotoxic activity of this compound on numerous cancer cell lines.[6] FDA approved the clinical use of cis-platin as an antineoplastic drug in 1979 and nowadays it is still one of the most used anticancer drugs in many chemotherapeutic regimens. Cis-platin is, in fact, very effective for treating ovarian and testicular cancer and also broadly employed in the treatment of cervical, oesophageal, bladder, head, neck and small cell lung cancer.[13]

### 1.1.1 *cis*-Platin

Platinum is a transition metal of the 10$^{th}$ group of the periodic table. Its usual oxidation states are Pt(0), Pt(II) and Pt(IV). According to the HSAB (hard soft acid base) theory, platinum is a soft metal, so it has a high affinity toward soft ligands such as thiols and thioethers.

Cis-platin (**Scheme 1.1**) is a $d^8$ Pt(II) complexes, with a planar squared coordination geometry, where two ammonia and two chloride substituents are coordinating the platinum center in *cis* position, respectively. The Pt-Cl bonds are semi-labile compared to the Pt-$NH_3$ ones, hence the $Cl^-$ ligands can be slowly substituted by nucleophiles, such as water. Pt-$OH_2$ bonds can further react with Lewis bases in cellular medium.

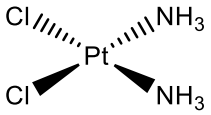


**Scheme 1.1** Chemical structures of cis-platin.

This complex exerts its cytotoxic action by covalent binding of DNA nucleobases, forming inter- and intra-strands adducts that bend the double chain and impede the DNA replication, leading to the cell death.[14]

Commonly, this drug is administered intravenously as a saline solution via injection or infusion, and it can diffuse rapidly to the tissues. In the blood stream cis-platin circulates as the neutral form since the plasma have a $Cl^-$ concentration around 100 mM.[15] The complex easily interacts with the thiols present in the plasma proteins and about 90% of it is sequestered by albumin, deactivating the drug.[14]

The remaining cisplatin can enter the cell membrane in three different ways. The major route is the passive diffusion through the membrane,[16] but it was recently discovered that OTs (Organic cations Transporters) and CTR1 (Copper transporter 1) are also involved in its transportation inside the cells.[17]

Once the complex passes the membrane, the lower $Cl^-$ concentration inside the cellular media (around 3-4 mM) causes the hydrolysis of the complex: $Cl^-$ ligands are substituted with water molecules or $OH^-$ ions forming mono- and di-aqua species[18] (**Scheme 1.2**).

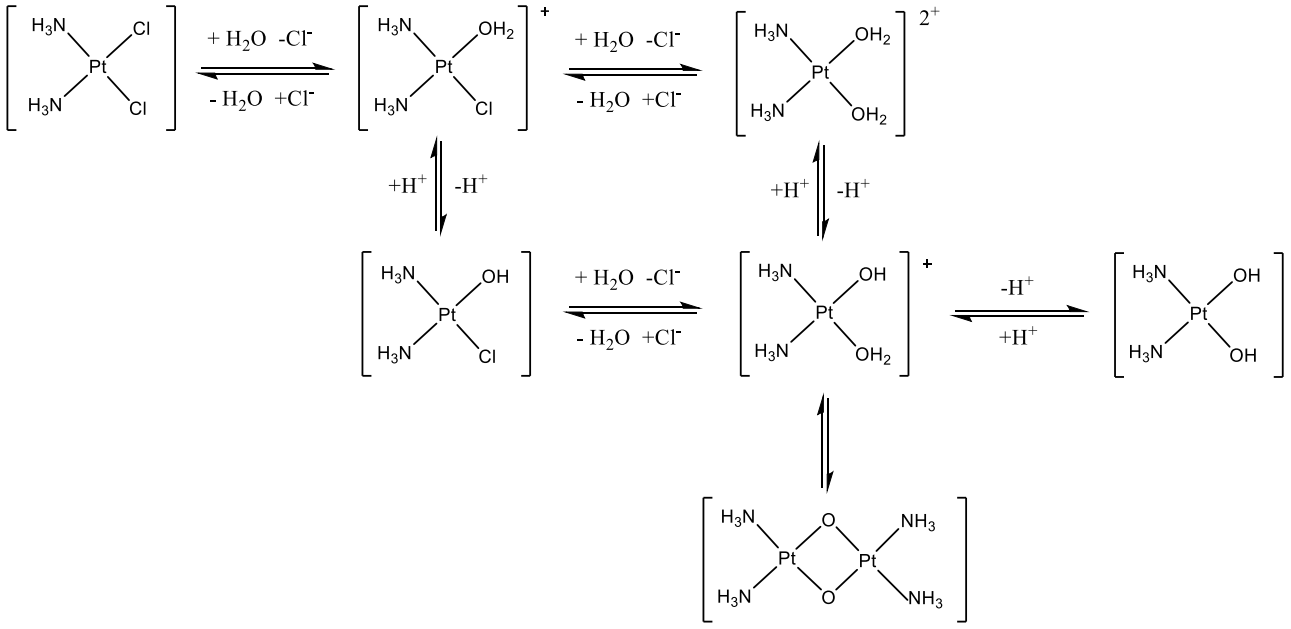


**Scheme 1.2** Equilibria of cis-platin hydrolysis in the aqueous cellular media.

The platinum aqua species are considered to be the active ones. These forms, having a more electrophilic Pt(II) center and possessing better leaving groups, can interact with DNA and many other nucleophiles in the cells, such as thiols of peptides and proteins, lipidic bilayers, RNA, metallothionein and glutathione.[14] Even if DNA is considered the main target, it is estimated that only a little amount of cis-platin that enters in the cell is able to interact with nuclear DNA.[19] When interacting with DNA, cis-platin binds preferentially with secondary and tertiary nitrogen bases, especially the purine ones (guanine and adenine),[18] because of the nucleophilicity of the imidazole group. The nitrogen in 7 position (N7) of guanine is the favored site of binding, since its broader exposure to the major groove.[14] The drug forms intra-strand bonds as major products, with around 65% Pt atoms coordinating the N7 atoms of two guanines (GpG) and 25% one guanine and one adenine (GpA).[17] The remaining cisplatin forms inter-strand bonds between guanines of different DNA filaments.[15] In the intra-strand adducts, Pt atoms are bridging the N7 atoms of two guanines (GpG), or one guanine and one adenine (GpA), in a planar geometry. An additional hydrogen bond between the $NH_3$ ligand and a 5'-phospate group of the nucleotide contributes to stabilize the adduct[15] (**Figure 1.1**).

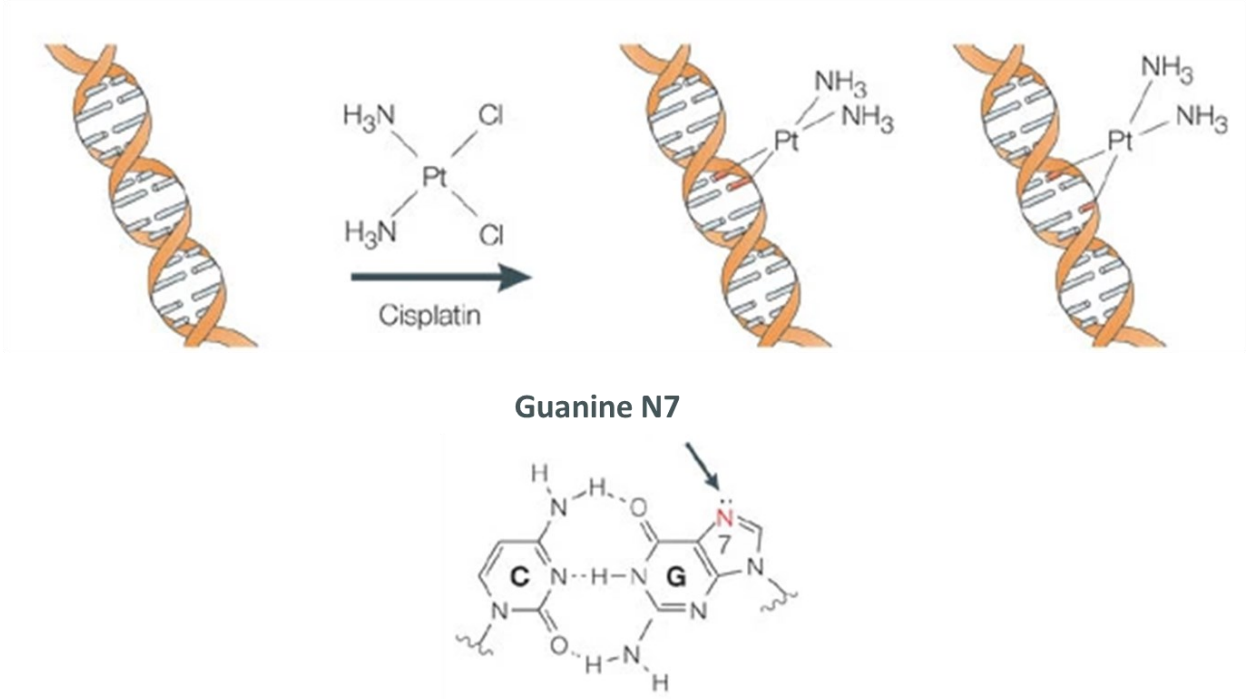


**Figure 1.1** Representation of cisplatin coordinating the N7 atom of guanines on the major groove. Adapted from ref.[18]

All these interactions cause distortion of the helices, that prevents DNA replication and transcription, activating a cascade of apoptotic events that finally results in cell death.[19]

Despite the fact that it is a very effective anticancer compound, cis-platin presents many drawbacks. It causes severe side effects, including nephrotoxicity, neurotoxicity, ototoxicity, nausea, vomiting and anemia.[14] Furthermore, some tumors display intrinsic cisplatin resistance (e.g. colorectal cancer and non-small cell lung cancer) and many others may develop acquired resistance after initial cisplatin treatments.[19]

### 1.1.2 Cis-platin analogues

In order to overcome the important side effects of cis-platin, several other Pt(II) analogues were synthetized and investigated.

Among the second-generation drugs, carboplatin displayed considerably less severe side effects: this compound, in fact, is less neurotoxic, nephrotoxic and ototoxic than cisplatin.[20] It is used commonly in the treatment of ovarian and small cell lung cancers. However, its potency is lower compared to the parent drug, thus it is usually administered in higher doses.[20] Carbo-platin has a cyclobutyldicarboxilato ligand in place of two $Cl^-$ (**Scheme 1.3**) and it has an analogue mechanism to cis-platin, hence it is not effective against cis-platin resistant tumors.[13]

Another second-generation drug is nedaplatin (**Scheme 1.3**), approved in Japan in the treatment of esophageal, head and neck cancer and different lung cancers. This complex works similarly to cisplatin, but it has a lower toxicity and weaker side effects.[21]

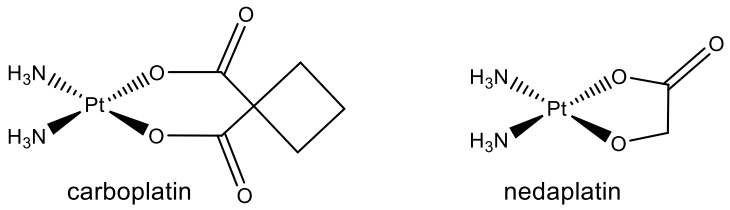


**Scheme 1.3** Chemical structures of second-generation analogues carboplatin and nedaplatin

Oxaliplatin (**Scheme 1.4**), in the third-generation of Pt(II) drugs, is a platinum complex efficient against cis-platin and carboplatin resistant tumors.[22] In this compound the amino ligands are replaced by a bidentate (*1R,2R*)-cyclohexane-1,2-diamine ligand. Oxaliplatin is particularly effective on colorectal cancer but has a broad range of antitumor activity on multiple types of cancer,[22] and its use is approved worldwide.

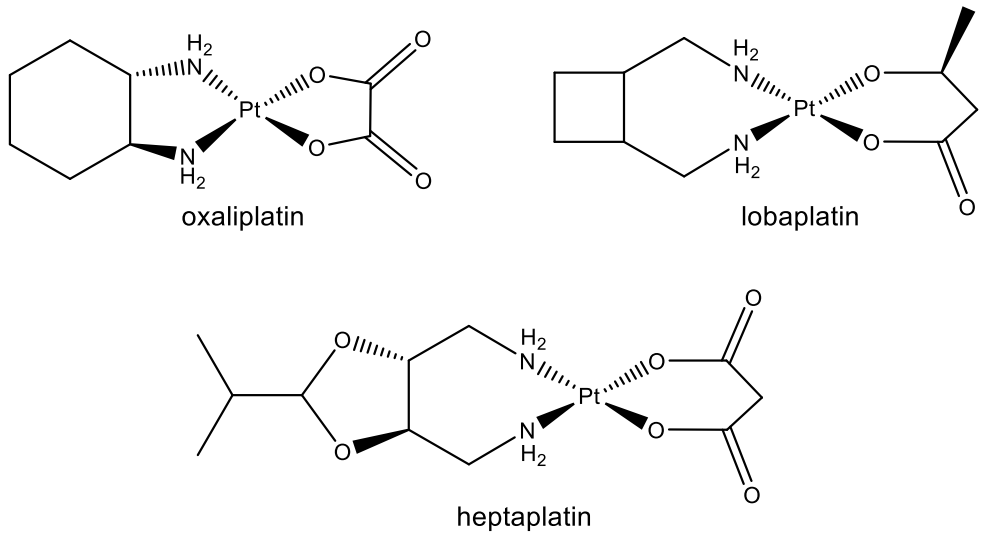


**Scheme 1.4** Chemical structures of the third-generation analogues oxaliplatin, lobaplatin and heptaplatin.

Other third generation compounds are heptaplatin and lobaplatin (**Scheme 1.4**), that are approved in clinical treatment respectively in Korea[23] and China.[24]

The research for new metal-based compounds with anticancer activity is still a very important topic. Several Pt(IV) complexes have been investigated, as Pt(II) pro-drugs. Pt(IV) complexes, having a better stability, can be administered orally and potentially cause less severe side effects.[25]

### 1.1.3 Ruthenium-based compounds with anticancer activity

Another metal that attracted attention in the search for promising anticancer compounds is ruthenium.[26] The investigation of Ru complexes anticancer activity was developed on the basis cis-platin within the studies of Clarke et al.[27] Remarkably, in 1986 Keppler et al. reported on the water soluble Ru(III) complex imidazolium-bisimidazole-tetrachlororuthenate **KP418** (**Scheme 1.5**) with *in-vivo* antitumor activity against B16 melanoma and P388 leukemia.[28] Starting from this promising result, many other related complexes have been developed and studied. Within the most notable complexes of this class are the trans-$[RuCl_4(Ind)_2]$ **KP1339** and **KP1019** and [*trans*-RuCl4(dmso-S)(Im)] **NAMI** and **NAMI-A** (**Scheme 1.5**).

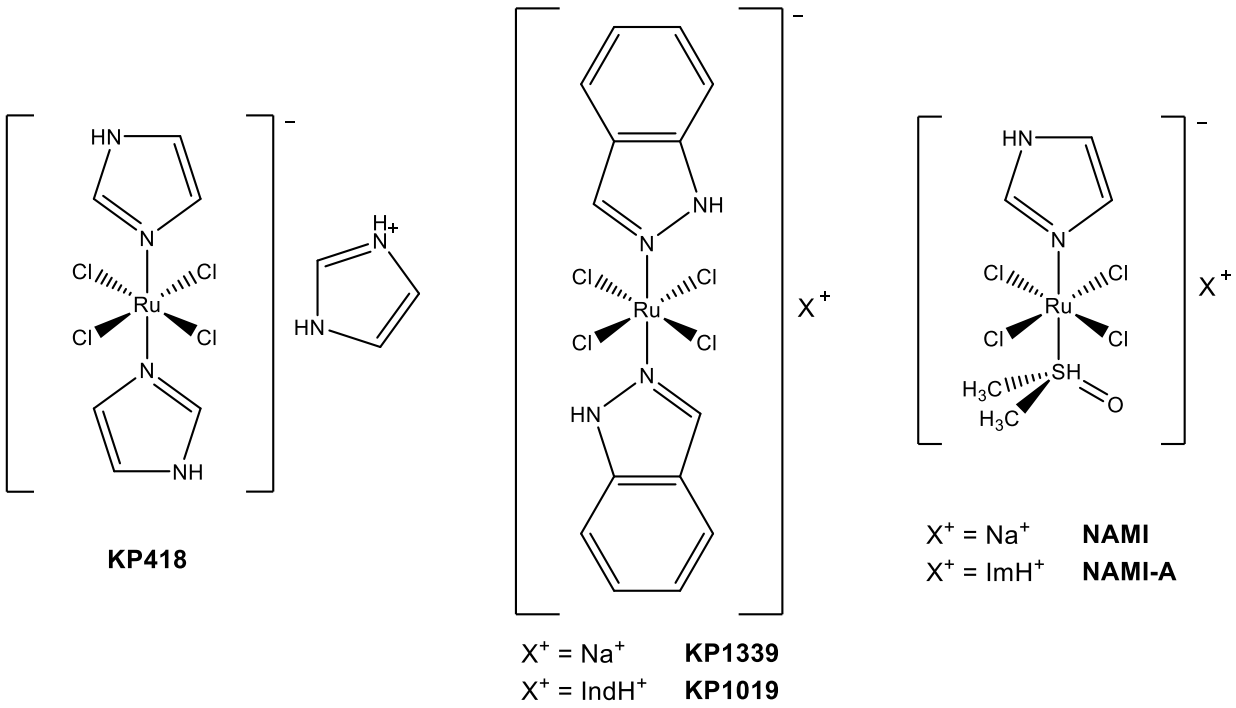


**Scheme 1.5** Chemical structure of the Ru complexes with an interesting anticancer activity **KP418**, **KP1339**, **KP1019, NAMI** and **NAMI-A**.

Complexes **KP1339** and **KP1019**, developed by Keppler et al., demonstrated high efficacy against colorectal cancers, inducing apoptosis in platinum-resistant colorectal carcinoma cells.[29] The antitumor activity of these compounds is related to their cytotoxicity, caused by the disturbance of the redox balance in the cells. These complexes, in fact, are activated by reduction to the reactive Ru(II) species, which can react with various biomolecules.[30] **KP1339** was successfully investigated in a phase I clinical trial on solid cancers, showing very limited side effects.[30]

Sava et al. disclosed the **NAMI** and **NAMI-A** Ru(III) complexes, characterized by very low cytotoxicity and by antimetastatic activity on solid tumors.[31] The antimetastatic activity of the **NAMI** compounds is thought to be based on integrin-dependent inhibition of the cancer cells motility and invasiveness, as well as their angiogenesis inhibitory action in the tumor tissues.[32] Compound **NAMI-A** was investigated in a phase I/II study in combination with gemcitabine in non-small cell lung cancer patients after first line therapy.[33]

Apart from Platinum and Ruthenium, other metals have been investigated as well, developing numerous compounds with interesting antiproliferative activity, such as palladium, iron, gold, bismuth and copper complexes.[34]

## 1.2 Copper-based anticancer compounds

The research of metal-compounds with anticancer activity has moved forward, to find innovative candidates, evaluating alternative targets and mechanisms involved in tumor development and thriving.

Among the investigated metals, copper emerged because of some interesting features: in cancer cells the level of this ion is altered respect to healthy cells, and it has a significant role in angiogenesis,[35] a key component in tumor growth and metastasis formation. Moreover, copper is an endogenous metal, as opposed to platinum. The employment of an endogenous metal could be an ideal strategy to obtain new candidates with reduces side effects.[36]

In the following paragraphs there is an overview of the role of copper in biological systems, of copper homeostasis and the role of this metal in cancer, followed by the description of some relevant copper complexes investigated as antitumor compounds.

### 1.2.1 Copper in biological systems

Copper is an essential trace metal in living organisms, the third in abundance after zinc and iron; in fact, approximatively 100 mg of Cu are present in an adult human (male).[37] Copper acts as structural and catalytic cofactor for several enzymes involved in cellular metabolism, energy generation, blood clotting, oxygen transport, iron acquisition and other functions.[37] Some examples of copper-dependent enzymes are tyrosinase, implicated in the melanin biosynthesis,[38] and ceruloplasmin, involved in iron metabolism.[39] Another copper-dependent enzyme, cytochrome c oxidase, participates in energy production being part of mitochondrial oxidate phosphorylation.[40] Zn,Cu-superoxide dismutase (CuZnSOD), being involved the conversion of toxic superoxides ions, takes an important part in antioxidative defence of the body.[41]

In the biological systems, copper ions exist in two oxidative states: $Cu^{+}$ (reduced) and $Cu^{2+}$ (oxidized). The coordination chemistry of the Cu(I) is generally characterized by a tetrahedral geometry, preferring sulphur "soft" donor species, such as methionine and cysteine.[37] The $Cu^{2+}$ ions have coordination numbers 4 or 6; the hexacoordinated Cu(II) ions generally present a distorted octahedral geometry, due to Jahn-Teller effects. The $Cu^{2+}$ ions prefer the coordination with harder donor species respect to Cu(I), such as the oxygen and nitrogen donor atoms of glutamic acid or histidine.[42]

$Cu^{2+}$ is the most stable oxidation state, while $Cu^{+}$ undergoes rapidly dismutation or oxidation. The redox activity of these ions is fundamental in the functioning of many enzymes involving redox processes and in the scavenge of free radicals.[43]

The concentration of free copper ions into the cells is very low, estimated to be about $10^{-13}$ M in human blood plasma,[43] and higher concentration can cause damage to the cell membrane, nucleic acids and proteins. The main mechanism that is thought to be responsible for copper-induced toxic activity in cells derives from the tendency of copper species, both Cu(II) and Cu(I), to form reactive oxygen species (ROS).[44] In the presence of superoxide ions ($^{\bullet}O_2^-$) or other reducing agents such as ascorbic acid, Cu(II) can be reduced to Cu(I). Cu(I) is then able to catalyze the formation of hydroxylic radicals ($^{\bullet}OH$) from $H_2O_2$ via Fenton and Haber-Weiss reaction (**Scheme 1.6**).[45]

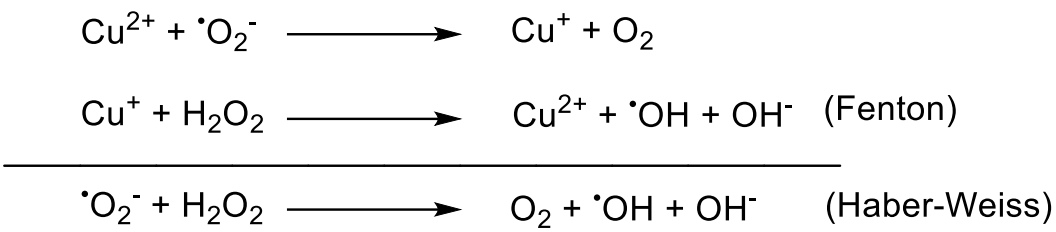


**Scheme 1.6** Fenton and Haber-Weiss reactions catalysed by copper(II) ions.

•OH radical species are particularly reactive, hence they can interfere with several biological molecules, causing oxidative damages to the cell. Additionally, an excess of Cu can exert a toxic effect by replacing other metal co-factors. For instance, it was shown that $Cu^{2+}$ can substitute $Zn^{2+}$ ions in the *zinc finger* domain of DNA-binding proteins, causing damage to these proteins.[46] This was proposed as an alternative mechanism of toxicity exerted by copper ions. To avoid all these effects, copper homeostasis is tightly regulated in the body.

#### 1.2.1.1 Copper homeostasis

Copper homeostasis is an important process since both an excess and a deficiency of this essential element can cause a detrimental effect in the health of organisms.

After being absorbed in the intestine, copper(II) in the blood stream binds rapidly to plasma proteins (ceruloplasmine, albumin and transcuprein) that transport the ions to the cell membrane.[47] Cu enters the cells through the transmembrane protein transporters CTR1 and CTR2 (Copper Transporter 1 and 2), and divalent metal transporter 1 (DMT1)[48] as Cu(I), after being reduced by the metalloreductase protein STEAP[49]. Once inside the cells, copper is bound to chaperone proteins that are specific for Cu delivery to copper-dependent proteins. For instance, COX17 (cytochrome C oxidase chaperone) participates in the activation of cytochrome C oxidase and CCS (copper chaperone for SOD1) provides copper to SOD1.[50] ATOX1 (antioxidant protein 1) delivers copper to several proteins in the trans Golgi network, such as APT7A and APT7B, that are responsible for transferring the copper to other enzymes and for removing the copper excess from the cells.[50]

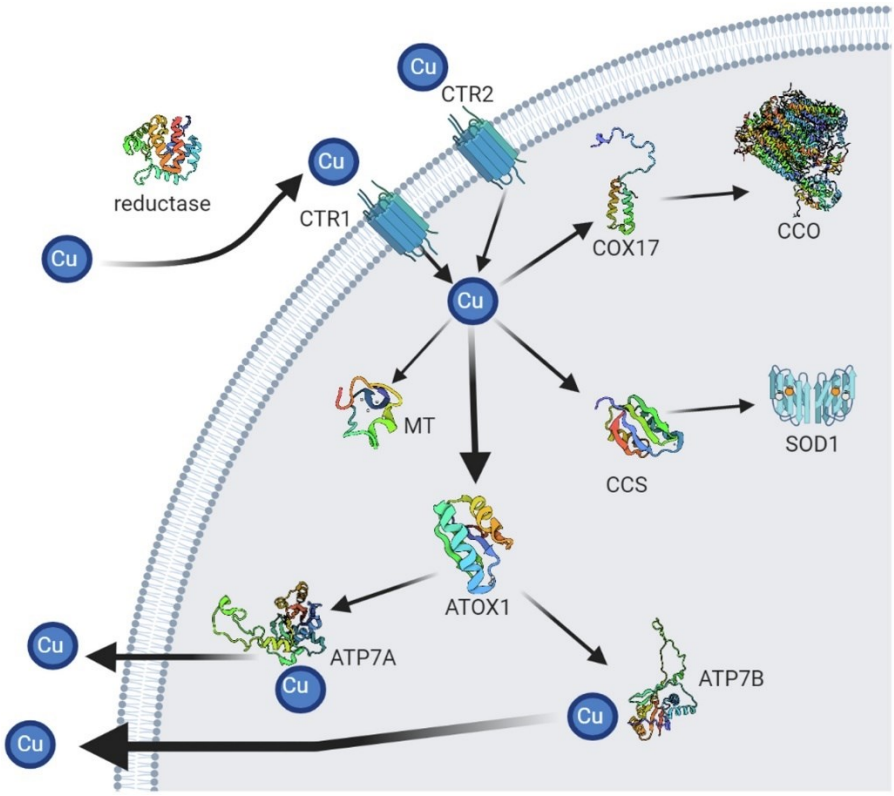


**Figure 1.2** Schematic representation of copper metabolism inside the cell. Copper penetrates in the cell through CTR1 receptor. Receptor CTR2 mediates the release of copper from intracellular vesicles. Intracellular copper is bound with several copper chaperones to many proteins (MT, COX17, CSS, ATOX1), that can deliver copper to specific copper enzymes. Copper is removed from the cells by ATP7A and ATP7B. Da Silva et al.[42]

The balance of the free Cu ions concentration is mainly controlled by the binding of copper with glutathione (GSH), a tripeptide that possesses antioxidant functions.[51] In cells the GSH concentration is greater than free Cu ions, hence GSH acts as a buffer to prevent toxic levels of free Cu ions. In fact, the first acceptor of copper ions after they enter the cell is GSH, then copper is either transferred to chaperone

proteins or to metallothioneins (MTs).[52] MT is a family of proteins rich in cysteines that can bind to Cu ions preventing an overload of the metal in the cytosol and serving as a copper storage.[53]

An altered copper homeostasis can lead to serious disorders, in fact several diseases are related to imbalanced levels of copper. Wilson's disease is characterized by an excessive accumulation of copper in liver.[54] It is caused by a mutation in genes coding for ATP7B, a Cu transporter protein involved in the trafficking of Cu,[54] that causes a failure of copper excretion onto the bile. This disease is responsible for neurological manifestations, acute hepatitis and cirrhosis.[55] Menkes disease, on the other hand, is characterized by a copper deficiency. It is a genetic disease caused by mutation in genes coding for ATP7A,[56] a copper transporter that regulates Cu entry in the bloodstream through enterocytes. This mutation impairs the copper absorption in the intestine, leading to very low copper level in the organism. This pathology causes nervous system abnormalities, such as developmental retardation and disability and generally severe patients do not reach three years of age.[57]

Additionally, abnormal copper accumulation is linked with neurodegenerative diseases (e.g. Alzheimer's and Parkinson's disease),[37] and with other pathologies like epilepsy, diabetes, rheumatoid arthritis and cancer.[36]

#### 1.2.1.2 Copper and cancer

WHO defines the term cancer as a large group of diseases, that can affect any tissue or organs, characterized by abnormal and uncontrolled cells growing, that eventually spread to other part of the body (metastasis). Cancer is identified as the second leading cause of death worldwide. Generally, the origin of a tumor is associated with cell genetic mutations. The first altered cell acquires an increased capacity of proliferation, consequently transmitting the alteration to other cells originated from it. The uncontrolled proliferation forms then a solid and complex mass of cells (parenchyma) plus an extracellular matrix and an interplay of cells (stroma) surrounding the solid tumor. Tumor microenvironment (TME) is a term that indicates all these cells together with molecules and macromolecules secreted by the tumoral cells. The composition of a TME varies significantly between tumor types, but the characteristic features include stromal cells, immune cells, blood vessels and the extracellular matrix.[58]

Many studies evidence that cancer tissues and serum from cancer patients have increased level of copper. In several *ex vivo* cancer tissues (e.g., lung, prostate, breast, breast, bladder, hepatocellular carcinoma, haematological malignancies) was found a higher concentration of copper compared to normal tissues.[36][59][60][61][62][63][64] In fact, cancer cells may exhibit a different copper homeostasis, and this can be considered an interesting target for antitumor therapy.[42]

It was demonstrated that a different expression of copper chaperones and pumps involved in uptake and distribution of copper is implicated in cancer. For example, it was showed that ATOX1,[65] upon binding with copper, and ATP7A[66] are required for cell proliferation. Different studies report the involvement and overexpression of CTR1, ATP7A, ATP7B, COX17 and ATOX1 in various types of tumors.[67][68] Additionally, copper, via binding different protein kinases, appears to be involved in a signal cascade that leads to cell proliferation and tumorigenesis.[69][70] Copper takes part also in the regulation of apoptosis cancer cell death. The X-linked inhibitor of Apoptosis Protein (XIAP) allows cell proliferation by preventing apoptosis events. XIAP is able to bind copper interacting with CCS and its overexpression in various tumors is associated with a worse prognosis for the patients.[71]

It has been proved that copper is not only involved in cell proliferation but also in tumor cells spreading. This spreading process requires a conversion of cancer cells, from epithelial to mesenchymal phenotype called Epithelial to Mesenchymal Transition (EMT), necessary for the metastasis. Different copper-binding proteins participates in the EMT, such as CTR1[72] and CCS.[73] Furthermore, in order for the cells to migrate it is necessary a remodelling of the extracellular matrix. The family of copper-enzymes Lysine Oxidase (LOX) is essential for this process, catalysing the lysine oxidation to elastin and collagen. It was shown that LOXs have a key role in promoting stiffness in colorectal cancer, that induces an increased proliferation and invasion.[74] Additionally, a protein associated with migration and metastasis of breast cancer cells, Mediator of ErbB2-driven cell Motility (MEMO1), was proved to be a Cu(II) binding protein.[75]

Another crucial process for the growth of cancer tissues is angiogenesis, i.e. the vascularization and formation of new blood vessels. Copper is required in the activation of many actors of angiogenesis, such as angiogenin, Vascular-Endothelial Growth Factor (VEGF) and ceruloplasmin.[76] Angiogenin protein is overexpressed in numerous types of tumors, and upon copper(II) binding it is associated with a stronger interaction with epithelial cell receptors, resulting in increased cells proliferation and migration.[77]

The involvement of copper in all these cancer pathways makes this metal a good candidate for the development of antitumor drugs.

Several copper chelating agents were tested for cancer treatment, in particular D-penicillamine (D-pen), triethylenetetramine (TETA) and tetrathiomolibdate (TTM) (**Scheme 1.7**), all of them known for the treatment of Wilson disease or copper toxicosis.

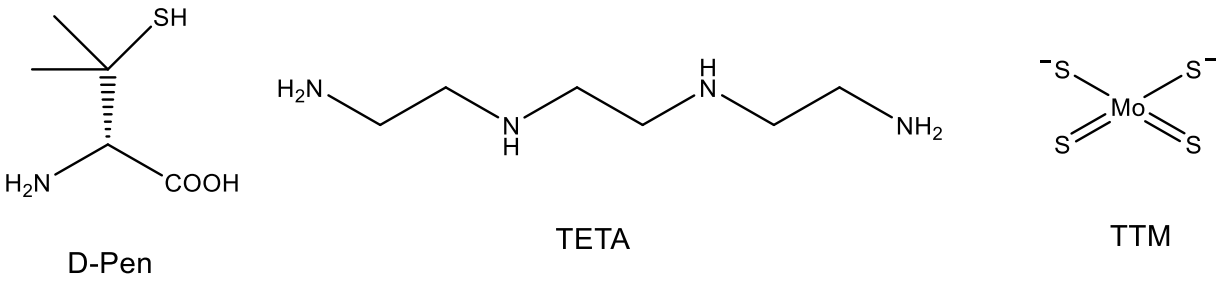


**Scheme 1.7** Structure of the copper chelating compounds D-Pen, TETA and TTM.

Following the positive results on animal models of brain tumors, clinical trials were started with D-pen being administered, together with a low-Cu diet, to glioblastoma multiforme patients. The D-pen treatment was well-tolerated by the patients, however, unfortunately no significant increase in the survival rate was observed.[78]

TETA was tested in clinical practice for cancer therapy. Its anticancer activity is linked to inhibition of SOD1, telomerase and angiogenesis.[79] In clinical trials TETA was used in combination with carboplatin and other drugs for the treatment of peritoneal, ovarian and tubal cancers. Within these trials no dose-limiting toxicity was observed, but no correlation between the copper levels (or ceruloplasmin) and the clinical response of patients was reported.[80]

Tetrathiomolybdate (TTM) showed anticancer properties *in vitro* and *in vivo*, related to its copper chelating activity.[81] Several clinical trials involving TTM indicates that this compound is relatively well tolerated; however, its efficiency when administered as a sole therapy could be limited, especially in metastatic and large tumors.[81][82]

### 1.2.2 Copper complexes with antitumor activity

Complementary to the strategy of copper chelation and sequestration from cancer cells, the use of copper-complexes may represent a suitable strategy to selectively target cancer cells. In fact, copper complexes can exert anticancer activity via various mechanisms towards interesting targets in cancer therapy.

A critical factor in the success of copper-based anticancer compounds is the choice of the ligands, since it can regulate the hard/soft properties of the metal center, its redox potential and hydrophilic/lipophilic characteristic of the complexes, resulting in their solubility in extracellular fluids and/or in their ability to permeate though the lipidic bilayer of the membranes. Moreover, the stability of the complex is of crucial importance: it should be stable enough to reach the desired target, but relatively labile to engage with the binding site. Choosing different chemical scaffolds coordinating the copper can tune all these properties, together with the metal bioavailability and the complex toxicity.

A large variety of classes of copper complexes with anticancer activity have been studied over the years,[36] and within the most studied are thiosemicarbazones (TSCs) and polypyridine copper(II) complexes.[42]

Of the latter class, copper(II) complexes of ligands named Casiopeinas® (general formula $[Cu(N–N)(L–L)]^{n+}$ with: n = 1, 2, N–N = 4,7-dimethyl-1,10-phenanthroline or 4,4'-dimethyl-2,2'-bipyridine, and L–L = different bidentate chelates) resulted having particularly interesting antiproliferative activity,[83][83][84] and copper(II) compound Casiopeina III-ia (Cas-III-ia, **Scheme 1.8**) is currently been studied in a phase I clinical trial.[85]

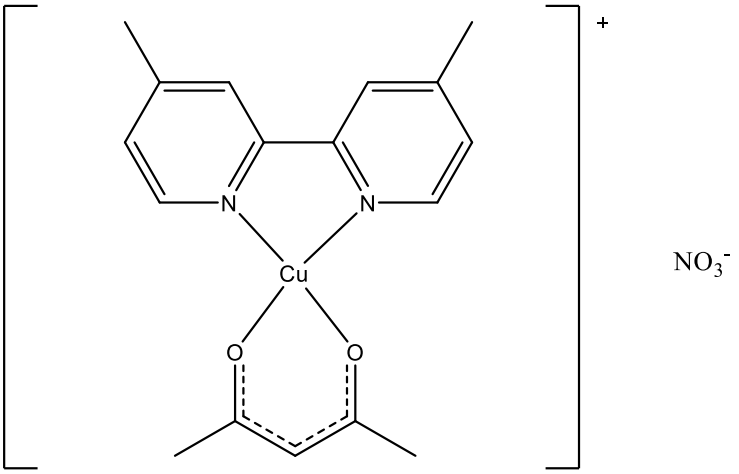


**Scheme 1.8** Chemical structure of Cas-III-ia copper(II) complexes, compound in phase I clinical trial for cancer treatment.

In case of copper(I) complexes, on the other hand, one of the most important class of ligands is the phosphines.[36] Copper(I) species are particularly labile and subject to redox reactions. These species can be stabilized by robust metal-ligand interactions such as copper-phosphine. Several $[Cu(P)_4]^+$ complexes have been tested for their anticancer activity. For instance, a water-soluble tris(hydroxymethyl)-phosphine Cu(I) complex (**Scheme 1.9**) was investigated *in vitro* against a large panel of human cancer cell line, showing a significant antitumor activity.[86] This compound, in fact, displayed a greater activity compared to cisplatin used as a reference and work with a different mechanism of action than cisplatin, overcoming the issue of platinum drug resistance.[86]

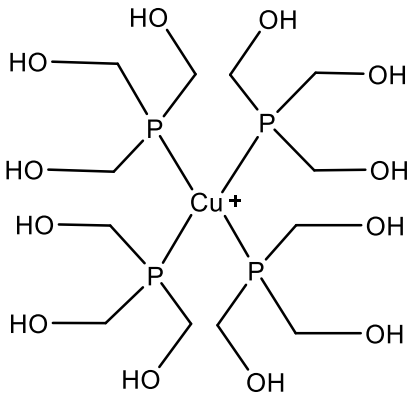


**Scheme 1.9** Structures of the cationic portion of the $[Cu(P)_4]^+$ complex with tris(hydroxymethyl)-phosphine ligands.

Copper-based compounds are believed to have a broader activity and lower toxicity compared to cis-platin and the other platinum drugs. The proposed mechanisms of action of copper complexes, in fact, are differentiated from the platinum complexes that bind covalently to DNA. Anticancer activity of some copper compounds was related to their ability to interact with DNA, while in the most recent years many other targets complexes are emerging, as detailed in the following paragraph.[42]

### 1.2.2.1 Anticancer mechanisms of copper-based compounds

Carcinogenic cells often have a faster metabolism rate compared to normal cells, generally leading to higher levels of ROS. Furthermore, cancer cells usually have low activity in SODs,[87] antioxidant enzymes that convert superoxide radicals. The excess of superoxide can further be metabolised in peroxynitrite and perhydroxyl radical, involved in tumor formation.[88] ROS species are important regulator factors in programmed cell death, in fact an imbalance in ROS production or depletion can mediate a signal for apoptosis or paraptosis cell death.[89] Some of the accredited copper complexes mechanisms of anticancer activity are the production of ROS species (through Fenton-like reactions)[90] and/or acting as a CuZnSOD mimetic.[91] These mechanisms create a redox imbalance, that combined with the already greater ROS level of cancer cell leads to excessive oxidative stress that activates programmed cell death. For instance, some bis- and tris-chelate copper complexes incorporating 1,10-phen have a good anticancer activity and act as SOD mimetic in mammalian cells[92][91] causing cell apoptosis.[93] Apoptosis is not the only type of programmed cell death induced by copper complexes: some of them can also cause paraptosis, a non-apoptotic death, as described for example for a thioxotriazole copper(II) complex[94] and for some phosphine copper(I) complexes.[95]

The ability of copper to bind DNA is known since the sixties[96] and in 1991 a structured depicting a DNA-Cu adduct obtained after soaking with $CuCl_2$ was published. This structure describes the copper bound to N7 atom of a guanine residue[97], analogously to what observed for cisplatin. According to these findings, also several copper complexes has been investigated as DNA-targeting drugs. It has been found that copper derivatives are capable of forming non-covalent interactions with DNA, rather than covalent adducts. In particular, these noncovalent interactions comprise electrostatic, intercalative, and groove binding of the copper complexes along the minor and major DNA grooves.[36] To mentions a few, copper(II) complexes containing 1,10-phen[98] and similar diimines[99] and recently other ligands (such as flavonoids[100] and Schiff base ligands[101]) have been studied for their DNA targeting activity. These studies showed in many cases that the intercalation causes deformation of the DNA structure favouring cleavage processes, achieved through different pathways involving nucleobase or deoxyribose oxidation or hydrolysis of phosphate esters.[36]

It was also reported that some copper complexes can inhibit topoisomerases (topos). Topos are essential enzymes located in the nuclei that control the underwinding and overwinding of DNA supercoils, therefore playing a vital role in the DNA replication and transcription. These class of enzymes catalyses interconversion between different topological isomers of DNAs,[102] hence the name. Among others, it was shown that the ability to inhibit leukemia cell proliferation by a salicylaldoxime copper complex is related to its interference with Topo II, that induces an enzyme-linked single strand break in the DNA.[103] Additionally, a $\alpha$-heterocyclic TSCs copper complex and its free ligand exhibit a greater *in vitro* inhibition of Topo II than etoposide, a well-known Topo II inhibitor.[104] Together with other metals complexes, a copper pyrophosphate-bridged complexes was found to inhibit Topo I in the millimolar concentration range. This mechanism, combined to DNA interaction and oxidative stress, contribute to the cytotoxic action of these compounds on the adriamycin-resistant ovarian cancer cell line.[105]

Another target of copper compounds with antitumor activity is proteasome, a large multiprotein complex situated in the nucleus and cytoplasm that modulates the degradation of intracellular proteins. In particular, the ubiquitin proteasome-dependent degradation system is involved in many processes crucial for the tumor and metastasis formation, such as cell proliferation, angiogenesis and apoptosis.[106] Furthermore, it was shown that cancer cells are more receptive to proteasome inhibition than healthy cells, undergoing a rapid apoptotic process.[107] Hence, the ubiquitin proteosome pathway appears to be a promising anticancer strategy and a large number of compounds have been extensively investigated for

their activity on proteasome. The first class of copper compounds reported to be capable of proteasome inhibition were Cu(II) complexes with bidentate ligands of the 8-OH quinoline family, that induced apoptosis in human leukemia cells *in vitro*.[108] After these compounds, many other copper complexes proteosome inhibitors have been discovered, such as pyridinyl methylamino methylphenol Cu(II) complexes[109] and neocuproine Cu(I) and Cu(II) complexes.[110] In this study it was highlighted that the Cu(I) complex have a slightly higher activity on purified 20S proteosome, causing apoptosis in breast cancer cells. It was also observed that the proteasome was able to reduce Cu(II) to Cu(I), suggesting is the Cu(I) species that possibly reacts with the target.[110]

Protein disulfide isomerase (PDI) have quite recently emerged as a novel target of some TSCs copper complexes. PDI is a family of enzymes that reside in the endoplasmic reticulum, cell surface and cytosol.[111] PDI possess protein folding, molecular chaperon and disulfide isomerase/oxidoreductase functions,[111] which means they break, form or rearrange disulfide bonds between cysteines residues of proteins. It was found to be a copper binding protein,[112] and it has emerged as an important player in many diseases including cancer, for its role in cell migration and adhesion.[113] For these reasons it was investigated and identified as a target of some Cu(II) copper complexes with anticancer activity. These complexes inhibit PDI activity,[114][115][116] while the free ligands are not active, suggesting the necessity of copper coordination for the PDI inhibition.[115]

### 1.3 Thiosemicarbazones as anticancer agents

The thiosemicarbazones (TSCs, **Scheme 1.10**) have gained interest in the research of a good drug candidate, because of their relatively easy and cheap synthesis and their different biological properties (anticancer, antiviral and antifungal).[117] In the next paragraph it will follow a brief discussion on TSC chemistry and anticancer activity of TSC ligands and their Cu(II) complexes as anticancer compounds.

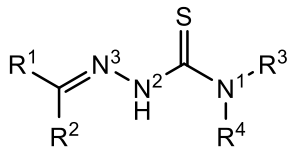

**Scheme 1.10** General structure of TSC scaffold.

#### 1.3.1 Thiosemicarbazone chemistry

TSCs are a class of Schiff's bases, usually prepared through condensation reaction between an aldehyde or ketone and a thiosemicarbazide. These compounds display tautomerism in solution, between the thione and the thiol form (**Scheme 1.11**). The deprotonation of the thiol leads to the anionic form of the TSC. These ligands can coordinate transition and non-transition metals, both in the thiol and in the anionic form.[118]

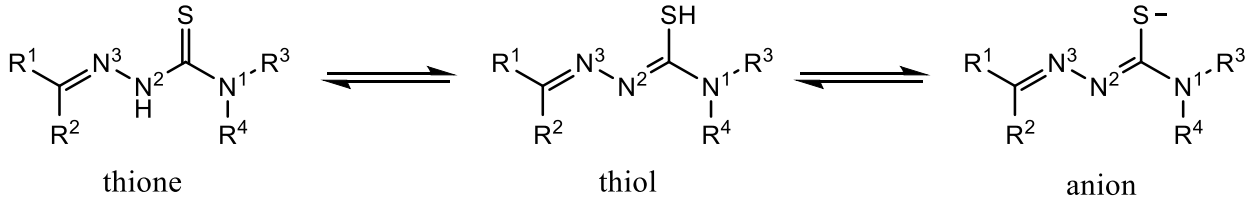


**Scheme 1.11** Thione-thiol tautomerism in the thiosemicarbazones; deprotonation of the thiol leads to the anionic form.

Different binding modes have been observed for TSCs in the anionic and neutral forms, and their denticity can vary depending on the substituents on the scaffold. TSCs can behave as N,S bidentate, N,S,D (D=O,N) tridentate or tetradentate ligands, in case they possess additional donor atoms on $R^1$ or $R^2$.[36]

The neutral form can coordinate a metal via various modes, showed in **Figure 1.3**: $\eta^1$-S (a), $\mu_2$-S (b), $\eta^2$-$N^3$, S-chelation (c), $\eta^2$-$N^3$, S-bridging and S-chelation (d).[118]

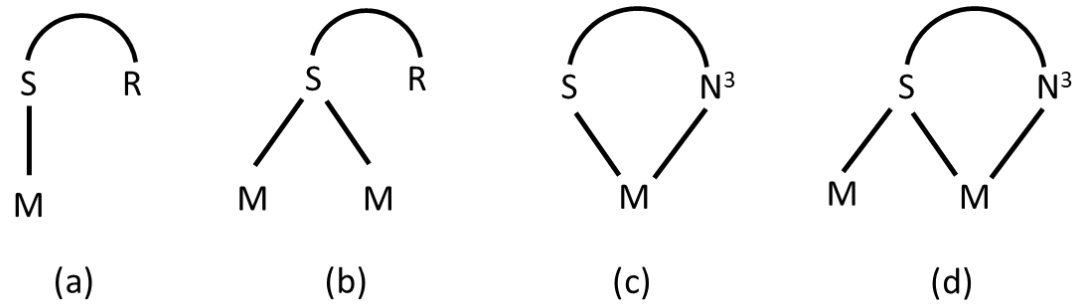


**Figure 1.3** Metal binding modes of TSCs.

Nevertheless, if the TSC bears a $R^1$ or $R^2$ substituent containing a donor atom (D), additional binding modes (**Figure 1.4**) can occur: $\eta^3$-D, $N^3$, S-chelation (e), $\eta^4$-D, $N^3$, S-chelation and S-bridging (f), and $\eta^4$-D, $N^3$, S-chelation and D-bridging (g).[118]

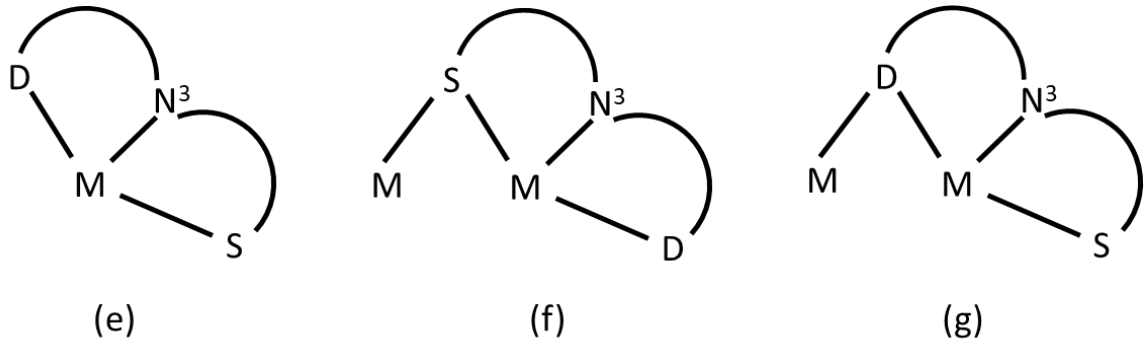


**Figure 1.4** Metal binding modes of TSCs bearing a donor atom on $R^1$ or $R^2$ substituents.

The same binding modes of the neutral TSC form (a-g) can also be observed with the anionic form of the ligands. Additionally, other modes that involve atom $N^2$ have been found (**Figure 1.5**): $\eta^2$-$N^2$, S (h) and $N^2$, S-bridging and S bridging (i).[118]

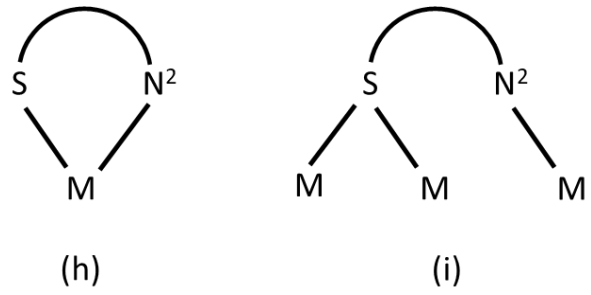


**Figure 1.5** Metal binding modes of the anionic form of TSCs.

TSCs pharmacological applications are tightly related to their ability to bind transition metal ions, such as iron, zinc and copper, often times forming lipophilic, neutral and stable complexes.[119] TSCs commonly act as ionophores, chelating the metal ions in the extracellular medium and transporting them through the membranes into the cell.[47] Ionophores, in contrast to traditional chelating agents that cause elimination of a metal, typically enable the intracellular access of the metal, increasing its concentration inside the cell.[119]

The activity of a metal ionophore is dependent on the concentration of the metal, hence decreased level of the metal ions and the use of metal free ligands frequently cause either no or lower activity.

### 1.3.2 Thiosemicarbazones with anticancer activity

The first reported TSC derivative with antitumor activity dates in the 1950s,[120] and after broad investigation on structure-activity relationship, the most promising candidate 5-hydroxyl-2-formylpyridine thiosemicarbazone (5-HP) (**Scheme 1.12**) was tested in phase I clinical trials, showing anticancer activity on leukemia patients but not on solid tumors.[121] Unfortunately, these tests also revealed fast inactivation of the drug and severe side effects, hence the clinical investigations on this compound were withdrawn.[121] Further optimization studies led to the identification of 3-aminopyridine-2-carboxaldehyde thiosemicarbazone (Triapine or 3-AP) (**Scheme 1.12**). Triapine has been investigated in dozens of phases I and II clinical trials as anticancer, both as a monotherapy or in combination.[122][123][124][125][47] Similarly to 5-HP, it showed encouraging activity against hematologic cancers, while the activity on solid tumors is not significant.

More recently, two α-N-heterocyclic thiosemicarbazone derivatives demonstrate a remarkable anticancer activity and entered clinical evaluations. COTI-2 (**Scheme 1.12**) is a third generation TSC compound, that has demonstrated a potent anti-proliferative action against a large set of human cancer cell lines, both *in vitro* and *in vivo*, displaying a greater activity than cetuximab and erlotinib[126] approved chemotherapeutic drugs. Furthermore, it also proved to be very effective (with $IC_{50}$ values in the nM range) towards triple negative breast cancer.[127] Currently, COTI-2 is undergoing a phase I clinical trial for the treatment of recurrent or advanced cancers in mono- or combination therapy (NCT02433626).

TSC derivative Dpc (**Scheme 1.12**) is able to inhibit pancreatic cancer cell lines *in vivo* with $IC_{50}$ in the low nanomolar range, showing a significantly greater activity compared to Gemcitabine and 5-Fluorouracil[128] (employed in the treatment of these tumors). In 2016 started a phase I trial to assess DpC[129] pharmacokinetics and the tolerated doses in patients with advanced solid tumors (NCT02688101).

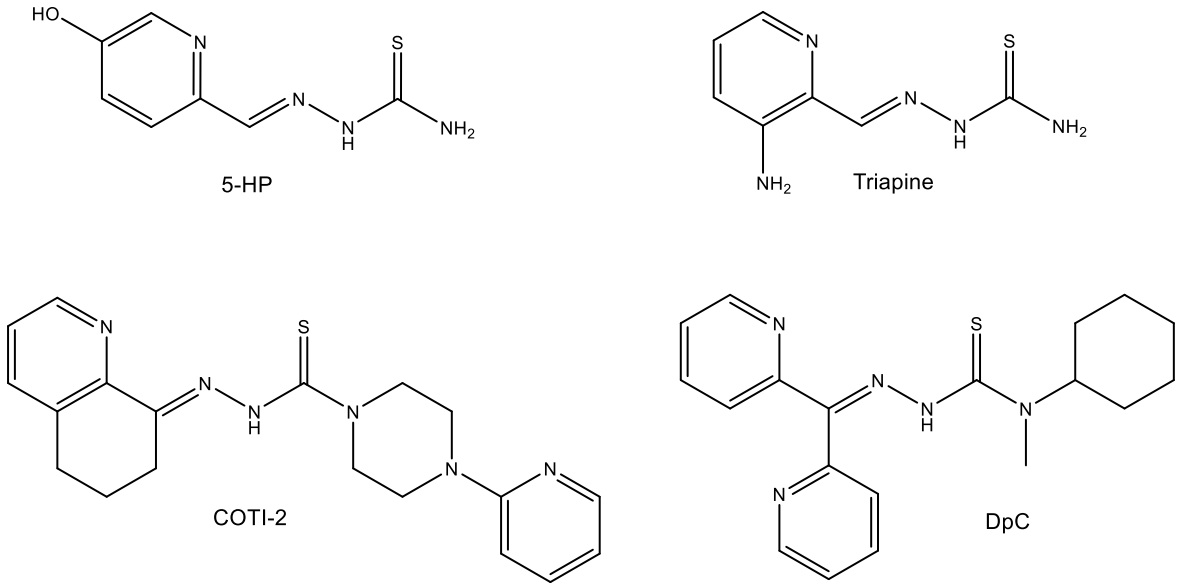


**Scheme 1.12** Chemical structures of some TSCs clinically investigated as anticancer.

TSCs can exert their anticancer activity via different pathways, depending on their structural variations that can also modulate their coordination properties. In fact, the ability of TSC to interact with both Fe and Cu is considered to be related in multiple ways with the anticancer activity of these ligands.[114] Copper and iron, can be involved in the production of ROS and in the activation of various redox cycles. Notably, often TSC metal complexes show an improved cytotoxic activity and a different mode of action compared to their

ligands. One of the most studied and recognized targets of this class of compound is ribonucleotide reductase (RR).[120] RR is an iron binding enzyme crucial for the DNA synthesis and DNA damage repair. This enzyme is regularly overexpressed in cancer cells, therefore results to be an effective target for anticancer compounds.

### 1.3.3 Copper complexes of thiosemicarbazones with anticancer activity

A large variety of copper complexes of TSC derivatives has been investigated for their anticancer potential.[36][42] In **Scheme 1.13** are reported some of the Cu-TSC copper complexes with good anticancer activity developed in the last years. Richardson et al.[130] reported that the copper complexes of di-2-pyridylketone thiosemicarbazones (**Scheme 1.13-a**) display an $IC_{50}$ in the nanomolar range on SK-N-MC neuroepithelioma cells, with an increased potency respect to the free ligands and the analogue iron complexes. Yang and colleagues described a new N-heterocyclic thiosemicarbazone complex containing copper(I) and copper(II)[131] (**Scheme 1.13-b**) with very effective activity toward several tumor cell types and antimetastatic activity. Some steroidal TSC-derivatives (**Scheme 1.13-c**) reported by Cui et al. resulted to be more active than cisplatin in *in vitro* tests on human liver carcinoma and human cervical carcinoma cells, while displaying a similar cytotoxicity towards normal kidney epithelial cells.[132]

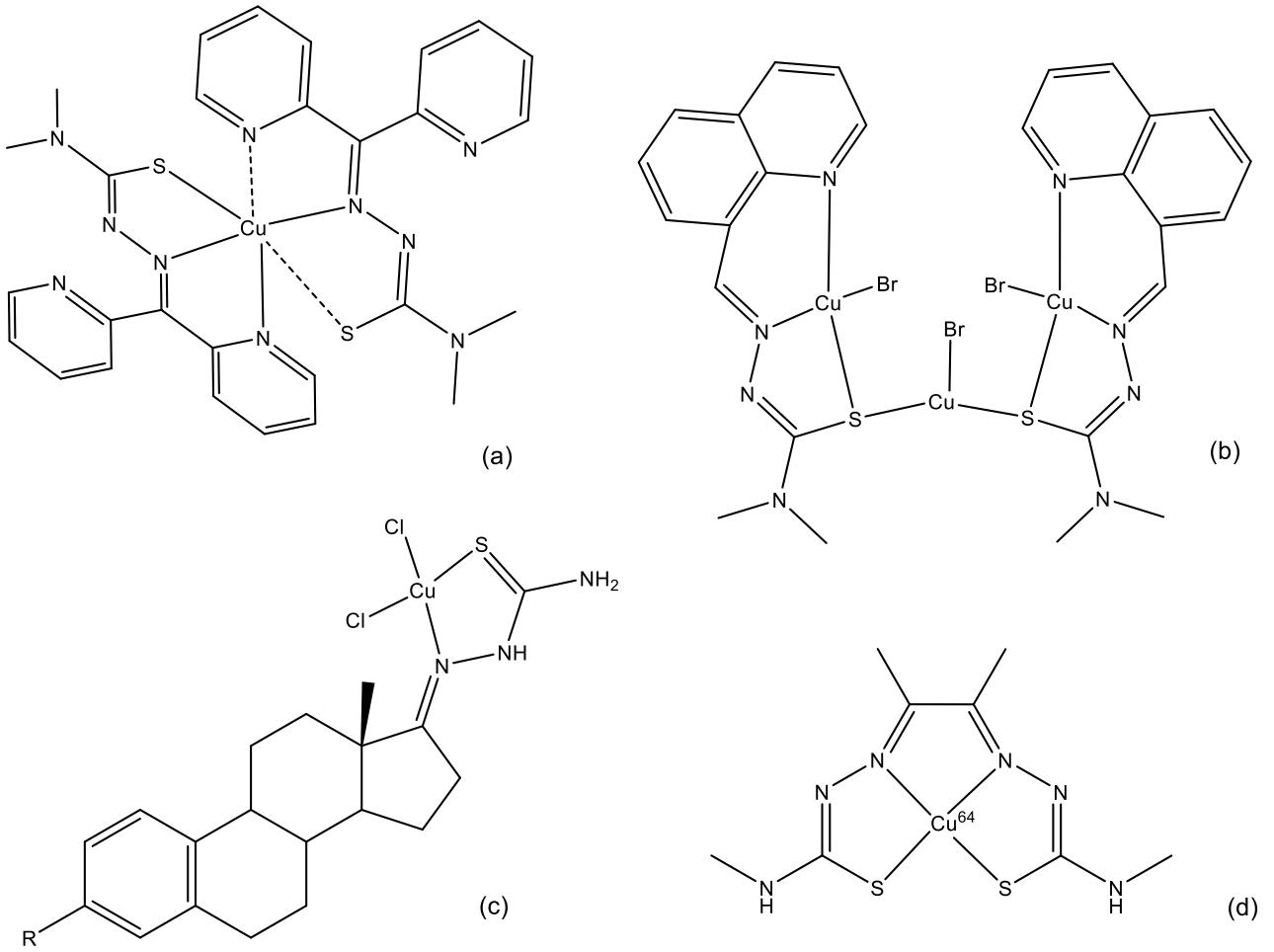


**Scheme 1.13** Chemical structures of Cu(II)-TSC complexes with anticancer activity (a, b, c), and Cu(II)bisTSC complex for PET imaging (d).

Given the importance of copper in the tumor microenvironment, the use of $Cu^{64}$ as a radiometal was investigated. $Cu^{64}$ radioisotope has a half-life of ≈ 12 hours and decays with positron and beta particles emission, making it suitable for both radiotherapy and positron emission tomography (PET) imaging. During the sixties it was found that some bisthiosemicarbazone compounds were not just effective as anticancer, but they also accumulate in the tumoral tissues.[42] Within this context, the complex of bis thiosemicarbazone $^{64}$Cu-ATSM (**Scheme 1.13-d**) demonstrated selectivity for hypoxic cancer tissues, in both

preclinical and clinical studies.[133] This compound is successfully employed as hypoxia-specific PET imaging agent.

In our research group, previous studies investigated the cytotoxic activity towards cancer cells of some 2,3-dihydroxy- and 2-hydroxy-3-methoxy-benzaldehyde thiosemicarbazones ad their copper(II) complexes (**Scheme 1.14**).[116]

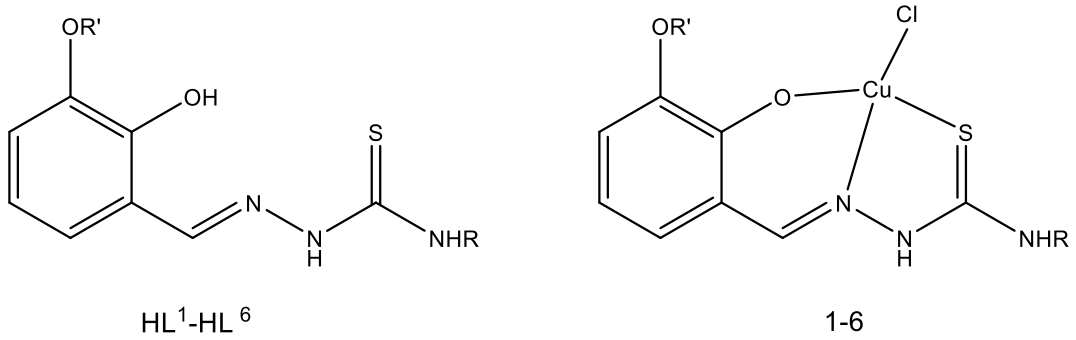


$HL^1$-$HL^6$ 1-6

**Scheme 1.14** Chemical structures of salicylaldehyde TSC derivatives and their copper(II) complexes.

The complexes displayed a considerable activity on the screened cancer cell lines (**Table 1.1**), in some cases in the low nanomolar range.

| | $IC_{50}$ (μM) ± SD | | | | | |
|---|---|---|---|---|---|---|
| | **2008** | **HCT-15** | **PSN1** | **A375** | **BxPC3** | **BCPAP** |
| **$HL^1$** | 0.78 ± 0.21 | 0.51 ± 0.14 | 0.51 ± 0.12 | 0.10 ± 0.030 | 0.005 ± 0.001 | 0.51 ± 0.09 |
| **1** | 0.013 ± 0.008 | 0.004 ± 0.001 | 0.008 ± 0.002 | 0.003 ± 0.0004 | 0.03 ± 0.01 | 0.033 ± 0.01 |
| **$HL^2$** | 4.85 ± 1.12 | 3.97 ± 0.38 | 6.82 ± 1.08 | 2.11 ± 0.4 | 0.98± 0.25 | 3.15 ± 0.62 |
| **2** | 0.035 ± 0.011 | 0.017 ± 0.006 | 0.32 ± 0.10 | 0.009 ± 0.001 | 0.002 ± 0.0005 | 0.84 ± 0.16 |
| **$HL^3$** | 1.97 ± 0.66 | 2.22 ± 0.76 | 3.13 ± 1.11 | 2.23 ± 0.78 | 1.11 ± 0.76 | 0.51 ± 0.090 |
| **3** | 0.010 ± 0.001 | 0.036 ± 0.012 | 0.021 ± 0.090 | 0.019 ± 0.004 | 0.015 ± 0.006 | 0.041± 0.011 |
| **$HL^4$** | ND | ND | ND | ND | ND | ND |
| **4** | 0.098 ± 0.004 | 0.091 ± 0.06 | 0.36 ± 0.010 | 0.029 ± 0.006 | 0.011 ± 0.004 | 0.35 ± 0.09 |
| **$HL^5$** | ND | ND | ND | ND | ND | ND |
| **5** | 0.71 ± 0.15 | 0.82 ± 0.14 | 0.51 ± 0.12 | 0.28 ± 0.09 | 0.11 ± 0.09 | 0.83 ± 0.11 |
| **$HL^6$** | ND | ND | ND | ND | ND | ND |
| **6** | 0.16 ± 0.04 | 0.23 ± 0.09 | 0.029 ± 0.008 | 0.069 ± 0.020 | 0.029 ± 0.011 | 0.072 ±0.012 |
| **CDDP** | 2.17 ± 1.37 | 13.92 ± 1.68 | 12.10 ± 2.87 | 3.11 ± 0.98 | 13.98 ± 1.23 | 6.65 ± 2.85 |

**Table 1.1** $IC_{50}$ values of compound **$HL^1$-$HL^6$** and Cu(II)complexes **1-6**. Cells were treated for 72 h with increasing concentrations of the tested compounds. Cytotoxicity was assessed by MTT test. S.D. = standard deviation. ND = non detectable. CDDP = cisplatin.

The complexes were additionally screened against 3D spheroids of pancreatic and colon cancer cells, with good results. Furthermore, preliminary *in vivo* anticancer activity of the best Cu(II) candidate was evaluated on a solid tumor model of highly aggressive syngeneic murine Lewis Lung Carcinoma (LLC). The results are very promising, since the Cu(II)TSC complex induced a tumor mass reduction comparable to the cisplatin control, while producing a smaller body weight loss in the treated mice.[116]

# Chapter 2: **Synthesis of water soluble thiosemicarbazones and their copper(II) complexes as anticancer compounds**

## 2.1 Aim of the project

The previously mentioned results suggest that salicylaldehyde TSC derivatives copper(II) complexes could be a promising starting point to develop an efficient anticancer drug candidate. Nevertheless, the preliminary *in vivo* experiments on mice were partially limited by the poor solubility of the tested Cu(II)TSC complexes,[116] highlighting the need to improve the water solubility of these compounds. Enhancing water solubility could, in fact, improve the pharmacological features of these compounds, e.g. make them more easily administered intravenously.

For this reason, this project focuses on the synthesis of 2,3-dihydroxy- and 2-hydroxy-3-methoxy-benzaldehyde TSC derivatives with an improved water solubility. To pursue this aim, it was chosen the strategy of sulfonating the benzene moiety of the salicylaldehyde.

Interesting results have been described for other sulfonate-salycilaldehyde TSCs derivatives in terms of cytotoxic profiles,[134][135][136] suggesting the insertion of a sulfonate group is a suitable strategy to improve water solubility maintaining a good anticancer activity.

## 2.2 Results and discussions

### 2.2.1 Synthesis and characterization of sulfonated TSCs

A first panel of sulfonated TSCs and their copper(II) complexes were synthetized (**Scheme 2.1**).

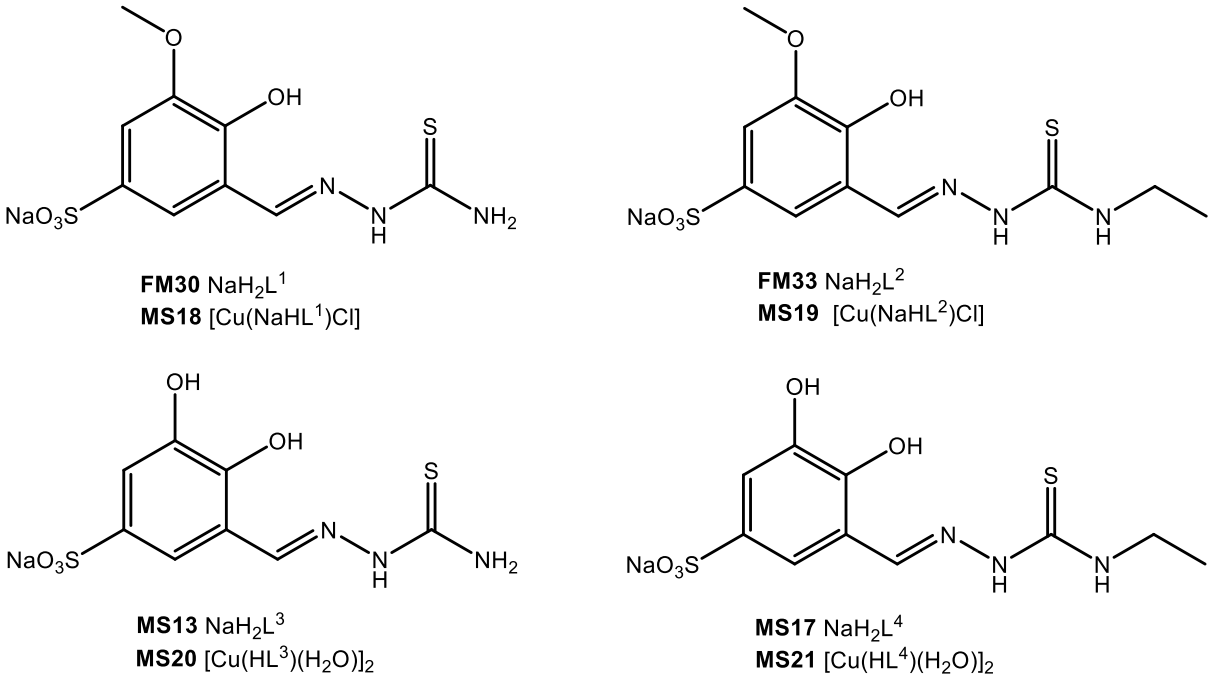


**Scheme 2.1** Structure of the sulfonated TSC ligands **FM30**, **FM33**, **MS13**, **MS17** ($NaH_2L^{1-4}$) and of their Cu(II) complexes **MS18**, **MS19** ($[Cu(NaHL^{1-2})Cl]$) and **MS20**, **MS21** ($[Cu(HL^{3-4})(H_2O)]_2$).

The first approach to their synthesis was the sulfonation of the pre-formed TSC ligands, as descripted in **Scheme 2.2**.

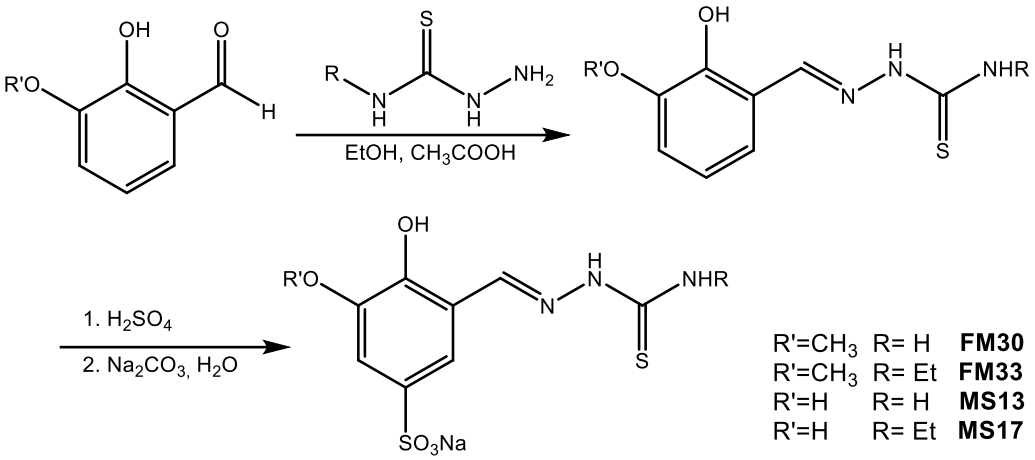


**Scheme 2.2** General procedure for the sulfonation of the TSC ligands **FM30**, **FM33**, **MS13**, **MS17**.

3-Hydroxy or 3-methoxy salicyl aldehyde (1 eqv) were reacted with thiosemicarbazide or 4-ethyl thiosemicarbazide (1 eqv), in EtOH at reflux, with a few drops of acetic acid. After a few hours, the thiosemicarbazones are isolated by filtration and obtained with high yields (90-95%).

For the insertion of the sulfonate group, the appropriate TSC ligand was put in a flask with a large excess (18 eqv) of $H_2SO_4$ (95-97%) and left reacting overnight at 35°C. The reaction mixture was then added with iced-water and after work-up and crystallization the sulfonated TSC was recovered.

In **Figure 2.1** it is reported the comparison between $^1$H-NMR spectra of **FM33** and its precursor **AC02**. The positive outcome of the reaction is confirmed by the disappearance of the signal at 6.78 ppm, corresponding to the aromatic proton in position 5, in the sulfonated ligand, accompanied by a change in the multiplicity and chemical shift in the signals of the others aromatic protons.

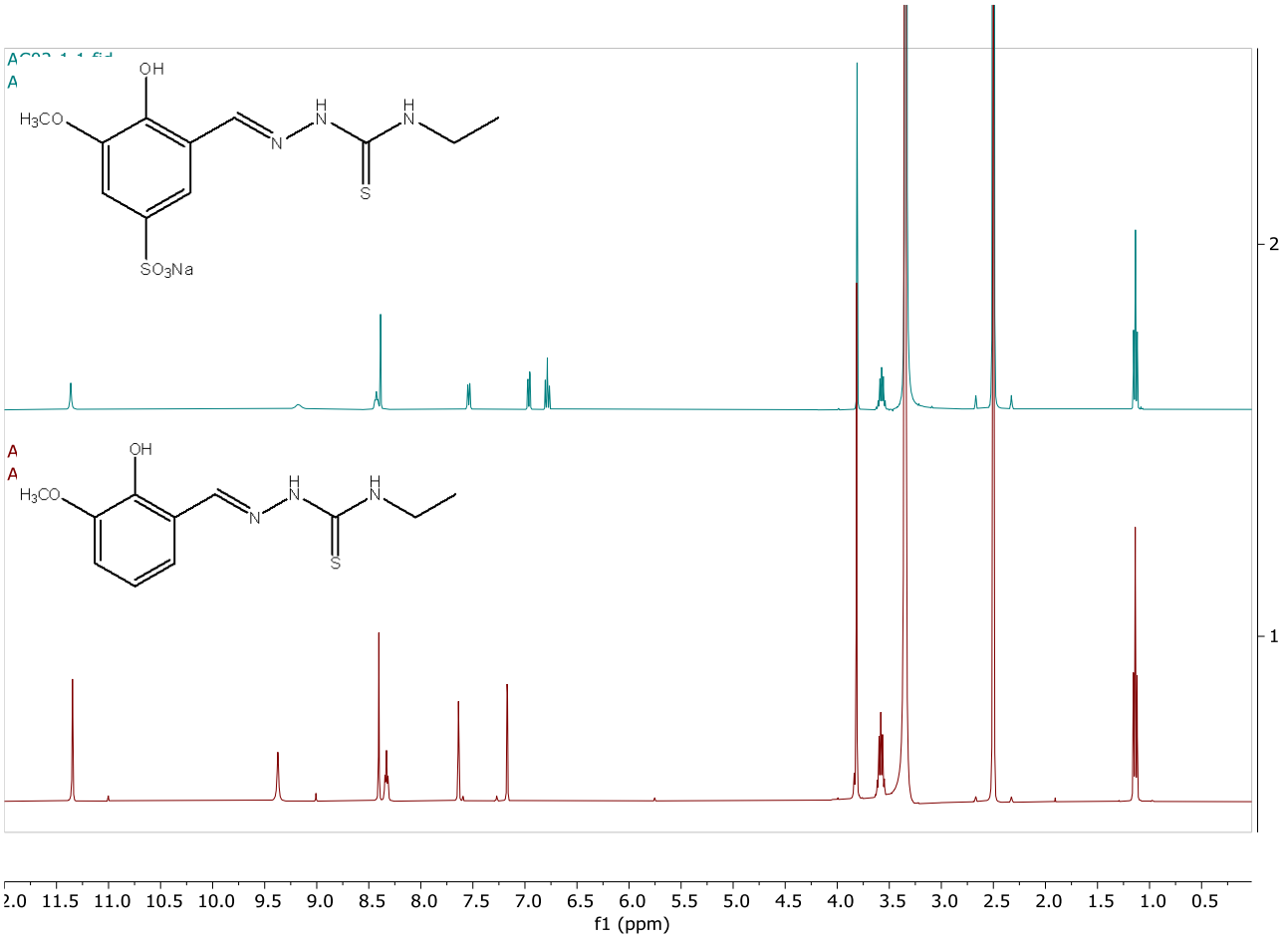


**Figure 2.1** Comparison between the $^1$H NMR spectra (25°C, 400 MHz, DMSO-$d_6$) of the sulfonated ligand **FM33** (top) and its precursor **AC02** (bottom).

Notably, in $H_2SO_4$ concentrated at 35°C the hydrolysis of the iminic bond was not observed. However, this procedure proved to be not ideal, because of the difficult separation of the sulfonated TSC from the large amount of $Na_2SO_4$ formed during the work-up of the reaction. Several attempts were made, and the best results were obtained with neutralizing the reaction media with $Na_2CO_3$ and recrystallizing the product from water. With this procedure three TSC ligands (**FM30**, **FM33** and **MS13**) were obtained with a satisfying purity, but poor yields (5-30%). Ligand **MS17** was not separated efficiently from $Na_2SO_4$. The complicated and not always reproducible purification method and the modest yields suggested the need for a more efficient synthesis.

For these reasons, a new synthetic pathway was pursued, following the procedure reported by Hager et al. for the synthesis of some sulfonated aldehydes[137] (**Scheme 2.3**).

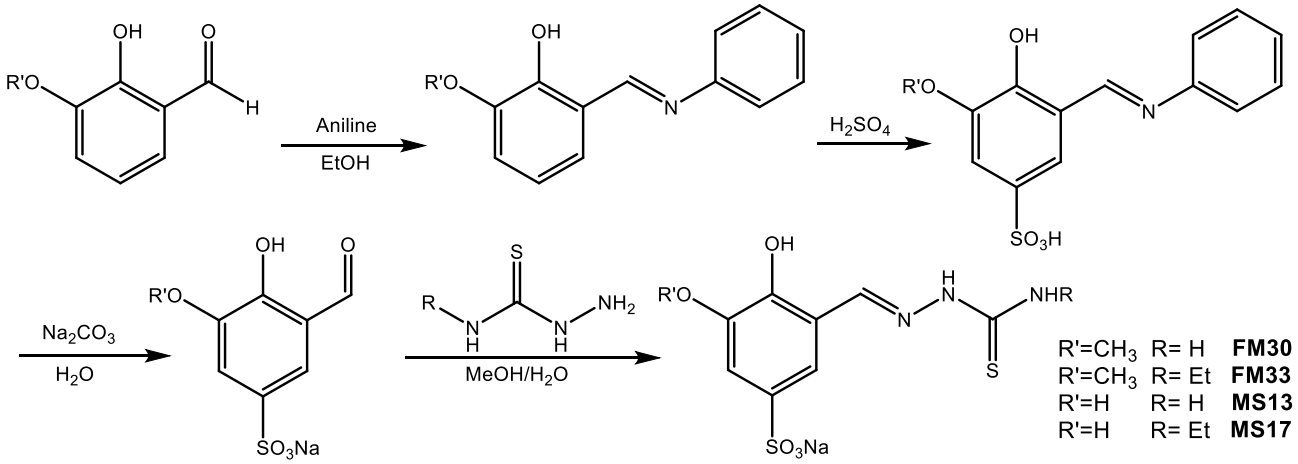


**Scheme 2.3** Synthesis of the sulfonated TSC ligands *via* sulfonated aldehydes.

First, 3-methoxy or 3-hydroxy salicyl aldehyde (1 eqv) underwent condensation with aniline, to obtain the respective imines (**FM27** and **FM31**) in almost quantitative yields.

These intermediates were then reacted with $H_2SO_4$ 95-97% at 105°C for 2 hrs. After that time, ice was added into the reaction flask. With the iced-water addition, a bright yellow solid started to precipitate. The solid was filtered and washed with cold water, then recrystallized from water. These intermediates were added with a $Na_2CO_3$ aqueous solution and boiled vigorously for 2 hours, then reaction mixture was cooled to r.t. and brought to pH=5 with $CH_3COOH$ addition. The crude was dried and recrystallized with EtOH/water mixture, obtaining the sulfonated aldehydes **FM29** and **FM34**.

In **Figure 2.2** the $^1$H-NMR of the newly synthetized sulfonated aldehyde **FM34** is reported, that shows two doublets signals in the aromatic region and a singlet at 10.02 ppm, corresponding to the aldehydic proton.

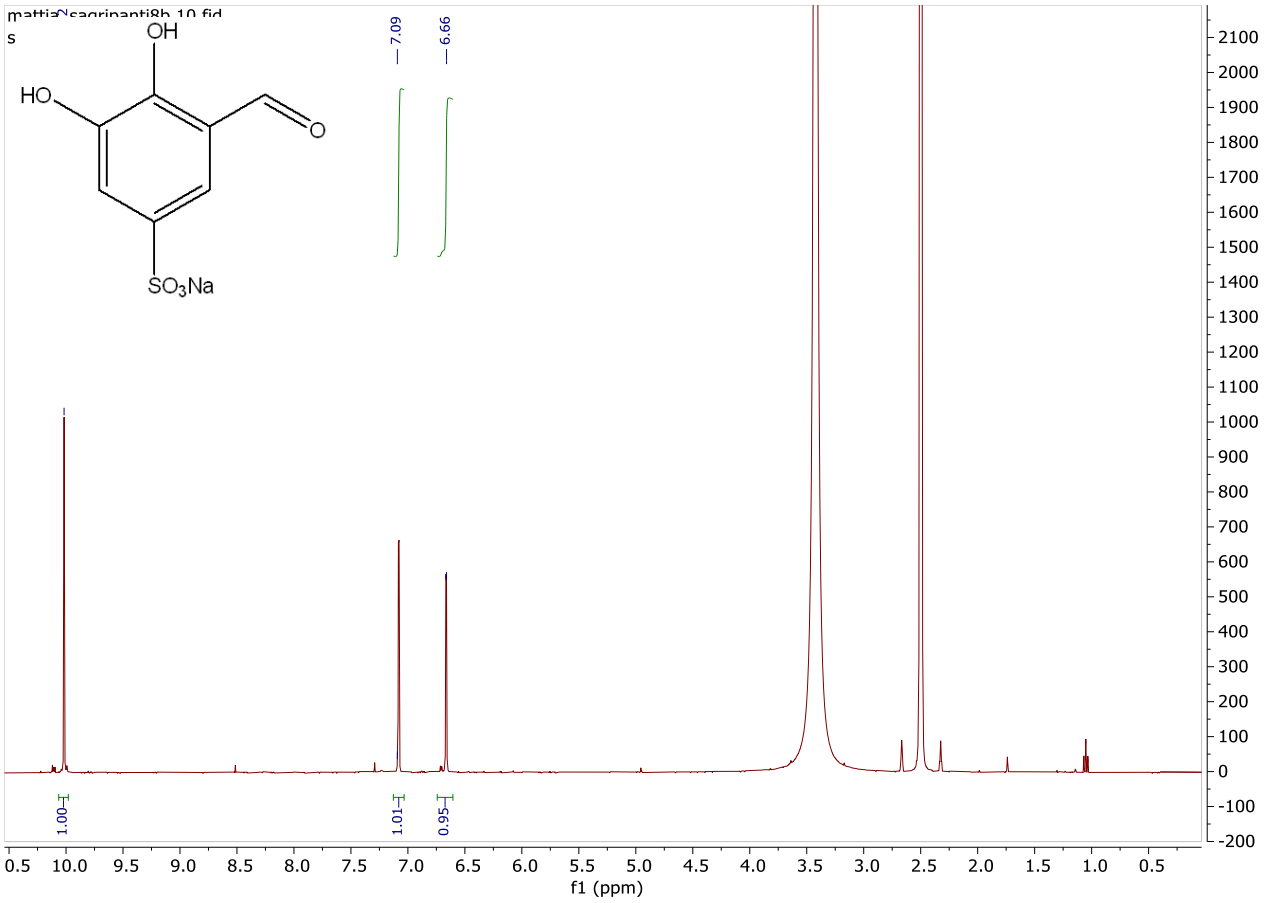


**Figure 2.2** $^{1}$H-NMR spectra (25°C, 400 MHz, DMSO-$d_6$) of the sulfonated aldehyde **FM34**.

The sulfonated aldehydes **FM29** and **FM34** (1 eqv) were then employed in the condensation reaction with the appropriate thiosemicarbazides, in a mixture of MeOH/$H_2O$: 5:1 at reflux for 4 hours. After that time, the sulfonated TSCs were recovered by filtration, without further purification. Using the 3,4-dihydroxy aldehyde **FM34**, the reactions were conducted in $N_2$ atmosphere, to avoid the formation of oxidated by-products.

The ligands were characterized by $^{1}$H and $^{13}$C NMR spectroscopy, AT-IR and ESI-MS. Moreover, elemental analyses were conducted to confirm their purity. In **Figure 2.3** the $^{1}$H and deptq $^{13}$C NMR spectra of **MS17** are reported, as a representative of the sulfonated TSCs.

The $^{1}$H NMR spectrum in DMSO-$d_6$ confirmed the outcome of reaction, with the disappearance of the aldehydic proton at 10 ppm and the presence of the iminic proton signal at 8.37 ppm, as well as the $CH_3$ triplet and $CH_2$ quartet at 1.14 and 3.58 ppm respectively. Only the thione *E*-form is present in DMSO-$d_6$ solution at room temperature.

The deptq $^{13}$C NMR spectrum also confirm the structure of the ligand, in which are present one $CH_2$ and five Cq signals phased positively and a $CH_3$ signal, two CH signal in the aromatic region and a CH signal at 140.9 ppm, corresponding to the iminic carbon, phased negatively.

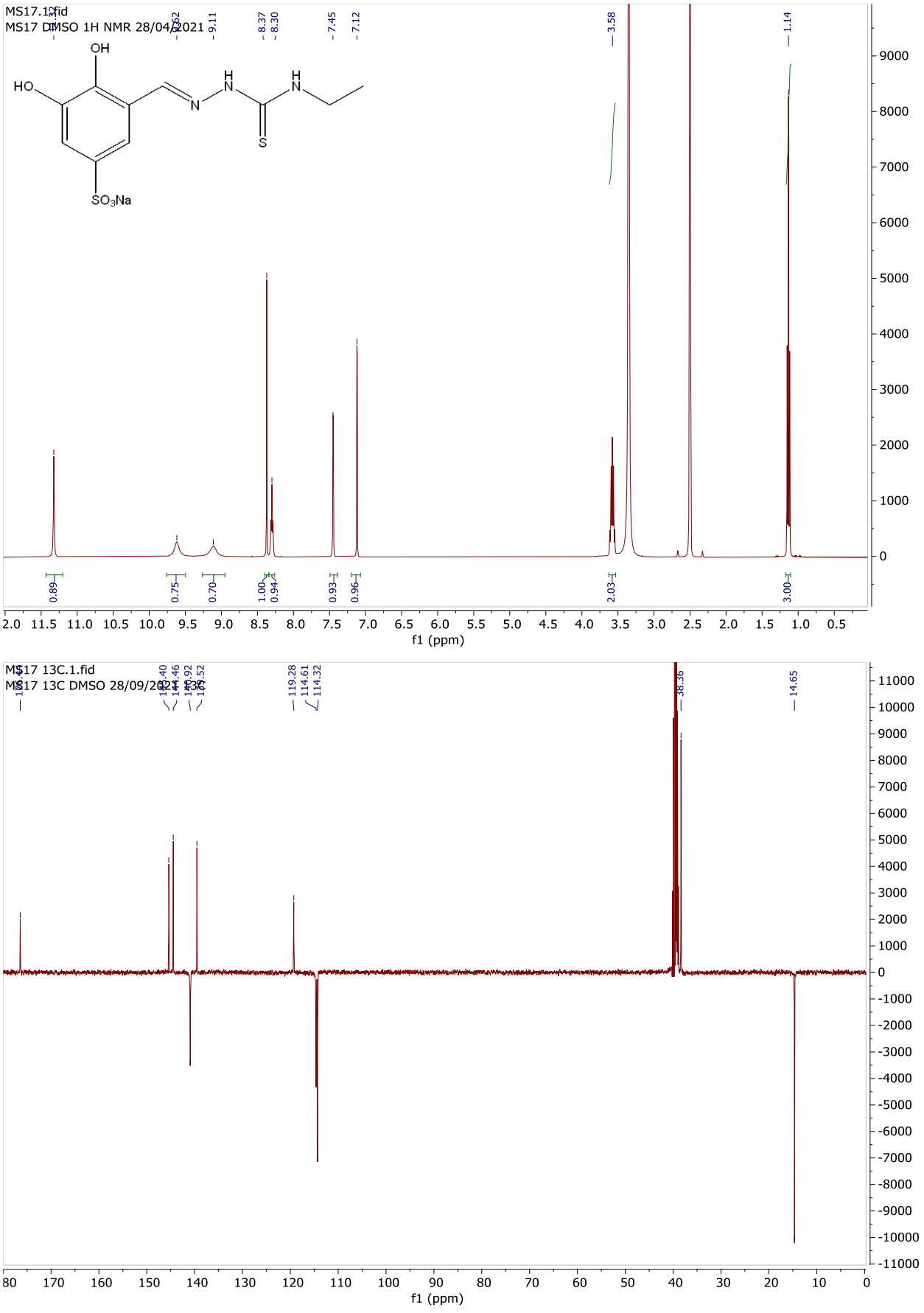


**Figure 2.3** $^{1}$H NMR (25°C, 400 MHz, DMSO-$d_6$) and $^{13}$C deptq (25°C, 101 MHz, DMSO-$d_6$) NMR spectra of **MS17**.

In the IR spectrum of **MS17** (**Figure 2.4**, top) it can be seen a stretching band at 1556 $cm^{-1}$ relative to the C=N bond and two bands at 1175 and 1047 $cm^{-1}$ characteristic of the $SO_3^-$ group. The TSCs can give rise to thione-thiol tautomerism, but in the IR spectrum the absence of a S-H stretching band around 2600 $cm^{-1}$ and the presence of a stretching N-H band around 3000 $cm^{-1}$ are representative of the thione form in the solid state.

In **MS17** ESI-MS spectra (**Figure 2.4**, bottom) the molecular ion signal is visible in the negative ionization mode. It is also possible to observe signals related to the binuclear and trinuclear species.

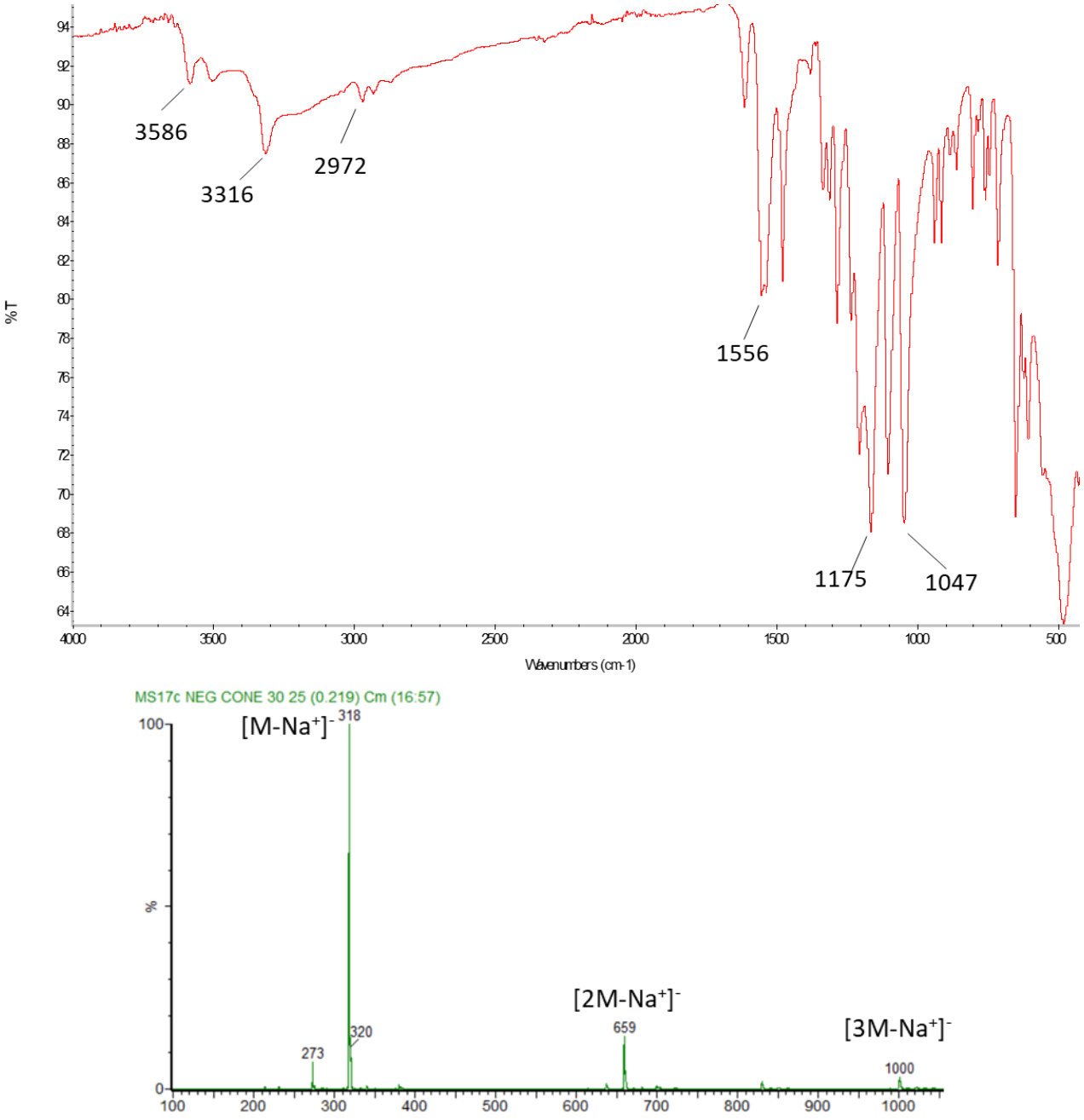


**Figure 2.4** FT-IR (top) and ESI-MS (negative ionization 30 eV) (bottom) spectra for **MS17**.

The second synthetic strategy, through the synthesis of sulfonated aldehydes, resulted more convenient compared to the first one.

The step of aniline addition is functional to a better and easier purification after the sulfonation reaction: this sulfonated intermediate has a lower water solubility compared to the sulfonated TSC, so it can be precipitated by adding ice in the flask, and the excess $H_2SO_4$ can be washed away from the solid in the filtration process, without the need to neutralize it forming $Na_2SO_4$. The following basic hydrolysis step breaks the imine bond and salify the sulfonate group, giving the desired sulfonated aldehyde.

With this strategy all four desired sulfonated TSCs were isolated, with a more straightforward purification. In **Table 2.1** are reported the final yield of sulfonated TSCs, calculated from the starting 3-methoxy or 3-hydroxy salicyl aldehydes. Even though it did not lead to particularly high yields, the second synthetic strategy gave overall better results, even if it requires four steps compared to the two steps of the first procedure. Furthermore, with this strategy it was possible to obtain the sulfonated ligand **MS17**, that was not possible to isolate with the first synthetic attempt.

| | FM30 | FM33 | MS13 | MS17 |
|---|---|---|---|---|
| **Sulfonation of aldehydes** | 23% | 22% | 27% | 12% |
| **Sulfonation of TSCs** | 30% | 13% | 5% | 0% |

**Table 2.1** Yield of the sulfonated TSCs **FM30**, **FM33**, **MS13**, **MS17** obtained through the two synthetic strategies, calculated from 3-methoxy or 3-hydroxy salicyl aldehyde as starting materials.

Once the ligands were obtained, they were used in the synthesis of the Cu(II) complexes.

To a solution of the ligand (1 eqv) in MeOH, a few drops of a NaOH solution were added, followed by the addition of $CuCl_2$ (1 eqv) solution in MeOH. The reaction was left stirring under $N_2$ atmosphere for 4.30 h. After that time, the solvent was concentrated by vacuum, if needed, and a green solid was filtered and washed with cold MeOH, recovering the copper complex. The reactions were conducted at pH≈8 to help deprotonation of the OH of the ligand and under $N_2$ atmosphere to prevent intramolecular oxidative cyclization. TSCs, in fact, in presence of bases, redox-active metals or oxidants, can give 1,2,4-triazole-3-thione derivatives or other cyclic by-products.[138]

The TSC copper(II) complexes **MS18**, **MS19**, **MS20** and **MS21** were characterised by means of elemental analysis, FT-IR, ESI-MS and ICP-AES.

This type of TSC ligands can coordinate the transition metal ions in a tridentate fashion, involving the three donor atoms S, N and O. The comparison between the IR spectra of the free ligands and the complexes supported the tridentate coordination of the ligand to the copper ions.

As it can be inferred from the IR spectra comparison between **MS13** and its copper complex **MS20** (**Figure 2.5**), the O-H band around 3460 $cm^{-1}$ disappears in the complex spectrum, indicating the deprotonation of the ligand on the hydroxy group. Furthermore, a shift to higher value of the C=N and C=S band suggest their involvement in the complexation.

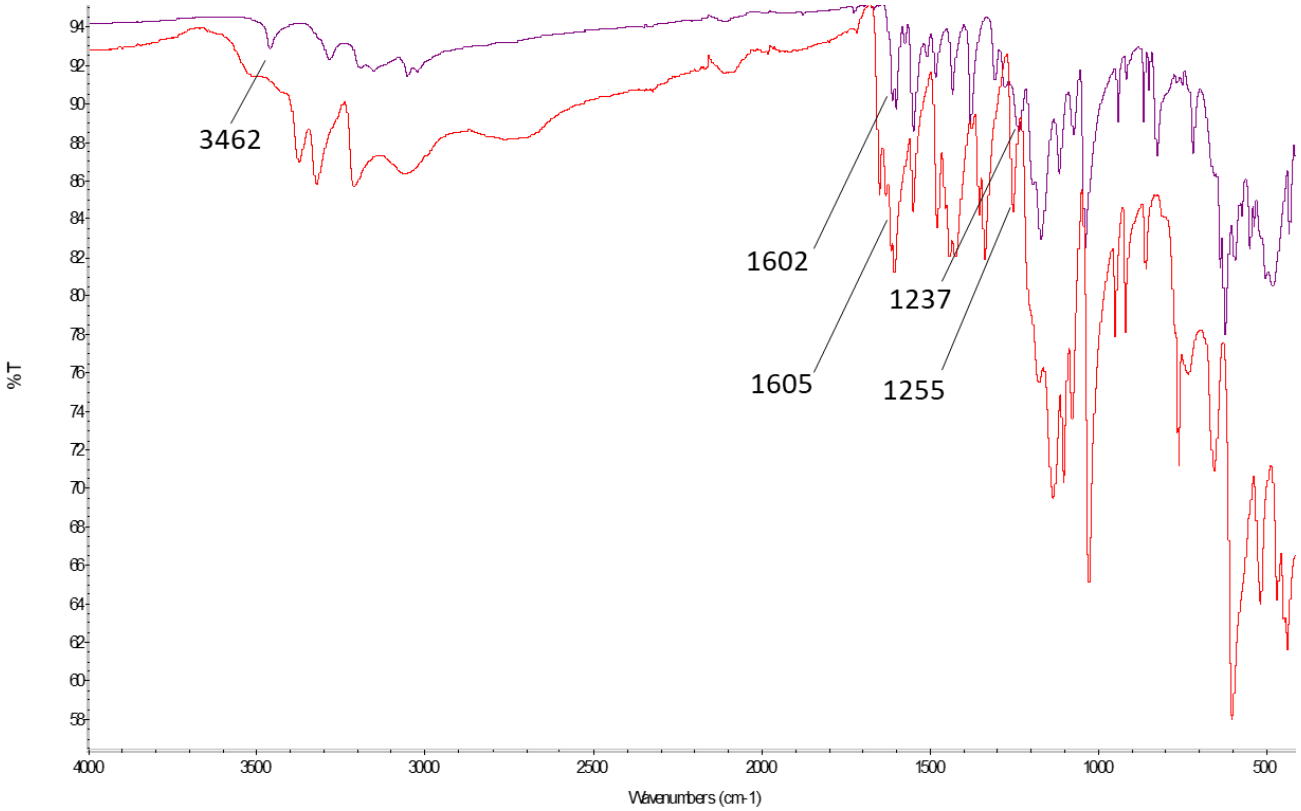


**Figure 2.5** FT-IR spectra of the ligand **MS13** (violet) and its copper(II) complex **MS20** (red).

Interestingly, elemental analysis suggested that the complexes isolated in the solid state were of two different types, monomeric and dimeric complexes, depending on the nature of the ligands.

The two complexes with the hydroxy methoxy ligands are monomeric (**MS18** and **MS19**) (**Scheme 2.4**), with the copper ion coordinated by the TSC and by a chloride ion. On the other hand, microanalysis suggested the presence of a dimeric complex for the complexes with di-hydroxy ligands (**MS20** and **MS21**), (**Scheme 2.4**).

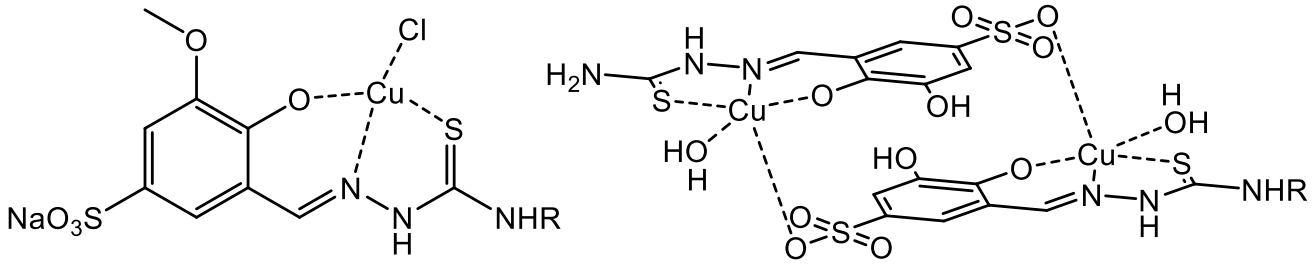


**Scheme 2.4** Monomeric complexes **MS18**, **MS19,** and dimeric complexes **MS20**, **MS21**.

Considering the sulfonated ligand as $NaH_2L$, the synthetized monomeric complexes can be described as [Cu(NaHL)Cl] and the dimeric as $[Cu(HL)(H_2O)]_2$.

Both monomeric and dimeric forms are described in the literature for similar complexes. In fact, several examples of squared planar monomeric Cu(II) complexes with the copper coordinated by the TSC and by a

chloride ion had been reported in the literature employing salycil thiosemicarbazones as ligands.[139][140][141] Furthermore, the formation of dimeric complexes with the participation of the sulfonate group was already reported for some copper(II) complexes with sulfonated salicylaldehyde TSC derivatives.[136][142]

This structural hypothesis is also corroborated by the ICP-AES analysis: for the monomeric complexes the found percentage of Na is around 4-5%, while for the dimeric complexes, not containing sodium, it is very close to 0%.

ESI-MS in methanol for both monomeric and dimeric compounds presented the corresponding molecular ion peaks of the species, without the presence of species containing the $Cl^-$ ion. In all the spectra, peaks corresponding to dimeric adducts were visible.

In order to evaluate if the solution media influenced the species detected, ESI-MS analysis were also conducted in an aqueous solution of NaCl 10 mM. Within the presence of NaCl, weak peaks of species containing $Cl^-$ ion were observed for all the complexes.

In **Figure 2.6** the ESI-MS in spectra of **MS19** in methanol and 10 mM NaCl solution are reported.

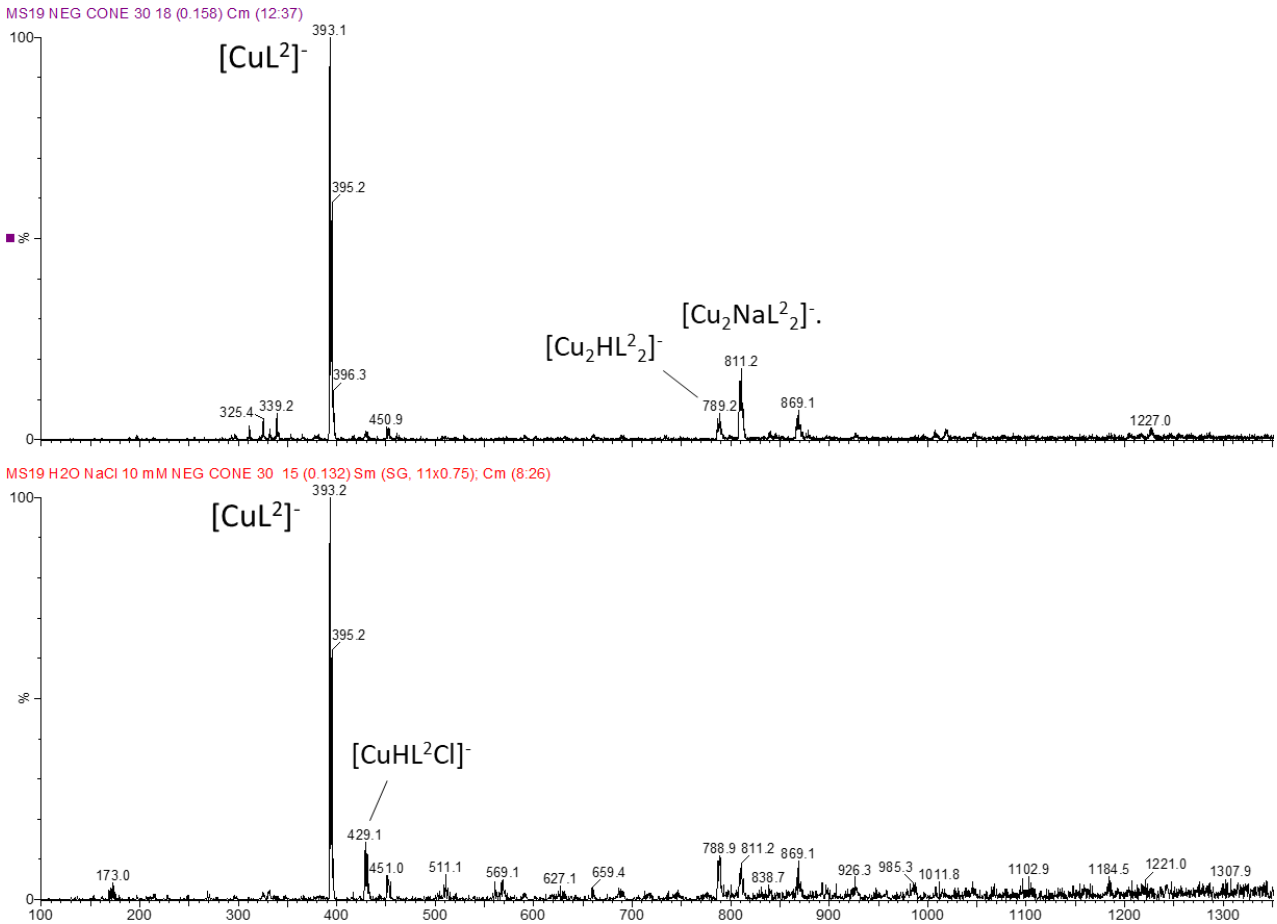


**Figure 2.6** ESI-MS spectra for **MS19** in MeOH (top) and $H_2O$ NaCl 10mM (bottom), negative ions 30 eV.

For **MS19** in methanol we can observe the peak at 393 m/z corresponding to the species $[CuL^2]^-$ and the peaks at 789 and 811 respectively of the adduct species $[Cu_2HL^2_2]^-$ and $[Cu_2NaL^2_2]^-$. In presence of NaCl in solution, it can also be observed a 429 m/z peak of the species $[CuHL^2Cl]^-$.

To have further insights on these structures, several crystallization attempts were tried, obtaining crystals suitable for SC-XRD. From slow evaporation of MeOH solutions of **MS21** and **MS18**, single crystals were obtained, and their structures refined by Professor Giorgio Pelosi's group, University of Parma (**Figure 2.7**).

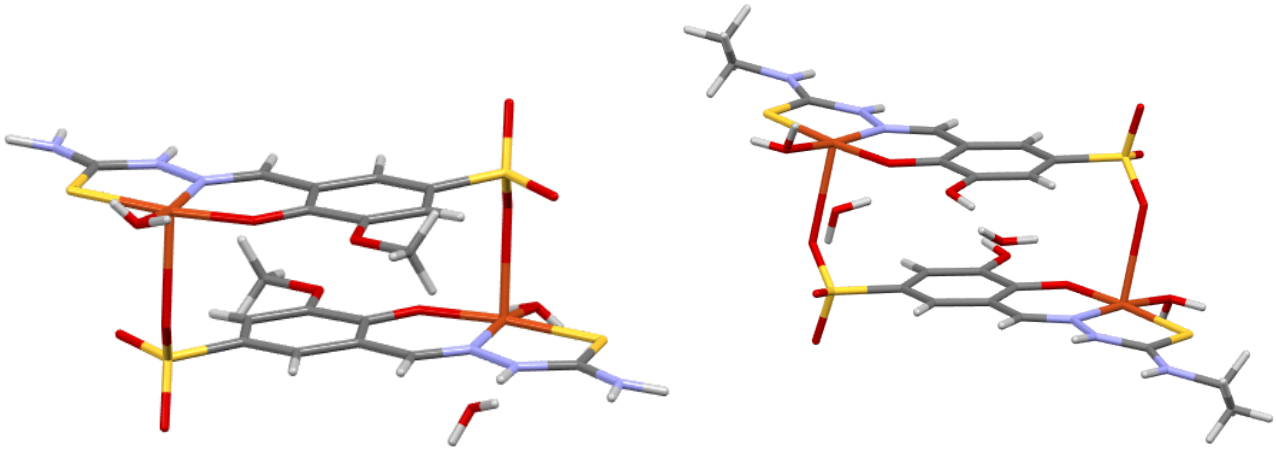

**Figure 2.7** Structures of $[Cu(HL^1)(H_2O)]_2$ (left) and $[Cu(HL^4)(H_2O)]_2$ (right). Both crystals were obtained by slow evaporation of methanolic solutions.

In the crystal structure of $[Cu(HL^4)(H_2O)]_2$ the ligand is in the *E* form, with respect to the CH=N bond. The copper is coordinated in a square pyramidal geometry by the TSC as a tridentate O,N,S ligand and one water molecule and apically by a negatively charged oxygen of the sulfonate group of a nearby ligand, forming head-to-tail dimers. The ligand is protonated on the $N^2$ of the thiosemicarbazone moiety, and the C=S bond length is in accordance with the thione form. This crystal has a dimeric structure, as it was found for the powders of complex **MS21**, used for the recrystallization.

The crystal structure of $[Cu(HL^1)(H_2O)]_2$ is as well dimeric, and very similar to $[Cu(HL^4)(H_2O)]_2$ structure.

The two structures, however, differ in the disposition of the non-coordinating water molecules in the crystal. Apart from the water that is integral part of the coordination of the copper ion, there are, in fact, two more waters that contribute to the packing in the crystals. These molecules intervene in the packing through different hydrogen bonds network scheme in the two compounds.

They also present differences in the intensity of π···π interaction between the aromatic moieties in the dimers. For $[Cu(HL^4)(H_2O)]_2$ this π···π interaction is remarkable (with a centroid···centroid contact of 3.405 Å) (**Figure 2.8**), whereas for $[Cu(HL^1)(H_2O)]_2$ is rather weak (about 4 Å).

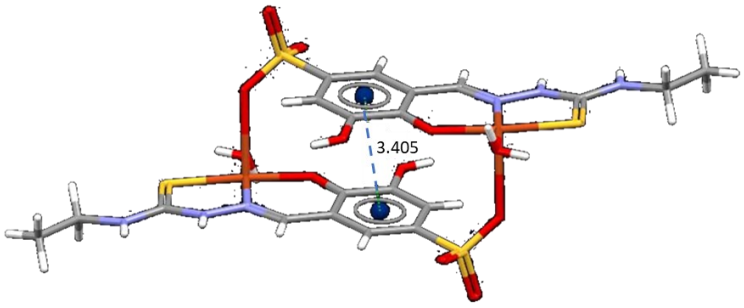


**Figure 2.8** Dimeric XRD structure of $[Cu(HL^4)(H_2O)]_2$, with highlighted centroid···centroid distance.

The $[Cu(HL^1)(H_2O)]_2$ structure was different from what expected, since the analyses on the **MS18** powder agreed with a monomeric form of the complex. It is plausible that, during the crystallization, a rearrangement in solution took place with release of $Na^+$ and $Cl^-$ from the monomer, to form the dimeric form of the complex (**Scheme 2.5**).

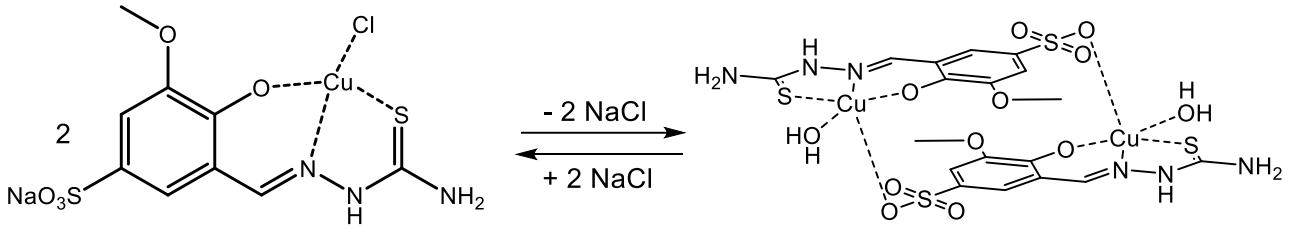


**Scheme 2.5** Proposed equilibrium in solution between monomeric and dimeric form of the complex **MS18**.

Considering the involvement of the $Na^+$ and $Cl^-$ species between monomeric and dimeric form, efforts to crystallize the monomeric complexes in an aqueous NaCl solution 0.9% were made, with the aim to shift the putative equilibrium towards the monomeric form.

Crystals suitable for SC-XRD were obtained from slow evaporation of a solution of **MS19** in $H_2O$ NaCl 0.9% and the structure refined (**Figure 2.9**).

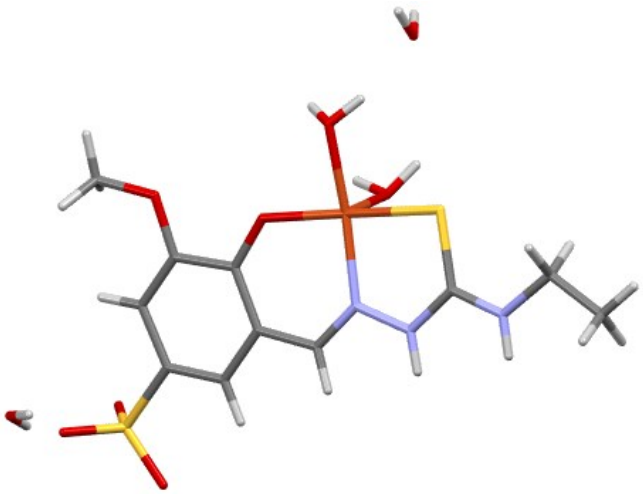

**Figure 2.9** Structure of $[Cu(HL^2)(H_2O)_2]$**.** Crystals obtained by slow evaporation of the complex in NaCl 0.9% aqueous solution.

This structure is monomeric, with the ligand present in the *E* form, with respect to the iminic bond. The copper is coordinated in a square pyramidal geometry by the TSC, behaving as a tridentate O,N,S ligand, and by two molecules of water. As for the dimeric structures, the ligand is protonated on the $N^2$ and the C=S bond length suggests it is in the thione form.

Comparing this with the structural hypothesis [Cu(NaHL)Cl], it can be noticed the $Na^+$ and $Cl^-$ ions are not present and the chloride anion is replaced by a water molecule in the coordination sphere.

We can speculate that this structure is an intermediate form between [Cu(NaHL)Cl], that is the structure of complex in powder, and its dimeric form, $[Cu(HL)(H_2O)]_2$, since the tendency to release $Na^+$ and $Cl^-$ to form dimeric crystals was also observed for **MS18**.

Finally, stability of the complexes in solution was evaluated over 72 hours, recording their UV spectra in solution (C≈ 40-50 µM) in 25 mM of HEPES buffer, at pH=7.4 in $H_2O$ NaCl 0.9%. These conditions were chosen to simulate the solution used for the *in vitro* tests with cancer cells lines. In **Figure 2.10** are reported the UV spectra for **MS18** and **MS20**, as examples of the behaviour of monomeric and dimeric compounds.

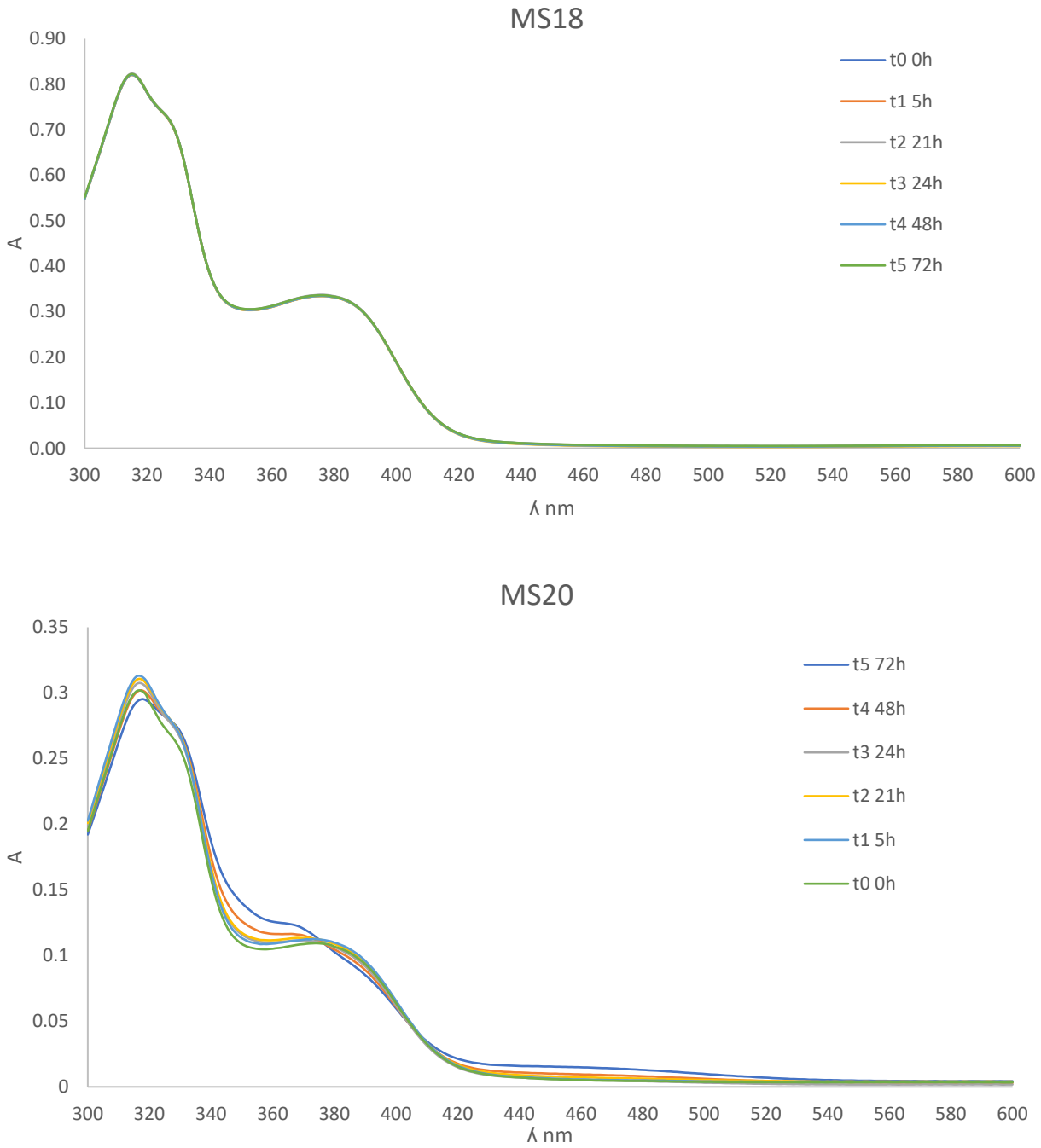


**Figure 2.10** UV spectra of **MS18** (c≈40 mM) and **MS20** (c≈40 mM) in 25 mM HEPES buffer (pH=7.4) in $H_2O$ NaCl 0.9%, recorded over 72 hrs.

Monomeric complexes **MS18** and **MS19** retained the same spectra over the 72 hours, with no observable differences arising over time (**Figure 2.10** for **MS18)**, confirming the stability of the complexes in these conditions.

By contrast, dimeric complexes **MS20** and **MS21** absorbance bands displayed visible shifts over time, as in as it can be seen for **MS20** in **Figure 2.10**. In this graph it is possible to observe two isosbetic points at 375 and 407 nm, implying the presence of different complex species. This finding suggests that the dimeric complexes, in this solution conditions, undergo speciation equilibria.

Having observed this behaviour only for **MS20** and **MS21**, dimeric in solid state, it was wondered whether the presence of $Na^+$ and $Cl^-$ ions was influencing the stability of the species in solution toward the formation of the monomer forms.

For this reason, another stability evaluation was performed, with the same conditions (HEPES buffer 25 mM, pH=7.4) in water (**MS18** and **MS20** spectra reported in **Figure 2.11**).

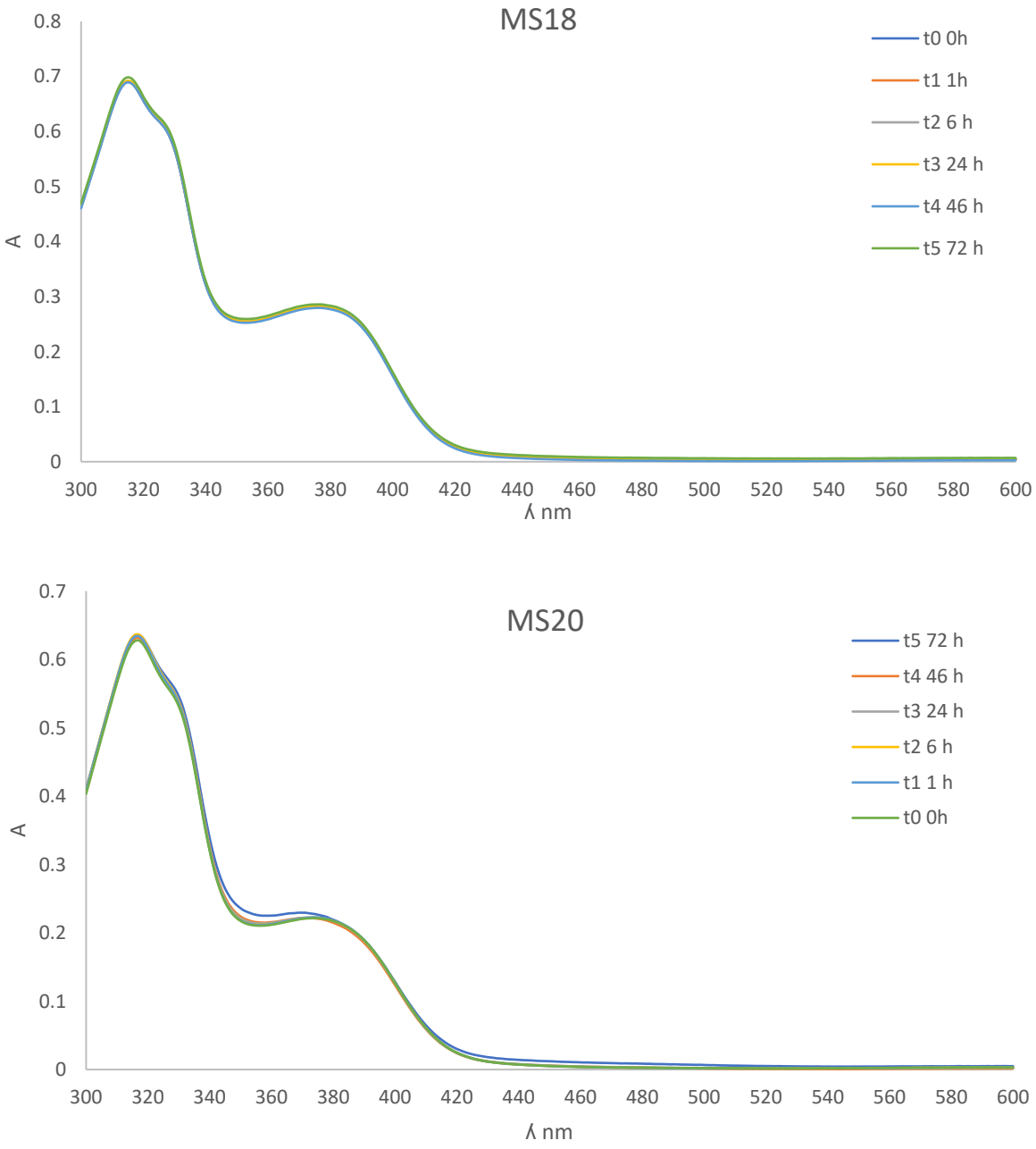


**Figure 2.11** UV spectra of **MS18** (c≈40 mM) and **MS20** (c≈50 mM) in 25 mM HEPES buffer (pH=7.4) in $H_2O$, recorded over 72 hrs.

In 25 mM buffer aqueous solution, without the presence of NaCl, both monomeric and dimeric complexes retained substantially the same spectra over 72 hours, as shown in picture. This improvement in the stability of the dimeric complexes in solution corroborates the idea of the involvement of $Na^+$ and $Cl^-$ in the variation occurred in the first stability evaluation.

### 2.2.2 Further modifications in the sulfonated TSC complexes

Once obtained and characterized the previously described ligands and copper complexes, several structural modifications on the ligand scaffold and on the nature of the metal were explored, in order to obtain structure-activity data.

First, to highlight the role of copper in the activity of the complex, complexes of ligand **FM30** with Zn(II) and Ni(II) were synthetized, through a similar synthetic procedure as for the copper(II) complexes, by using $Zn(CH_3COO)_2$ and $NiCl_2$, respectively (**Scheme 2.6**).

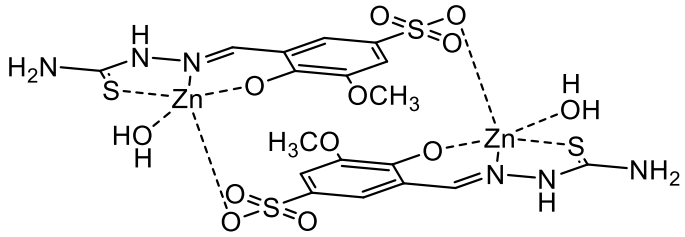

**MS32**

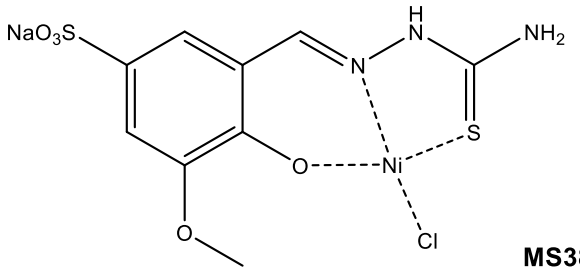

**MS38**

**Scheme 2.6** Structure of Zn(II) complex **MS32** and of Ni(II) complex **MS38.**

The complexes were characterized as previously described for the copper ones. The **MS32** zinc complex being diamagnetic was also characterized by $^1$H-NMR spectroscopy. The Ni(II) complex **MS38**, on the other hand, resulted to be paramagnetic.

In **Figure 2.12** the $^1$H-NMR spectrum of **MS32** is reported. The DMSO-$d_6$ spectrum of **MS32** presents the singlet of the iminic proton (8.16 ppm), two doublet corresponding to the two aromatic protons (6.97 and 6.93 ppm), a broad $NH_2$ signal at 6.10 ppm and the $OCH_3$ singlet at 3.71 ppm. The absence of the OH signal in the spectrum (found at 9.38 ppm in the ligand) indicates that this moiety is involved in the coordination of the zinc atom.

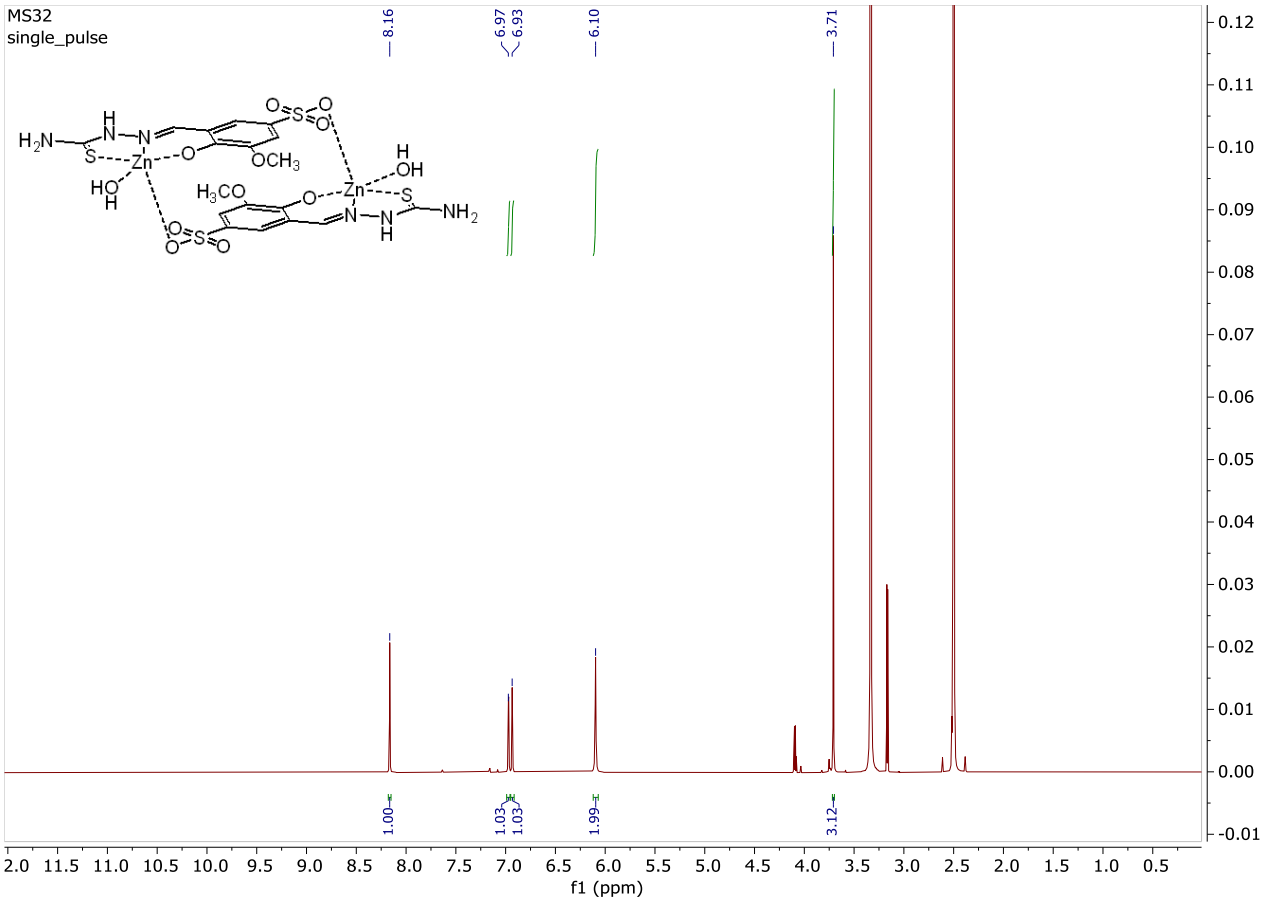


**Figure 2.12** $^{1}$H NMR (25°C, 600 MHz, DMSO-$d_6$) spectrum of the Zn(II) complex **MS32.**

Elemental and ICP analyses on the powders suggested that the nickel complex **MS38** has a monomeric structure, with stoichiometry [Ni(NaHL)Cl], analogously to the structure of the copper complexes with the hydroxy-methoxy ligands. Interestingly, the same analyses on the zinc complex **MS32** suggested a dimer, even though it bears the same TSC ligand.

Secondly, several structural modifications on the TSC ligands were made obtaining **MS29**, **MS25** and **MS26**. These compounds were then employed to synthesised their respective Cu(II) complexes (**Scheme 2.7**).

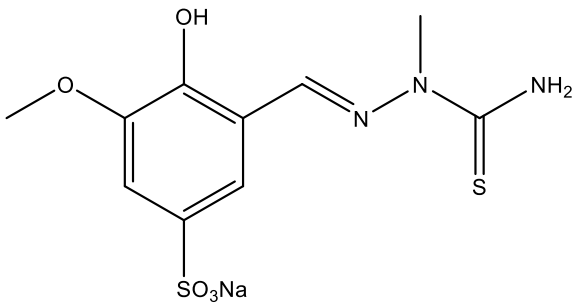

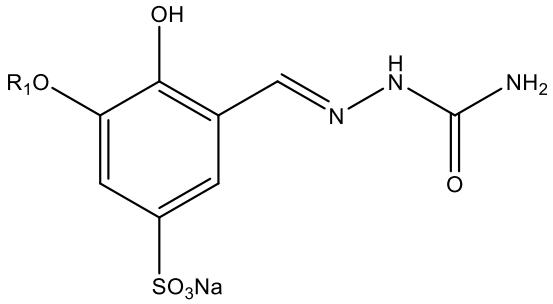

**MS29** $NaH_2L^5$ | $R^1$= H | **MS25** $NaH_2L^6$ | **MS27** $[Cu(HL^6)(H_2O)]_2$

**MS30** $[Cu(NaHL^5)Cl]$ | $R^1$= $CH_3$ | **MS26** $NaH_2L^7$ | **MS28** $[Cu(HL^7)(H_2O)]_2$

**Scheme 2.7** Structure of **MS29** ($NaH_2L^5$) and **MS25**, **MS26** ($NaH_2L^{6-7}$) ligands and of their copper(II) complexes **MS30**, **MS27** and **MS28**.

**MS29**, methylated on the N of the thiosemicarbazone moiety, was synthesised to assess the role of the NH, while **MS25** and **MS26** to evaluate the importance of the C=S bond for the activity of these molecules.

All the ligands were characterized by $^{1}H$ and $^{13}C$ NMR spectroscopy, AT-IR, ESI-MS and elemental analysis. As for the other ligands, NMR spectroscopy revealed that only thione *E*-form is present in solution at room temperature.

Comparing $^{1}H$ NMR spectra of the N-methylated ligand **MS29** with its analogue **FM33** (**Figure 2.13**), it can be noticed the disappearance of the NH signal at 11.41 ppm and the presence of 2 $CH_3$ signals between 3.7 and 3.8 ppm, as expected.

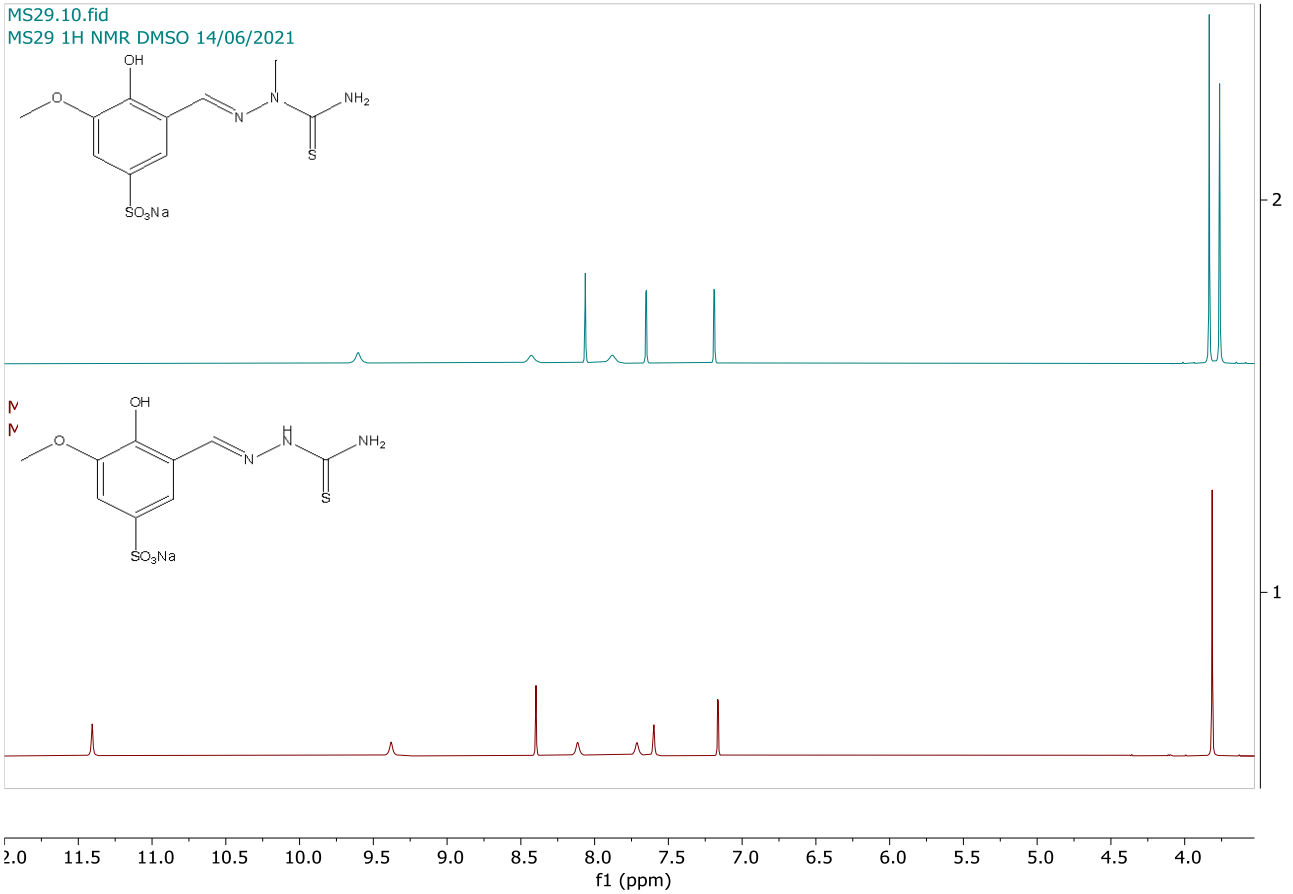


**Figure 2.13** Comparison of $^{1}H$ NMR spectra (25°C, 400 MHz, DMSO-$d_6$) of **MS29** (top) and **FM33** (bottom).

In the FT-IR spectrum of the semicarbazone **MS25** (**Figure 2.14**) it is visible a band around 1690 $cm^{-1}$, characteristic of the C=O bond stretching.

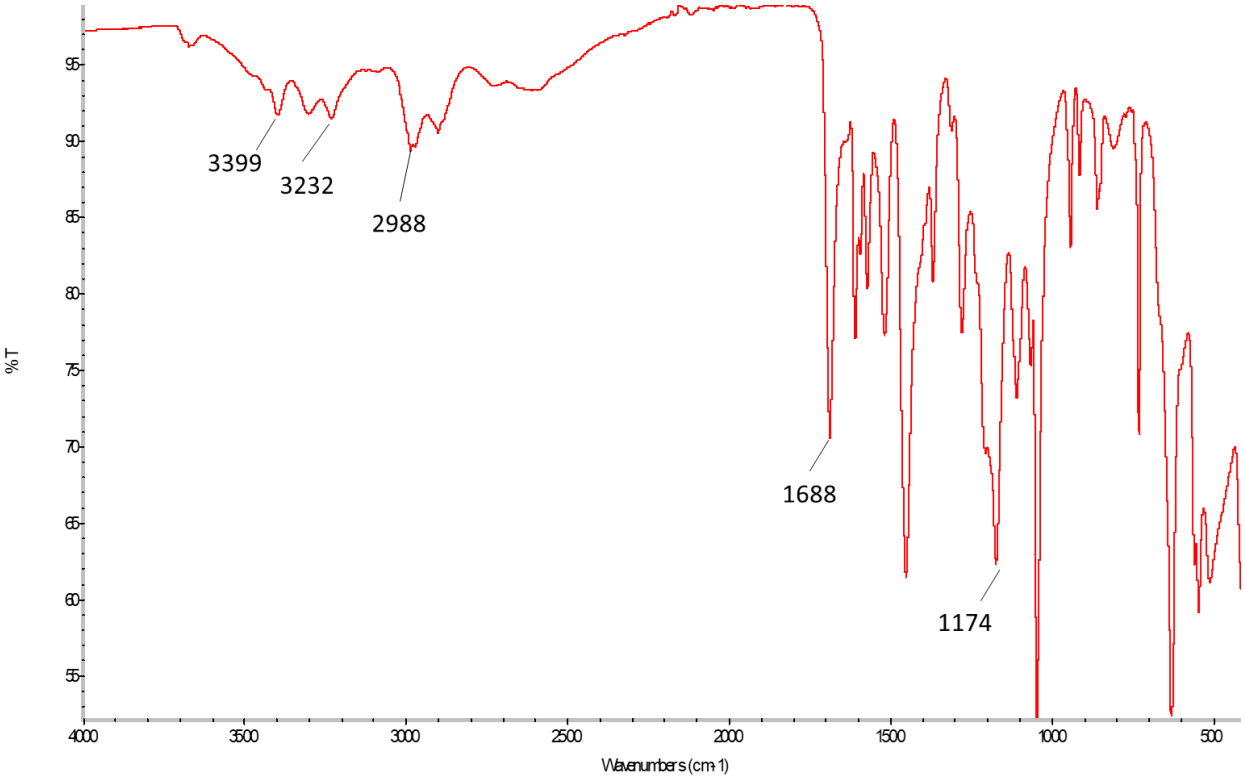


**Figure 2.14** FT-IR spectrum of the sulfonated semicarbazone **MS25.**

Copper(II) complexes of these ligands were prepared with the procedure previously described for the complexes. The complexes presented a solid state stoichiometry already observed for the sulfonated thiosemicarbazones: **MS27**, that has a di-hydroxy TSC ligand, has coherent analysis with the dimeric structure, while **MS28** and **MS30**, that bear hydroxy methoxy ligands, with a monomeric structure.

Furthermore, other modifications on the tridentate sulfonated ligands were explored, preparing two different hydrazones, **FC05** and **FC06** (**Scheme 2.8**). The modified ligand **FC05**, bearing a pyridine ring, was synthetised to evaluate the effect an heteroaromatic point of protonation on the sulfonated hydrazones. Ligand **FC06**, having a a 7 carbons linear chain, was prepared to compare the activity and cellular uptake of these ligand and complex bearing a more lypophlic portion on the sulfonated hydrazone moitey.

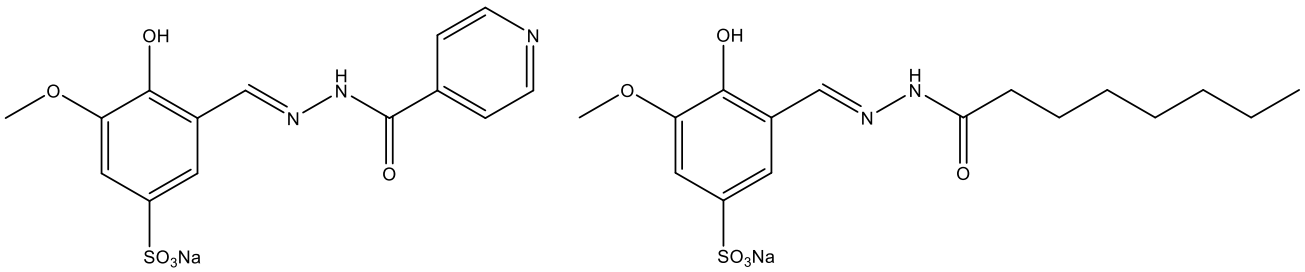


**FC05** $NaH_2L^8$
**FC08** $[Cu(HL^8)(H_2O)]_2$

**FC06** $NaH_2L^9$
**FC09** $[Cu(NaHL^9)Cl]$

**Scheme 2.8** Structure of **FC05** and **FC06** ($NaH_2L^{8-9}$) and of their copper(II) complexes **FC08** ($[Cu(HL^8)(H_2O)]_2$) and **FC09** ($[Cu(NaHL^9)Cl]$).

$^{1}$H NMR analysis revealed that **FC05** is present in DMSO-$d_6$ solution in the E form respect to the iminic bond. **FC06**, on the contrary, in DMSO-d6 solution is present in a mixture E/Z approximatively 2:1, as showed in **Figure 2.15**.

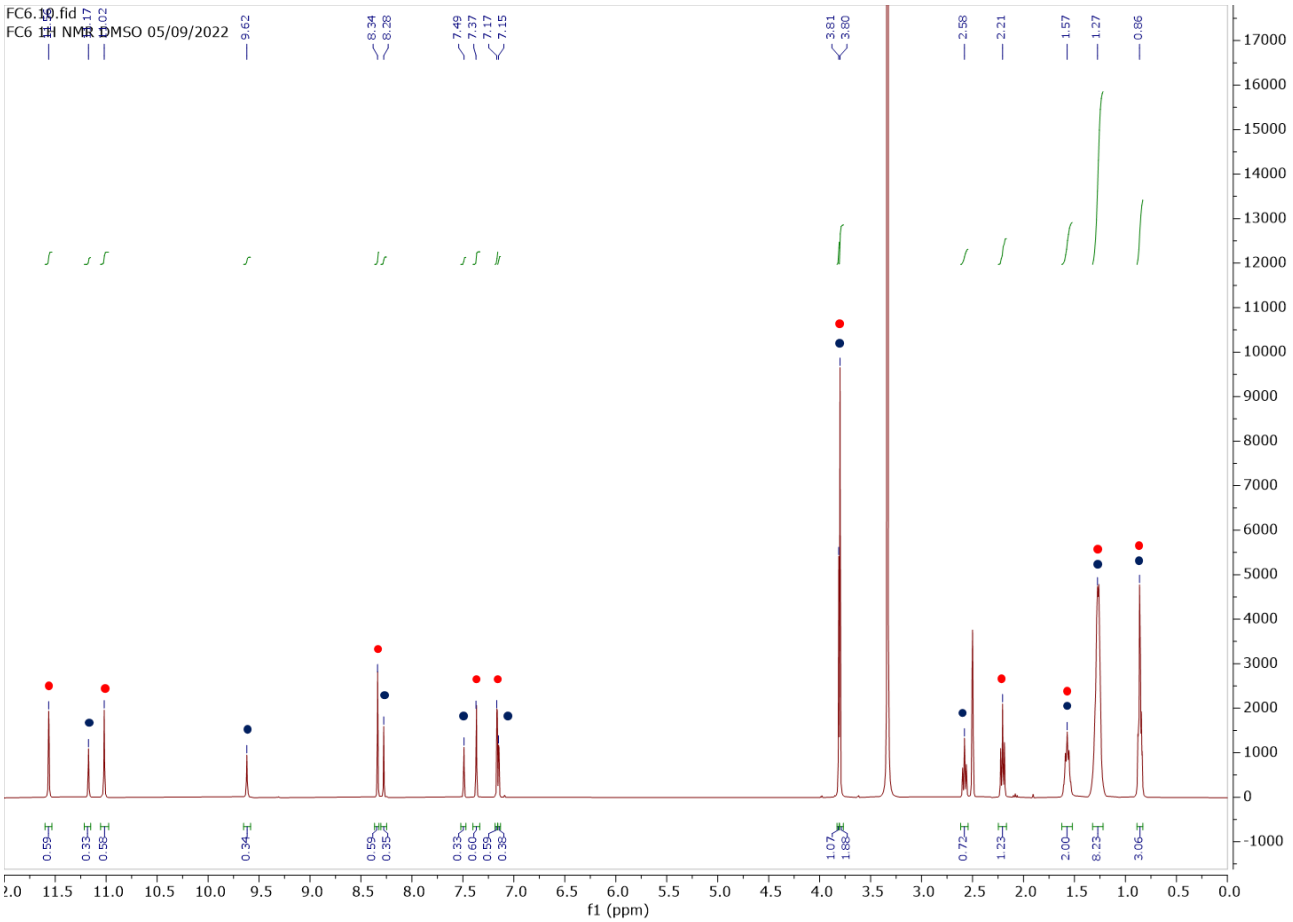


**Figure 2.15** $^{1}$H NMR of **FC06** (25°C, 400 MHz, DMSO-$d_6$), as a mixture of *E* (red dots) and *Z* (blue dots) isomers.

Copper(II) complexes of these ligands were prepared as described for the previous Cu complexes. The compounds were characterized by elemental analysis, ESI-MS and FT-IR.

Elemental analysis suggested a solid-state dimeric complex in case of the pyridine ligand (complex **FC08**) and a monomeric complex for **FC09** (**Scheme 2.9**)

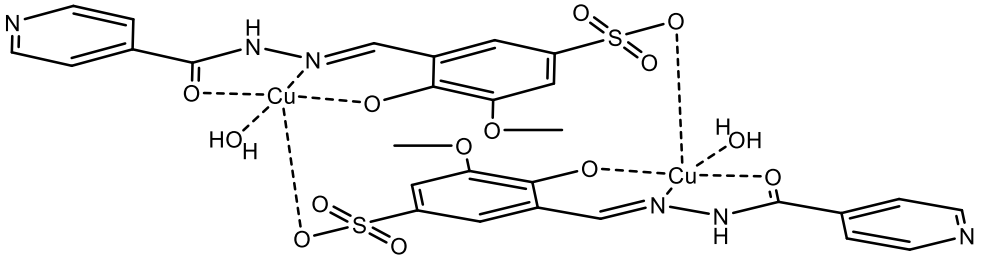

**FC08**

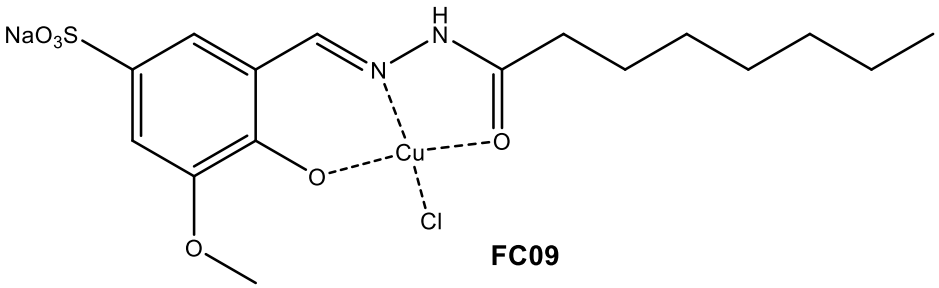

**FC09**

**Scheme 2.9** Structure of the copper(II) complexes **FC08** (top) and **FC09** (bottom).

### 2.2.3 Preliminary biological evaluation

Antitumor assays on ligands (**FM30**, **FM33**, **MS13**, **MS17**) and metal complexes (**MS18**-**21**, **MS31**-**32**) were conducted on several tumoral cellular lines, by the group of prof. Valentina Gandin at the Department of Pharmaceutical and Pharmacological Sciences of the University of Padova.

In particular, the 2D cancer cell line panel contains examples of ovarian (2008), colon (HCT-15), pancreatic (PSN1), and epidermoid carcinoma (A431) cancer cells.

The sulfonated TSC ligands displayed $IC_{50}$ > 50 µM in 2D tests, while the sulfonated TSC copper(II) complexes showed very interesting $IC_{50}$ values in the low micromolar range (**Table 2.2**). This trend is in line with many other TSC, where the metal complexes are often found to have an increased cytotoxic activity compared to the free ligands.

Sulfonated TSC Ni(II) complex **MS31** and sulfonated TSC Zn(II) complex **MS32**, on the other hand, showed $IC_{50}$ > 50 µM, suggesting that the involvement of copper is fundamental for anticancer activity.

| $IC_{50}$ (µM) ± SD | | | | |
|---|---|---|---|---|
| | **2008** | **HCT-15** | **PSN1** | **A431** |
| **FM30** | >50 | >50 | >50 | >50 |
| **FM33** | >50 | >50 | >50 | >50 |
| **MS13** | >50 | >50 | >50 | >50 |
| **MS17** | >50 | >50 | >50 | >50 |
| **MS18 (Cu)** | 8.1±2.8 | 7.5±2.5 | 4.5±1.2 | 10.5±4.1 |
| **MS19 (Cu)** | 9.2±1.6 | 6.2±1.1 | 5.1±1.5 | 9.5±2.5 |
| **MS20 (Cu)** | 8.8±2.6 | 4.1±0.4 | 4.1±0.9 | 2.9±0.9 |
| **MS21 (Cu)** | 5.1±0.8 | 0.9±0.3 | 3.1±1.0 | 1.8±0.4 |
| **MS31 (Ni)** | >50 | >50 | >50 | >50 |
| **MS32 (Zn)** | >50 | >50 | >50 | >50 |
| **CDDP** | 2.2 ± 0.9 | 11.3±1.5 | 6.2±1.4 | 3.1±1.0 |

**Table 2.2** $IC_{50}$ (µM) ± standard deviation on tumor cellular lines 2008, HCT-15, PSN1 and A431. Cells (3-8 x $10^3$ $mL^{-1}$) were treated for 72 h with increasing concentrations of the tested compounds. The cytotoxicity was assessed by the MTT test. CDDP: cis-platin, used as reference.

Comparing the *in vitro* antitumor activity of these compounds with their parent not sulfonated analogues,[116] the $IC_{50}$ values are higher, hence their cytotoxic activity diminished. This can be due to reduced membrane permeability of the ionic compounds in comparison to the parent neutral ones. However, the found anticancer activity is still remarkable, being comparable or greater than cytotoxicity reported for other similar sulfonated TSC complexes and of cis-platin.[142][143][136][134]

The copper(II) complexes were also tested on spheroids (3D models) of ovarian (2008) and colon (HCT-15) cancer cell lines. Tumor spheroids, being tridimensional, can simulate better the cancer tissues complexity compared to 2D cell lines.

The results of this test are very encouraging: all complexes, in fact, exhibited higher activity that cisplatin (CDDP), used as a reference (**Table 2.3**).

| $IC_{50}$ (μM) ± SD | | |
|---|---|---|
| | **2008** | **HCT-15** |
| **MS18** | 11.5±2.8 | 19.3±2.9 |
| **MS19** | 20.5±5.7 | 37.4±4.8 |
| **MS20** | 6.3±1.6 | 8.1±0.8 |
| **MS21** | 5.1±0.8 | 19.7±2.2 |
| **CDDP** | 36.5±6.1 | 68.2±4.6 |

**Table 2.3** $IC_{50}$ (μM) ± standard deviation on spheroids of tumor cellular lines 2008 and HCT-15. Spheroids ($2.5 \times 10^3$ cells/well) were treated for 72h with increasing concentrations of the tested compounds. The growth inhibitory effect was evaluated by means of APH test. CDDP: cis-platin, used as reference.

Comparing the $IC_{50}$ on the cancer spheroids with the not sulfonated analogues (≈1 μM for all the complexes),[116] these complexes have a slightly lower activity. Nonetheless, the $IC_{50}$ values on spheroids are good and not dramatically higher than on 2D cells, suggesting that the complexes could penetrate in the spheroid and exert their anticancer activity.

The Cu(II) complexes bearing the di-hydroxy ligands, **MS20** and **MS21,** showed the best activity profile in both 2D and 3D assays.

## 2.3 Conclusions

Within this research project, a panel of sulfonated TSC derivatives and their Cu(II) complexes were synthetized and characterized. Furthermore, their cytotoxic activity toward several cancer cell lines was evaluated, together with a Ni(II) and a Zn(II) complexes.

Two different synthetic pathways were investigated for the synthesis of the ligands. The synthesis of sulfonated aldehydes resulted to be more favourable compared to the sulfonation of the preformed TSC ligands.

For the copper(II) complexes different stoichiometries in the solid states were observed, indicating monomeric and dimeric complexes.

The *in vitro* biological evaluation of the panel gave encouraging results, implying that the presence of Cu(II) is of crucial importance for the anticancer activity of these water-soluble compounds. 3D *in vitro* assays conducted with the copper complexes gave excellent $IC_{50}$ values for this kind of sulfonated ligands. Altogether, the results suggest that these compounds have an interesting anticancer profile and deserve further investigations.

Additionally, a panel of structurally modified ligands, comprising sulfonated TSC, semicarbazones and hydrazones and their Cu(II) complexes have been synthetised and characterized. The biological evaluation of this expanded panel is ongoing and it will give a better insight on the structure-activity relationship of these compounds.

## 2.4 Experimental

### 2.4.1 Materials and methods

#### 2.4.1.1 Chemistry

All reagents of commercial quality were purchased from Sigma-Aldrich and used without further purification. The purity of the synthesized compounds was determined by elemental analysis and verified to be ≥ 95%.

NMR spectra were recorded on a Bruker Advance spectrometer operating at 400 MHz for the $^{1}H$ and at 101 MHz for $^{13}C$ nuclei, at 25°C. All chemical shifts are expressed in ppm.

The ATR-IR spectra were recorded by means of a Nicolet-Nexus (Thermo Fisher) spectrophotometer by using a diamond crystal plate in the range of 4000-400 $cm^{-1}$.

Elemental analyses were performed by using a FlashEA 1112 series CHNS/O analyzer (Thermo Fisher) with gas-chromatographic separation.

Electrospray mass spectral analyses (ESI-MS) were performed with an electrospray ionization (ESI) time-of-flight Micromass 4LCZ spectrometer. Samples were dissolved in methanol or water. MS spectra were acquired with a DSQII Thermo Fisher apparatus, equipped with a single quadrupole analyzer in positive EI mode, by means of a DEP-probe (Direct Exposure Probe) equipped with a Re-filament.

ICP-AES analysis (Inductively Coupled Plasma – Atomic Emission Spectroscopy) was performed as follows: 5 mg of solid sample were suspended in 5 mL of $HNO_3$ 65% and 1 mL of $H_2O_2$ 30%, then digested in a *Milestone* microwave MLS-1200 MEGA (digestion sequence: 1 min at 250 Watt, 1 min at 0 Watt, 5 min at 250 Watt, 5 min at 400 Watt, 5 min at 650 Watt, 5 min of cooling). The solutions were diluted to 50 mL with bi-distilled water and analyzed by using an emission spectrometer JY 2501 with coupled plasma induction in radial configuration HORIBA Jobin Yvon (Kyoto, Japan), ULTIMA2 model. Instrumental features: monochromator Model JY 2501; focal length 1 m; resolution 5 pm; nitrogen flow 2 l/min. ICP source: nebulizer Meinhard, cyclonic spraying chamber; argon flow 12 l/min; wavelengths range 160-785 nm; optical bench temperature 32 °C. The wavelength used for quantitative analysis was chosen by examining the emission line with greater relative intensity, ensuring that there was no spectral interference with the Argon emission lines. Acquisition parameters: wavelength Cu (nm): 224.700; Voltage (V): 580; Gain: 100; wavelength Na (nm): 588.995; Voltage (V): 570; Gain: 10. The quantitative analysis was performed after the acquisition of a calibration line using standard solutions in $HNO_3$ 10%, to simulate the final acidity of the samples; the concentration range of the standards varied from 0.5 mg/L to 100 mg/L. Data acquisitions and processing were performed using the ICP JY v 5.2 software (Jobin Yvon).

The UV-vis spectra were collected using a Thermo Evolution 260 Bio spectrophotometer provided with a thermostating Peltier device, and quartz cuvettes with 1 cm path length.

### 2.4.1.2 Crystallography

Single crystals were mounted on a glass fiber and the intensity data were collected with a SMART APEX2 diffractometer equipped with a Bruker AXS CCD detector using Mo-Ka radiation and a graphite crystal monochromator [λ(Mo-Kα) = 0.71073 Å]. The SAINT[144] software was used for the integration of reflection intensities and scaling, and SADABS[145] for the absorption correction. The structures were solved by direct methods using SIR97[146] and refined by full-matrix least-squares on all F2 using SHELXL97[147] implemented in the WinGX package[148]. All the non-hydrogen atoms in the molecules were refined anisotropically. The hydrogen atoms were partly found and partly placed in ideal positions using riding models. The structures were solved by direct methods and difference Fourier synthesis using the SHELX suite of programs as implemented within the WINGX software. Thermal ellipsoid plots were generated using the program ORTEP-333 integrated within the WinGX suite of programs.

### 2.4.2 Chemistry

**2-Methoxy-6-((phenylimino)methyl)phenol (FM27)**

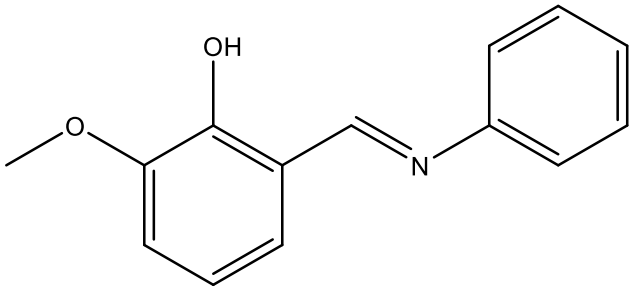


To a solution of 3-methoxy salicylaldehyde (1.52 g, 0.01 mol) in EtOH (20 mL) a solution of aniline (0.913 mL, 0.01 mol) in EtOH (2mL) was added. The reaction was left stirring at reflux for 2 hours. After that time the solvent was evaporated by vacuum and 2.25 g of **FM27** were obtained as a bright orange solid (Y=99%).
$^1$H-NMR ($CDCl_3$, 400 MHz, 25°C), ppm: 13.25 (b, 1H, OH); 8.96 (s, 1H, CH=N); 7.48 (dd, *J* = 8.4, 7.0 Hz, 2H, $CH_{arom}$); 7.43 (m, 2H, $CH_{arom}$); 7.33 (m, 1H, $CH_{arom}$); 7.25 (dd, *J* = 7.8, 1.5 Hz, 1H, $CH_{arom}$); 7.14 (dd, *J* = 8.0, 1.5 Hz, 1H, $CH_{arom}$); 6.92 (t, *J* = 7.9 Hz, 1H, $CH_{arom}$); 3.83 (s, 3H, $OCH_3$).
IR (ATR, $cm^{-1}$): ν(C-$H_{arom}$) = 2957; ν(C=N) = 1655.

**Sodium 3-formyl-4-hydroxy-5-methoxybenzenesulfonate (FM29)**

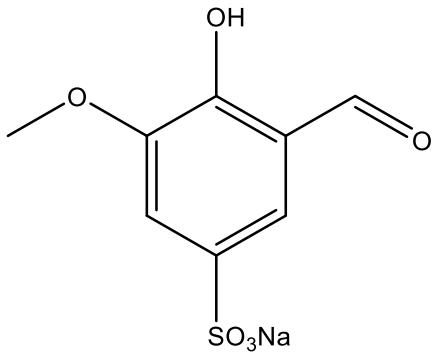


**FM27** (3.659 g, 160 mol) was dissolved in 9.5 mL of $H_2SO_4$ and the mixture wass stirred at 105°C for 2 h. After that time, ice water was added in the flask and a yellow-orange solid precipitate. The solid was filtered, wash with cold water and then completely dissolved in hot water. The solution was left reaching 5°C and recrystallized, giving a yellow-orange solid 4-hydroxy-3-methoxy-5-((phenylimino) methyl)benzenesulfonic acid.

To a suspension of 4-hydroxy-3-methoxy-5-((phenylimino)methyl)benzenesulfonic acid (3.1 g, 101 mmol) in 7 mL of water was added a solution of $Na_2CO_3$ (1.5 g, 141 mol) in 7 mL of water. The mixture was left stirring and boiling in an open flask for 2 h. After that time the mixture was cooled and $CH_3COOH$ was added till pH=5. The mixture was then recrystallized in a $H_2O$/EtOH mixture obtaining sodium 3-formyl-4-hydroxy-5-methoxybenzenesulfonate as a beige solid (Y=41%, over two steps).

$^1$H-NMR (DMSO-$d_6$, 400 MHz, 25°C), ppm: 10.23 (s, 1H, CH=O), 7.48 (d, *J* = 1.9 Hz, 1H, $CH_{arom}$), 7.31 (d, *J* = 1.9 Hz, 1H, $CH_{arom}$); 3.83 (s, 3H, $OCH_3$).

$^{13}$C-NMR (DMSO-$d_6$, 101 MHz, 25°C), ppm: 191.6; 152.9; 148.2; 138.4; 121.1; 117.3; 114.0; 56.0.

ESI-MS: $(M-Na)^-$: 231.2.

IR (ATR, $cm^{-1}$): ν(C=O) = 1668; ν($SO_3^-$) = 1188, 1043.

**2-Hydroxy-6-((phenylimino)methyl)phenol (FM31)**

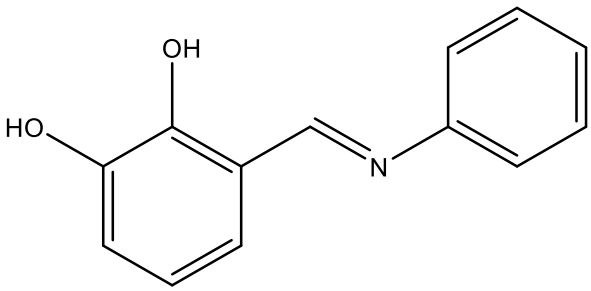


The product was obtained as a bright red solid with the same synthetic procedure for **FM27**, starting from 3-hydroxy salicylaldehyde (Y=97 %).

$^1$H NMR (400 MHz, DMSO-$d_6$, 25° C) δ 13.18 (b, 1H, OH); 8.92 (s, 1H, CH=N); 7.47 (td, *J* = 8.4, 7.0 Hz, 2H, $CH_{arom}$); 7.41 (m, 2H, $CH_{arom}$); 7.32 (m, 1H, $CH_{arom}$); 7.10 (dd, *J* = 7.8, 1.6 Hz, 1H, $CH_{arom}$); 6.95 (dd, *J* = 7.8, 1.6 Hz, 1H, $CH_{arom}$); 6.79 (t, *J* = 7.8 Hz, 1H, $CH_{arom}$).

IR (ATR, $cm^{-1}$): ν(OH) = 3380, 3315; ν(C=N) = 1620.

**Sodium 3-formyl-4,5-dihydroxybenzenesulfonate (FM34)**

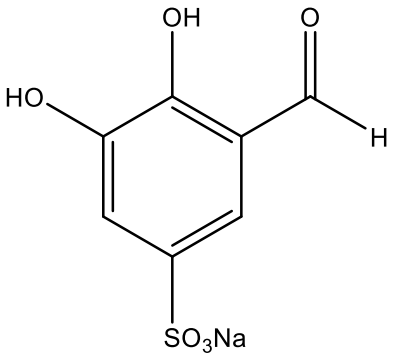


The product was obtained as a yellow solid with the same synthetic procedure for **FM29**, starting from **FM31** (Y= 37%, over two steps).

$^{1}$H-NMR (DMSO-$d_6$, 400 MHz, 25°C), ppm: 9.97 (s, 1H, CH=O); 7.10 (d, *J* = 2.1 Hz, 1H, $CH_{arom}$); 6.71 (d, *J* = 2.1 Hz, 1H, $CH_{arom}$).

$^{13}$C-NMR (DMSO-$d_6$, 101 MHz, 25°C), ppm: 190.0 (CH=O); 167.5 (Cq); 150.5 (Cq); 128.2 (Cq); 118.3 (Cq); 116.4 (CH); 109.7 (CH).

ESI-MS: $(M\text{-}Na)^-$: 217.4.

IR (ATR, $cm^{-1}$): ν(OH) = 3482; ν(C-$H_{arom}$) = 3070; ν(C=N) = 1645; ν($SO_3^-$) = 1154, 1020.

***General procedure 1 for the synthesis of thiosemicarbazones, semicarbazones and hydrazones:***

**FM34** or **FM29** were dissolved in a mixture of MeOH/$H_2O$: 5/1 at reflux, and the appropriate thiosemicarbazide or semicarbazide was added in an equimolar amount. The reaction was left stirring at reflux for 4 hours (under $N_2$ atmosphere for the reactions involving **FM34**). After that time the solution was cooled to 0°C, the solid was filtered and washed with cold MeOH, obtaining the final products without further purifications.

**Sodium 2-hydroxy-3-methoxy-5-sulfonate-benzaldehyde-3-thiosemicarbazone (FM30)** $NaH_2L^1$

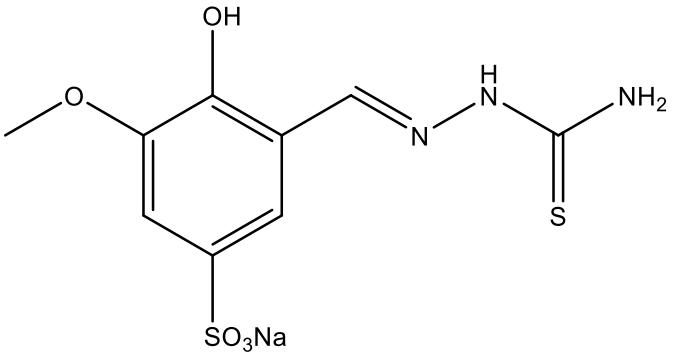


The product was obtained with the general procedure 1 as a beige solid. (Y= 57%)

$^{1}$H NMR (400 MHz, DMSO-$d_6$, 25° C) δ 11.41 (b, 1H, NH), 9.38 (b, 1H, OH), 8.40 (s, 1H, CH=N), 8.11 (b, 1H, NH), 7.71 (b, 1H, NH), 7.60 (d, *J* = 1.9 Hz, 1H, $CH_{arom}$), 7.16 (d, *J* = 1.9 Hz, 1H, $CH_{arom}$), 3.81 (s, 3H, $OCH_3$).

$^{13}$C NMR (101 MHz, DMSO-$d_6$, 25° C) δ 177.7 (Cq), 146.9 (Cq), 146.2 (Cq), 140.5 (CH), 139.7 (Cq), 119.1 (Cq), 115.6 (CH), 110.4 (CH), 55.9 ($CH_3$).

ESI-MS: $(M\text{-}Na)^-$: 304.3.

IR (ATR, $cm^{-1}$): ν($NH_2$)+ν(OH) = 3384; ν(NH) = 3173; ν(C=N) = 1609; ν(C=S) = 1257; ν($SO_3^-$) = 1104, 1038.

E.A. calculated for $C_9H_{10}N_3NaO_5S_2 \cdot H_2O$: C 31.30, H 3.50, N 12.17, S 18.57. Found: C 31.56, H 3.17, N 12.17, S 18.98.

**Sodium 2-hydroxy-3-methoxy-5-sulfonate-benzaldehyde-4-ethyl-3-thiosemicarbazone (FM33)** $NaH_2L^2$

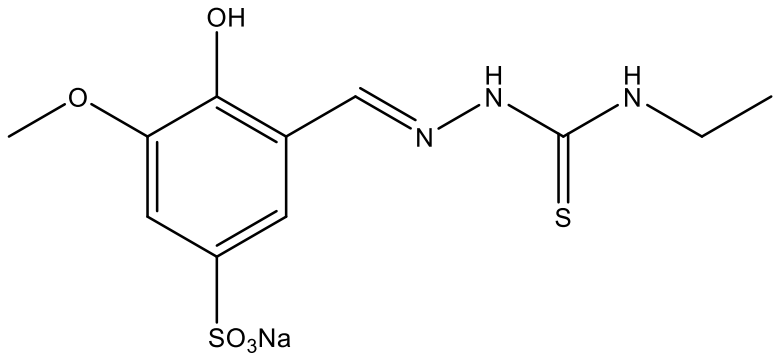


The product was obtained with the general procedure 1 as a beige solid. (Y=54%)

$^1$H NMR (400 MHz, DMSO-$d_6$, 25° C) δ 11.35 (s, 1H, NH), 9.37 (b, 1H, OH), 8.41 (s, 1H, CH=N), 8.33 (t, *J* = 6.0 Hz, 1H, NH), 7.63 (d, *J* = 1.9 Hz, 1H $CH_{arom}$), 7.17 (d, *J* = 1.9 Hz , 1H, $CH_{arom}$), 3.81 (s, 3H, $OCH_3$), 3.58 (p, *J* = 6.9 Hz, 2H, $CH_2$), 1.14 (t, *J* = 7.1 Hz, 3H, $CH_3$).

$^{13}$C NMR (101 MHz, DMSO-$d_6$, 25° C) δ 176.5, 146.8, 146.1, 140.0, 139.6, 119.4, 115.6, 110.4, 55.9, 18.6, 14.7.

ESI-MS: $(M\text{-}Na)^-$: 332.2.

IR (ATR, $cm^{-1}$): ν(OH) = 3384; ν(NH) = 3173; ν(C=N) = 1609; ν(C=S) = 1257; ν($SO_3^-$) = 1104, 1038.

E.A. calculated for $C_{11}H_{14}N_3S_2O_5Na$: C 37.17, H 3.97, N 11.82, S 18.05. Found: C 37.08, H 4.30, N 11.19, S 18.11.

**Sodium 2,3-dihydroxy -5-sulfonate-benzaldehyde-3-thiosemicarbazone (MS13)** $NaH_2L^3$

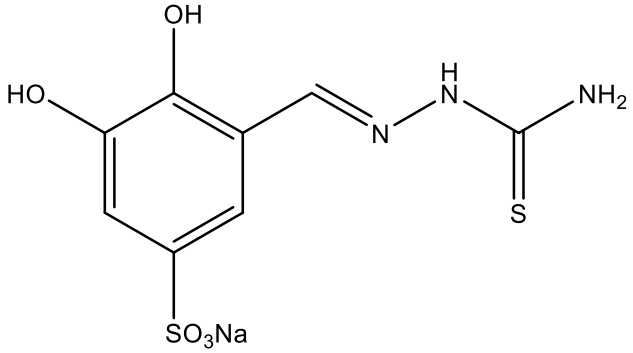


The product was obtained with the general procedure 1 as a beige solid. (Y= 76%)

$^1$H NMR (400 MHz, DMSO-$d_6$, 25° C) δ 11.37 (s, 1H, NH), 9.61 (b, 1H, OH), 9.10 (b, 1H, OH), 8.36 (s, 1H, CH=N), 8.09 (b, 1H, NH), 7.68 (b, 1H, NH), 7.42 (d, *J* = 2.0 Hz, 1H, $CH_{arom}$), 7.12 (d, *J* = 2.0 Hz, 1H, $CH_{arom}$).

$^{13}$C NMR (101 MHz, DMSO-$d_6$, 25° C) δ 177.6, 145.5, 144.6, 141.3, 139.5, 119.2, 114.7, 114.4.

ESI-MS: $(M\text{-}Na)^-$: 290.3.

IR (ATR, $cm^{-1}$): ν(OH)+ν(NH2) = 3462, 3285; ν(NH) = 3190; ν(C=N) = 1602; ν(C=S) = 1237; ν(SO3-) = 1172, 1039.

E.A. calculated for $C_8H_8N_3NaO_5S_2 \cdot H_2O$: C 29.00, H 3.04, N 12.68, S 19.36. Found: C 28.92, H 3.19, N 12.29, S 19.76.

**Sodium 2,3-dihydroxy-3-methoxy-5-sulfonate-benzaldehyde-4-ethyl-3-thiosemicarbazone (MS17)** $NaH_2L^4$

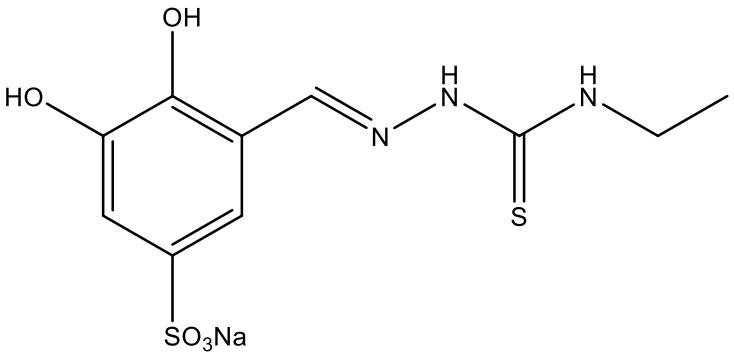


The product was obtained with the general procedure 1 as a beige solid. (Y=34%)

$^1$H NMR (400 MHz, DMSO-$d_6$, 25° C) δ 11.32 (b, 1H, NH), 9.4 (b, 2H, OH), 8.37 (s, 1H, CH=N), 8.30 (t, *J* = 5.9 Hz, 1H, NH), 7.45 (d, *J* = 2.0 Hz, 1H, $CH_{arom}$), 7.12 (d, *J* = 2.0 Hz, 1H, $CH_{arom}$), 3.58 (p, *J* = 6.9 Hz, 2H, $CH_2$), 1.13 (t, *J* = 7.1 Hz 3H, $CH_3$).

$^{13}$C NMR (101 MHz, DMSO-$d_6$, 25° C) δ 176.4 (Cq), 145.4 (Cq), 144.5 (Cq), 140.9 (CH), 139.5 (Cq), 119.3 (Cq), 114.6 (CH), 114.3 (CH), 38.4 ($CH_2$), 14.7 ($CH_3$).

ESI-MS: $(M\text{-}Na)^-$: 318.3.

IR (ATR, $cm^{-1}$): ν(OH) = 3329; ν(NH) = 2974; ν(C=N) = 1615; ν(C=S) = 1284; ν($SO_3^-$) = 1175, 1047.

E.A. calculated for $C_{10}H_{12}N_3NaO_5S_2 \cdot H_2O$: C 33.42, H 3.93, N 11.69, S 17.85. Found: C 33.08, H 3.90, N 11.23, S 18.08.

**Sodium 2,3-dihydroxy -5-sulfonate-benzaldehyde-3-semicarbazone (MS25)** $NaH_2L^6$

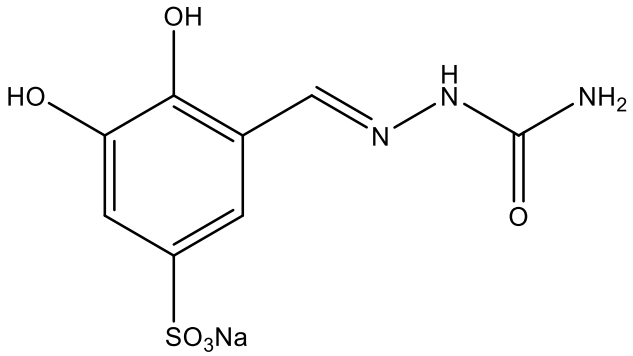


The product was obtained with the general procedure 1 as a beige solid. (Y=76%)

$^1$H NMR (400 MHz, DMSO-$d_6$, 25° C) δ 10.19 (s, 1H, NH), 9.47 (b, 2H, OH), 8.11 (s, 1H, CH=N), 7.29 (d, *J* = 2.0 Hz, 1H, $CH_{arom}$), 7.06 (d, *J* = 2.0 Hz, 1H, $CH_{arom}$), 6.27 (2H, s, $NH_2$).

$^{13}$C NMR (101 MHz, DMSO-$d_6$, 25° C) δ 156.3, 144.9, 144.5, 139.3, 139.1, 119.4, 114.8, 113.7.

ESI-MS: $(M\text{-}Na)^-$: 274.3.

IR (ATR, $cm^{-1}$): ν(OH) +ν($NH_2$) = 3399, 3232; ν(NH) = 2988; ν(C=O) = 1688; ν($SO_3^-$) = 1174, 1047.

E.A. calculated for $C_8H_8N_3NaO_6S \cdot H_2O$: C 30.48, H 3.20, N 13.33, S 10.08. Found: C 30.33, H 3.11, N 12.93, S 10.14.

**Sodium 2-hydroxy-3-methoxy-5-sulfonate-benzaldehyde-3-semicarbazone (MS26)** $NaH_2L^7$

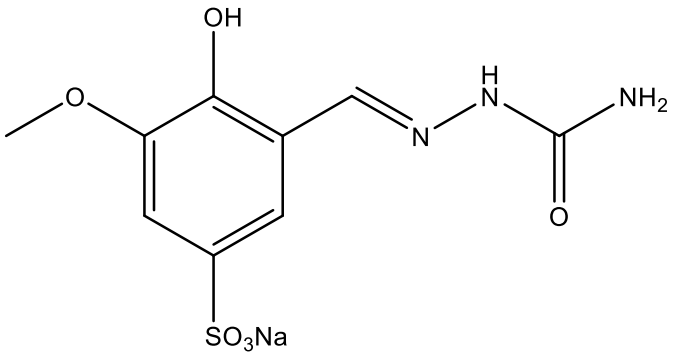


The product was obtained with the general procedure 1 as a pale yellow solid. (Y=47%)
$^1$H NMR (400 MHz, DMSO-$d_6$, 25° C) δ 10.24 (s, 1H, NH), 9.63 (b, 1H, OH), 8.17 (s, 1H, CH=N), 7.51 (d, *J* = 1.9 Hz, 1H, $CH_{arom}$), 7.15 (d, *J* = 1.9 Hz, 1H, $CH_{arom}$), 6.30 (s, 2H, $NH_2$), 3.81 (s, 1H, $OCH_3$).
$^{13}$C NMR (101 MHz, DMSO-$d_6$, 25° C) δ 156.4, 146.9, 145.8, 139.3, 138.2, 119.5, 115.8, 109.8, 55.9.
ESI-MS: $(M-Na)^-$: 288.3.
IR (ATR, $cm^{-1}$): ν(OH) +ν($NH_2$) = 3415; ν(NH) = 2944; ν(C=O) = 1693; ν($SO_3^-$) = 1193, 1050.
E.A. calculated for $C_9H_{10}N_3NaO_6S \cdot H_2O$: C 32.83, H 3.67, N 12.76, S 9.74. Found: C 32.64, H 3.66, N 12.47, S 9.66.

**Sodium 2-hydroxy-3-methoxy-5-sulfonate-benzaldehyde-3-methyl-thiosemicarbazone (MS29)** $NaH_2L^5$

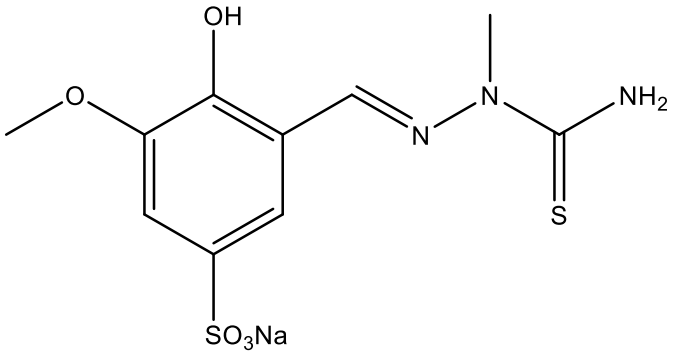


The product was obtained with the general procedure 1 as a beige solid. (Y=46%)
$^1$H NMR (400 MHz, DMSO-$d_6$, 25° C) δ 9.60 (s, 1H, OH), 8.43 (b, 1H, NH), 8.06 (s, 1H, CH=N), 7.88 (s, 1H, NH), 7.65 (d, *J* = 1.9 Hz, 1H, $CH_{arom}$), 7.19 (d, *J* = 1.9 Hz, 1H, $CH_{arom}$), 3.83 (s, 1H, $CH_3$), 3.76 (s, 1H, $CH_3$).
$^{13}$C NMR (101 MHz, DMSO-$d_6$, 25° C) δ 180.5, 147.0, 146.4, 139.7, 137.7, 119.4, 115.5, 110.4, 55.9, 32.6.
ESI-MS: $(M-Na)^-$: 318.3.
IR (ATR, $cm^{-1}$): ν(OH)+ν($NH_2$) = 3452, 3323; ν(C=N) = 1574; ν(C=S) = 1274; ν($SO_3^-$) = 1180, 1051.
E.A. calculated for $C_{10}H_{12}N_3NaO_5S \cdot 1.5\ H_2O$: C 32.61, H 4.10, N 11.41, S 17.41. Found: C 32.28, H 4.00, N 10.80, S 17.41.

**Sodium 2-hydroxy-3-methoxy-5-sulfonate-benzaldehyde-4-pyridyl-hydrazone (FC5)** $NaH_2L^8$

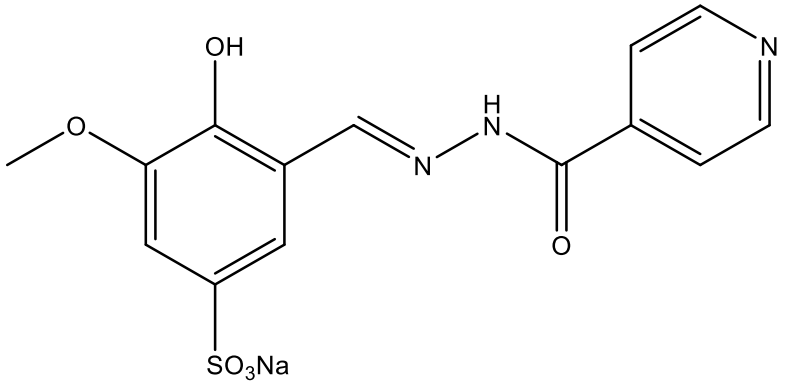


The product was obtained with the general procedure 1 as a beige solid. (Y= 64%)

$^1$H NMR (400 MHz, DMSO-$d_6$, 25° C) δ 12.28 (s, 1H, OH), 10.76 (s, 1H, NH), 8.79 (m, 2H, $CH_{arom}$), 8.70 (s, 1H, CH=N), 7.85 (m, 2H, $CH_{arom}$), 7.51 (d, J = 1.9 Hz, 1H, $CH_{arom}$), 7.21 (d, J = 1.9 Hz, 1H, $CH_{arom}$), 3.83 (s, 3H, $OCH_3$).

$^{13}$C NMR (101 MHz, DMSO-$d_6$, 25° C) δ 161.4 (Cq), 150.4 (CH), 148.3 (CH), 147.2 (Cq), 147.0 (Cq), 140.1 (Cq), 139.7 (Cq), 121.6 (CH), 117.8 (Cq), 117.4 (CH), 111.1 (CH), 55.8 ($CH_3$).

ESI-MS: $(M\text{-}Na^+)^-$: 350.0.

IR (ATR, $cm^{-1}$): ν(C=O) = 1680; ν(C=N) = 1558; ν($SO_3^-$) = 1192, 1045.

E.A. calculated for $C_{14}H_{12}N_3NaO_6S$: C 45.04, H 3.24, N 11.26, S 8.59. Found: C 44.98, H 3.26, N 11.33, S 8.43.

**Sodium 2-hydroxy-3-methoxy-5-sulfonate-benzaldehyde-4-heptyl-hydrazone (FC6)** $NaH_2L^9$

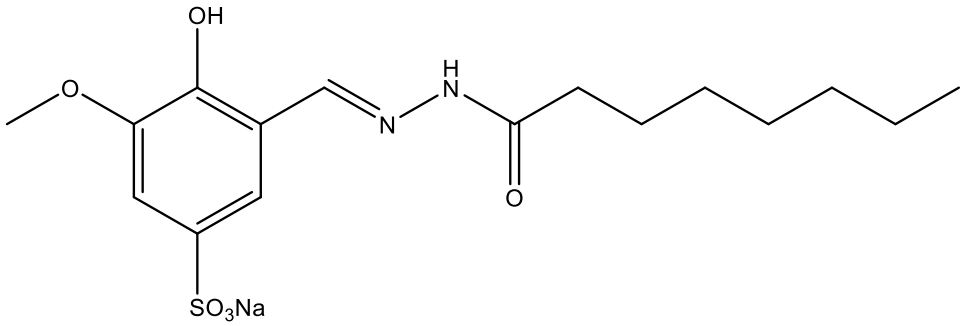


The product was obtained with the general procedure 1 as a beige solid. (Y= 66%)

The product was obtained as a mixture of isomer *E*/*Z* approximatively 2/1.

$^1$H NMR (400 MHz, DMSO-$d_6$, 25° C) δ 11.56 (s, 1H, OH, *E*), 11.17 (s, 1H, OH, *Z*), 11.02 (s, 1H, NH, *E*), 9.62 (s, 1H, NH, *Z*), 8.34 (s, 1H, CH=N, *E*), 8.28 (s, 1H, CH=N, *Z*), 7.50 (d, *J* = 1.8 Hz, 1H, $CH_{arom}$, *Z*), 7.37 (d, *J* = 1.9 Hz, 1H, $CH_{arom}$, *E*), 7.17 (d, *J* = 1.9 Hz, 1H, $CH_{arom}$, *E*), 7.16 (d, *J* = 1.8 Hz, 1H, $CH_{arom}$, *Z*), 3.81 (s, 3H, $OCH_3$, *Z*), 3.80 (s, 3H, $OCH_3$, *E*), 2.58 (t, *J* = 7.4 Hz, 2H, *Z*), 2.21 (t, *J* = 7.4 Hz, 1H, *E*), 1.57 (t, *J* = 7.3 Hz, 2H, *E*+*Z*), 1.28 (m, 8H, CH2, *E*+*Z*), 0.86 (m, 3H, $CH_3$, *E*+*Z*).

$^{13}$C NMR (101 MHz, DMSO-$d_6$, 25° C) δ 173.9 (Cq), 168.4 (Cq), 147.0 (Cq), 146.9 (Cq), 146.8$_7$ (Cq), 146.0 (CH), 145.9 (Cq), 140.4 (CH), 139.8 (Cq), 139.7 (Cq), 119.2 (Cq), 118.0 (CH), 117.6 (Cq), 115.3 (CH), 110.8 (CH), 110.1 (CH), 55.8 ($OCH_3$), 55.8 ($OCH_3$), 33.9 ($CH_2$), 31.8 ($CH_2$), 31.2$_1$ ($CH_2$), 31.1$_5$ ($CH_2$), 28.8 ($CH_2$), 28.6$_3$ ($CH_2$), 28.6$_1$ ($CH_2$), 28.4 ($CH_2$), 24.9 ($CH_2$), 24.1 ($CH_2$), 22.1 ($CH_2$), 13.9$_8$ ($CH_3$), 13.9$_5$ ($CH_3$).

ESI-MS: $(M\text{-}Na^+)^-$: 371.2.

IR (ATR, $cm^{-1}$): ν(OH)+ν($NH_2$) = 3375; ν(C=O) = 1667; ν(C=N) = 1578; ν($SO_3^-$) = 1194, 1053.

E.A. calculated for $C_{16}H_{23}N_2NaO_6S \cdot 0.5\ H_2O$: C 47.63, H 6.00, N 6.94, S 7.95. Found: C 47.15, H 5.79, N 7.00, S 7.87.

**General procedures 2 for the synthesis of M(II) complexes:**

To a solution of the ligand (1 eqv) in MeOH, a few drops of a NaOH solution are added, followed by the addition of a solution of $CuCl_2$ (or $NiCl_2$ or $Zn(CH_3COO)_2$ ) (1 eqv) in MeOH. The reaction is left stirring under $N_2$ atmosphere for 4.30 h. After that time, the solvent is partially removed under vacuum and the solid is filtered and washed with cold MeOH, obtaining the complexes without further purification.

**[Cu(NaHL$^1$)Cl] (MS18)**

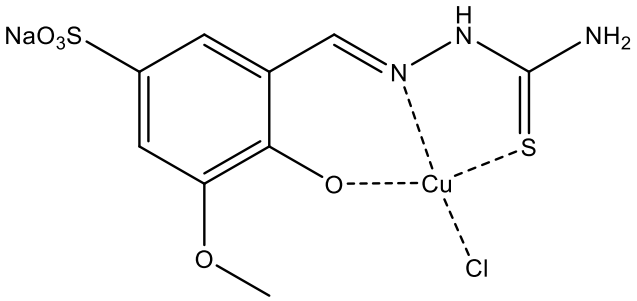


The product was obtained with the general procedure 2 as a green solid. (Y=77%)
ESI-MS: $(M\text{-}NaCl\text{-}H^+)^-$: 365.1
IR (ATR, $cm^{-1}$): ν(OH)+ν($NH_2$) = 3433, 3317; ν(C=N) = 1650; ν(C=S) = 1248; ν($SO_3^-$) = 1170, 1040.
ICP-AES calculated for $C_9H_9N_3NaO_5S_2CuCl$: Cu 14.94, Na 5.41. Found: Cu 15.0, Na 5.03.
E.A. calculated for $C_9H_9N_3NaO_5S_2CuCl$: C 25.42, H 2.13, N 9.88, S 15.08. Found: C 25.23, H 2.26, N 9.49, S 15.47.
Crystals suitable for SC-XRD were obtained by slow evaporation from a methanolic solution of the complex.

**[Cu(NaHL$^2$)Cl] (MS19)**

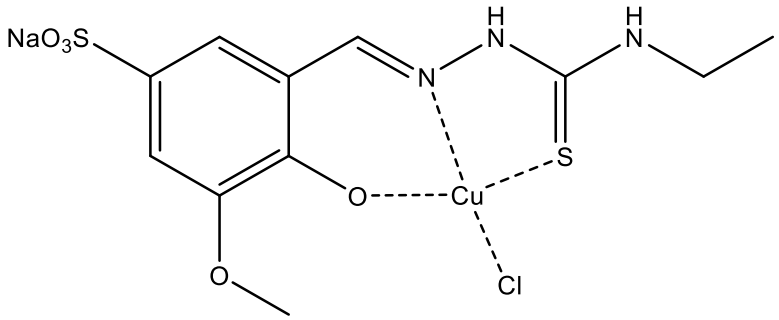


The product was obtained with the general procedure 2 as a green solid. (Y=91%)
ESI-MS: $(M\text{-}NaCl\text{-}H^+)^-$: 393.3.
IR (ATR, $cm^{-1}$): ν(NH) = 3154, 3053; ν(C=N)= 1606; ν(C=S) = 1245; ν($SO_3^-$) = 1176, 1036.
ICP-AES calculated for $C_{11}H_{13}N_3NaO_5S_2CuCl \cdot H_2O$: Cu 13.48, Na 4.88. Found: Cu 13.76, Na 4.74.
E.A. calculated for $C_{11}H_{13}N_3NaO_5S_2CuCl \cdot H_2O$: C 28.03, H 3.21, N 8.91, S 13.61. Found: C 27.89, H 3.20, N 8.65, S 14.01.
Crystals suitable for SC-XRD were obtained by slow evaporation from a solution of the complex in $H_2O$ NaCl 0.9%.

**[Cu(HL$^3$)(H$_2$O)]$_2$ (MS20)**

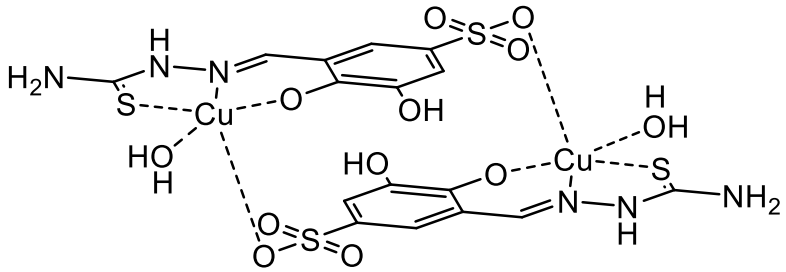

The product was obtained with the general procedure 2 as a green solid. (Y=77%)
ESI-MS: (M-H$^+$)$^-$: 351.1.
IR (ATR, cm$^{-1}$): ν(OH)+ν(NH$_2$) = 3376, 3212; ν(NH) =3061; ν(C=N) = 1605; ν(C=S) = 1255; ν(SO$_3^-$) = 1136, 1029.
ICP-AES calculated for $C_8H_7N_3O_5S_2Cu \cdot 2H_2O$: Cu 16.34, Na 0. Found: Cu 15.9, Na 0.16.
E.A. calculated for $C_8H_7N_3O_5S_2Cu \cdot 2H_2O$: C 24.71, H 2.85, N 10.81, S 16.49. Found: C 24.49, H 2.97, N 10.81, S 17.03.

**[Cu(HL$^4$)(H$_2$O)]$_2$ (MS21)**

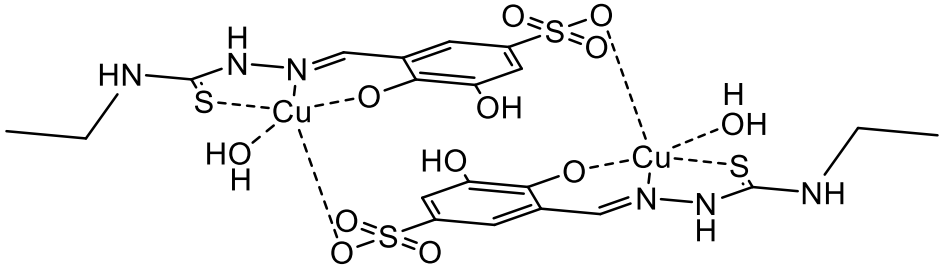

The product was obtained with the general procedure 2 as a green solid. (Y=68%)
ESI-MS: (M-H$^+$)$^-$: 379.2.
IR (ATR, cm$^{-1}$): ν(OH) = 3310; ν(C=N) = 1598; ν(C=S) = 1243; ν(SO$_3^-$) = 1160, 1036.
ICP-AES calculated for $C_{10}H_{11}N_3O_5S_2Cu \cdot 3H_2O$: Cu 14.61, Na 0. Found: Cu 15.1, Na 0.064.
E.A. calculated for $C_{10}H_{11}N_3O_5S_2Cu \cdot 3H_2O$: C 27.62, H 3.94, N 9.66, S 14.74. Found: C 27.86, H 3.91, N 9.48, S 15.17.
Crystals suitable for SC-XRD were obtained by slow evaporation from a methanolic solution of the complex.

**[Cu(HL$^6$)(H$_2$O)]$_2$ (MS27)**

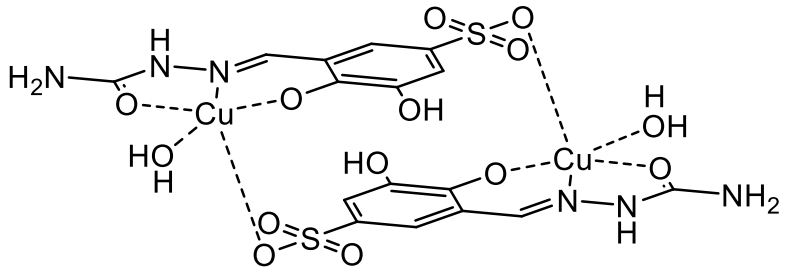

The product was obtained with the general procedure 2 as a green solid. (Y=77%)
ESI-MS: (M-H$^+$)$^-$: 335.3
IR (ATR, cm$^{-1}$): ν(NH$_2$)+ν(OH)= 3428, 3336; ν(C=O) = 1668; ν(C=N) = 1553; ν(SO$_3^-$) = 1141, 1032.
ICP-AES calculated for $C_8H_8N_3O_6SCu \cdot H_2O$: Cu 17.86, Na 0. Found: Cu 18.1, Na 0.10.
E.A. calculated for $C_8H_8N_3O_6SCu \cdot 3H_2O$: C 24.59, H 3.35, N 10.75, S 8.20. Found: C 24.82, H 2.96, N 10.61, S 8.29.

**[Cu(NaHL$^7$)Cl] MS28**

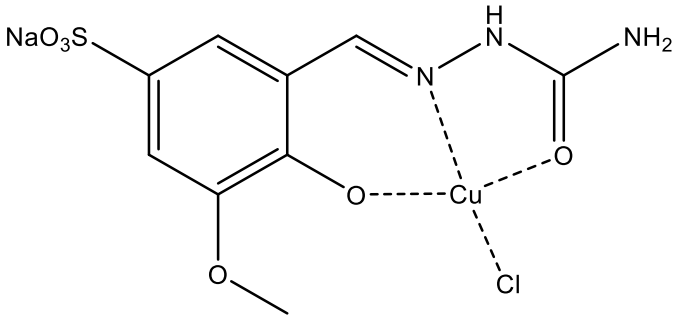

The product was obtained with the general procedure 2 as a green solid. (Y=80%)
ESI-MS: $(M\text{-}NaCl\text{-}H^+)^-$: 349.3.
IR (ATR, $cm^{-1}$): $\nu(NH_2)$ = 3318; $\nu(C=O)$ = 1659; $\nu(C=N)$ = 1545; $\nu(SO_3^-)$ = 1154, 1045.
ICP-AES calculated for $C_9H_9N_3NaO_6SCuCl$: Cu 15.53, Na 5.62. Found: Cu 16.4, Na 4.88.
E.A. calculated for $C_9H_9N_3NaO_6SCuCl$: C 26.41, H 2.22, N 10.27, S 7.84. Found: C 26.03, H 2.32, N 9.72, S 7.78.

**[Cu(NaHL$^5$)Cl] (MS30)**

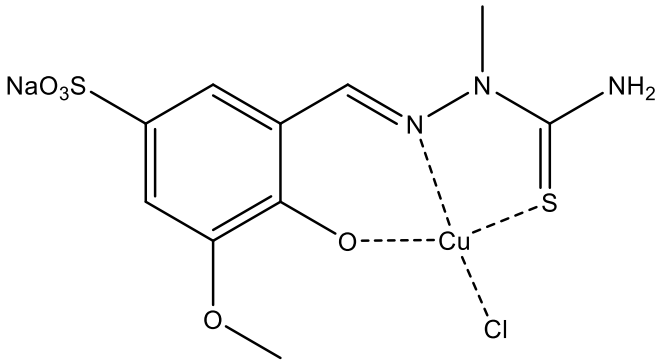

The product was obtained with the general procedure 2 as a green solid. (Y=68%)
ESI-MS: $(M\text{-}NaCl\text{-}H^+)^-$: 379.1.
IR (ATR, $cm^{-1}$): $\nu(NH_2)$ = 3364; $\nu(C=N)$ = 1605; $\nu(C=S)$ = 1251; $\nu(SO_3^-)$ = 1177, 1046.
ICP-AES calculated for $C_{10}H_{11}N_3NaO_5S_2CuCl \cdot 0.5\ H_2O$: Cu 14.17, Na 5.13. Found: Cu 15.2, Na 4.94.
E.A. calculated for $C_{10}H_{11}N_3NaO_5S_2CuCl \cdot 0.5\ H_2O$: C 26.79, H 2.70, N 9.37, S 14.30. Found: C 26.91, H 2.89, N 9.40, S 14.29.

**[Cu(HL$^8$)(H$_2$O)]$_2$ (FC8)**

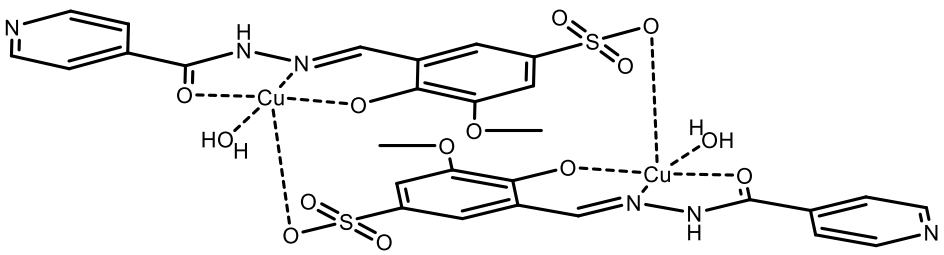

The product was obtained with the general procedure 2 as a green solid. (Y=73%)
ESI-MS: $(M\text{-}H^+)^-$: 411.0.
E.A. calculated for $C_{14}H_{11}CuN_3O_6S \cdot 3\ H_2O$: C 36.01, H 3.67, N 9.00, S 6.87. Found: C 36.29, H 3.54, N 8.87, S 6.98.
IR (ATR, $cm^{-1}$): $\nu(NH_2)$ = 3435; $\nu(C=O)$ = 1600; $\nu(C=N)$ = 1547; $\nu(SO_3^-)$ = 1166, 1031.

**[Cu(NaHL$^{9}$)Cl] (FC9)**

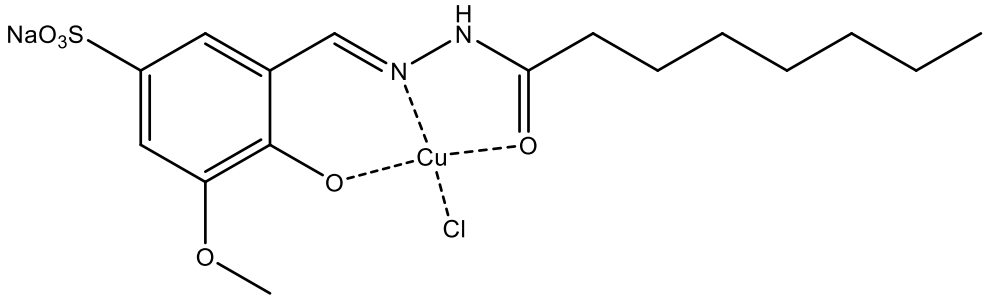

The product was obtained with the general procedure 2 as a green solid. (Y=70%)
ESI-MS: $(M\text{-}Cl^{-})^{+}$: 456.3.
E.A. calculated for $C_{16}H_{22}ClCuN_2NaO_6S \cdot H_2O$: C 37.65, H 4.74, N 5.49, S 6.28. Found: C 37.79, H 4.77, N 5.44, S 6.33.
IR (ATR, $cm^{-1}$): $\nu(NH_2)$ = 3323; $\nu(C=O)$ = 1625; $\nu(C=N)$ = 1577; $\nu(SO_3^{-})$ = 1109, 1028.

**[Zn(HL$^{3}$)(H$_2$O)]$_2$ (MS32)**

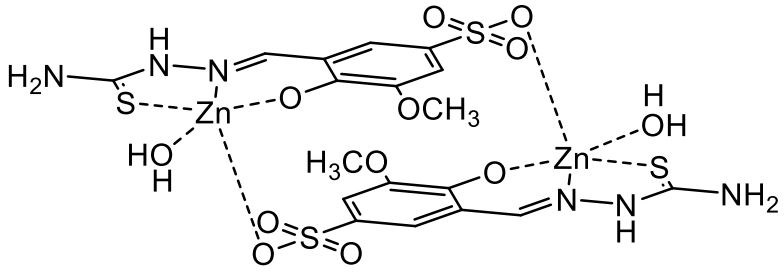

The product was obtained with the general procedure 2 as a yellow solid. (Y=81%)
$^{1}$H NMR (600 MHz, DMSO, 25° C) δ 8.17 (s, 1H, CH=N), 6.98 (d, *J* = 2.2 Hz, 1H, $CH_{arom}$), 6.93 (d, *J* = 2.2 Hz, 1H, $CH_{arom}$), 6.13 (b, 2H, $NH_2$), 3.71 (s, 3H, $OCH_3$).
ESI-MS: $(M\text{-}H^{+})^{-}$: 366.0.
IR (ATR, $cm^{-1}$): $\nu(NH_2)$ = 3373; $\nu(NH)$ = 3181; $\nu(C=N)$ = 1636; $\nu(C=S)$ = 1251; $\nu(SO_3^{-})$ = 1159, 1036.
E.A. calculated for $C_9H_{10}N_3O_5S_2Zn \cdot 3H_2O$: C 25.51, H 3.81, N 9.92, S 15.43. Found: C 25.69, H 3.61, N 9.65, S 15.15.

**[Ni(NaHL$^{3}$)Cl] (MS38)**

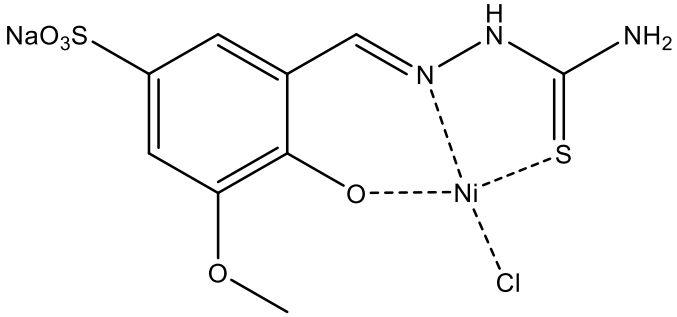

The product was obtained with the general procedure 2 as a brown solid. (Y=33%)
ESI-MS: $(M\text{-}Na^{+})^{-}$: 396.0
IR (ATR, $cm^{-1}$): $\nu(NH_2)$ = 3298; $\nu(NH)$ = 3185; $\nu(C=N)$ = 1598; $\nu(C=S)$ = 1248; $\nu(SO_3^{-})$ = 1156, 1034.
E.A. calculated for $C_9H_{10}N_3NaO_5S_2NiCl \cdot 3H_2O$: C 22.73, H 3.39, N 8.84, S 13.49. Found: C 23.07, H 3.06, N 8.66, S 13.54.

### 2.4.3 Biological Experiments

Complexes and organic ligands were solubilized in stock 0.9% NaCl solutions (10 mg/mL) and diluted in the culture medium. Cisplatin (CDDP) and oxaliplatin were solubilized in 0.9% NaCl solutions. MTT (3-(4,5-dimethylthiazol-2-yl)-2,5-diphenyltetrazolium bromide), cisplatin and oxaliplatin were obtained from Sigma Chemical Co, St. Louis, USA.

#### 2.4.3.1 Cell Cultures

Human colon HCT-15 carcinoma cell lines were obtained from American Type Culture Collection (ATCC, Rockville, MD, USA). Human pancreatic BPSN1 carcinoma cells were obtained from European Collection of Cell Culture (ECACC, Salisbury, UK). Human ovarian 2008 cancer cells were kindly provided by Prof. G. Marverti (Dept. of Biomedical Science of Modena University, Modena, Italy). Cell lines were maintained in culture in the logarithmic phase at 37 °C in a 5% carbon dioxide atmosphere using the following media added of 10% fetal calf serum (Euroclone, Milan, Italy), antibiotics (50 units/mL penicillin and 50 µg/mL streptomycin), and 2 mM L-glutamine: RPMI-1640 medium (Euroclone) for HCT-15, PSN1 and 2008 cells.

#### 2.4.3.2 Spheroid Cultures

Spheroid cultures were obtained by seeding $2.5\times10^3$ HCT-15 or PSN1 cells/well in round bottom non-tissue culture treated 96 well-plate (Greiner Bio-one, Kremsmünster, Austria) in phenol red free RPMI-1640 medium (Sigma Chemical Co.), containing 10% FCS and supplemented with 20% methyl cellulose stock solution.

#### 2.4.3.3 MTT Assay

The growth inhibitory effect towards 2D tumor cell lines was evaluated by means of the MTT assay as previously described.[149] $IC_{50}$ values were calculated by four parameter logistic (4-PL) model.

#### 2.4.3.4 Acid Phosphatase (APH) Assay

An APH modified assay was used for determining cell viability in 3D spheroids, as previously described[150]. $IC_{50}$ values were calculated with 4-PL model.

# Chapter 3: **Synthesis of glyco-conjugated thiosemicarbazones and of their copper(II) complexes as anticancer compounds**

## 3.1 Glyco-conjugation for the development of anticancer compounds

The metabolism of cancer cells displays a generally increased need for many biorelevant precursors, such as carbohydrates, peptides and amino acids. Warburg first discovered that cancer cells have a different glucose metabolism compared to healthy cells.[151] Normal cells glucose metabolism mainly works via aerobic mitochondrial oxidative phosphorylation, a process that required oxygen. In cancer cells, instead, there is a high level of glucose uptake and glycolysis followed by lactic acid fermentation takes place in the cytosol (anaerobic glycolysis) even when there is a sufficient amount of oxygen.[152] (**Figure 3.1**)

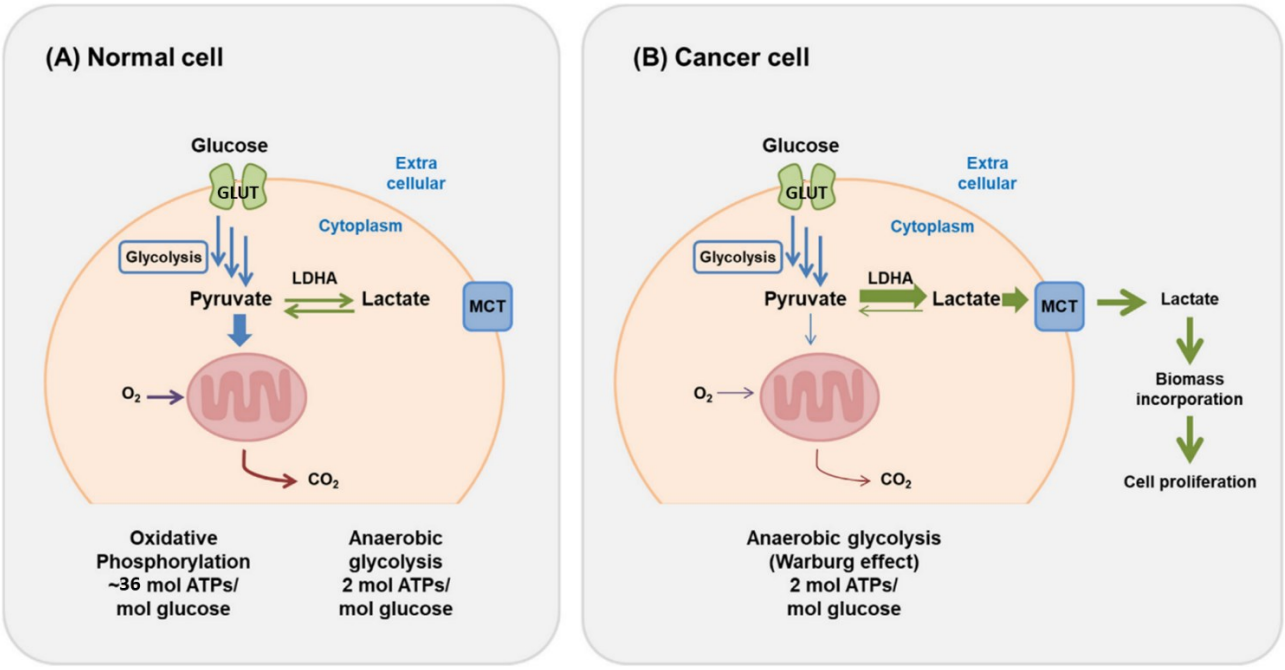


**Figure 3.1** Schematic representation of the different glycolytic pathways between normal (A) and cancer cells (B). Adapted from ref.[152]

Anaerobic glycolysis is less efficient in terms of energy generation, producing 2 molecules of ATP for each glucose molecules, compared with of ≈36 ATP molecules formed with the oxidative phosphorylation.[153] In addition, cancer cells are characterized by high proliferation rates. For these reasons, cancer cells require an increased glucose consumption to compensate for the low efficiency in energy production. To ensure an increased uptake of glucose, cancer cells present an overexpression of glucose transporters (GLUTs).[154] Considering this distinctive metabolism of cancer cells, many glycolytic transporters and enzymes involved in tumor glycolysis are interesting candidates as anticancer targets.[155]

An alternative strategy to the inhibition of the activity of transporters and glycolytic enzyme, is to take advantage of their overexpression in cancer cells for a site-specific delivery of the active compound. This strategy is based on the conjugation of glucose or glycomimetic substrates to a therapeutic agent.[156] The rationale behind the glyco-conjugation is that the chemical scaffold anchored to the glucose should be

recognized by GLUTs and internalized as a whole. This could enhance the drug uptake in the tumor cells, improving its activity and selectivity towards cancer cells.[157]

There are many examples of successful applications of this concept, such as glucofosfamide (**Scheme 3.1**). Glucofosfamide is the beta-D-glucose conjugate of isophosphoramide mustard. *In vitro* studies suggest that the cellular internalization of glucofosfamide is mediated by the glucose transmembrane transport system.[158] This compound entered preclinical trials for its interesting anticancer profile.[158]

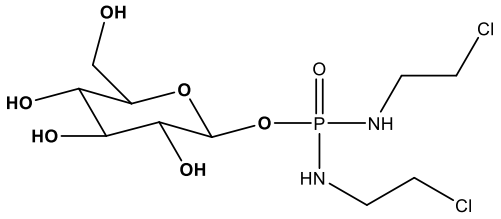


**Scheme 3.1** Chemical structure of the anticancer agent glucofosfamide internalized by GLUTs.

Glyco-conjugation has been vastly explored for many compounds with known anticancer activity, such as chlorambucil.[159] This strategy was also applied to metal-based compounds, with the investigation of several glyco-derivatives of Pt complexes.[157][160] Despite the fact that copper compounds have been extensively investigated for their anticancer properties, just a small number of glyco-conjugate Cu(II) derivatives with anticancer activity have been explored and reported.[157][160]

Moreover, few examples of glyco-functionalized TSCs with cytotoxic activity toward cancer cells have been described in the literature. Toan et al. reported the synthesis and biological characterization of some substituted isatin N-(2,3,4,6-tetra-O-acetyl-b-D-glucopyranosyl) thiosemicarbazones.[161] These compounds showed some antifungal, antibacterial and antioxidant properties. The best candidate (**Scheme 3.2**, a) was also tested for its anticancer activity, showing a selective cytotoxicity against some cancer cell lines, with $IC_{50}$ values in the low micromolar range.[161]

Tomat and Akam described the synthesis of the glycosylated thiosemicarbazones **G6TC4** and **M6TC4** (**Scheme 3.2**, b) designed as Fe prochelators.[162] These glycoconjugates showed to compete with glucose for transporters mediated cellular uptake and displayed improved selectivity compared to their aglycone analogues.[162]

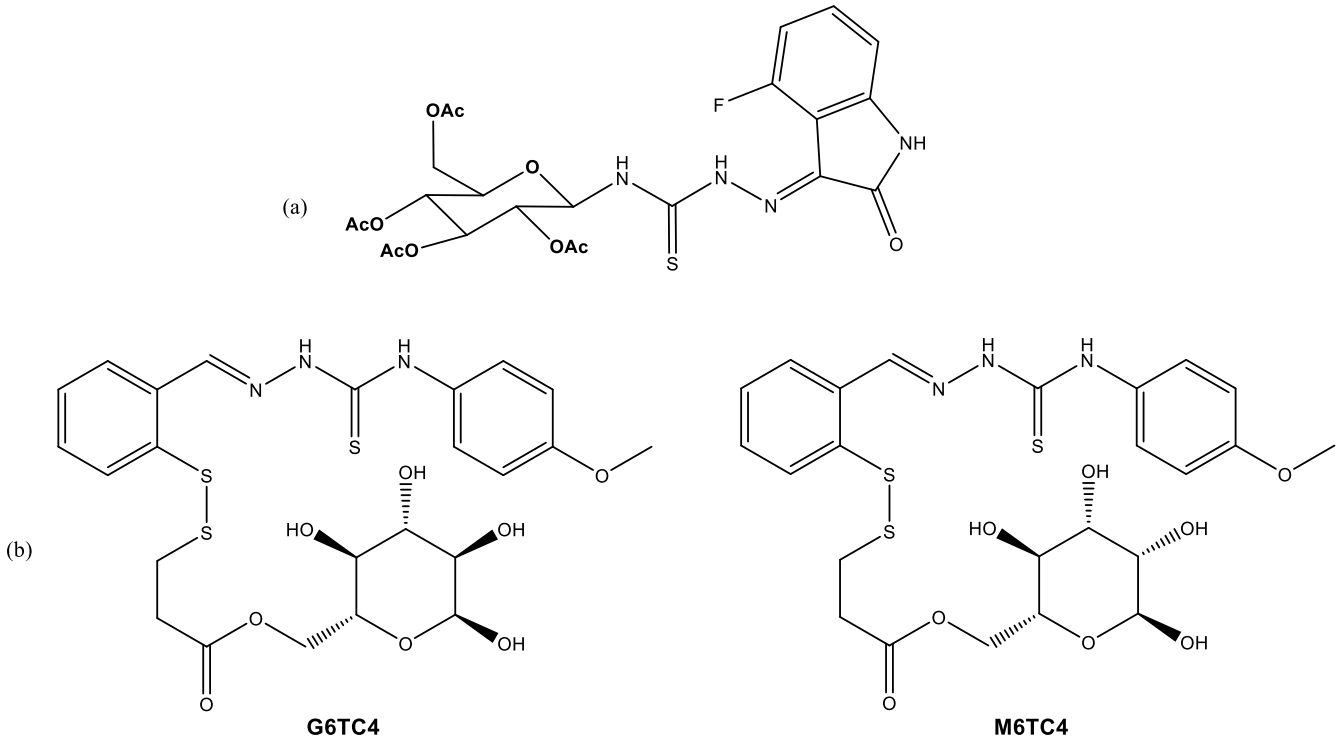


**Scheme 3.2.** Structure of some glycosylated TSCs with anticancer activity.

Furthermore, a glycosylated thiocarbohydrazone (THC) (**Scheme 3.3**) had been described by Rizzarelli et al.[163]

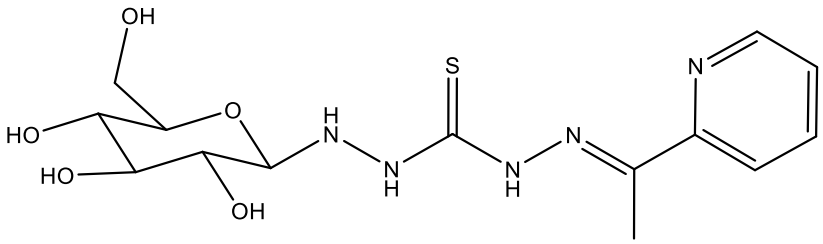


**Scheme 3.3** Structure of the glycosylated THC with anticancer activity described by Rizzarelli *et al*.[163].

This compound has a good *in vitro* cytotoxicity towards PC-3 human prostate adenocarcinoma and MDA-MB-231 breast cancer cells, with similar $IC_{50}$ values to that of its aglycone analogues. Moreover, it was demonstrated that the presence of Cu(II) ions improves the anticancer activity.[163]

## 3.2 Aim of the project

Continuing to search for an improved water solubility of salicyl thiosemicarbazones, the possibility to add a glucose moiety to the ligands was explored. Glyco-conjugation, in addition to improve the water solubility, can potentially increase the anticancer properties of the compounds. The addition of a glucose moiety can, in fact, potentially increase the compound selectivity towards cancer cells.

Glyco-conjugated copper complexes have not been broadly investigated; hence the evaluation of these compounds can help to better understand the potential of this class of molecules. A few examples of glyco-TSC suggest that glyco-conjugation is a viable strategy improve the selectivity of anticancer compounds.

Starting from these considerations, a new series of O-glycosilated thiosemicarbazones and their copper(II) complexes were synthesized, with the aim of combining the anticancer properties of TSC and their Cu(II) complexes, water solubility and a favourable internalization of the glucose moiety by glucose transporters, overexpressed in cancer cells.

This project was carried out during a period of research in Professor D. Montagner's laboratory in Maynooth University, Ireland.

## 3.3 Results and discussion

A new panel of O-glycosilated thiosemicarbazones and their copper(II) complexes (**Scheme 3.4**) were synthesized.

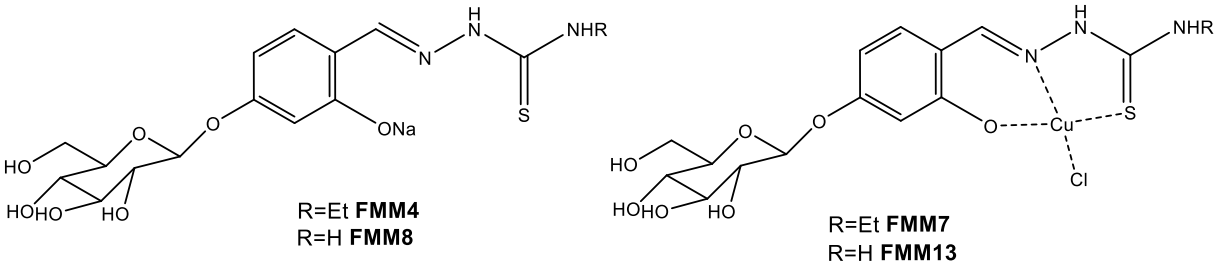


**Scheme 3.4.** Structure of the glycosylated TSCs ligands **FMM4**, **FMM8** and their copper(II) complexes **FMM7, FMM13**.

The synthesis of the glycosylated-TSC ligands was carried out as in the scheme reported below.

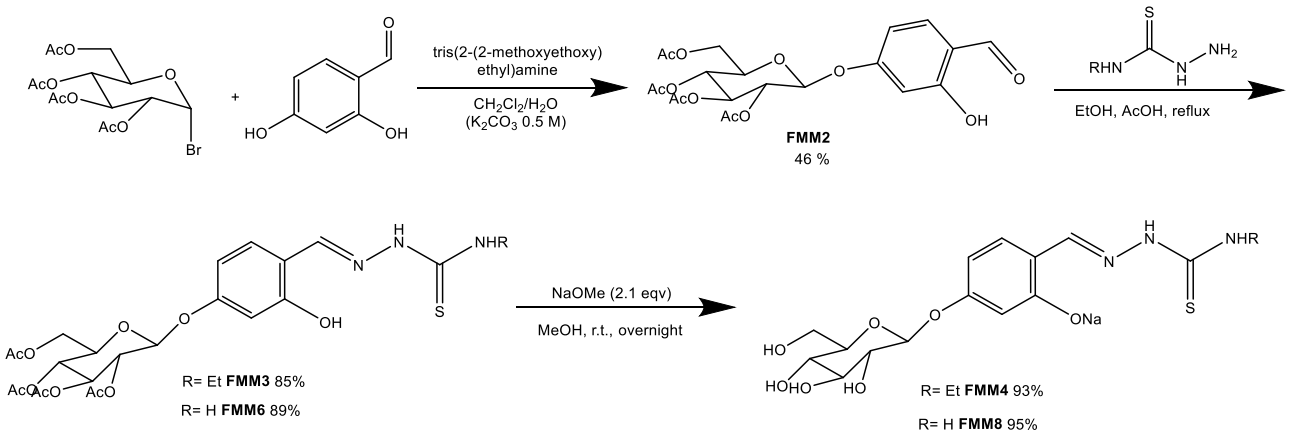


**Scheme 3.5** Synthetic route to the glycosylated TSCs ligands.

First, glycosylation reaction between acetobromo-α-D-glucose and 2,4-dihydroxy benzaldehyde was carried out, using a similar procedure as reported by Brouillard et al. [164]

The reaction was conducted in bi-phasic conditions by using DCM, an aqueous solution of $K_2CO_3$, and tris(2-(2-methoxyethoxyethyl)amine as a phase transfer catalyst, at reflux for 3 days. After work-up and a chromatographic separation, **FMM2** was obtained with 46% yield as a white powder.

The $^1$H-NMR spectrum in $CDCl_3$ (**Figure 3.2**) is in concordance with the data reported for this molecule.[165]

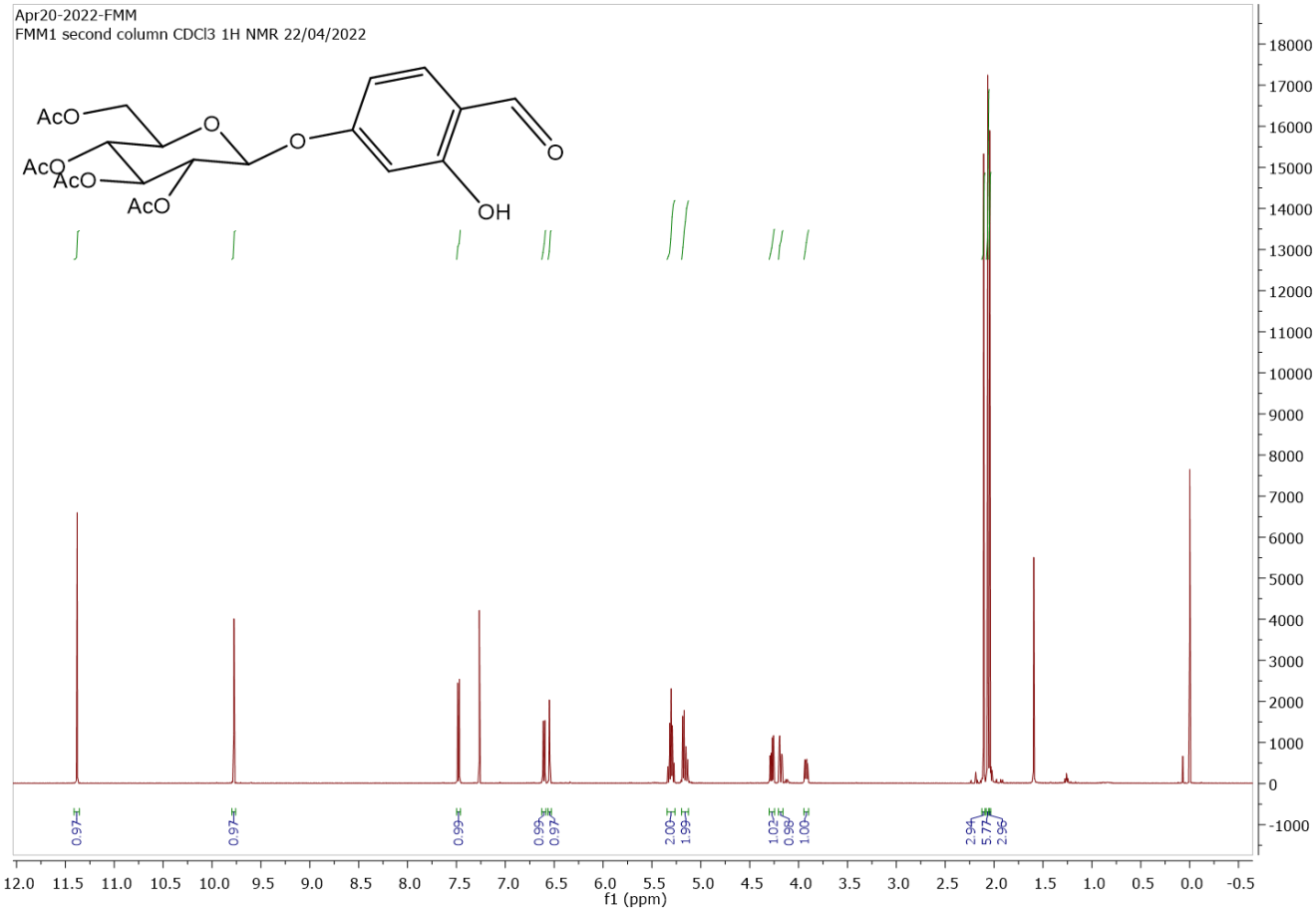


**Figure 3.2** $^{1}$H-NMR spectrum (25°C, 400 MHz, $CDCl_3$) of compound **FMM2.**

**FMM2** was then reacted with thiosemicarbazide or ethyl thiosemicarbazide to obtain the two new glyco-TSCs **FMM6** and **FMM3,** respectively. These reactions were performed in EtOH at reflux for 4 hours, with few drops of $CH_3COOH$ leading to the isolation of the product by filtration. In the synthesis of **FMM6,** water was added before filtration to promote precipitation of the product.

The new glyco-TSCs **FMM3** and **FMM6** were characterized with $^{1}$H and $^{13}$C NMR spectroscopy, AT-IR, HRMS and elemental analysis.

In **Figure 3.3** is reported the $^{1}$H NMR spectrum in DMSO of ligand **FMM3**, as an example. The spectrum confirmed the outcome of the reaction, with the disappearance of the aldehydic proton and the appearance of the characteristic iminic proton signal at 8.27 ppm, as well as the $CH_3$ triplet (1.97 ppm) and $CH_2$ quartet (4.22 ppm) signals. Only the thione *E*-form appears to be present in DMSO-$d_6$ solution at room temperature.

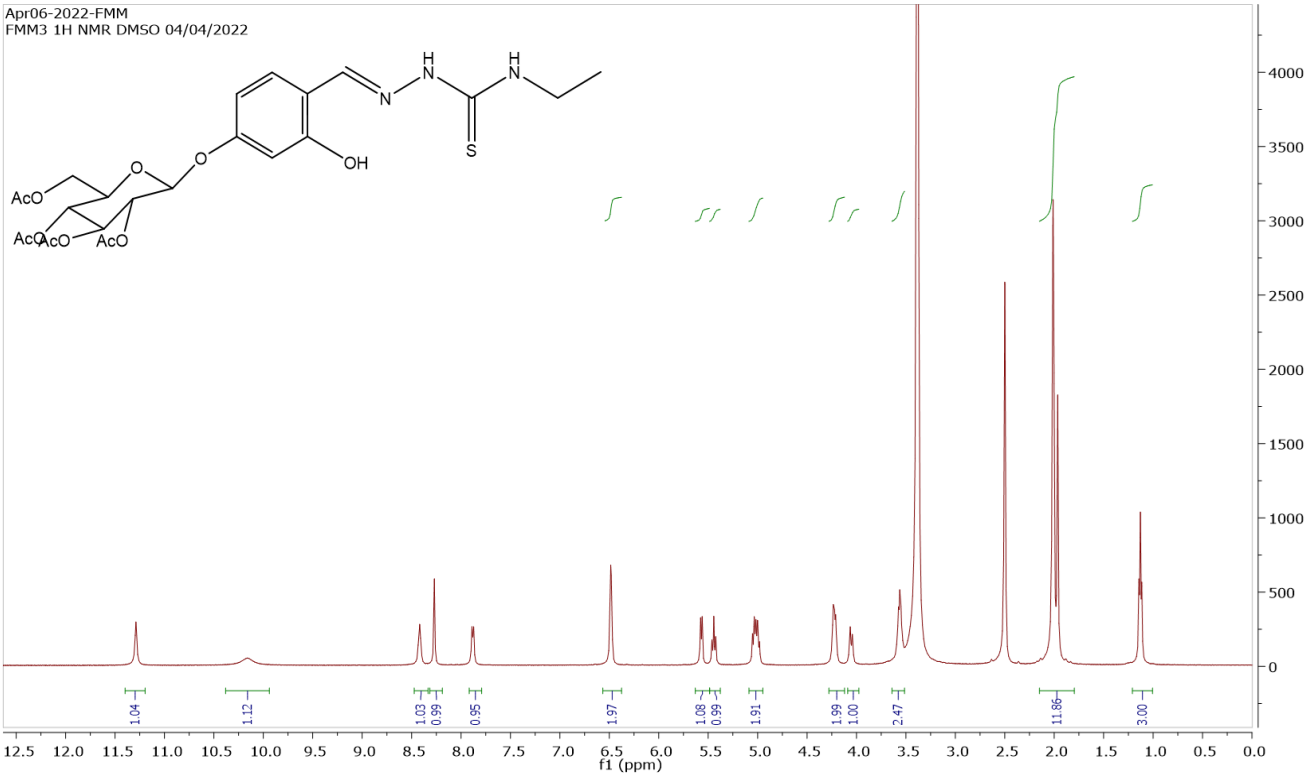


**Figure 3.3** $^{1}$H-NMR spectrum (25°C, 400 MHz, DMSO-$d_6$) of compound **FMM3.**

Ligands **FMM3** and **FMM6** were then reacted with 2.1 equivalents of NaOMe in MeOH at room temperature, in order to obtain their respective de-acetylated forms **FMM4** and **FMM8**. TLC checking (in 100% EtOAc) of the reaction indicated that the complete conversion was obtained overnight, then acetic acid was added until pH≈6. Ligands were recovered after chromatographic column (DCM/MeOH/$NH_4OH_{(aq)}$ 8/2/0.02 and DCM/MeOH/$NH_4OH_{(aq)}$ 75/25/0.05) with excellent yields (93% and 95% respectively).

The compounds were characterized with $^{1}$H and $^{13}$C NMR spectroscopy, AT-IR, HRMS and elemental analysis.

Comparing the $^{1}$H-NMR spectra of de-acetylated **FMM4** with **FMM3** (**Figure 3.4**), the complete conversion of the isolated compound is confirmed by the disappearance of the 12 H signals around 2 ppm, corresponding to the $CH_3$ of the acetyl groups. Furthermore, it is possible to observe a shift at lower ppm and an increase in the multiplicity of the CH signals of the glucose, typical of the deprotected sugar moiety.

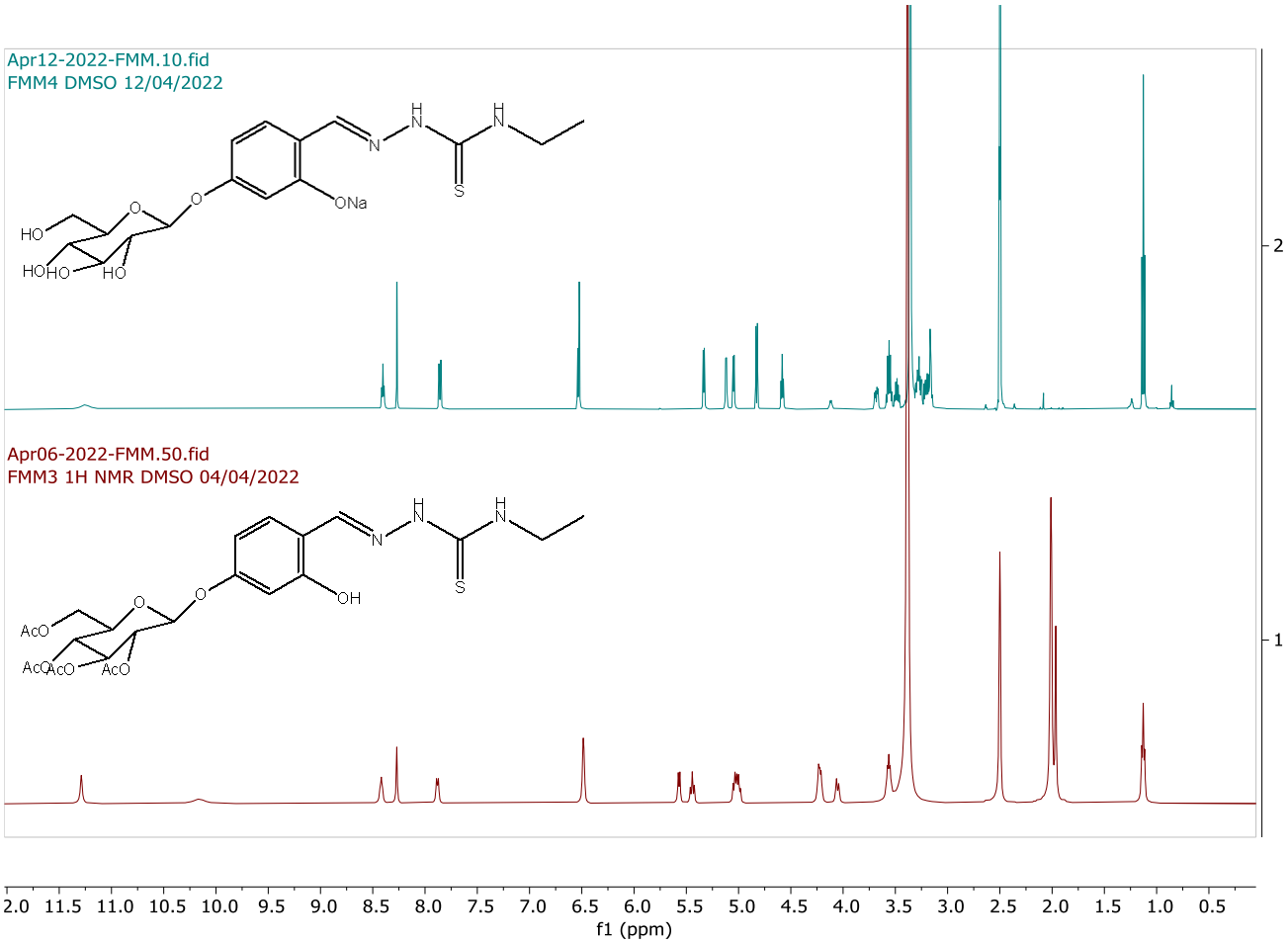


**Figure 3.4** $^{1}$H-NMR spectra (25°C, 400 MHz, DMSO-$d_6$) of the de-acetylated **FMM4** (top) and of the acetylated **FMM3** (bottom).

Comparison of the IR spectra of the acetylated and deacetylated ligands as well confirms the outcome of the reaction. As it can be observed in the superimposing of IR spectra of **FMM6** and **FMM8** (**Figure 3.5**), the absence of the C=O band around 1740 $cm^{-1}$ and the very broad signal in the O-H area indicates the complete conversion of the acetylated sugar into the free sugar moiety. Furthermore, looking at the spectra individually it can be observed the absence of a S-H stretching band (2600 $cm^{-1}$) and the presence of a stretching N-H bands (3000-3100 $cm^{-1}$), suggesting that both ligands are in the thione form in the solid state, as observed with the sulfonated TSCs.

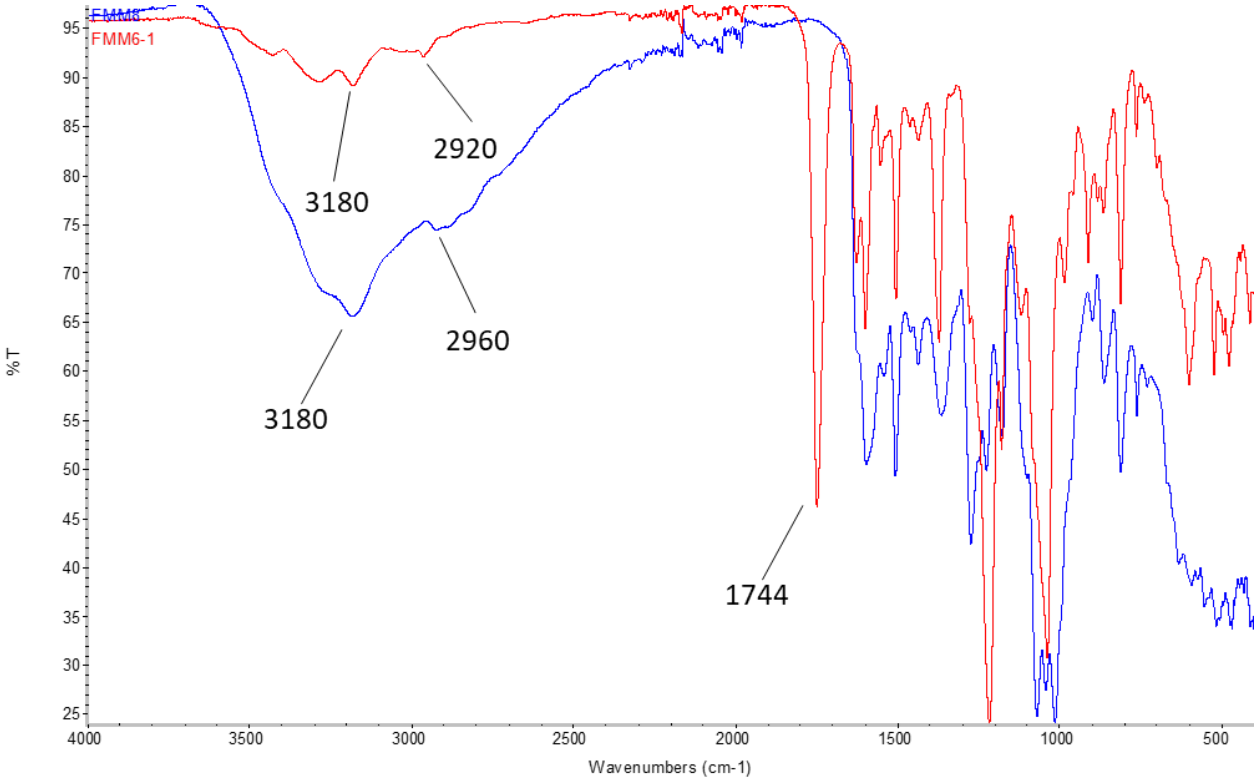


**Figure 3.5** FT-IR spectra of the acetylated **FMM6** (red) and de-acetylated TSC **FMM8** (blue).

HRMS analysis was employed to further characterize the ligands, where it was possible to observe the molecular ion peaks in both positive and negative ionization modes. In **Figure 3.6** are reported the extracted ion chromatograms of compound **FMM4.**

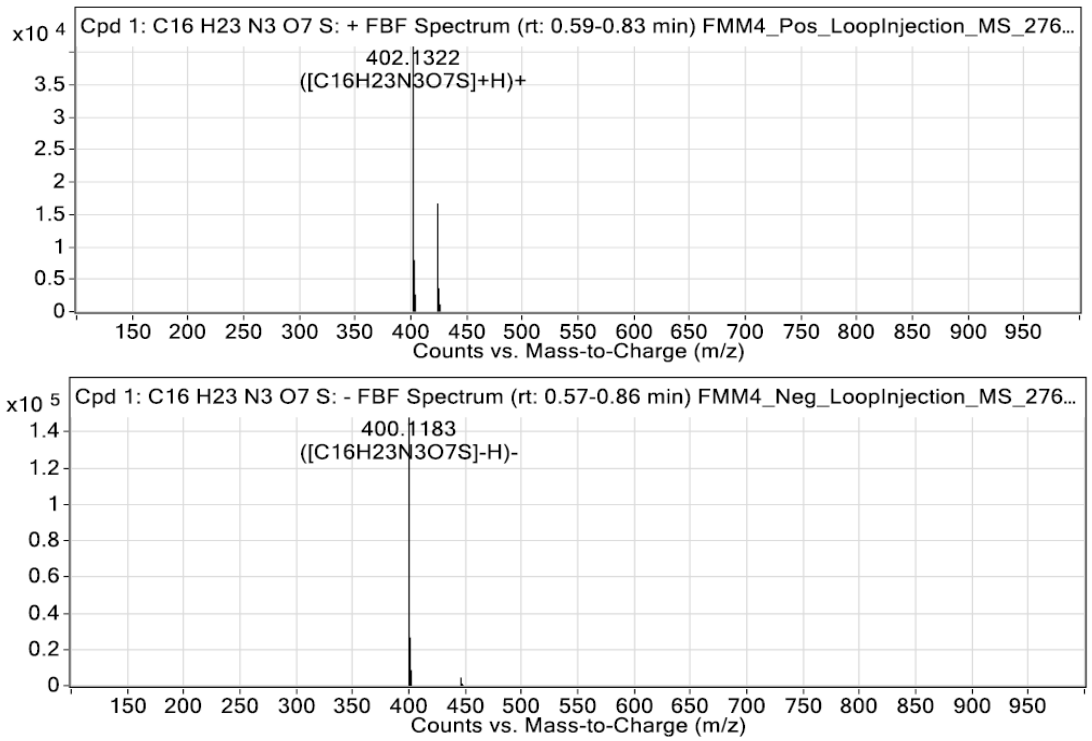


**Figure 3.6** Extracted ion chromatogram for compound **FMM4** in MeOH positive ionization, 125 eV (top) and negative ionization 125 eV (bottom).

Elemental analysis results were coherent with the presence of deprotected sugar moiety thiosemicarbazone ligands with a sodium atom, suggesting the recovery of the ligands as sodium salts on the phenolic hydroxy group.

Copper(II) complexes were synthesized both with the acetylated and the deprotected sugar moiety, in order to evaluate their anticancer activity and different cellular uptake. These ligands, and therefore the relative complexes, have different hydrophilicity. The presence of the acetylated sugar moiety should impair a possible entrance through glucose transporters, but it can favour a passage through the membrane, being the compounds more lipophilic.

The copper(II) complexes were synthetised in a similar manner to that described for the sulfonated TSC, with one equivalent of $CuCl_2$ under nitrogen, at pH≈8 for 3 hours (**Scheme 3.6**).

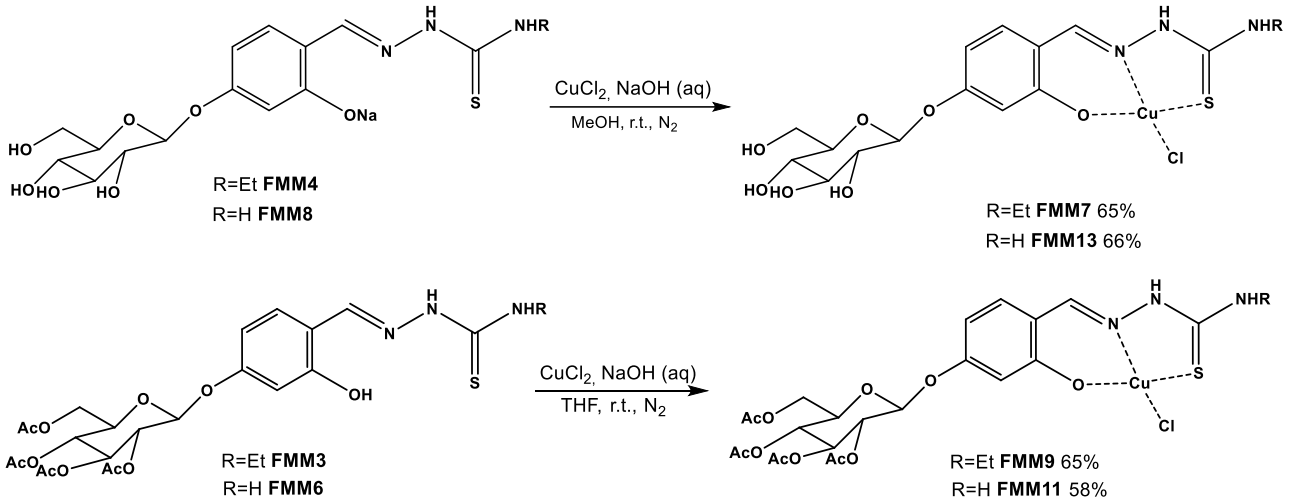


**Scheme 3.6.** Synthesis of the glycosylated TSC copper(II) complexes.

Ligands **FMM4** and **FMM8** were dissolved in methanol and their relative copper complexes **FMM7** and **FMM13** were recovered through filtration, having the complex very low solubility.

For the acetylated ligands **FMM3** and **FMM6**, on the other hand, the reaction was conducted in THF, since the ligands are practically insoluble in methanol. After 3 hours no precipitation was observed, then $Et_2O$ was slowly added to the reaction mixture to induce the precipitation of the copper complexes **FMM9** and **FMM11**, later recovered by filtration.

The TSC copper(II) complexes **FMM7, FMM9, FMM11** and **FMM13** were characterised through elemental analysis, FT-IR, and HRMS.

The comparison between the IR spectra of the complexes with the free ligands indicates the tridentate coordination of the ligands to the copper ions. As its noticeable, for instance, in the comparison of **FMM6** (ligand) and its copper complex **FMM11** (**Figure 3.7**), the O-H band around 3400 $cm^{-1}$ disappears in the complex spectra, indicating the deprotonation of the ligand on the hydroxy group. Furthermore, a shift to higher $cm^{-1}$ of the C=N and C=S band suggest the participation of these groups in the complexation.

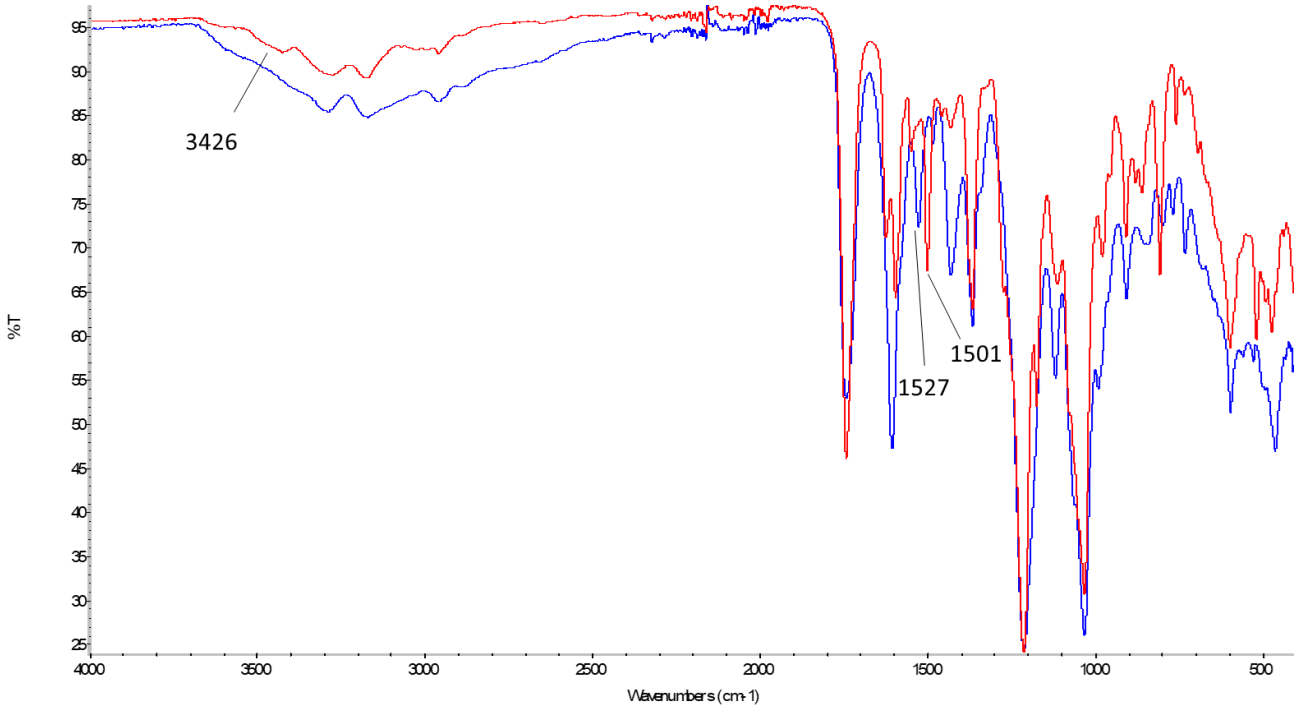


**Figure 3.7** FT-IR spectra of the acetylated **FMM6** (red) and its copper(II) complex **FMM11** (blue).

Elemental analysis results are in accordance with complexes of stoichiometry [Cu(HL)Cl], with the copper ion coordinated by the mono-deprotonated TSC and by a chloride ion.

HRMS spectra of the complexes also suggests the postulated structures. For all complexes, molecular ions are visible in positive ionization mode, as $Na^+$ adducts (**Figure 3.8**).

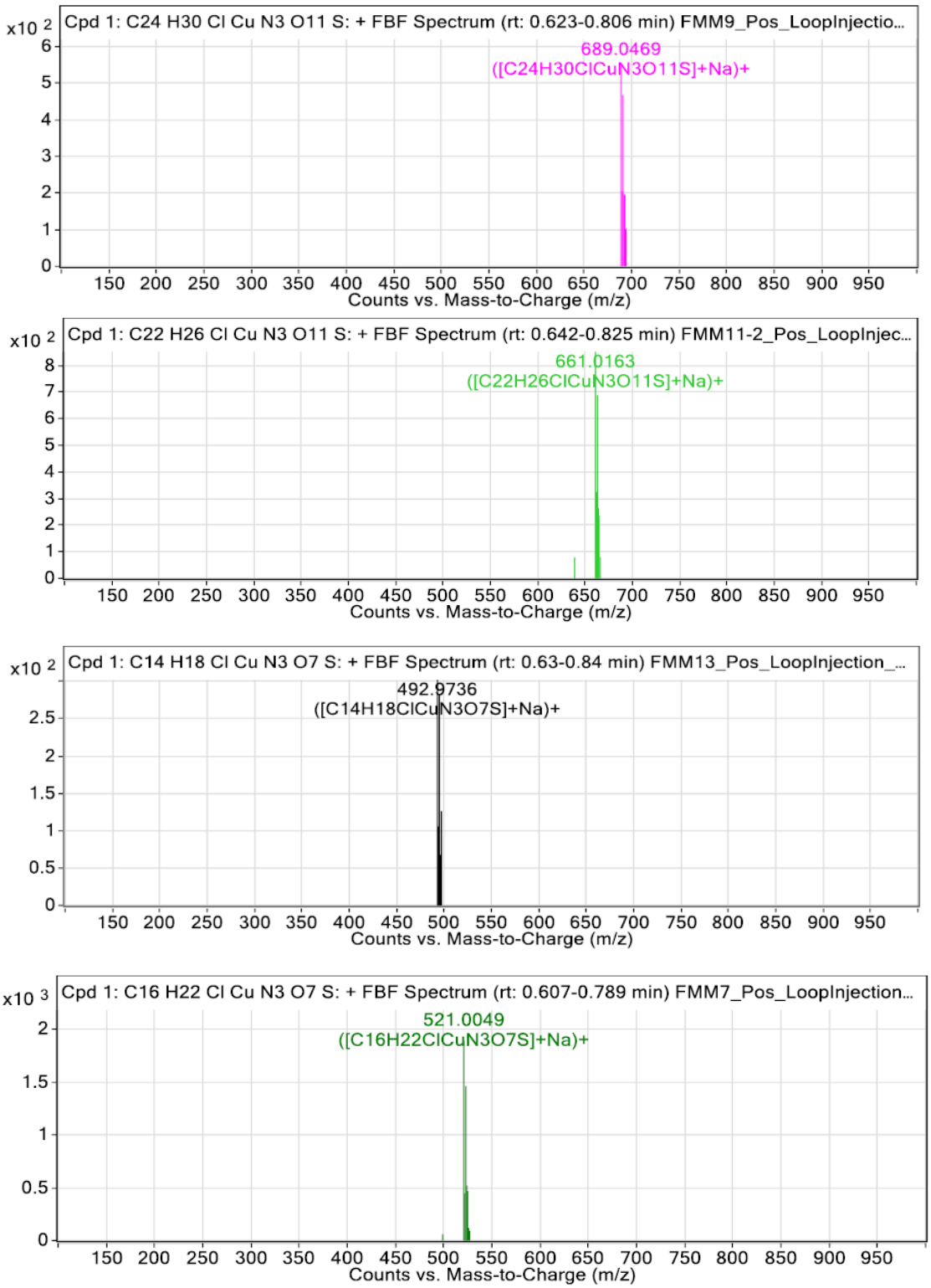


**Figure 3.8** Extracted ion chromatogram in MeOH (positive ionization, 125 eV) of compounds **FMM9** (purple), **FMM11** (light green), **FMM13** (black) and **FMM7** (dark green).

In case of **FMM7**, the molecular ion peak was also observed with the negative ionization mode (**Figure 3.9**).

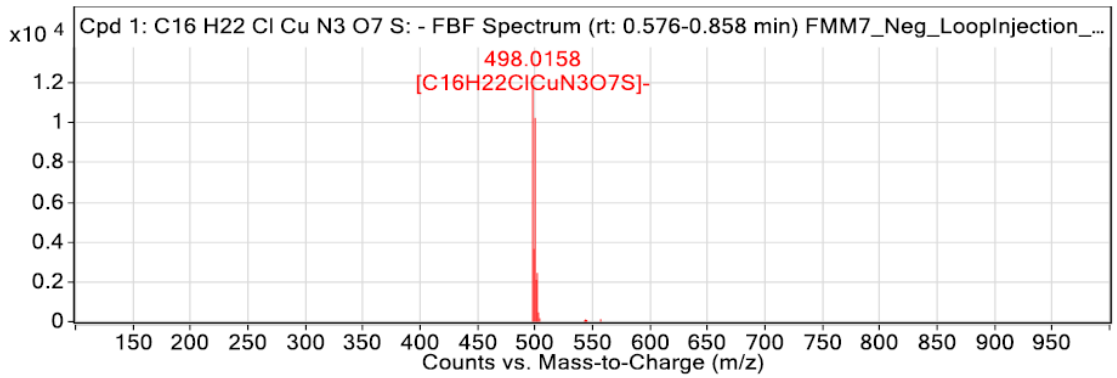


**Figure 3.9** Extracted ion chromatogram in MeOH (negative ionization, 125 eV) of **FMM7.**

Finally, the stability of the copper complexes was evaluated recording the UV spectra of the compounds in solution (C≈ 40-50 µM in 25 mM of HEPES buffer, at pH=7.4 in $H_2O$ NaCl 0.9%) over 72 hours.

In case of the acetylated sugar moiety analogues, the final solutions contained 2% of DMSO, because these complexes are not completely soluble in water. These conditions allow to simulate the solution used for the in-vitro tests with cancer cells lines.

In **Figure 3.10** are reported the UV spectra of the copper complexes.

The glyco-TSC Cu complexes **FMM7** and **FMM13** retained the same UV spectra in the 72 hours, indicating the stability in these solution conditions. Acetylated glyco-TSC Cu complex **FMM11** spectra were unchanged over time, while for complex **FMM9** it was observed a significant change in the absorbance value. The alteration of the UV spectra over time is probably due to the low solubility of the acetylated copper complex in these conditions. In fact, the absorbance values started to decrease rapidly a few hours after the first recording and, in concomitance with these change in the UV spectra, a precipitate, that was not present at time 0, was observed in the cuvette.

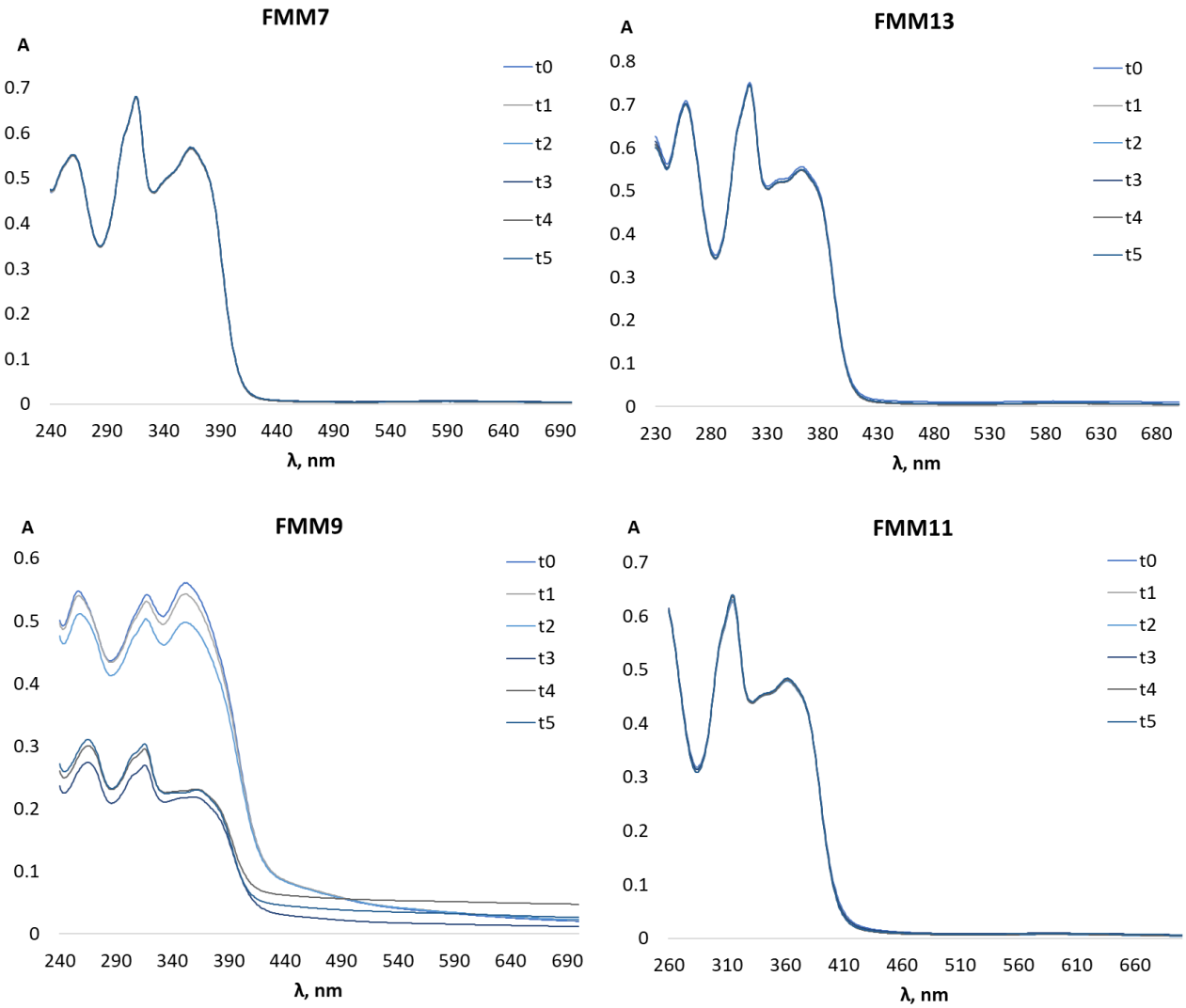


**Figure 3.10** UV spectra of **FMM7**, **FMM13**, **FMM9** and **FMM11** (c≈40-50 mM) in 25 mM HEPES buffer (pH=7.4) in $H_2O$, recorded over 72 hrs. **FMM9** and **FMM11** final solution contains 2% DMSO.

After the characterization of the glyco-TSC copper(II) complexes, a symmetric bis-thiocarbohydrazone (THC) (**FMM10**) and its copper complex (**FMM14**) were synthetised (**Scheme 3.7**).

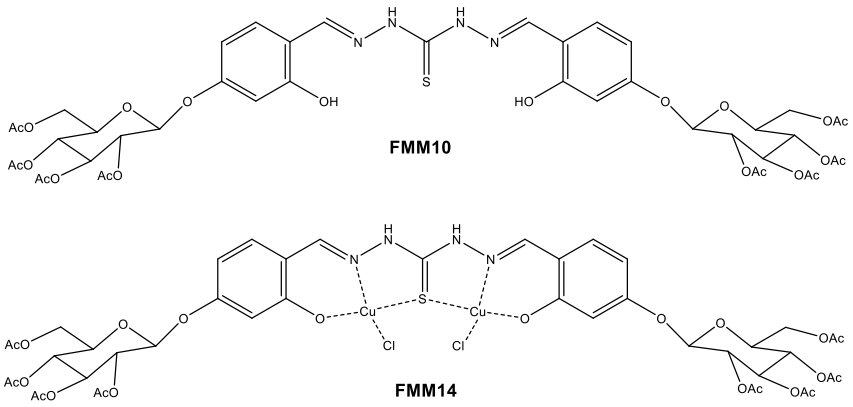


**Scheme 3.7** Structures of the glyco-bis THC **FMM10** and its copper complex **FMM14**.

Briefly, **FMM2** (2 eqv) was reacted with thiocarbohydrazide (1 eqv) in EtOH at reflux, with a few drops of acetic acid. After 4 hours, the reaction was cooled to r.t. and a pale yellow solid was filtered and washed with EtOH and water, obtaining **FMM10** with 87% yield.

The ligand was charactherized with $^{1}H$ and $^{13}C$-NMR spectroscopy, HRMS, FT-IR and elemental analysis.

The $^{1}H$-NMR spectrum in DMSO-$d_6$ of the compound confirmed the outcome of the reaction. This kind of molecules can have different isomeric forms in solution, as can be inferred looking at the proton NMR spectrum (**Figure 3.11**).

The absence of signals around 15 ppm (S-H proton signal) suggests that the ligand is present in solution in the thione form. The presence of distinct signals for the iminic protons (8.67 and 8.39 ppm), for the 5' aromatic protons (8.01 and 7.35 ppm) and 4 different signals for OH and NH protons (11.95, 11.89, 11.78 and 10.23 ppm) indicates that the ligand in solution is not symmetric. This spectrum is in accord to the presence of the (E,Z) isomer form in solution, analogously to what is reported for similar bis THC. [166]

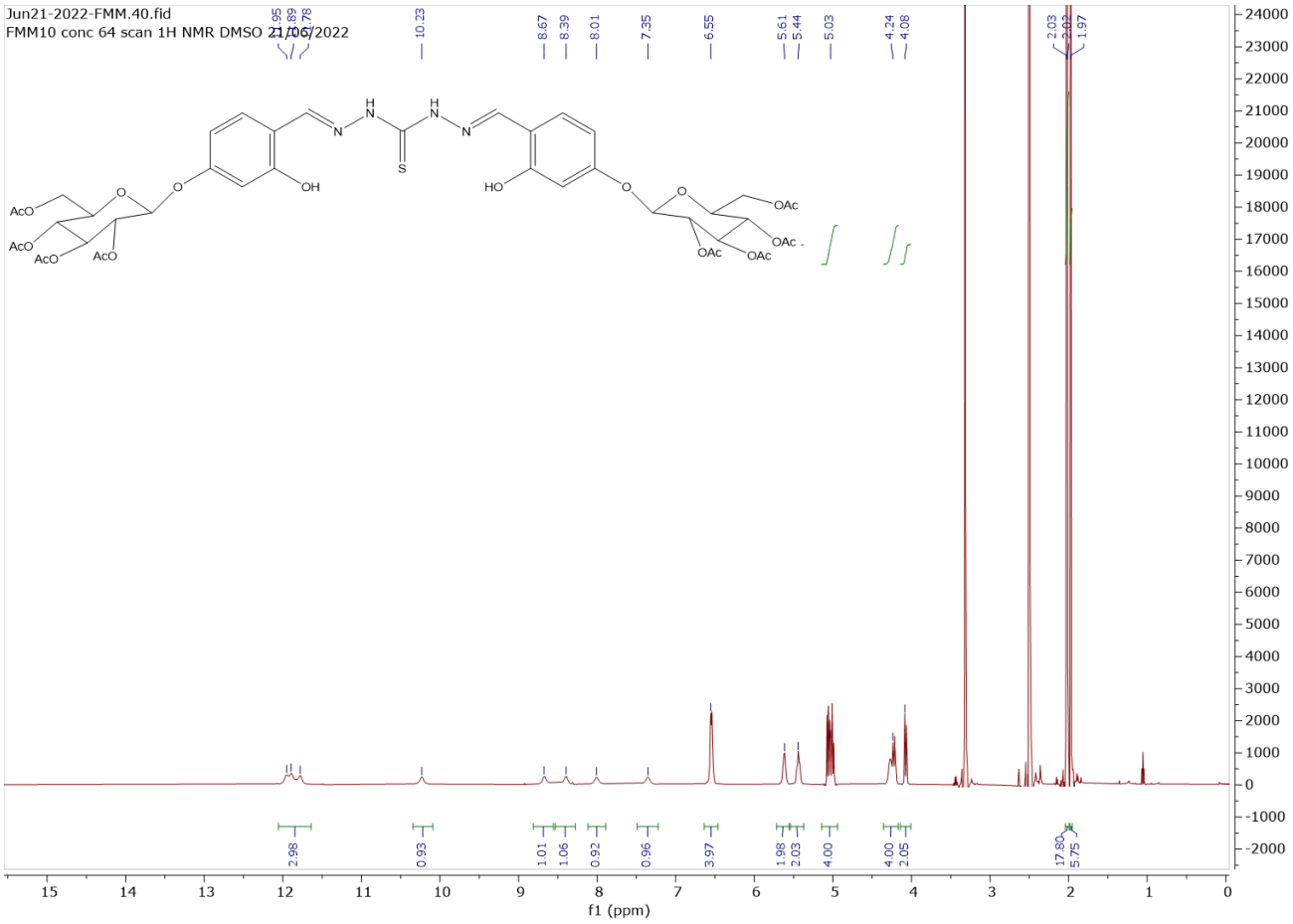


**Figure 3.11** $^{1}H$-NMR spectrum (25°C, 400 MHz, DMSO-$d_6$) of compound **FMM10.**

After the glyco-THC ligand was obtained and characterized, the copper (II) complex **FMM14** was synthetised with the same procedure used for the acetylated TSCs.

The comparison of the IR spectra of **FMM10** and **FMM14** (**Figure 3.12**) confirms the formation of the complex. A shift of $cm^{-1}$ values of the C=N and C=S bands indicate the involvement of these groups in the complexation of the copper ions.

Elemental analysis of the complex also confirmed the complexation of two copper(II) atoms by the glyco-THC ligand.

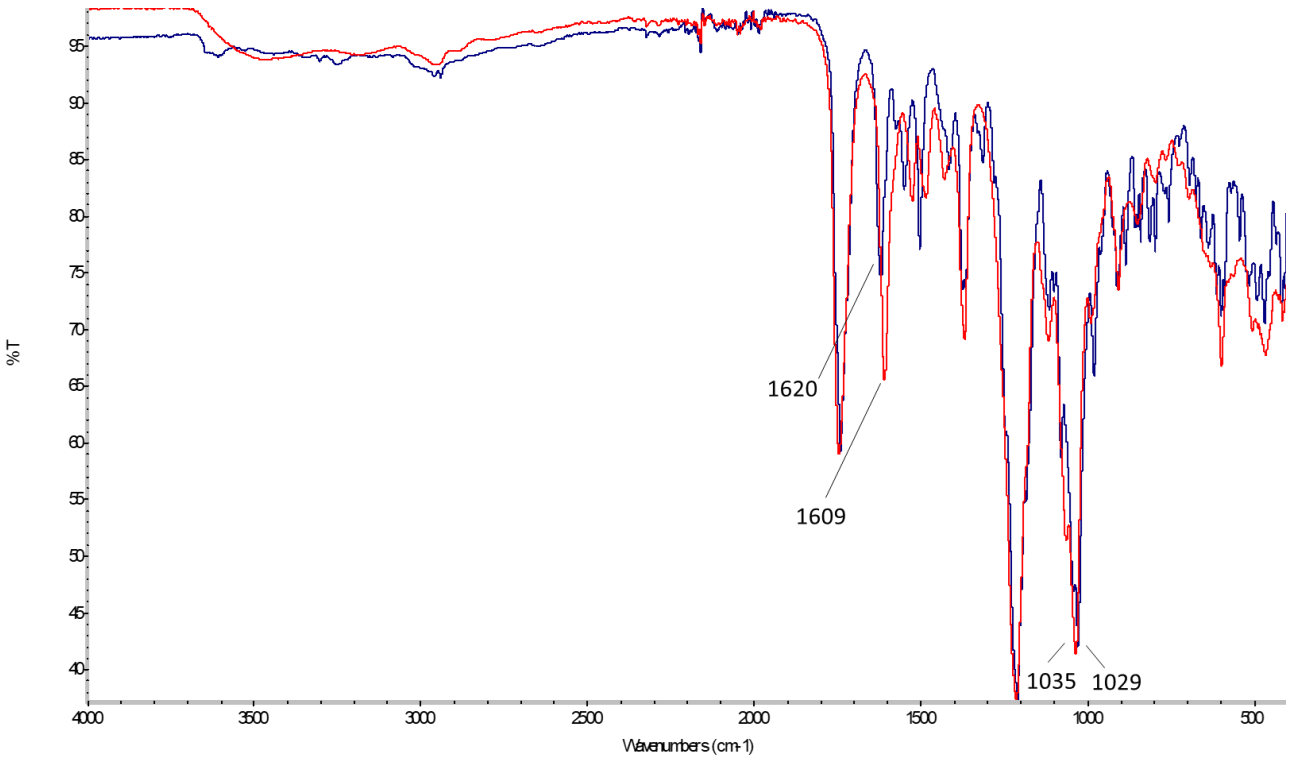


**Figure 3.12** FT-IR spectra of bis THC **FMM10** (blue) and its copper(II) complex **FMM14** (red).

Future work will focus on the synthesis and characterization of a THC with a deprotected sugar moiety and its copper(II) complex.

The panel of glyco-TSCs and acetylated glyco-TSCs ligands and complexes are currently under evaluation of their cytotoxic activity towards cancer cells at professor V. Gandin's laboratory. Furthermore, studies on their diffusion through glucose transporter will also be conducted, to investigate the way these compounds enter the cells.

## 3.4 Conclusions

During this project, a new series of glyco-conjugate TSC derivatives and their Cu(II) have been synthetised and characterized. The acetylated analogues of both ligands and complexes have also been prepared, in order to compare their biological activity.

These compounds were obtained with good yields and with a few synthetic steps, overcoming the common drawback of the difficult and tedious sugar chemistry. Additionally, an acetylated glyco-conjugate TCH derivative was also synthetized.

The ongoing evaluation of the cytotoxic activity of these water-soluble compounds will give interesting information on the conjugation of glucose moiety to TSCs and in the activity of Cu(II) glyco-functionalized derivatives, that have not been extensively investigated.

## 3.5 Experimental

### 3.5.1 Materials and methods

All reagents and reactants were purchased from commercial sources and use without any further purification. All solvents were used without further purification.

NMR spectra were recorded on a Bruker Advance spectrometer operating at 500 MHz for the $^{1}H$ and at 125 MHz for $^{13}C$ nuclei, at 25°C. All chemical shifts are expressed in ppm.

Infrared (IR) spectra were recorded in the region 4000 - 400 $cm^{-1}$ on a Perkin Elmer precisely spectrum 100 FT/IR spectrometer, samples were run using ATR.

MS spectra were acquired with a Bruker MaXis HD ESI-QTOF mass spectrometer coupled to a Thermo Scientific Dionex Ultra High Performance Liquid Chromatography (UPLC) unit.

Elemental analyses (carbon, hydrogen and nitrogen) were performed with a PerkinElmer 2400 series II analyser or a FlashEA 1112 series CHNS/O analyzer (Thermo Fisher) with gas-chromatographic separation (carbon, hydrogen, nitrogen and sulphur).

UV-Vis spectra were recorded in a Perkin Elmer precisely Lambda 35 UV/Vis spectrometer.

### 3.5.2 Chemistry

**4-(2',3',4',6'-Tetra-O-acetyl-β-D-glucopyranosyloxy)-2- hydroxybenzaldehyde (FMM2)**

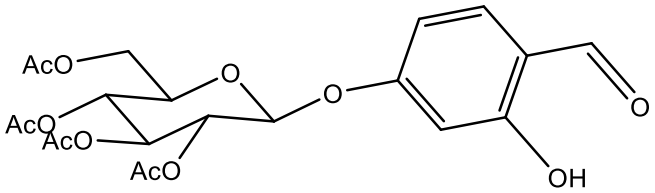


2,4-dihydroxy benzaldehyde (0.896 g, 6.48 mmol, 1 eqv) was dissolved in an aqueous $K_2CO_3$ solution (0.5 M, 11 mL) with trismethoxyethoxy ethylamine (3.11 mL, 9.73 mmol, 1.5 eqv), then a solution of α-D-acetobrome glucose (4.000 g, 9.73 mmol, 1.5 eqv) in DCM (11 mL) was added. The reaction mixture was left stirring at 47°C for 3 days. After that time the reaction was cooled to r.t. and 40 mL of water are added. The organic phase was separated and the aqueous phase was extracted 3 times with DCM. The combined organic phases were washed with HCl 1M (1x) and with water (2x), then dried over $Na_2SO_4$, filtered and concentrated. The residue was purified with a silica chromatographic column (EtPet/EtOAc 65/35) obtaining **FMM1** as a white solid (1.066g, 2.28 mmol, Y= 46%).
$^{1}H$ NMR (500 MHz, $CDCl_3$) δ 11.38 (s, 1H), 9.77 (s, 1H), 7.47 (d, *J* = 8.6 Hz, 1H), 6.60 (dd, *J* = 8.6, 2.3 Hz, 1H), 6.54 (d, *J* = 2.3 Hz, 1H), 5.30 (m, 2H), 5.15 (m, 2H), 4.27 (dd, *J* = 12.3, 6.0 Hz, 1H), 4.18 (dd, *J* = 12.3, 2.4 Hz, 1H), 3.92 (ddd, *J* = 10.1, 6.0, 2.4 Hz, 1H), 2.10 (s, 3H), $2.06_2$ (s, 3H), 2.06 (s, 3H), 2.04 (s, 3H).
$^{13}C$ NMR (125 MHz, $CDCl_3$) δ 194.8, 170.6, 170.2, 169.4, 169.2, 164.0, 163.2, 135.4, 116.7, 109.7, 103.6, 97.7, 72.5, 72.4, 70.9, 68.1, 61.9, 20.6.

**4-(2',3',4',6'-Tetra-O-acetyl-β-D-glucopyranosyloxy)-2- hydroxybenzaldehyde-4-ethyl-3-thiosemicarbazone (FMM3)** $H_2L$[10]

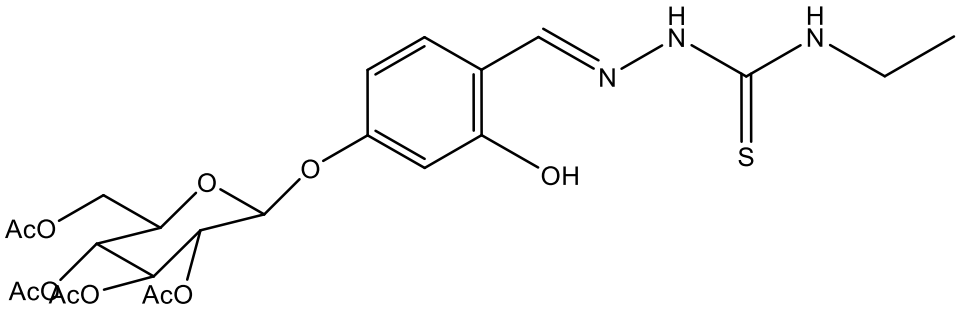


**FMM2** (0.250g, 0.534 mmol, 1 eqv) was dissolved at reflux in ethanol (4 mL), then ethylthiosemicarbazide (64mg, 0.534 mmol, 1 eqv) and few drops of $CH_3COOH$ were added. The reaction mixture was left stirring at reflux for 4 hours. After that time, the reaction was cooled to 0°C, filtered and washed with cold EtOH, obtaining **FMM3** as a white solid (0.259g, 0.455 mmol, Y= 85%).

$^1$H NMR (500 MHz, DMSO-$d_6$) δ 11.30 (s, 1H), 10.16 (b, 1H), 8.43 (t, *J* = 5.9 Hz, 1H), 8.28 (s, 1H), 7.89 (d, *J* = 8.9 Hz, 1H), 6.50 (s, 2H), 5.58 (d, *J* = 8.0 Hz, 1H), 5.46 (t, *J* = 9.6 Hz, 1H), 5.03 (m, 2H), 4.23 (m, 2H), 4.07 (d, 1H), 3.57 (m, 2H), 2.02 (s, 9H), 1.98 (s, 3H), 1.14 (t, *J* = 7.1 Hz, 3H).

$^{13}$C NMR (126 MHz, DMSO-$d_6$) δ 176.4, 170.1, 169.7, 169.4, 169.2, 158.6, 157.6, 138.8, 128.0, 115.8, 107.7, 103.9, 96.9, 71.9, 70.9, 70.7, 68.0, 61.6, 38.3, 20.6, 20.4, 20.4, 20.3, 14.7.

HRMS: $(M+Na)^+$ = 592.1567.

IR (ATR, $cm^{-1}$): $\nu_{O-H}$ =3354; $\nu_{N-H}$ =3194, 2967; $\nu_{C=O}$ =1746; $\nu_{C=N}$ =1555; $\nu_{C=S}$ =1032, 802.

E.A. calculated for $C_{24}H_{31}N_3O_{11}S$: C 50.61, H 5.49, N 7.38, S 5.63. Found: C 50.57, H 5.49, N 7.32, S 5.63.

**4-(2',3',4',6'-Tetra-hydroxy-β-D-glucopyranosyloxy)-2-hydroxybenzaldehyde-4-ethyl-3-thiosemicarbazone (FMM4)** $NaHL$[11]

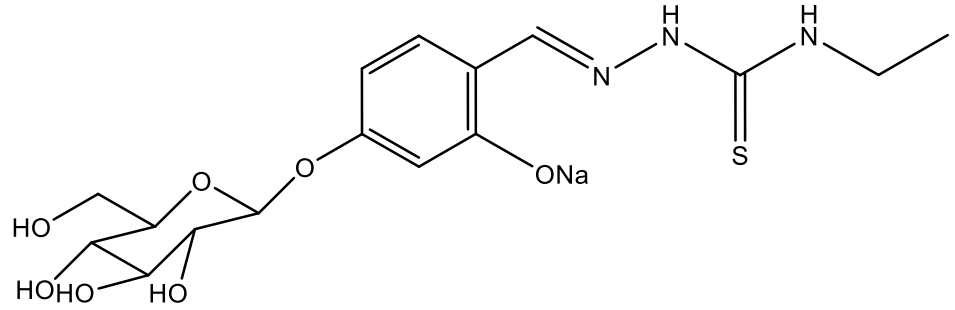


**FMM3** (130 mg, 0.23 mmol, 1 eqv) was suspended in 4 mL of MeOH, then NaOMe (26 mg, 0.48 mmol, 2.1 eqv) was added, the reaction is left stirring overnight. After that time HCl is added till pH=6, then the solvent is removed by rotovap. The crude is purified by column chromatography in DCM/MeOH/$NH_4OH_{(aq)}$ 8/2/0.02 obtaining a yellow powder (86 mg, 0.21 mmol, Y=93%).

$^1$H NMR (500 MHz, DMSO-$d_6$) δ 11.25 (b, 1H), 8.40 (t, *J* = 6.0 Hz, 1H), 8.27 (s, 1H), 7.86 (m, 1H), 6.53 (m, 2H), 5.33 (d, *J* = 5.2 Hz, 1H), 5.12 (d *J* = 4.8 Hz, 1H), 5.05 (d, *J* = 5.2 Hz, 1H), 4.83 (d, *J* = 7.6 Hz, 1H), 4.58 (t, *J* = 5.8 Hz, 1H), 3.68 (ddd, *J* = 11.8, 5.2, 2.1 Hz, 1H), 3.56 (m, 2H), 3.48 (dt, *J* = 11.7, 5.8 Hz, 1H), 3.24 (m, 4H), 1.13 (t, *J* = 7.1 Hz, 3H).

$^{13}$C NMR (126 MHz, DMSO-$d_6$) δ 176.3, 159.8, 157.5, 139.1, 127.8, 114.6, 107.8, 103.4, 100.1, 77.1, 76.6, 73.2, 69.6, 60.6, 38.2, 14.7.

HRMS: $(M+H)^+$= 402.1322.

IR (ATR, $cm^{-1}$): $\nu_{O-H}$ =3304-3271; $\nu_{N-H}$ =3163, 3003; $\nu_{C=N}$ =1552; $\nu_{C=S}$ =1035, 802.

E.A. calculated for $C_{16}H_{22}N_3NaO_7S \cdot 2.5\ H_2O$: C 41.01, H 5.81, N 8.97, S 6.84. Found: C 41.51, H 6.06, N 8.99, S 6.46.

**4-(2',3',4',6'-Tetra-O-acetyl-β-D-glucopyranosyloxy)-2- hydroxybenzaldehyde-3-thiosemicarbazone (FMM6)** $H_2L$[12]

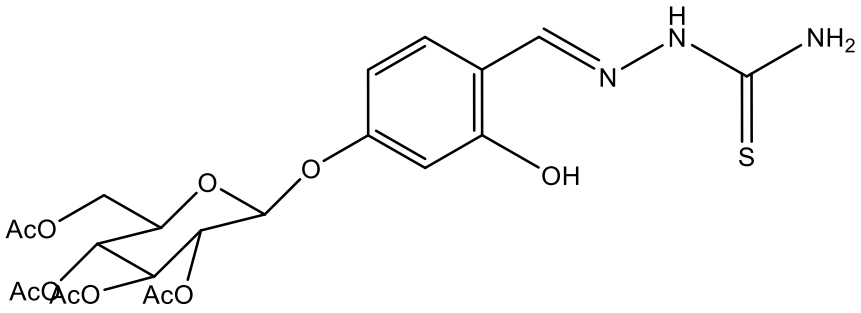


**FMM2** (0.200g, 0.427 mmol, 1 eqv) was dissolved at reflux in ethanol (3 mL), then thiosemicarbazide (0.039g, 0.427 mmol, 1 eqv) and few drops of $CH_3COOH$ were added. The reaction mixture was left stirring at reflux for 4 hours. After that time, water was added and the reaction was cooled to 0°C, filtered and washed with cold EtOH, obtaining **FMM6** as a white solid (0.199g, 0.367 mmol, Y= 86%).

$^1$H NMR (500 MHz, DMSO-$d_6$) δ 11.31 (s, 1H), 10.09 (b, 1H), 8.27 (1H), 8.07 (s, 1H), 7.88 (b, 1H), 7.86 (m, 1H), 6.47 (m, 2H), 5.57 (d, *J* = 7.9 Hz, 1H), 5.44 (t, *J* = 9.6 Hz, 1H), 5.02 (m, 2H), 4.22 (m, 2H), 4.05 (m, 1H), 2.02 (s, 6H, $CH_3$), 2.01 (s, 3H, $CH_3$), 1.97 (s, 3H, $CH_3$).

$^{13}$C NMR (126 MHz, DMSO-$d_6$) δ 177.4, 170.0, 169.6, 169.3, 169.1, 158.6, 157.6, 139.4, 128.2, 115.6, 107.7, 103.9, 96.9, 71.8, 70.8, 70.7, 68.0, 61.6, 20.5, 20.4, 20.4, 20.3.

HRMS: $(M+Na)^+$ = 564.1248.

IR (ATR, $cm^{-1}$): $\nu_{O-H}$ =3277; $\nu_{N-H}$ =3180, 2960; $\nu_{C=O}$ =1744; $\nu_{C=N}$ =1501; $\nu_{C=S}$ =1033, 808.

E.A. calculated for $C_{22}H_{27}N_3O_{11}S \cdot 0.5\ H_2O$: C 47.99, H 5.13, N 7.63, S 5.82. Found: C 47.96, H 5.03, N 7.63, S 5.82.

**4-(2',3',4',6'-Tetra-hydroxy-β-D-glucopyranosyloxy)-2- hydroxybenzaldehyde-3-thiosemicarbazone (FMM8)** NaHL[13]

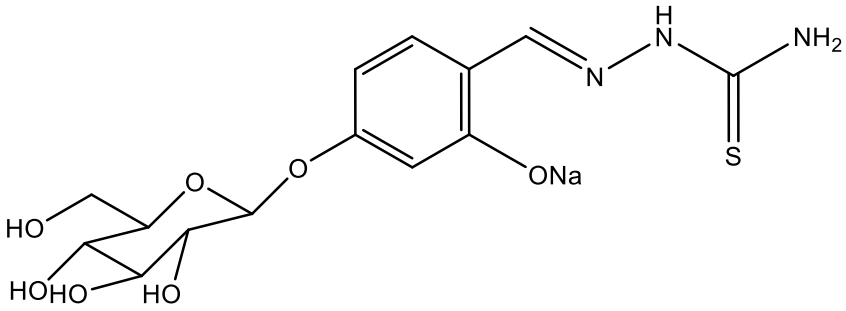


**FMM6** (270 mg, 0.50 mmol, 1 eqv) was suspended in 6 mL of MeOH, then NaOMe (57 mg, 1.05 mmol, 2.1 eqv) was added, the reaction is left stirring overnight. After that time HCl is added till pH=6, then the solvent was removed by rotovap. The crude was purified by column chromatography in DCM/MeOH/$NH_4OH_{(aq)}$ 75/25/0.05 obtaining a yellow powder (177 mg, 0.47 mmol, Y=94%).

$^1$H NMR (500 MHz, DMSO-$d_6$) δ 11.24 (b, 1H), 8.28 (s, 1H), 7.99 (b, 1H), 7.83 (b, 1H), 7.81 (b, 1H), 6.55 (d, *J* = 2.4 Hz, 1H), 6.51 (dd, *J* = 8.7, 2.4 Hz, 1H), 5.30 (d, *J* = 5.2 Hz, 1H), 5.08 (d, *J* = 4.8 Hz, 1H), 5.03 (d, *J* = 5.2 Hz, 1H), 4.84 (d, *J* = 7.6 Hz, 1H), 4.55 (t, *J* = 5.8 Hz, 1H), 3.69 (m, 1H), 3.49 (m, 1H), 3.28 (m, 2H), 3.20 (m, 2H).

$^{13}$C NMR (101 MHz, DMSO-$d_6$) δ 177.3 (Cq), 159.9 (Cq), 158.0 (Cq), 139.8 (CH), 127.8 (CH), 114.5 (Cq), 107.7 (CH), 103.5 (CH), 100.1 (CH), 77.1 (CH), 76.6 (CH), 73.2 (CH), 69.6 (CH), 60.6 ($CH_2$).

HRMS: $(M+H)^+$= 374.1016.

IR (ATR, $cm^{-1}$): $\nu_{O-H}$ =3350-3258; $\nu_{N-H}$ =3180, 2920; $\nu_{C=N}$ =1503; $\nu_{C=S}$ =1038, 808.

E.A. calculated for $C_{14}H_{18}N_3NaO_7S \cdot 2.5\ H_2O$: C 38.18, H 5.26, N 9.54, S 7.28. Found: C 37.56, H 5.13, N 10.06, S 7.04.

**Bis (4-(2',3',4',6'-Tetra-O-acetyl-β-D-glucopyranosyloxy)-2- hydroxybenzaldehyde-3) thiocarbohydrazone (FMM10)** $H_4L^{14}$

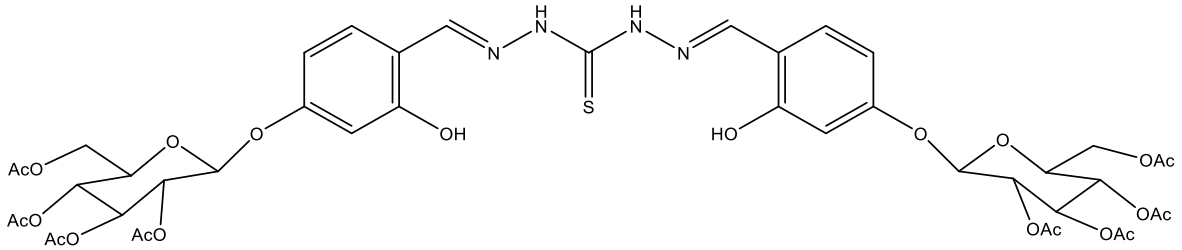

**FMM2** (0.500g, 1.067 mmol, 2 eqv) was dissolved at reflux in ethanol (4 mL), then thiocarbohydrazide (57 mg, 0.534 mmol, 1 eqv) and few drops of $CH_3COOH$ were added. The reaction mixture was left stirring at reflux for 4 hours. After that time, the reaction was cooled to r.t, filtered and washed with cold EtOH, obtaining **FMM10** as a pale yellow solid (0.469g, 0.465 mmol, Y= 87%).

$^1$H NMR (500 MHz, DMSO-$d_6$) δ 11.95 (b, 1H), 11.89 (b, 1H), 11.77 (b, 1H), 10.22 (b, 1H), 8.67 (b, 1H), 8.39 (b, 1H), 8.00 (b, 1H), 7.36 (b, 1H), 6.55 (d, *J* = 8.1 Hz, 4H), 5.62 (m, 2H), 5.44 (m, 2H), 5.03 (m, 4H), 4.24 (m, 4H), 4.07 (m, 2H), 2.03 (s, 12 H), 2.02 (s, 6H), 1.97 (s, 6H).

HRMS: $(M+H)^+$= 1007.2701.

IR (ATR, $cm^{-1}$): $\nu_{C=O}$ = 1741; $\nu_{C=N}$ =1620; $\nu_{C=S}$ =1029.

E.A. calculated for $C_{16}H_{22}N_3O_7S \cdot 2\ H_2O$: C 49.52, H 5.22, N 5.37, S 3.07. Found: C 49.50, H 4.96, N 5.25, S 3.03.

**[Cu(HL$^{11}$)Cl] (FMM7)**

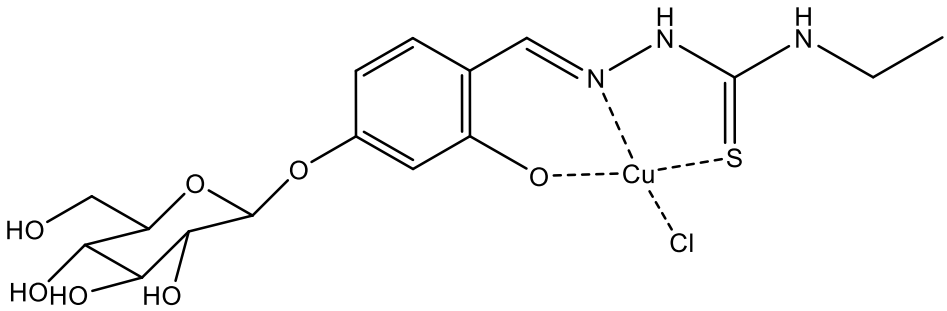

**FMM4** (88 mg, 0.22 mmol, 1 eqv) was dissolved in 2 mL of MeOH, then 2 drops of NaOH 1M were added, followed by a solution of $CuCl_2 \cdot 2H_2O$ (38 mg, 0.22 mmol, 1 eqv) in 3 mL of MeOH. The reaction was left stirring at r.t., under $N_2$ for 3 hours, then the dark green/blue solid was filtered and washed with MeOH (73 mg, 0.14 mmol, Y=61%).

IR (ATR, $cm^{-1}$): $\nu_{N-H}$ =3207, 2981; $\nu_{C=N}$ =1537; $\nu_{C=S}$ =1044.

HRMS: $(M+Na)^+$= 521.0049.

E.A. calculated for $C_{16}H_{22}ClCuN_3O_7S \cdot 2\ H_2O$: C 35.89, H 4.89, N 7.85. Found: C 35.75, H 4.89, N 7.88.

**[Cu(HL[10])Cl]** (**FMM9)**

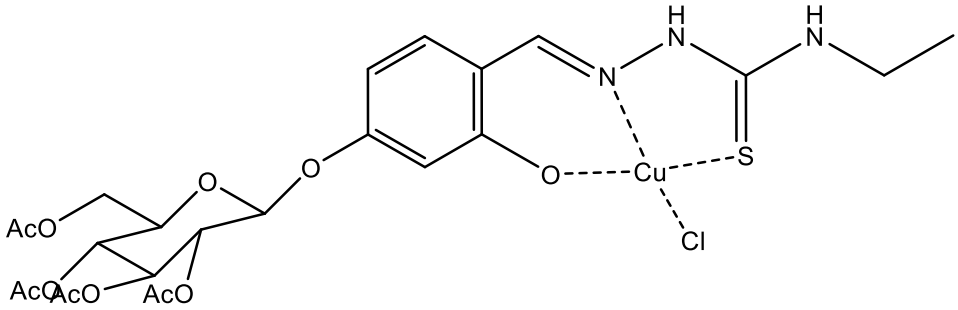


**FMM3** (67 mg, 0.12 mmol, 1 eqv) was dissolved in 2 mL of THF, then 2 drops of NaOH 1M were added, followed by a solution of $CuCl_2 \cdot 2H_2O$ (20 mg, 0.12 mmol, 1 eqv) in 2 mL of THF. The reaction was left stirring at r.t., under $N_2$ for 3 hours, then 15 mL of $Et_2O$ were added. The green solid was then recovered by filtration and washed with $Et_2O$ (53 mg, 0.08 mmol, Y=67%).
IR (ATR, $cm^{-1}$): $\nu_{N-H}$ =3228, 2980; $\nu_{C=O}$ =1752; $\nu_{C=N}$ =1530; $\nu_{C=S}$ =1045.
HRMS: $(M+Na)^+$= 689.0469.
E.A. calculated for $C_{24}H_{30}ClCuN_3O_{11}S \cdot 2\ H_2O$: C 40.97, H 4.87, N 5.97, S 4.56. Found: C 40.93, H 4.49, N 6.05, S 4.61.

**[Cu(HL[12])Cl]** (**FMM11)**

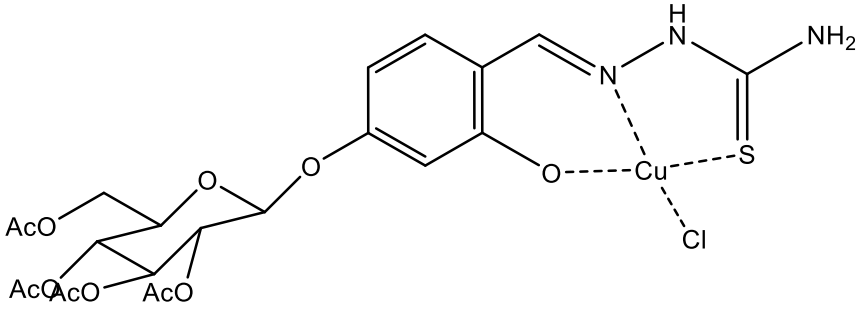


**FMM6** (100 mg, 0.18 mmol, 1 eqv) was dissolved in 2 mL of MeOH and 1 mL of THF, then 2 drops of NaOH 1M were added, followed by a solution of $CuCl_2 \cdot 2H_2O$ (31.5 mg, 0.18 mmol, 1 eqv) in 2 mL of MeOH. The reaction was left stirring at r.t., under $N_2$ for 3 hours, then 15 mL of $Et_2O$ are added. The green solid was then recovered by centrifugation and washed with $Et_2O$ (68 mg, 0.11 mmol, Y=58%).
IR (ATR, $cm^{-1}$): $\nu_{N-H}$ =3170, 2961; $\nu_{C=O}$ =1744; $\nu_{C=N}$ =1527; $\nu_{C=S}$ =1033.
HRMS: $(M+Na)^+$= 661.0163.
E.A. calculated for $C_{22}H_{26}ClCuN_3O_{11}S \cdot 2.5\ H_2O$: C 38.60, H 4.56, N 6.14, S 4.68. Found: C 38.27, H 4.14, N 6.11, S 4.71.

**[Cu(HL$^{13}$)Cl] (FMM13)**

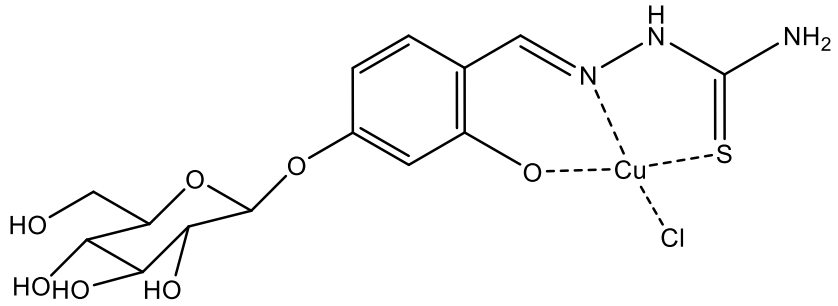

**FMM8** (115 mg, 0.31 mmol, 1 eqv) was dissolved in 2 mL of MeOH, then 3 drops of NaOH 1M were added, followed by a solution of $CuCl_2 \cdot 2H_2O$ (52.5 mg, 0.31 mmol, 1 eqv) in 3 mL of MeOH. The reaction was left stirring at r.t., under $N_2$ for 3 hours, then the dark green/blue solid was filtered and washed with MeOH (97 mg, 0.20 mmol, Y=66%).
IR (ATR, $cm^{-1}$): $\nu_{O-H}$ =3294; $\nu_{N-H}$ =3198, 3069, 2920; $\nu_{C=N}$ =1528; $\nu_{C=S}$ =1039.
HRMS: $(M+Na)^+$= 492.9736.
E.A. calculated for $C_{14}H_{18}ClCuN_3O_7S \cdot 2.5\ H_2O$: C 32.56, H 4.49, N 8.14. Found: C 32.83, H 4.40, N 7.67.

**[Cu$_2$(H$_2$L$^{14}$)Cl$_2$]** (**FMM14)**

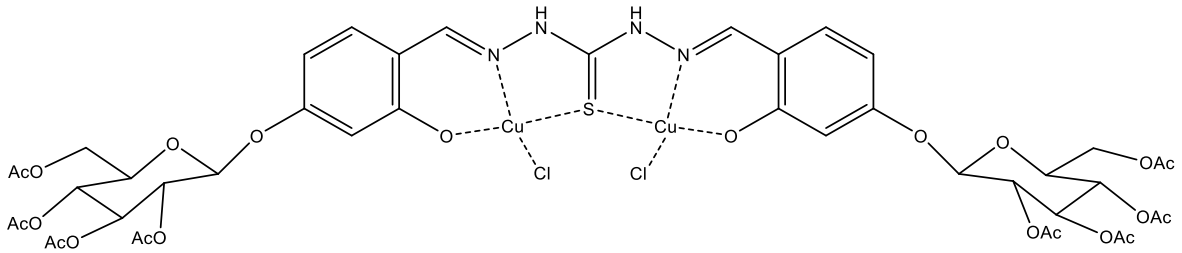

**FMM10** (122 mg, 0.12 mmol, 1 eqv) was dissolved in 4 mL of MeOH and 2 mL of THF, then 4 drops of NaOH 1M were added, followed by a solution of $CuCl_2 \cdot 2H_2O$ (41 mg, 0.24 mmol, 2 eqv) in 2 mL of MeOH. The reaction was left stirring at r.t., under $N_2$ for 3 hours, then 10 mL of $Et_2O$ were added. The green solid was then recovered by centrifugation and washed with $Et_2O$ (105 mg, Y=73%.).
IR (ATR, $cm^{-1}$): $\nu_{C=O}$=1747; $\nu_{C=N}$ =1609; $\nu_{C=S}$ =1035.
E.A. calculated for $C_{43}H_{48}Cl_2Cu_2N_4O_{22}S \cdot H_2O$: C 42.30, H 4.13, N 4.59, S 2.63. Found: C 42.06, H 4.29, N 4.60, S 2.63.

# Part 2:
# Chelating compounds as inhibitors of viral metal-dependent enzymes

# Chapter 4: **Introduction to Part 2**

## 4.1 Metal binding as a strategy in drug design

A large number of proteins requires the presence of metal ions to function properly and for this reason they are referred to as metalloprotein. Within these proteins, the role of the metal ions can be distinguished in two categories: functional or structural.

Structural metal ions are needed by certain metalloproteins to achieve their proper folding. The classic example of structural metal ion is the $Zn^{2+}$ ion in zinc finger proteins. In this class of proteins, in fact, the presence of the $Zn^{2+}$ ion allows the transformation of an unfolded polypeptide into the suitably folded domain responsible for the protein-nucleic acid or protein-protein binding.[167]

Functional metal ions can be found within the active site of enzymes and can be involved in a wide range of different processes, such as recognition and binding of substrate, electron transfer and catalysis.[168]

Altogether, different reviews in the literature suggest that a percentage between 40 and 50% of the enzymes need a metal ion to function,[169][170] hence they can be categorized as metal-dependent enzymes. Since metals play essential roles in a broad range of biological functions, metal-dependent enzymes are widely involved in many diseases' propagation. This can be caused by the dysregulation or overexpression of endogenous metal-dependent enzymes or by the action of pathogenic metal-dependent enzymes, such as viral polymerases or bacterial metallo-β-lactamases. Therefore, the study of this class of enzymes was widely explored in drug development and some of them are nowadays validated targets.

The majority of the metal-dependent inhibitor drugs approved by FDA is reported to act through the coordination of the metal ion (or ions) in the catalytic active site,[168] thus the "metal chelation strategy" has proven to be a suitable tool in the search of effective inhibitors.

It is important to specify that, in this case, "metal chelation" does not necessarily mean "metal sequestration", that is implicated, for examples, with chelating agents employed for the treatment of heavy metal poisonings. Here, compounds that can efficiently coordinate the metal cofactors in the active site may be capable of blocking enzymatic activity, preventing further interactions with the substrates.

The clinically approved metal-dependent enzymes inhibitors address a large variety of diseases, such as glaucoma, cancer, HIV/AIDS, hypertension, and fungal infections.[171]

In **Scheme 4.1** some examples of approved drugs of this class are reported.

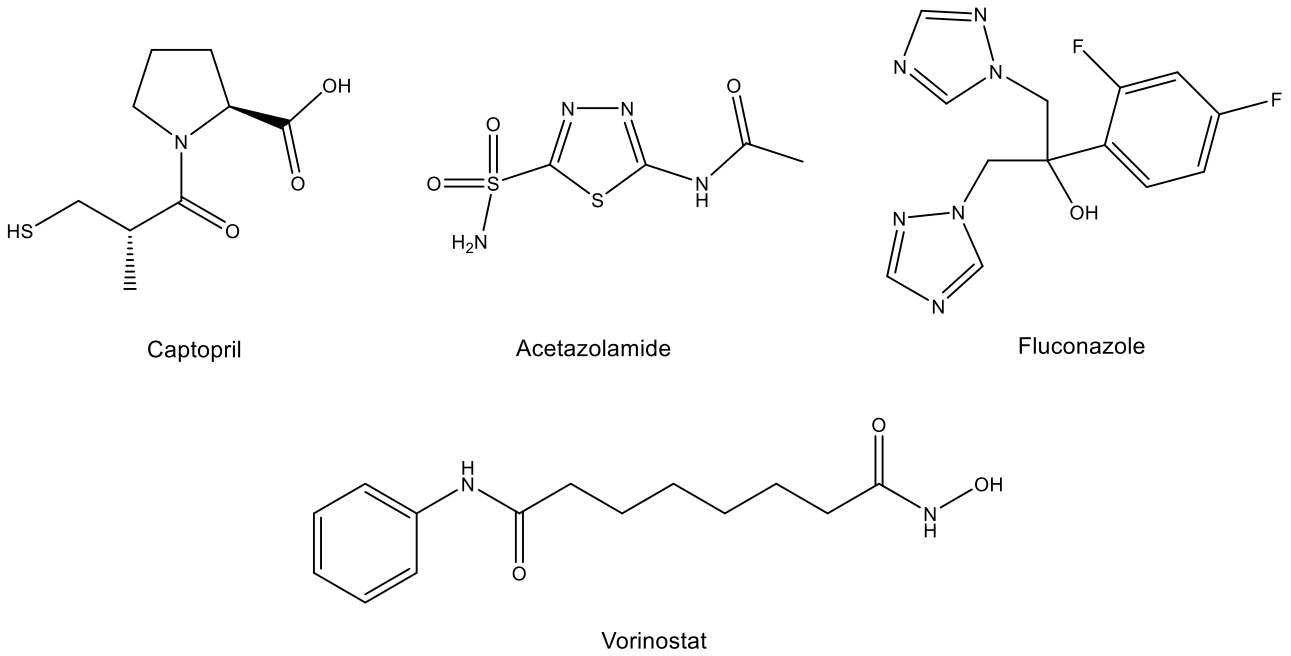


**Scheme 4.1** Structure of clinically approved inhibitors of the activity of some metal-dependent enzymes: Captopril, Acetazolamide, Fluconazole and Vorinostat.

Captopril (**Scheme 4.1**) is an angiotensin converting enzyme (ACE) inhibitor,[172] a zinc-dependent enzyme implicated in the transformation of angiotensin I into angiotensin II,[173] which is a vasoconstrictor. Notably, this compound interacts with the Zn(II) ion in the active site via direct coordination of the thiol group.[174] Its use is approved for the treatment of hypertension and some types of congestive heart failures.

Acetazolamide (**Scheme 4.1**), a potent carbonic anhydrase (CA) inhibitors, is vastly employed in the treatment of glaucoma acting reducing the intraocular pressure.[175] CA are primarily zinc-dependent enzymes that catalyse the hydration of carbon dioxide into bicarbonate and, reversely, the dehydration of bicarbonate.[176] The crystal structure obtained with human CAII and this inhibitor indicates that acetazolamide, aside from forming interaction with certain residues, binds directly to the Zn(II) in the active site.[177]

Fluconazole (**Scheme 4.1**), also known as Diflucan, is a triazole-derivative antifungal agent used in the treatment of localised or disseminated mycoses.[178] Fluconazole is a selective inhibitor of cytochrome P450 14α-sterol demethylase (CYP51),[178] that presents a heme-prosthetic group and therefore is an iron-dependent enzyme.[179] A crystal structure of CYP51 from *Mycobacterium tuberculosis* with Fluconazole showed the compound bound in the active site with a nitrogen atom of the triazole ring coordinating to the iron of heme.[180]

Moreover, suberoylanilide hydroxamic acid, known also as Vorinostat (**Scheme 4.1**), is a histone deacetylase (HDAC) inhibitor with anticancer activity, approved by the FDA for the treatment of cutaneous T-cell lymphoma.[181] HDACs are a class of enzymes that requires zinc;[182] they are involved in gene regulation and cell-cycle progression and differentiation.[183] Many evidences suggest that deregulation of these enzymes is associated with cancer.[183] Pavletich et al. reported the structure of a histone deacetylase homologue bound to Vorinostat in which the hydroxamic acid group is engaged in interactions with zinc and active site residues.[184]

Additionally, within the most representative drugs acting as metal-dependent enzymes inhibitors there are several potent antivirals, that will be discussed in the next paragraphs.

## 4.2 The metal chelation strategy in the development of antiviral agents

Targeting the metal cofactors in metal-dependent enzymes has become a successful and attractive strategy for the design of antiviral drugs.[185] One of the most significant results was the clinical approval of Raltegravir (also known as Isentress®). This drug was the first to act as a chelating inhibitor of human immunodeficiency virus type-1 integrase (HIV-1 IN).[10] In 2007 Raltegravir was included in anti-AIDS therapy in adults and in 2011 its use was expanded to children and adolescents.

The vast majority of enzymes that emerged as suitable targets for the development of efficient antivirals share the presence of magnesium ions as cofactor.[185] This metal has a key role in a large variety of enzymes, in particular those participating in the biochemistry of nucleic acids.[186]

The pervasive presence of $Mg^{2+}$ as enzyme cofactor is related to the high charge density caused by its small ionic radius, as well as to slow ligand exchange rate, good Lewis acidity and lack of redox activity. Additionally, $Mg^{2+}$ ions in the cytosol are quite abundant (≈0.5 mM), hence, to have metal coordination in physiological conditions it does not necessitate high-affinity binding sites.[187] Magnesium presents high affinity for water molecules and its 6-coordination number makes it an ideal cofactor for the interactions involving nucleic acids, enabling a series of condensations and hydrolysis reaction. In these enzymes, $Mg^{2+}$ can bind directly to residues of the protein side chain, usually with carboxylates groups (inner-sphere binding) or can engage interactions via bound water molecules (outer-sphere binding).[187]

What makes this class of Mg-dependent enzymes valuable targets is that the nucleic substrates modification plays an essential role in the viruses' lifecycle. In fact, the replication of the viral genome requires several proteins (such as nucleases, polymerases and integrases) that coordinate one or two $Mg^{2+}$ ions in the active sites[188] and that are involved in DNA cutting, pasting and binding.

While magnesium is the ion that is considered essential for the activity of these enzymes *in vivo*, $Mn^{2+}$ appears to be a proper substitute *in vitro*. It is generally accepted that magnesium is more likely the cofactor of these enzymes in cells,[185] considering that it has a cytosolic concentration one million-fold bigger than $Mn^{2+}$. Nonetheless, $Mn^{2+}$ is often the preferred metal cofactor for *in vitro* assays, since it determines an enhanced activity of the enzymes.[189] Additionally, $Mn^{2+}$ is commonly employed, instead of the lighter $Mg^{2+}$, for the purpose of growing crystals with greater diffraction quality.

The studies of Beese and Steitz on *Escherichia coli* DNA polymerase were an important advance for understanding the mechanism of enzyme-mediated hydrolysis of nucleic acids. In 1991 they proposed the so called "two metal ion mechanism",[190] that has grown into a general model to interpretate the hydrolysis of the phosphodiester backbone of nucleic acids catalysed by metals.[191] According to this model, two highly cooperative divalent metallic cations promote the cleavage of the phosphodiester bond. The two metal ions result approximatively 4 Å apart and interact in a structured $S_N2$-like mechanism with the phosphate group of the nucleic acid[192] (**Figure 4.1**).

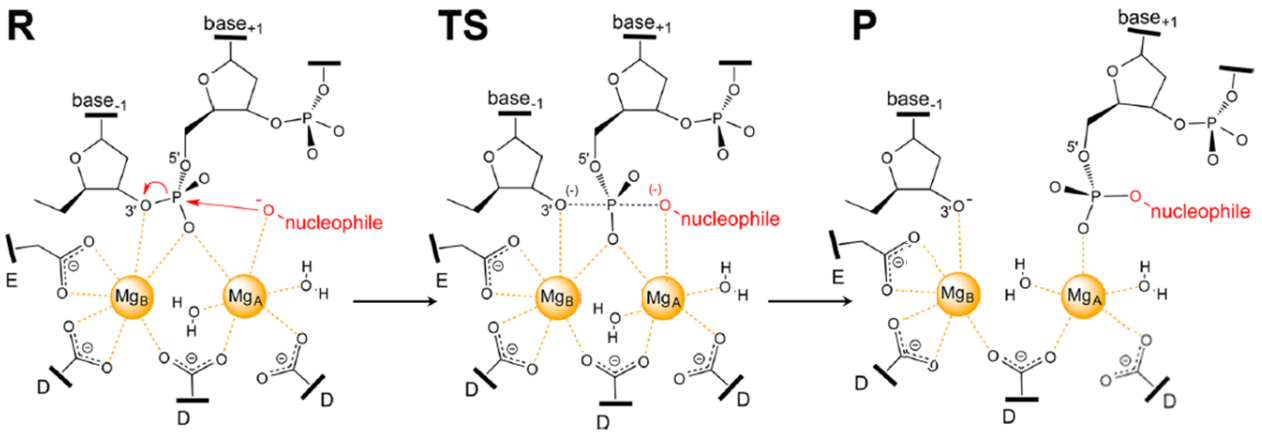


**Figure 4.1** Schematic representation of the two metal ion mechanism: the reactants (R), the transition state (TS) and the release of the products (P). Adapted from ref. [191]

This mechanism proposes that one of the metal ion (A) facilitates the attacking of the nucleophile, while the other one (B) helps the leaving of the 3' oxo-anion group.[193] Both metal ions help in the stabilization of the penta-coordinated transition state (TS).

In the next paragraphs will follow an overview regarding the chelating inhibitors of HIV integrase and influenza $PA_N$ endonuclease, two Mg-dependent enzymes that are validated targets in drug development.

### 4.2.1 Chelating inhibitors of HIV Integrase

HIV is the virus responsible for acquired immunodeficiency syndrome (AIDS), that has become a major pathology worldwide.[194] The therapy known as highly active antiretroviral therapy (HAART) was able to efficiently suppress the viral replication, but it was related with problems of drug toxicity, patients adherence to the therapy and emergence of drug resistant phenotypes.[195] For these reasons, efforts into develop new therapeutic approaches were pursued, in which the viral enzymes HIV Integrase (IN) emerged as a suitable target.[196]

The main function of HIV IN is to catalyse the insertion of the viral cDNA into the infected cells genome, process indicated as integration. The transcription of the viral genome and the viral proteins production require the cDNA of HIV to be fully integrated into a chromosome,[197] hence integration is essential for HIV replication. Integration is carried out by IN through two distinct reactions: 3'-processing and strand transfer.[197][198][199] First, the 3' terminal ends of the cDNA are selectively trimmed by IN in the cytosol, generating two CA-3'-hydroxyl ends, that are the reactive substrates in the following strand transfer step. The complex formed by IN bound to the CA-3'-hydroxyl is then reallocated into the nucleus of the infected cell. Once in the nucleus, the terminal CA-3'-hydroxyl groups attack the host cell DNA within the strand transfer step and the integration process is completed.

HIV IN is part of the family of polynucleotidyl transferases,[200] and its structure comprises three functional domains: the N-terminal domain, that contains a zinc(II) binding motif, the catalytic core domain, and the C-terminal domain, that binds DNA.[197] In the active site, within the catalytic core domain, there are three amino acids (two aspartates D64, D116 and one glutamate E152), that constitute the "D,D(35)E" motif, highly conserved in this family of enzymes.[199] Any substitution or removal of these residues results in significantly reduced catalytic activity.[201] The three amino acids of the catalytic triad are responsible for the coordination of the divalent metal ions. In fact, in the crystal structure of the full-length IN of prototype foamy virus (PFV) associated with viral DNA substrate, two metal ions were identified in the enzyme active site.[202]

The first class of compounds found to inhibit IN with promising results was the aryl diketo-acids (DKAs),[203] compounds that bears a diketo moiety and a carboxylic acid functionality, that can also be replaced by bioisosteres. In particular, compound S-1360 (**Scheme 4.2**), a DKA bioisoster disclosed by Shionogi, has been the first inhibitor of HIV IN to enter clinical trials evaluation.[204] However, its development was not further pursuit due to pharmacokinetic problems and lack of efficacy *in vivo*.

After DKAs, other chelating pharmacophores (**Scheme 4.2**) have been investigated and revealed inhibition of IN activity, such as salicyl hydrazide[205], the 4,5-dihydroxy-1H-isoindole-1,3(2H)-diene scaffold[206] and polyhydroxylated aromatics derivatives, such as quercetin[207] and (+)-D-chicoric acid[208].

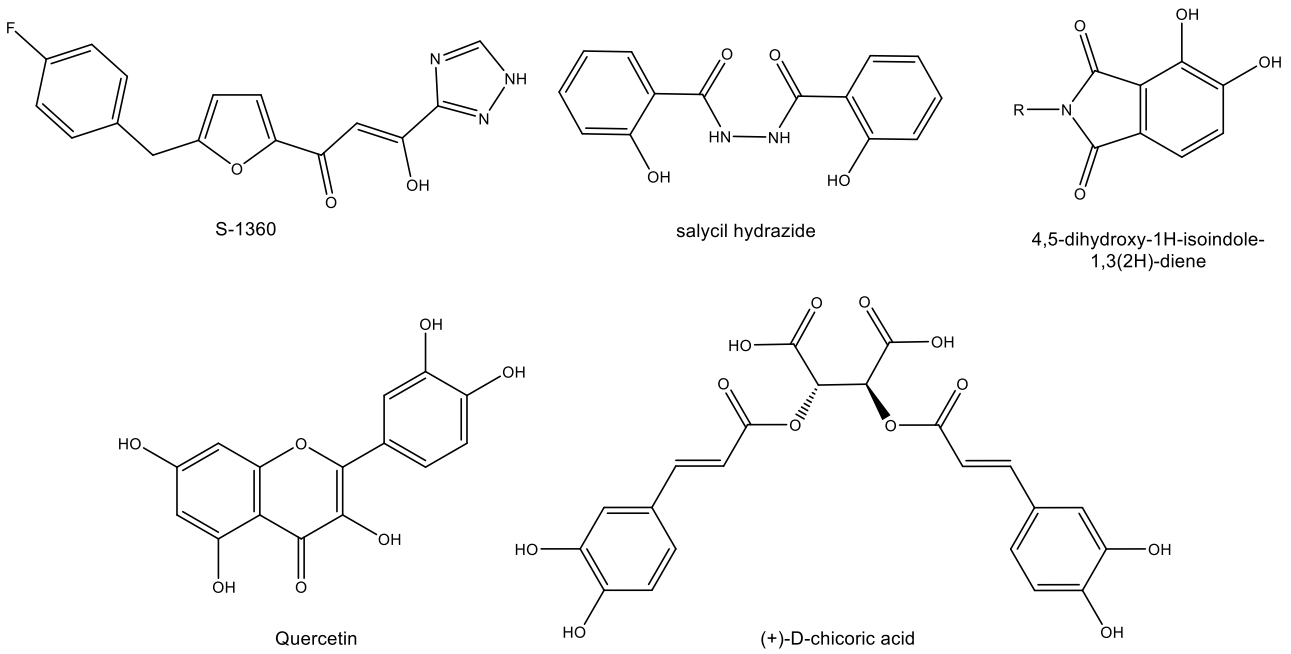


**Scheme 4.2** Chemical structures of some representative metal-chelating inhibitors of HIV IN: S-1360, salycil hydrazide, 4,5-dihydroxy-1H-isoindole-1,3(2H)-diene derivatives, quercetin, and (+)-D-chicoric acid.

As mentioned before, Raltegravir, developed by Merck and authorized in 2007, was the first clinically approved HIV IN inhibitor [10] and represents a milestone in the "metal chelation strategy".

Analysis of the structure of Raltegravir bound to full-length IN (**Figure 4.2**, A) of PFV (often employed as a HIV IN surrogate), shows that the drug has its chelating oxygen atoms pointing towards the metal cofactors, whereas the hydrophobic group fit into a tight pocket, created by the viral-RNA substrate displacement.[202] This finding underlines the importance of both the chelating moiety and the hydrophobic part of the molecule. Following the success and clinical relevance of this compound, much effort was put into optimizing the scaffold interaction with this enzyme.

Elvitegravir[209] (**Figure 4.2**, B), another clinically approved HIV IN inhibitor, displays a comparable binding mode[202] and a similar resistance profile to Raltegravir.

Dolutegravir, in the second generation of IN inhibitors, has a different resistance profile compared to the parent drugs.[210] The structure of Dolutegravir comprises a rigid and preorganized chelating moiety, that chelates the metal ions in the active site, and a benzyl-amide portion that is engaged with the nearby amino acids[211] (**Figure 4.2**, C).

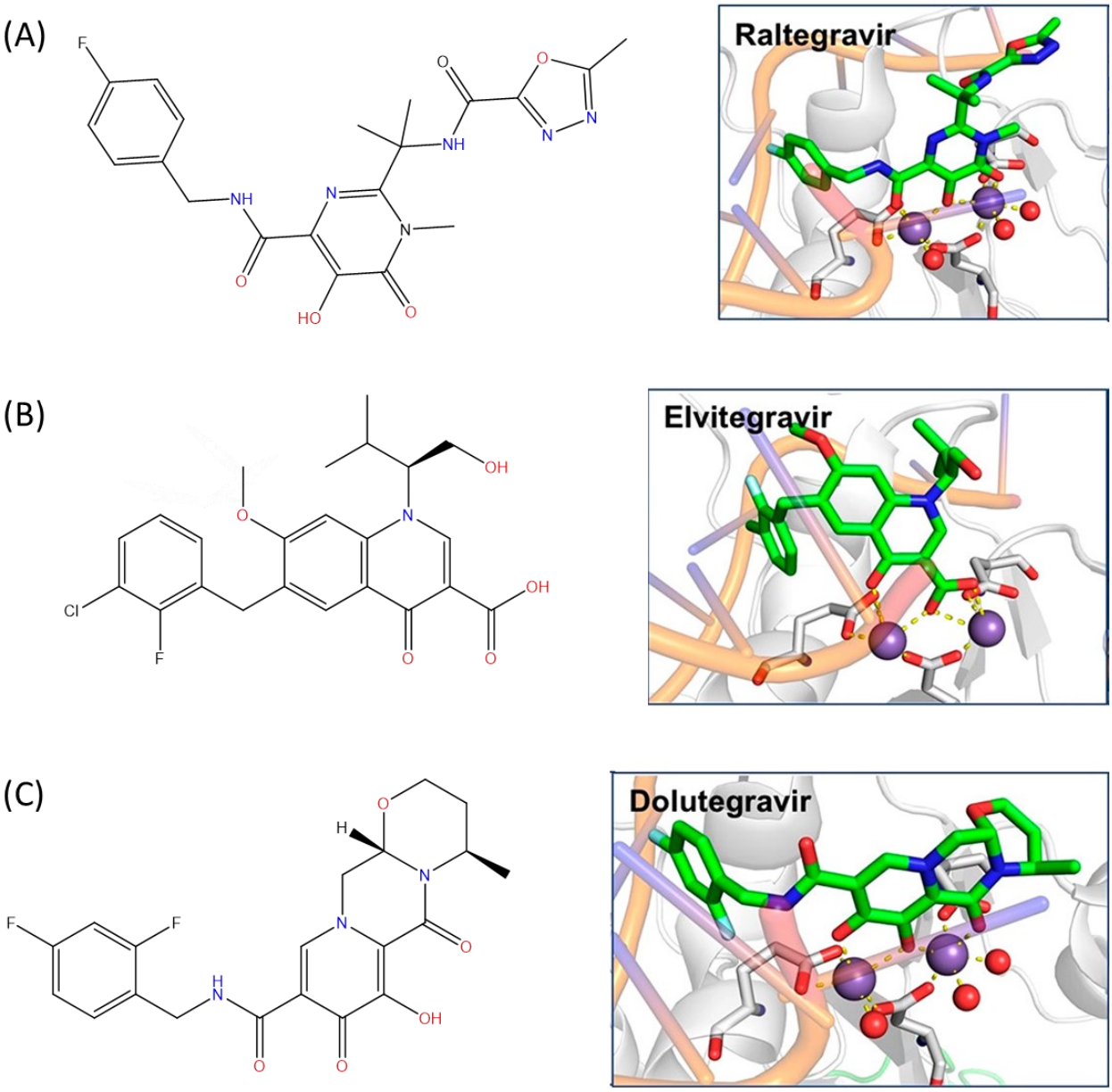


**Figure 4.2** Chemical structures of the clinically approved HIV IN inhibitors Raltegravir (A), Elvitegravir (B) and Dolutegravir (C), and their structures bound to PFV full-length IN: PDB 3OYA (A), PDB 3S3N (B) and PDB 3L2U (C). $Mn^{2+}$ ions are depicted as purple spheres, compounds (green) and active site residues (beige) as sticks. Bound nucleic acids are shown as tubes. Adapted from ref.[168]

Within the third generation HIV IN inhibitors, two other compounds with a scaffold similar to Dolutegravir, Cabotegravir[212] and Bictegravir[213] (Scheme), are approved in the treatment of HIV/AIDS.

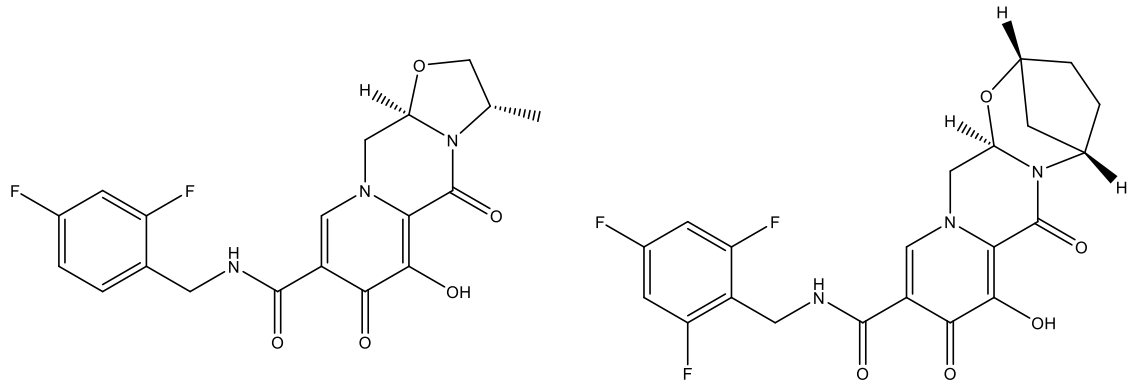

Cabotegravir

Bictegravir

**Scheme 4.3** Chemical structures of clinically approved HIV IN third generation inhibitors Cabotegravir and Bictegravir.

### 4.2.2 Chelating inhibitors of Influenza $PA_N$ endonuclease

Human influenza viruses are respiratory pathogens responsible for seasonal epidemics. This illness can cause serious complications, especially in children, elderly and other high-risk patients. Moreover, influenza A viruses are occasionally responsible for the outbreak of pandemics, such as the Spanish flu in 1918,[214] the avian H5N1[215] and the swine H1N1.[216]

Vaccinations is the primary strategy to fight the influenza epidemics, although antiviral agents have a fundamental role in the therapeutic treatment. In fact, vaccines may not be always administrable or available, and they must be readministered annually. Furthermore, the rapid mutation of these viruses contributes to the rise of strains resistant to the currently available antiviral drugs.[217] For these reasons, the development of new drugs for the treatment of influenza is still relevant.

Influenza viruses are segmented negative-sense single-stranded RNA viruses that belong to the *Orthomyxoviridae* family.[218] Their genome comprises eight segments and within the virion each segment is coated with multiple nucleoproteins and associated with a viral RNA-dependent RNA polymerase (RdRP). Influenza RdRP is an heterotrimeric complex, composed by three different subunits, PA, PB1 and PB2, and its function is fundamental to viral genome replication and translation.[219] Influenza RdRP cannot produce the mRNA caps that are necessary for translation in the eukaryotic host cells; hence, to create mRNA capped primers it uses a mechanism known as "cap-snatching".[220] First, the PB2 subunit bind to host cell capped mRNA, that are then cleaved 8-15 nucleotides downstream by the endonuclease domain in the PA subunit. The cleaved capped fragment is used by PB1 to initiate the polymerization, using the viral mRNA as a template. Finally, the chimeric capped mRNA is transported into the cytoplasm and used for the translation of the viral proteins.

The metal-dependent endonuclease domain of influenza was identified in the N terminal part of the PA subunit ($PA_N$) in 2009.[221][222] These structural studies revealed that the $PA_N$ endonuclease comprises an active site that binds two divalent metal cofactors ($Mg^{2+}$ or $Mn^{2+}$) with conserved catalytic residues, that correspond to a PD(E/D)XK motif. Altogether, evidence support that the $PA_N$ endonuclease works through a "two metal ion" mechanism.[223]

$PA_N$ endonuclease emerged as an attractive target for the development of new anti-influenza drugs since its activity is crucial for the viral replication and lifecycle, and is highly conserved among the different influenza strains.[224] Being a metal-dependent enzyme, the metal chelation strategy represents a useful tool in the development of $PA_N$ endonuclease inhibitors.

DKAs are between the first chelating moieties investigated as influenza $PA_N$ inhibitors, as it was for HIV IN. Merck identified a series of 2,4-diketobutenoic acids via high throughput screening. The structure activity relationship of the tested molecules revealed that the DKA moiety is required for the activity and that the presence of a lipophilic portion enhance the potency of the compounds, such as for one of the most active $PA_N$ inhibitor L-742,001 (**Figure 4.3**, A). This compound inhibits the endonuclease activity with $IC_{50}$= 0.33 µM, and its activity is metal dependent.[225][226] The crystal structure of L-742,001 bound to $PA_N$ endonuclease (**Figure 4.3**, A) shows that both metal ions in the active site are coordinated by the DKA moiety and that the additional aryl and alkyl moieties engage favourable interactions with the active site residues.[227] However, due to a suboptimal pharmacological profile these inhibitors were not further clinically developed.

Numerous other classes of chelating compounds were investigated, such as naturally occurring polyphenols. Among these, epigallocatechin gallate (EGCG) (**Figure 4.3**, B) activity on influenza endonuclease was extensively characterized. EGCG inhibits $PA_N$ endonuclease activity in the micromolar range.[228][229] The galloyl moiety was proved to be involved in the coordination of the two metal cofactors

in the active site, as confirmed by the X-ray structure of $PA_N$ endonuclease in complex with EGCG (**Figure 4.3**, B).[230]

A new class of chelating ligands, the 3-hydroxypyridin-2(1H)-ones, were identified through a X-ray fragment screening using a crystal form of $PA_N$ from pandemic 2009 H1N1 influenza A.[231] Via optimization of the scaffold, the better inhibition of endonuclease was obtained by compound P16 (**Figure 4.3**, C), displaying a $IC_{50}$ of 11 nM in the enzymatic assay.[232] The crystal structure of this compound within the 2009 H1N1 $PA_N$ (**Figure 4.3**, C) shows the oxygens of the scaffold coordinating the two metal ions. Furthermore, the pyridinone nitrogen atom establishes electrostatic interactions with a tyrosine residue of the active site, while the tetrazole ring forms hydrophobic interactions with several amino acid side chains that are responsible for a favourable orientation of the chelating moiety.[232]

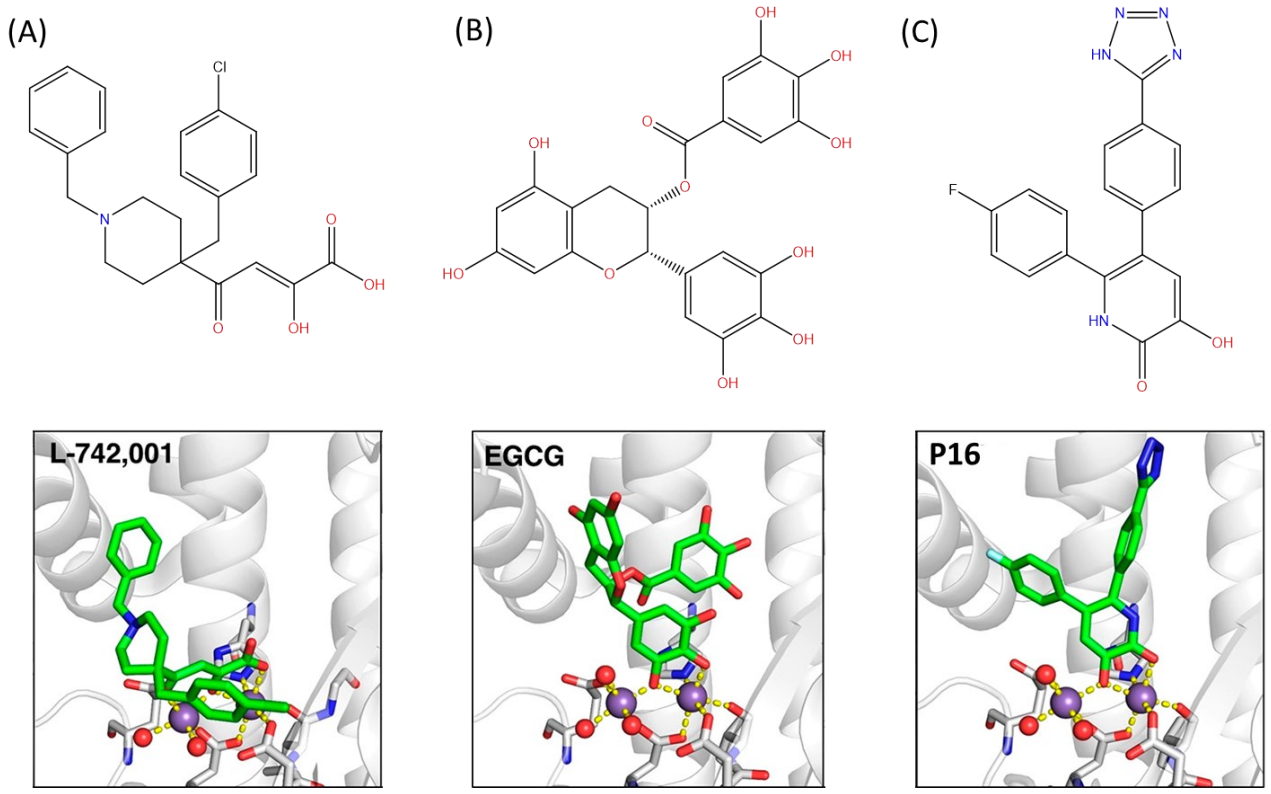


**Figure 4.3** Chemical structures of metal chelating inhibitors of influenza $PA_N$ endonuclease: L-742,001 (A), EGCG (B) and P16 (C) and their structures bound to 2009 H1N1 $PA_N$ endonuclease: PDB 5CGV (A), PDB 4AWM (B), and PDB 4M5U (C). $Mn^{2+}$ ions are depicted as purple spheres, compounds (green) and active site residues (beige) as sticks. Bound nucleic acids are shown as tubes. Adapted from ref.[168]

Another class of efficient inhibitors of endonuclease activity is represented by catechol and galloyl N-acylhydrazones.[233] Investigations on this scaffold led to the identification of N'-(3,4,5-trihydroxyphenyl)-3,4,5-trihydroxybenzoylhydrazide (**Figure 4.4**, A) as the most active compound, displaying an $IC_{50}$ of 8.7 µM in the endonuclease enzymatic assay and inhibition of the virus replication in MDCK cells with $EC_{90}$=3.5 µM.[234] The crystal structure obtained with $PA_N$ endonuclease (**Figure 4.4**, B) indicates that the galloyl moiety chelates the two catalytic manganese ions, whereas the trihydroxyphenyl group is stacking with the Tyr24 residue side chain. Furthermore, two of these hydroxyls are positioned in order to form hydrogen bonds with the surrounding amino acids (Glu26 and Lys34).[234]

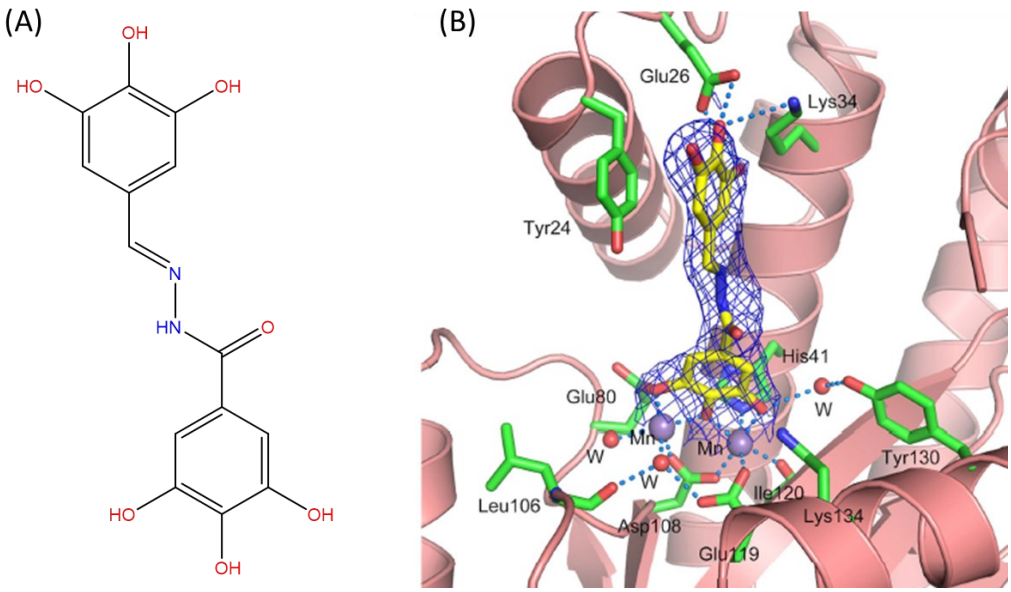


**Figure 4.4** (A) Chemical structure of chelating $PA_N$ endonuclease inhibitor N'-(3,4,5-trihydroxyphenyl)-3,4,5 trihydroxybenzoylhydrazide. (B) Crystal structure of the inhibitor bound to the endonuclease active site of $PA_N^{\Delta Loop}$ (PDB 5EGA). Interacting residues are shown as green sticks, $Mn^{2+}$ ions are indicated as purple spheres, water molecules as red spheres. Protein secondary structure is shown as ribbons. Inhibitor is shown in yellow sticks. Adapted from ref.[234]

The most successful chelating inhibitor of influenza $PA_N$ endonuclease is represented by Baloxavir Marboxil (BXM or Xofluza®) developed by Roche and Shionogi, a drug approved in 2018 for the treatment of uncomplicated flu in adults and children from 12 years of age.[235] BXM (**Figure 4.5**, A) is the prodrug of Baloxavir Acid (BXA), (**Figure 4.5**, B) a potent chelating inhibitor of influenza $PA_N$ endonuclease. BXA exhibits a broad-spectrum inhibition of endonuclease activity on influenza A and B (with $IC_{50}$ in enzymatic assays between 1.4–3.1 nM and 4.5–8.9 nM respectively) and an excellent activity in the cellular assays ($EC_{50}$ between 0.20-1.9 nM for influenza A strains and 3.3-13 nM for B strains).[236] The crystal structure of BXA bound to Influenza B/Memphis/13/03 $PA_N$ (**Figure 4.5**, C) was reported by Omoto et al.[237] BXA has a butterfly like form, comprising a chelating domain within the oxazino-pyridotriazin-dione scaffold and a lipophilic domain within the difluoro-dihydro-dibenzothiepine group. The chelating domain coordinates to the two $Mn^{2+}$ cations in the active site with the three donor oxygen atoms, as expected. The lipophilic group, on the other hand, engages van der Waals interactions with several amino acid side chains within the active site pockets, hence it is also referred to as 'specifity domain'.

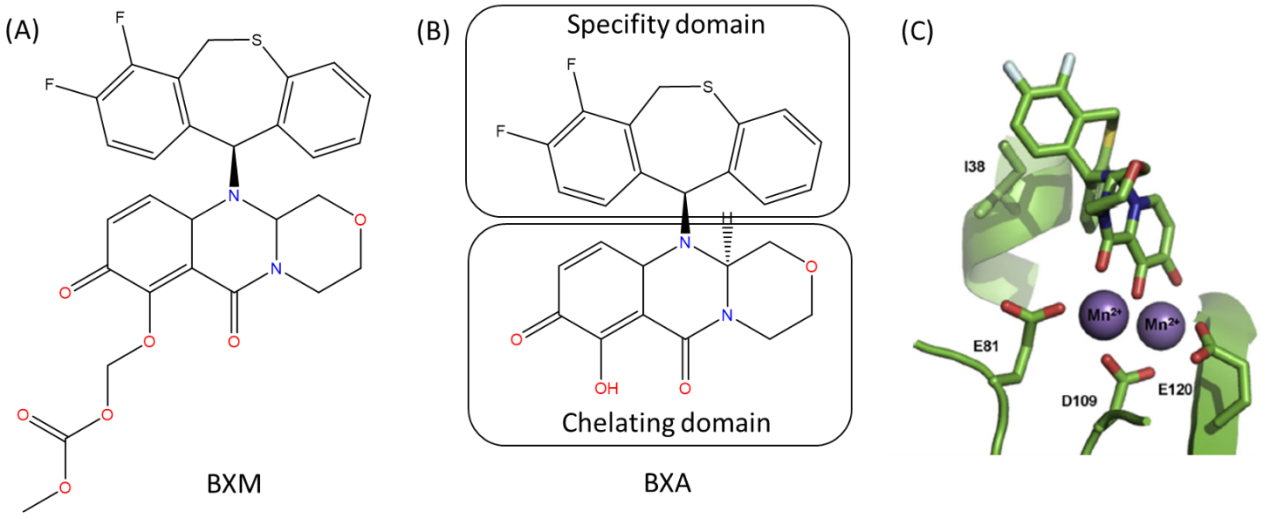


**Figure 4.5** Chemical structures of (A) Baloxavir Marboxil (BXM) and (B) Baloxavir Acid (BXA). (C) Crystal structure of BXA bound to the endonuclease active site of Influenza B/Memphis/13/03 (PDB 6FS8). Selected residues and BXA are depicted as sticks, the Mn(II) ions as purple spheres. Adapted from ref.[238]

## 4.3. Chelating antiviral agents targeting *Bunyavirales* Endonucleases

### 4.3.1 The *Bunyavirales* order

A group of related segmented negative-strand RNA viruses (sNSVs) were first classified by the International Committee on Taxonomy of Viruses together as the family *Bunyaviridae* in 1975.[239] In 2017 *Bunyavirales* were reclassified as an order[240] to include an increased number of related viruses and, according to the last update in 2019, this order comprises 12 families containing 46 genera.[241] Altogether, these viruses infect a wide range of different plants and animals.

Five of these families *(Hantaviridae, Arenaviridae, Naironviridae, Phenuiviridae* and *Peribunyaviridae*) (**Figure 4.6**) contain human pathogens, that can induce from mild to severe diseases, including fevers, encephalitis, respiratory and haemorrhagic diseases.[242] *Bunyavirales* related infections are primarily zoonotic, the viruses are transmitted from animals to humans. The main vectors are arthropods (such as ticks, mosquitoes and flies), transmitting the virus through bites.[243] Viruses belonging to *Hantaviridae* and *Arenaviridae* families are generally transmitted by rodents.[243] Transmissions between humans are rare, being commonly considered dead-end hosts. However, a few cases of human-human infections were described, as in the case of nosocomial transmission of Crimean-Cong haemorrhagic fever virus CCHFV.[244]

Bunyaviral pathogens constitute a serious threat to the public health, as testimonies the presence of some of these in the WHO list of “priority diseases for research and development in emergency contexts”. In fact, together with other diseases such as COVID-19 and Ebola, in the last update of the list are included Crimean-Cong haemorrhagic fever, Lassa fever and Rift Valley fever,[245] caused by viruses in the *Bunyavirales* order.

To date, there is no clinical approved antiviral therapy for diseases caused by bunyaviruses and the restricted therapeutic options are limited to the use of the broad-spectrum antiviral agent ribavirin.[246] However, the clinical benefits of this drug against *Bunyavirales* remain uncertain, since in some studies it was not associated with significant improvements in patients.[247] Clinical data suggest that this drug can be effective uniquely if administered during the first period of infection.[248] For all these reasons, the development of new and efficient antiviral drugs is of vital importance.

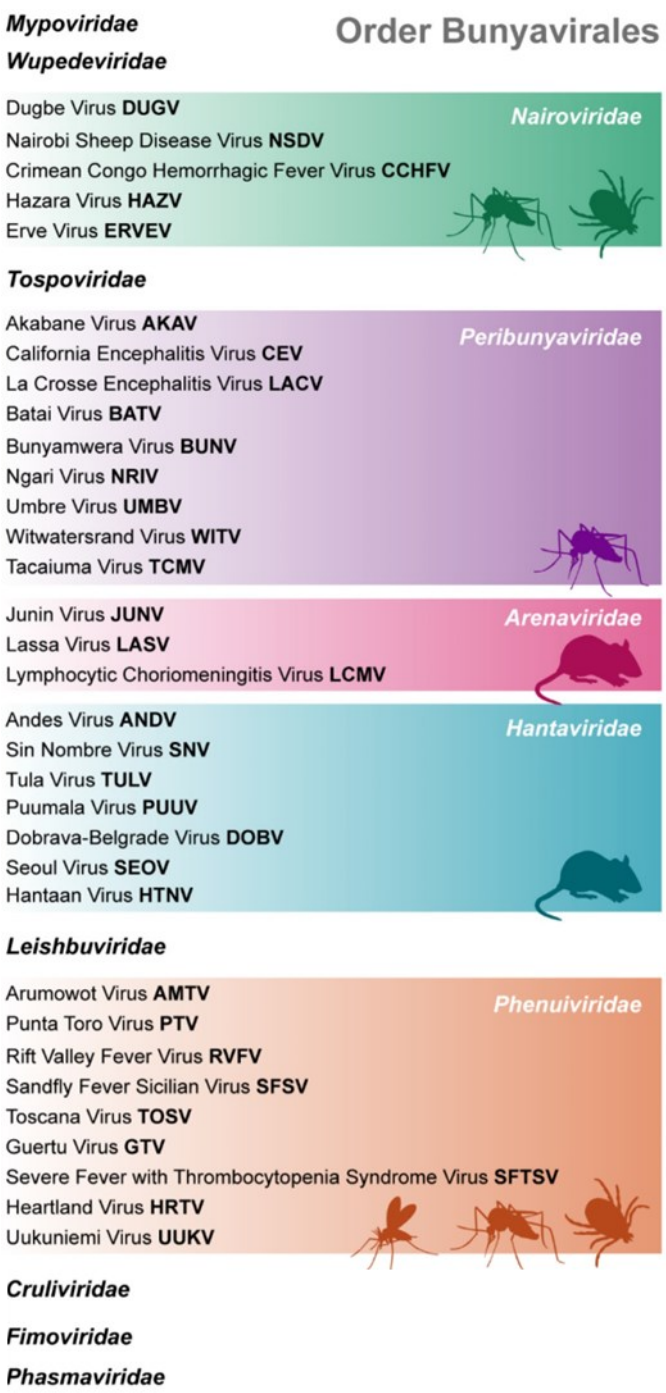


**Figure 4.6** Families within the *Bunyavirales* order. Some examples of relevant viruses are listed for the five families containing human pathogens. Indicative vectors are illustrated for the families: Nairoviridae (mosquito, tick), Peribunyaviridae (mosquito), Phenuiviridae (sandfly, mosquito, tick) and Arenaviridae, Hantaviridae (rodent). Adapted from ref.[242]

Bunyaviruses generally share a similar structure along the order, forming spherical particles of enveloped virions.[249] The virions (**Figure 4.7**) are composed by the encapsulated genome coated by a lipidic bilayer membrane, decorated with viral glycoproteins heterodimers. In most cases, bunyaviruses genome is divided in three segments, known as small (S), medium (M) and large (L). The single-stranded negative-sense RNA segments are incapsulated by nucleocapsid protein together with the viral RdRP, forming ribonucleoproteins on each segment.[249]

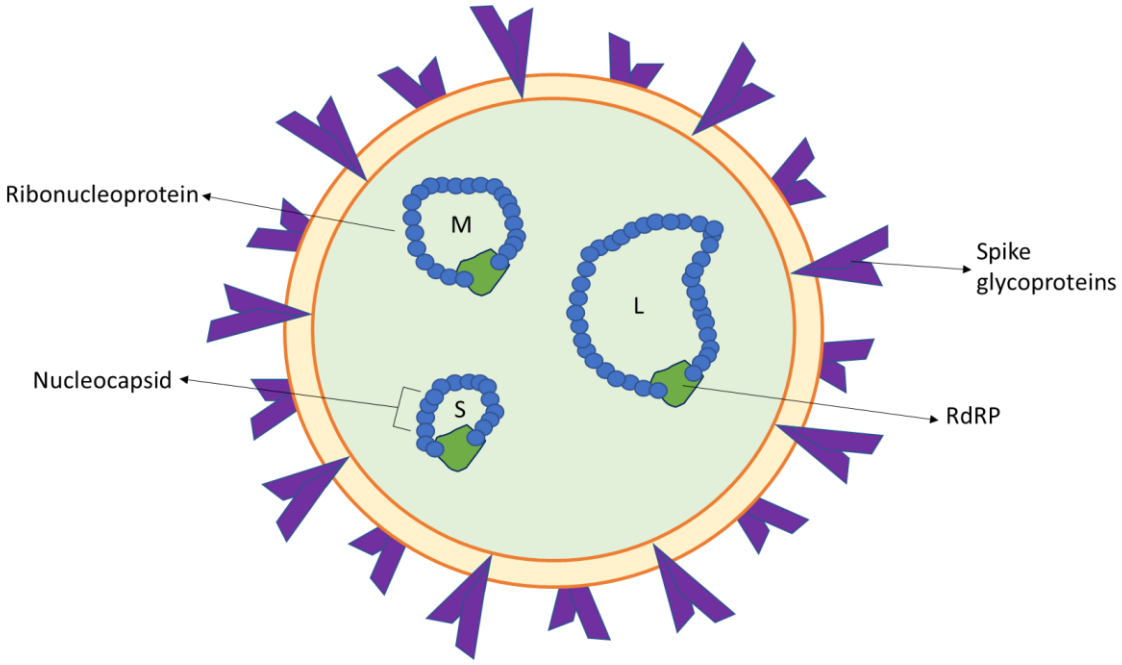


**Figure 4.7** Schematic representation of a bunyavirus virion. The virions are enveloped in a spherical shape, presenting glycoprotein spikes on the exterior membrane. The genome is composed by the three RNA segments (S, M and L) encapsulated with nucleocapsid and RdRP, forming ribonucleoproteins in a circular conformation.

In all bunyaviruses the S segment encodes for the nucleocapsid protein, whose main function is to form the ribonucleoproteins. Additionally, in some of these viruses it also encodes for non-structural proteins, that modulates the antiviral response of the host cell.[249] The M segment, on the other hand, encodes a polyprotein precursor that, after cleavage, forms the glycoproteins composing the spike heterodimer. This heterodimer is responsible for many essential functions in virus assembling, formation of virions and attachment to target cells.[249]

In all members of the order, the L segment is responsible for the encoding of a single protein, i.e. the RdRP (also called L protein).[250] The RdRP is crucial for the viral RNA transcription and replication and its structure is highly conserved in the *Bunyavirales* order.[251] Similarly to influenza, this enzyme possess a N-terminal domain with endonuclease activity,[250] that will be described in the next paragraph.

### 4.3.2 Bunyaviruses endonuclease: an attractive target for the development of antiviral agents

Bunyaviral L protein is a single chain polypeptide of molecular weigh between 250-450 kDa.[252] This protein functions as a RdRP, that catalyses transcription and replication of the viral RNA in the cytoplasm of the infected cells.[253] Similarly to other single-subunit polymerases, they display a right hand structure, with three subdomains (finger, palm and thumb).[251]

An endonuclease domain has been identified in the N-terminal region of a large number of bunyaviruses L proteins, all of which share a common kidney-shaped structure consisting of two lobes, displaying remarkable similarities with the influenza endonuclease[252] (**Figure 4.8**).

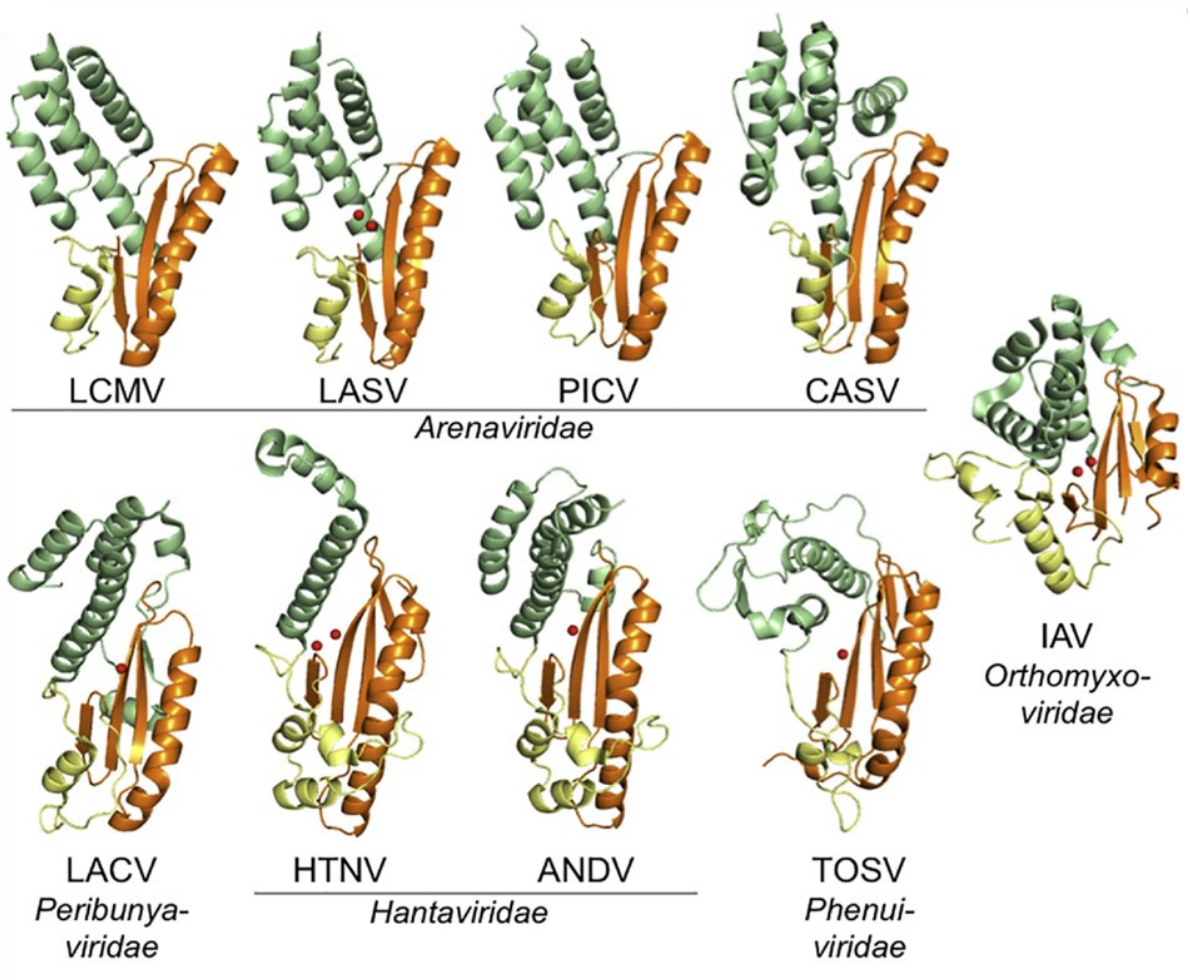


**Figure 4.8** Structures of some *Bunyavirales* endonucleases: LCMV, lymphocytic choriomeningitis virus (PDB 3JSB); LASV, Lassa virus (PDB 5J1P); PICV, Pichinde virus (PDB 4I1T); CASV, California Academy of Sciences virus, (PDB 5MV0); LACV, La Crosse virus (PDB 2XI5); HTNV, Hantaan virus (PDB 5IZE); ANDV, Andes virus, (PDB 5HSB); TOSV, Toscana virus (PDB 6QVV); IAV, influenza A virus, (PDB 2W69). Comparable structural components are displayed in the same colours. Divalent metal ions are shown as red spheres. Adapted from ref.[252]

One of the endonuclease lobes contains primarily α-helices, whereas the other lobe is composed by a β-sheet and an extended α-helix that comprises most of the residues of the active site. All these endonucleases present in their active site a PD(E/D)K motif, that is able to coordinate divalent metal ions that are indispensable for the enzyme activity.[254]

The bunyaviruses endonucleases have been divided in two different classes, His+ or His-, depending on the presence or absence of a histidine residue nearby the catalytic motif that helps coordination of one of the metal ion cofactors.[255] Generally, in *in vitro* assays His+ endonucleases have a higher catalytic activity in presence of $Mn^{2+}$ than $Mg^{2+}$[255], whereas His- endonucleases display either no or very weak activity.[254] However, His- endonucleases result active in *in vivo* test.

Bunyaviruses endonucleases share with influenza $PA_N$ not only structural but also functional similarities: these enzymes, in fact, are involved in a cap-snatching mechanism,[256][250] as it was first disclosed for influenza.[220] Cap-snatching (**Figure 4.9**) represents the first step of the RNA transcription for these viruses.

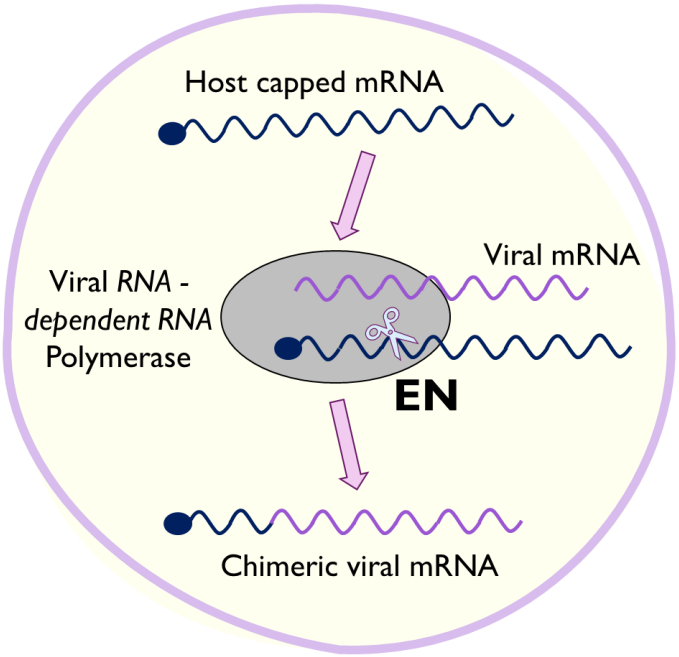


**Figure 4.9** Schematic representation of the cap-snatching mechanism in bunyaviruses. The host cell capped mRNA is cleaved by the endonuclease domain (EN) of the viral RdRP, to create a capped primer used in the synthesis of capped chimeric viral mRNA.

This class of viruses does not possess capping activity; hence it uses host cell capped mRNA to create a primer for the viral transcription. The viral RdRP is able to recognise and bind host cells mRNAs and the endonuclease domain cleaves them into short capped primers.[251] The endonuclease-mediated cleavage of this step, as for influenza $PA_N$, works through a "two metal ion"-like mechanism,[221] as described previously in paragraph 2. The formed capped primers are used for the synthesis of a chimeric viral mRNA, which will be transported to ribosomes for the translation process. Differently from influenza, the replication cycle of bunyaviruses takes place in the cytoplasm and not in the nucleus.[252]

Bunyaviruses endonuclease represent an interesting target[257] since its inhibition could directly block the viral replication in one of the initial steps. Furthermore, its active site is highly conserved among the *Bunyavirales* order, therefore a compound targeting endonuclease can potentially have a broad spectrum of activity. Finally, the bunyaviral endonuclease differs from the human endoribonucleases, so it is less likely to have crossed inhibition.

### 4.3.3 Metal chelating inhibitors of Bunyaviruses endonucleases

As mentioned before, the strategy of coordinating the metal ions in the active site of metal-dependent enzymes have proven successful in the search of effective inhibitors. Since influenza virus $PA_N$ endonuclease and bunyaviral endonuclease domains share numerous structural and functional features,[252] inhibitors of $PA_N$ can possibly be effective on the latter. For these reasons, the investigation on metal chelating inhibitors of bunyaviruses endonucleases started testing already known and effective inhibitors of influenza $PA_N$, such as DKA compounds.

In 2010, Reguera et al. published the structure of the N-ter domain of LACV L-protein with a 2,4-dioxo-4-phenylbutanoic acid (DPBA) molecule (**Figure 4.10**, A) bound in the active site coordinating the two catalytic $Mn^{2+}$ ions (**Figure 4.10**, B).[250] Additionally, they reported that a weak inhibition of endonuclease activity was observed with DPBA ($IC_{50}$ ≈ 25-50 μM). In a parallel thermal stability assay it was observed a shift of about 5°C in the thermal stability of the enzyme prebound with $Mn^{2+}$ ions in presence of DPBA. This result indicates that DPBA is likely to bind the metal ions in the active site, as it was noted in the crystal structure.[250]

An analogue investigation with DPBA was performed by Reguera et al. on TOSV endonuclease.[258] Thermal shift assays of TOSV endonuclease indicated a 10°C increase in thermal stability with DPBA. The TOSV endonuclease activity resulted completely inhibited by high concentration of this compound, dependent by the presence of $Mn^{2+}$ ions. Furthermore, the binding with the active site metal ions was observed in a crystal structure obtained in presence of $Mn^{2+}$ ions and DPBA (**Figure 4.10**, C).

Another DPBA-containing structure was reported by Saez-Ayala et al. for the LCMV endonuclease.[259] In this structure, similarly to the previous, DPBA coordinates the $Mn^{2+}$ ions in the active site (**Figure 4.10**, D). Enzymatic assays with LCMV endonuclease revealed a weak inhibition of the enzyme activity (≈250 μM).

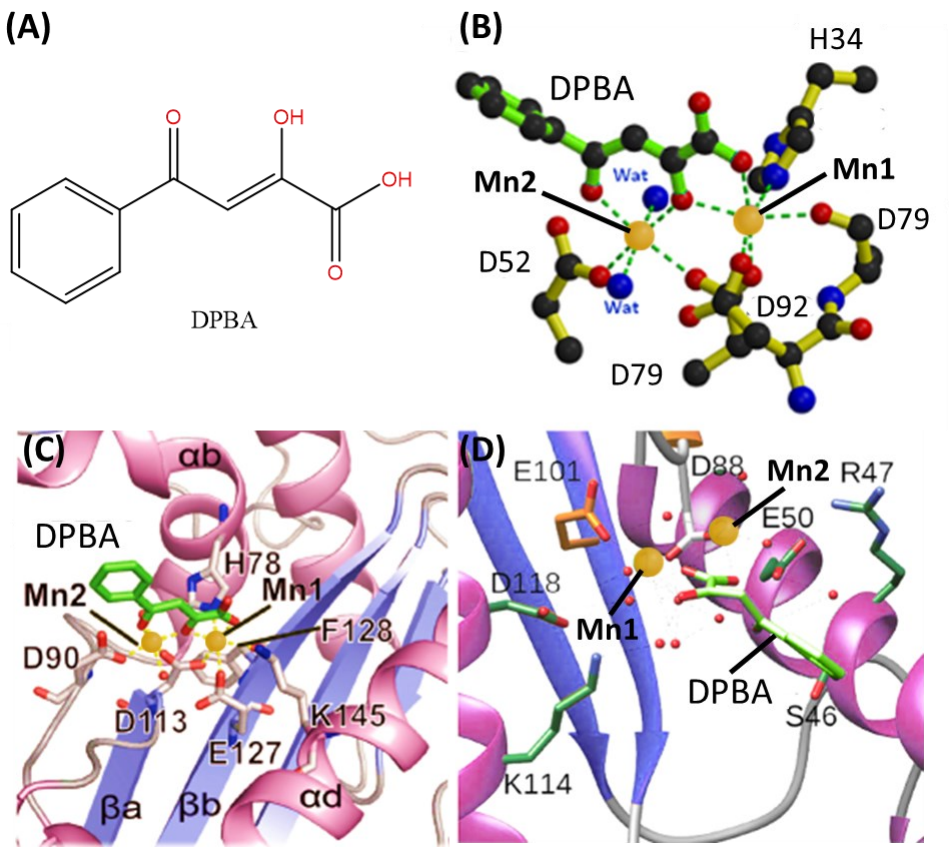


**Figure 4.10** (A) Chemical structure of DPBA. (B) Structure of LACV polymerase N-terminal domain with DPBA interacting with the catalytic $Mn^{2+}$ ions in the active site. Adapted from ref.[250] (B) Structure of TOSV polymerase N-terminal domain with DPBA interacting with the catalytic $Mn^{2+}$ ions in the active site. Adapted from ref.[258] (C) Structure of polymerase LCMV N-terminal domain with DPBA interacting with the catalytic $Mn^{2+}$ ions in the active site. EN Adapted from ref.[259]
$Mn^{2+}$ ions are indicated as golden spheres. DPBA is depicted in bright green. Active site residues coordinating $Mn^{2+}$ ions are represented as sticks.

In all these structures, DPBA interacts uniquely with the catalytic divalent metal ions and no interactions with the active site residues was observed. The absence of interactions between the amino acids and the compound causes residual flexibility and a suboptimal inhibition, hence it was suggested that improving the ligand occupancy, adding a larger aromatic moiety, could lead to an enhanced inhibition activity.[259]

To test this hypothesis, two new DKA derivatives, respectively with a biphenyl and phenanthryl moiety, were synthesized. Both the DKA derivatives displayed a higher affinity (tenfold to hundred-fold) compared to DPBA, suggesting that the structural modifications provide additional interactions and induce a gain in inhibition potency.[259]

In 2019 Saez-Ayala et al.[257] expanded the screening on LCMV endonuclease evaluating a library containing 59 compounds bearing different chelating moieties. Some DKAs and N-hydroxyisoquinoline-1,3-diones (HID) were identified as good binders and, in general, high binding affinity was correlated with *in vitro* inhibition of LCMV endonuclease activity (40-50% inhibition at 50 μM). Overall, for the DKA scaffold features as aromaticity, flexibility, and the possibility to make hydrogen bonds seem to be associated to further ligand stabilization.

Fernandez-García et al.[260] further investigated the activity of a panel of DKAs within three different bunyaviruses endonucleases (LACV, ANDV and RVFV). Several derivatives inhibited all the tested

endonucleases with $IC_{50}$ values between 2-20 µM, confirming that these enzymes are valid targets for the development of broad-spectrum antiviral drugs and that DKAs is an interesting class of inhibitors.

More recently, Baloxavir Marboxil (BXM), a prodrug of the chelating inhibitor BXA,[238] was approved as an anti-influenza drug. Given its great activity of $PA_N$, the activity of this pharmacophore was also tested against some bunyaviruses. In 2019, Ye et al. reported the activity of BXA on HNTV infected cells.[261] The study described that BXA inhibits virus replication on Vero E6 cells with $IC_{50}$ of 27.2 µM, a concentration that did not affect the cell viability, suggesting BXA has a potential as lead compound for the search of bunyaviral EN inhibitors. The potential of BXM was also confirmed in 2020 by Wang et al., that reported a remarkable inhibition activity in a FRET-based enzymatic assay against SFTSV and HRTV L proteins, with $IC_{50}$ values of 135 and 116 nM, respectively.[262]

The success of the metal-chelation concept for the development of bunyaviral inhibitors is corroborated by the deposition of a patent by Tavis et al.,[263] that involves the use of different chelating moieties (**Scheme 4.4**) as inhibitors of *Bunyavirales*.

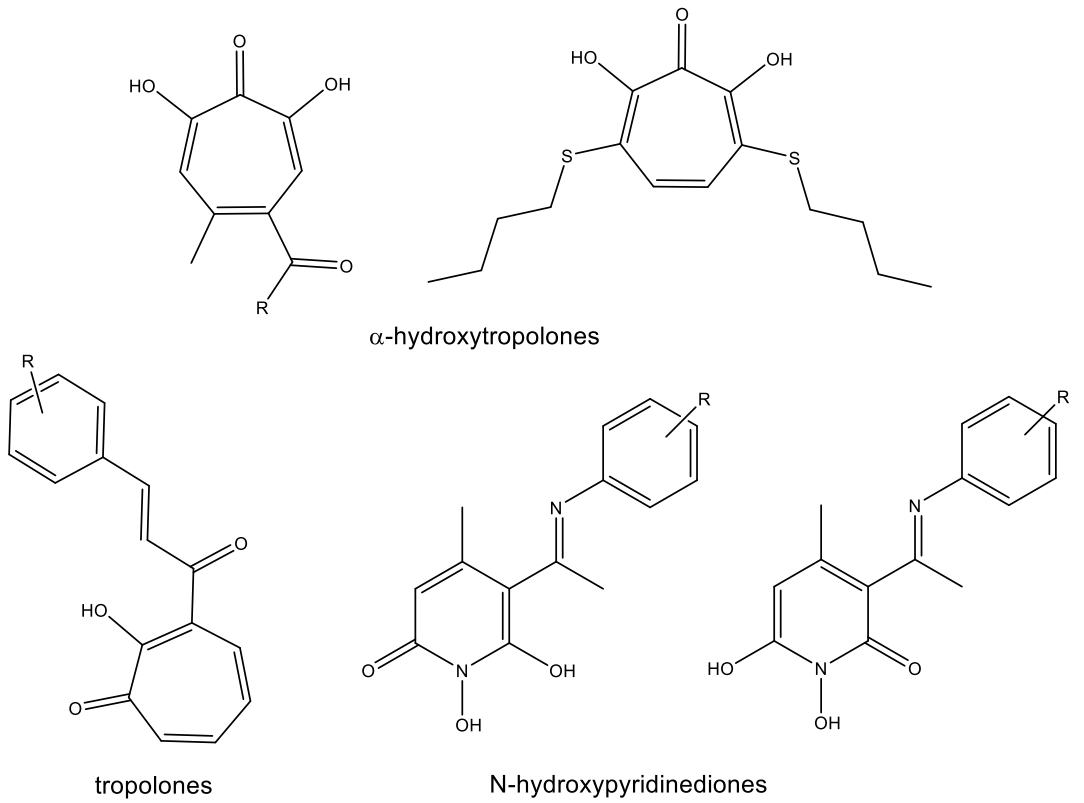


**Scheme 4.4** Examples of compounds bearing the chelating moieties (α-hydroxytropolones, tropolones and N-hydroxypyridinediones) covered by the patent application of Tavis et al.[263]

In this patent, the inventors investigated a large panel of chelating compounds for the inhibition of RVFV replication in cells. Complementary studies also include evaluation of cell viability and activity on the human counterpart ribonuclease H1. Mechanistic studies were not conducted, but the authors suggest that the most likely target of these molecules is the cap-snatching endonuclease domain of the RFVF L protein, considering the similarity of these moieties to known endonucleases inhibitors. In particular, their findings indicate that α-hydroxytropolones and N-hydroxypyridinediones are promising candidates for optimization into antiviral drugs targeting RVFV and other bunyaviruses.

# Chapter 5: **Synthesis and characterization of furopyrimidin-7-one derivatives as inhibitors of bunyaviral cap-snatching endonucleases**

## 5.1 Aim of the project

As already mentioned, bunyaviral endonucleases are a class of a metal-dependent enzymes that is emerging as an interesting target in the development of antiviral agents. The general strategy of chelating the metal cofactors in the active site of viral enzymes has proved to be useful to find effective inhibitors also against viruses within the *Bunyavirales* order. Many examples of compounds containing polyhydroxylated aromatic moieties have been investigated and displayed inhibition of viral metal-dependent enzymes activity. To cite a few, catechol containing compounds quercetin[207] and D-chicoric acid[208] (**Scheme 5.1**) are capable of inhibiting HIV IN activity, whereas catechol or galloyl N-acylhydrazones[233][234] (**Scheme 5.1**) represent an interesting class of influenza $PA_N$ endonuclease inhibitors.

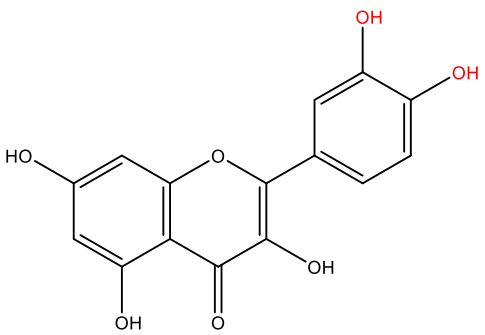


Quercetin

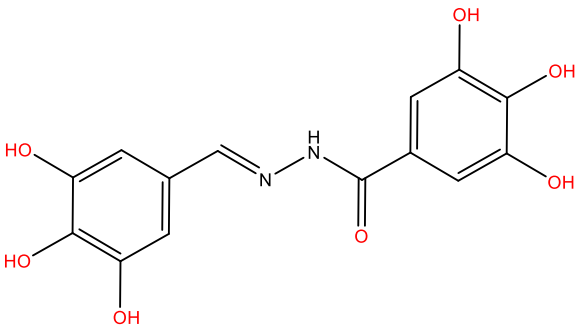


N'-(3,4,5-trihydroxyphenyl)-3,4,5 trihydroxybenzoylhydrazide

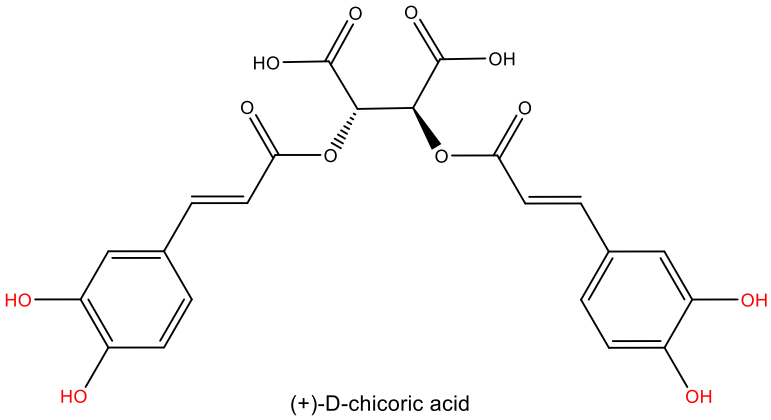


(+)-D-chicoric acid

**Scheme 5.1** Structure of quercetin, N'-(3,4,5-trihydroxyphenyl)-3,4,5 trihydroxybenzoylhydrazide and (+)-D-chicoric acid. Catechol and galloyl oxygen atoms depicted in red.

Structure-activity relationship studies on viral endonucleases suggest that, aside from the chelating moiety, the presence of a lipophilic domain can potentially enhance the inhibitor activity by interacting with hydrophobic surrounding pockets of the enzyme.

A series of purines bearing the 3-hydroxyaniline moiety showed interesting activity against Dengue virus (DENV).[264] Given the promising profile of compound MR-186 (**Scheme 5.2**), other modifications on this scaffold were explored. A series of molecules comprising the 5H-pyrrolopyrimidin-7(6H)-one scaffold

(**Scheme 5.2**) also exhibited inhibition of DENV replication.[265] One of these molecules' target is likely to be an hydrophobic pocket within the viral protein NS5, that acts as RdRP and methyltransferase.[266]

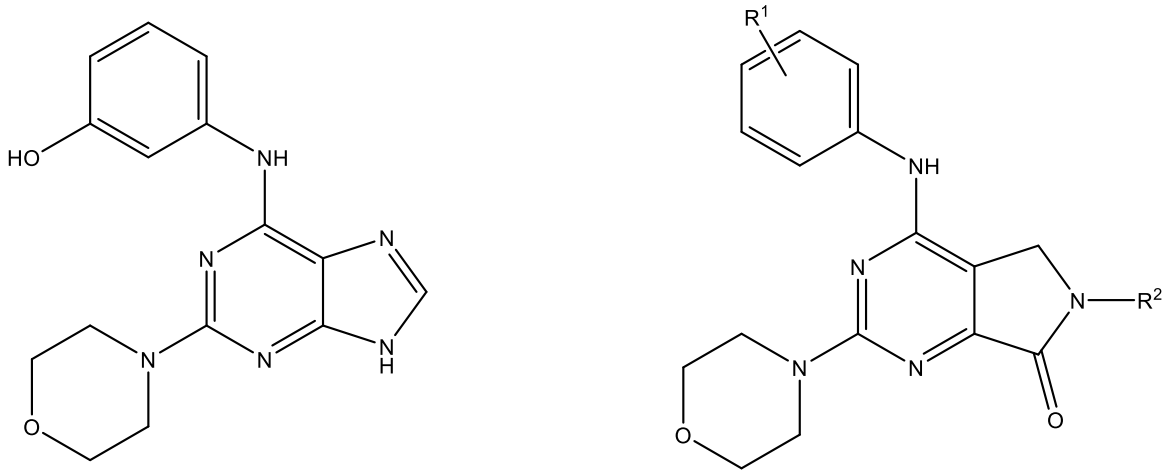


**Scheme 5.2.** Chemical structure of DENV inhibitors MR-186 (left) and 5H-pyrrolopyrimidin-7(6H)-one derivatives (right).[2]

Starting from these data present in the scientific literature, a series of new chelating molecules (**Scheme 5.3**) were designed, consisting of a hydrophobic scaffold linked to a polyhydroxylated chelating moiety; their evaluation as potential inhibitors of bunyaviral endonucleases was then carried on.

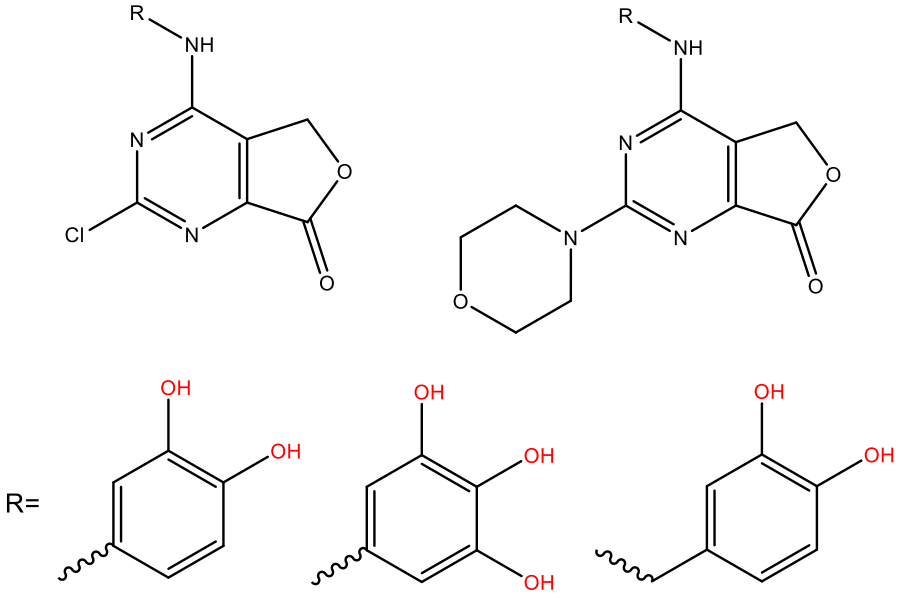


**Scheme 5.3** Structure of the target molecules.

## 5.2 Results and discussions

### 5.2.1 Synthesis and characterization

The first synthetic attempt to obtain furo[3,4-d]pyrimidin-7-one derivative chelating compounds (**Scheme 5.4**) was made following the procedure described by Radi et al.,[265] with slight modifications.

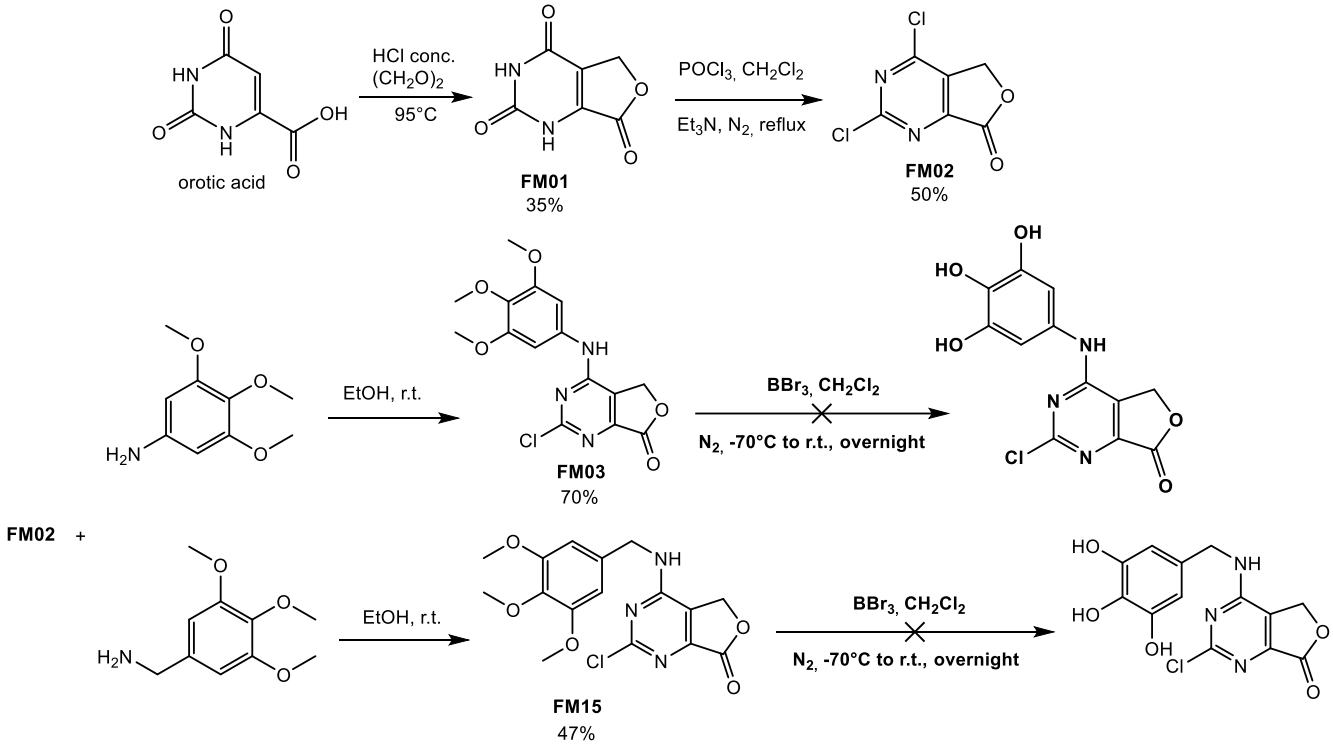


**Scheme 5.4** Synthetic pathway for the chelating furo[3,4-d]pyrimidin-7-one derivatives.

Orotic acid was reacted with paraformaldehyde in concentrated hydrochloric acid and stirred at 95°C overnight. After that time, the solvent was evaporated and water added. The mixture was then stirred at 60°C for one hour and a white solid filtered and washed with water, obtaining **FM01** with a 45% yield.

The cyclization reaction is confirmed by the $^{1}$H-NMR spectra comparison between **FM01** and orotic acid (**Figure 5.1**).

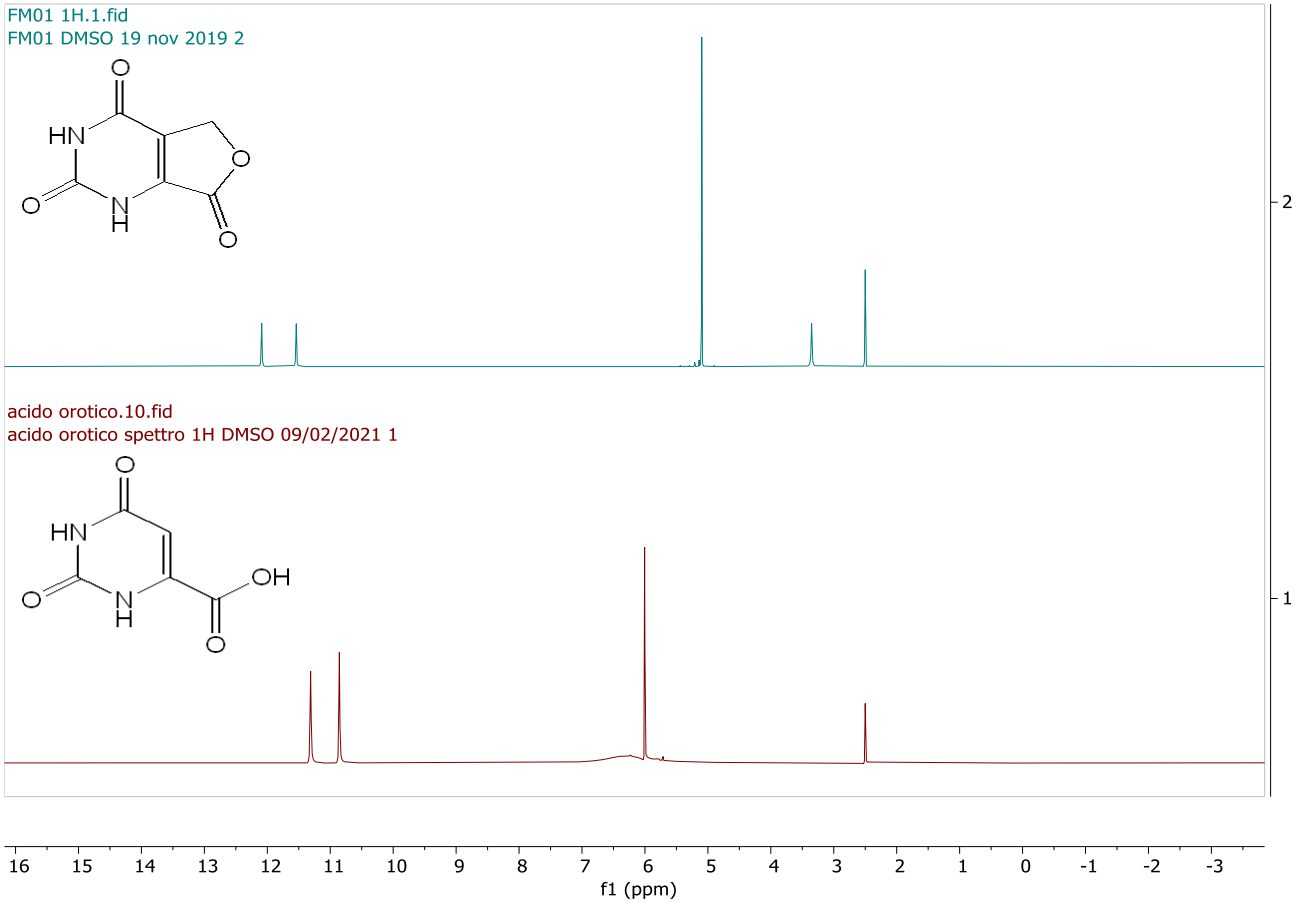


**Figure 5.1** $^{1}$H NMR spectra (25°C, 400 MHz, DMSO-$d_6$) of **FM01** (top) and orotic acid (bottom).

In the **FM01** spectrum it can be observed the absence of any aromatic proton signals, while orotic acid has its aromatic proton around 6 ppm. Furthermore, a new signal integrating for two protons is present at 5.10 ppm, correspondent to the $CH_2$ of the cycle.

After isolation and characterization, **FM01** was suspended in a mixture of dry $CH_2Cl_2$ and $POCl_3$, the suspension was cooled to 0°C and $Et_3N$ added dropwise. The reaction was stirred overnight at 90°C, and after that time, the solvents were removed by vacuum. Iced water was then added to the flask and the crude stirred for 1 hour, followed by an extraction with $CH_2Cl_2$. The dried organic phase was purified with a chromatographic column (EtOAc/Hex 5/1) and finally recrystallized in $CH_2Cl_2$/Hex, obtaining **FM02** as a brown solid (55% yield). **FM02** experimental spectra are in agreement with what reported in the literature for this compound.[267]

**FM02** was employed for the synthesis of the compound **FM03** and **FM15** (**Scheme 5.4**). Briefly, a substitution reaction between **FM02** and two different amines bearing an aromatic moiety was performed. The reactions were conducted in EtOH at r.t. for 4 hours, with 1.25 equivalents of the appropriate amine, and the products **FM03** and **FM15** were obtained by filtration, without further purification. As reported in the literature for this scaffold, substitution with primary amines occurs at C4 position in mild conditions.[268]

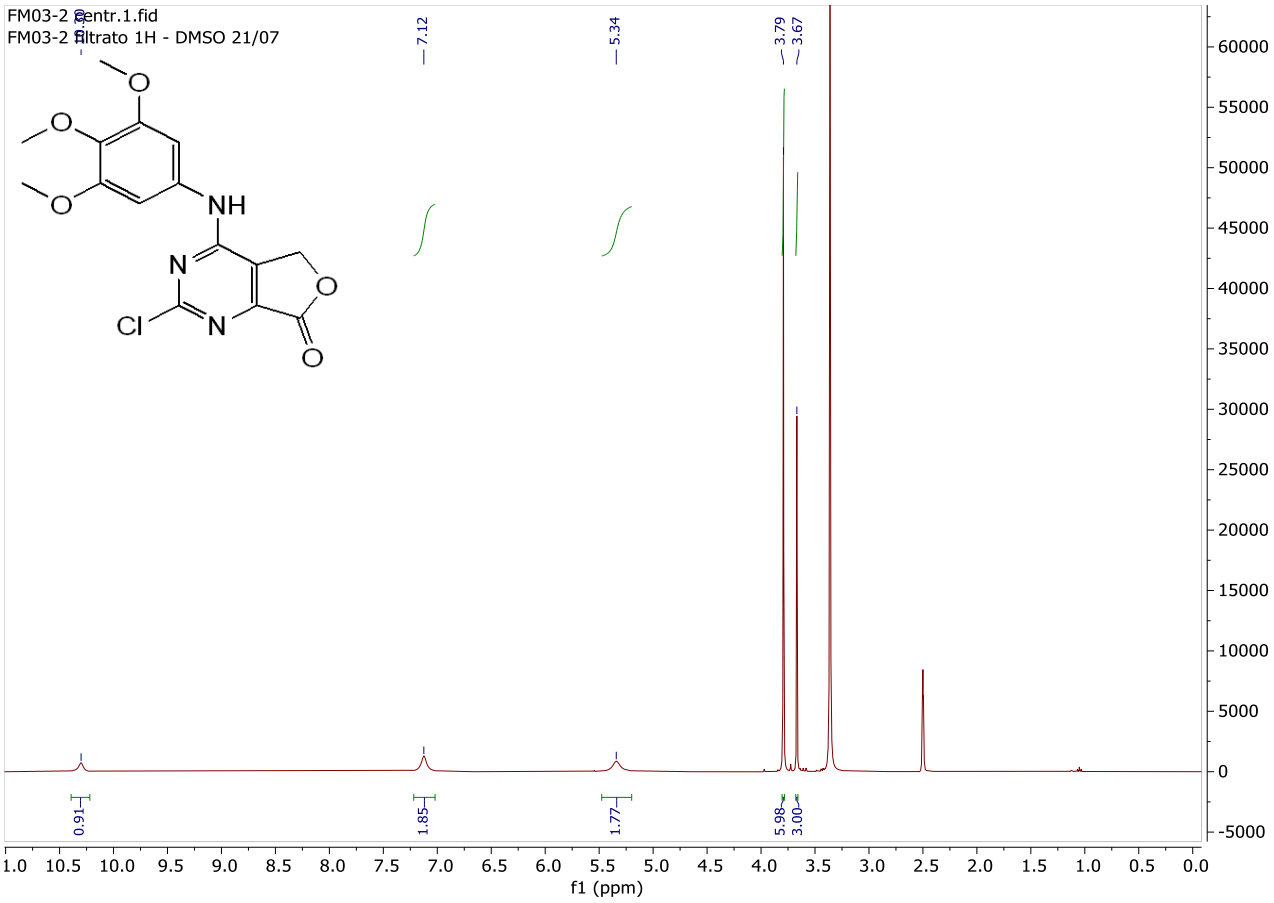


**Figure 5.2** $^{1}$H-NMR spectrum (25°C, 400 MHz, DMSO-$d_6$) of **FM03**.

In the spectrum of compound **FM03** (**Figure 5.2**) the signals of the methoxy groups are present at 3.67 and 3.79 ppm, the $CH_2$ at 5.34 ppm, the two aromatic protons at 7.12 ppm and the NH at 10.30 ppm. The $CH_2$ and the aromatic proton signals are unexpectedly broad, probably because of an hindered rotation of the bulky 3,4,5-methoxy aniline with respect to the furo[3,4-d]pyrimidin-7-one planar moiety.

To verify this hypothesis and try to obtain a spectrum with sharper signals, the acquisition was repeated at higher temperature.

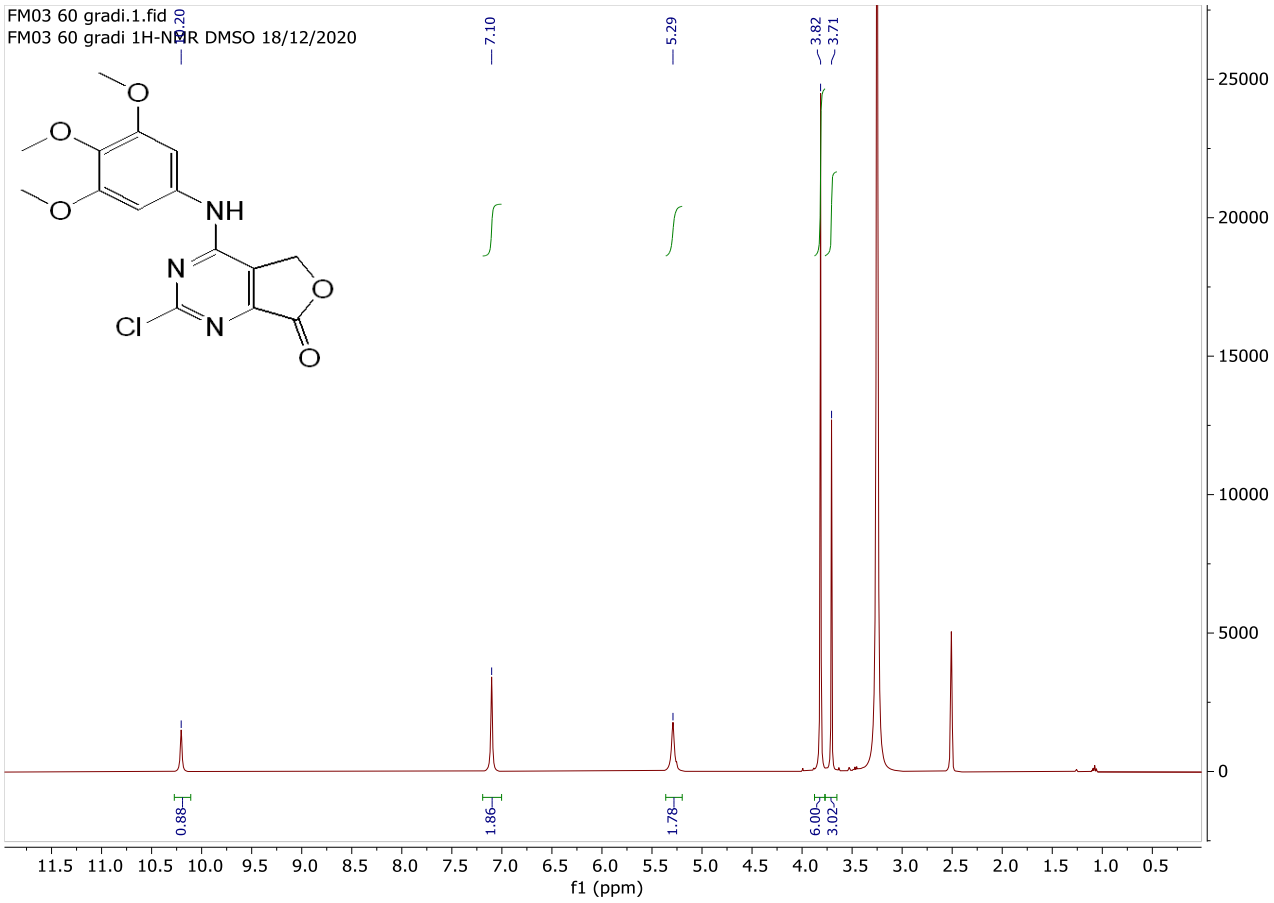


**Figure 5.3** $^{1}$H-NMR spectrum (60°C, 400 MHz, DMSO-$d_6$) of **FM03**.

The spectrum obtained at 60°C (**Figure 5.3**) presents effectively sharper signals. For this reason, the $^{13}$C-NMR spectrum was also acquired at 60°C. On the other hand, broadened signals were not observed in the spectrum of compound **FM15** (**Figure 5.4**), that has a longer spacer between the aromatic and the planar bicyclic moiety, bearing a 3,4,5-methoxy benzylamine moiety.

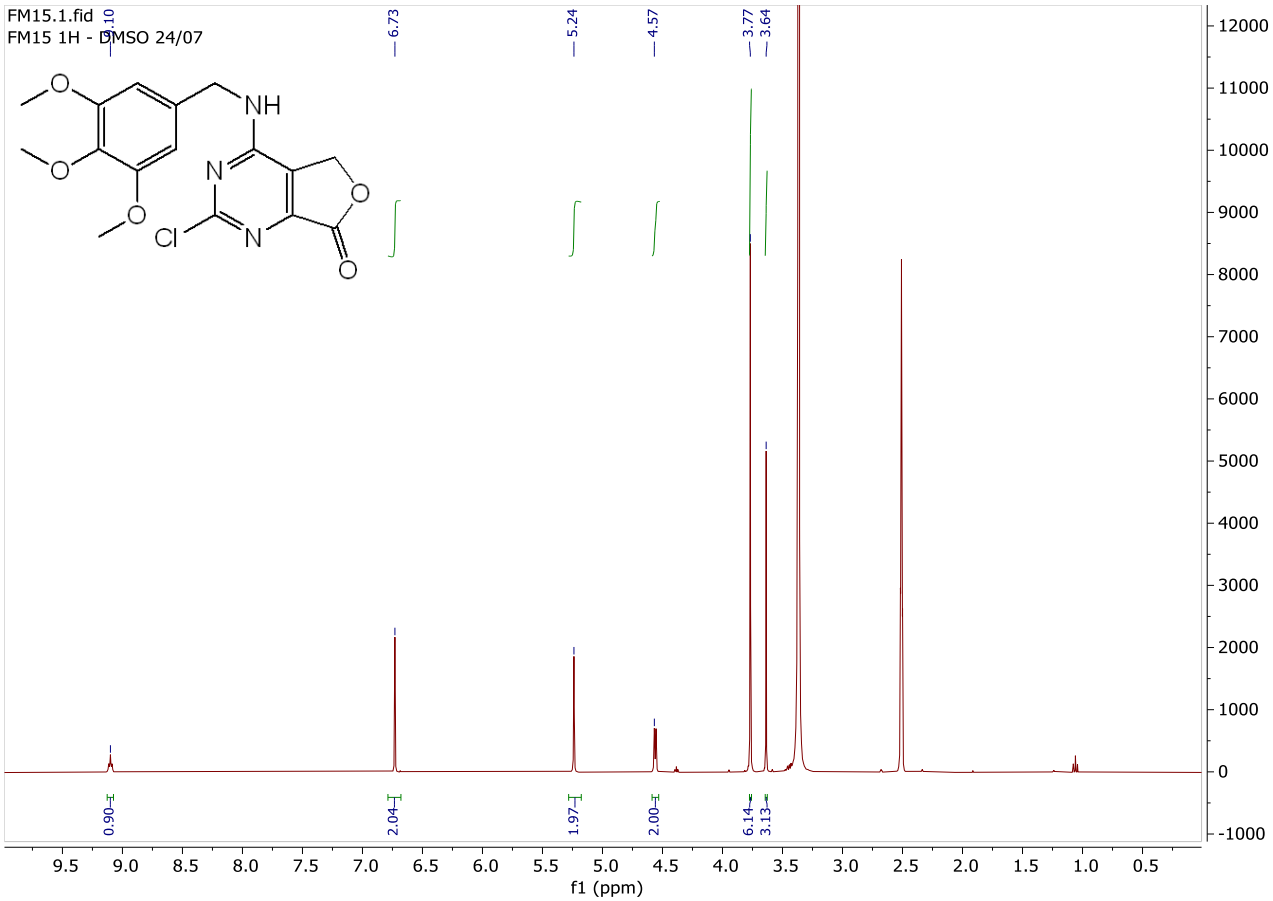


**Figure 5.4** $^{1}$H-NMR spectrum (25°C, 400 MHz, DMSO-$d_6$) of compound **FM15**.

After that **FM03** and **FM15** have been isolated and characterized, a demethylation reaction with $BBr_3$ was tried, in order to obtain their respective hydroxylated derivatives. However, the work-up and purification of these reactions resulted particularly problematic, and it was not possible to isolate the desired hydroxylated derivatives.

Hence, a new synthetic approach was pursuit. First, commercially available methoxylated amines were demethylated with $BBr_3$ and then the C4 substitution reaction with the hydroxylated amines was performed. Demethylation on the commercially available amines was conducted in dry $CH_2Cl_2$ under $N_2$, adding a $BBr_3$ solution at ≈-40°C, then the reaction was left reaching r.t. For the reaction quenching the flask was then cooled to 0°C and MeOH was slowly added. The solvents were removed by vacuum and the crude was recrystallized with a MeOH/$Et_2O$ or EtOH/$Et_2O$ mixtures (**Scheme 5.5**).

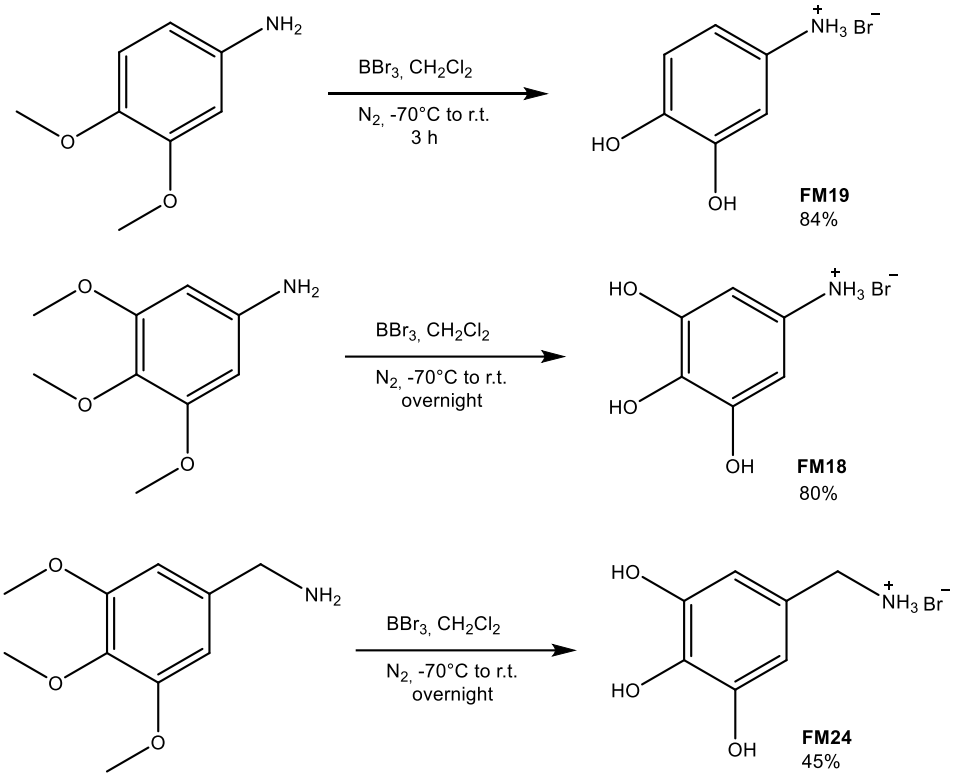


**Scheme 5.5** Demethylation reactions to obtain the hydroxylated amines **FM19**, **FM18** and **FM24**.

4 equivalents of $BBr_3$ were employed for the 3,4-dimethoxy aniline, and 6 equivalents for the 3,4,5-trimethoxy aniline and benzylamine. The full conversion of 3,4-dimethoxy aniline to compound **FM19** was obtained in 3 hours, whereas for the 3,4,5-trimethoxy amines it is necessary to perform the reaction overnight, in order to obtain the 3,4,5-hydroxy amines **FM18** and **FM24**.

The hydroxylated amines were characterized by $^{1}H$ and $^{13}C$-NMR spectroscopy, FT-IR, ESI-MS and elemental analysis. **Figure 5.5** displays the $^{1}H$-NMR and IR spectra of compound **FM19**, as an example.

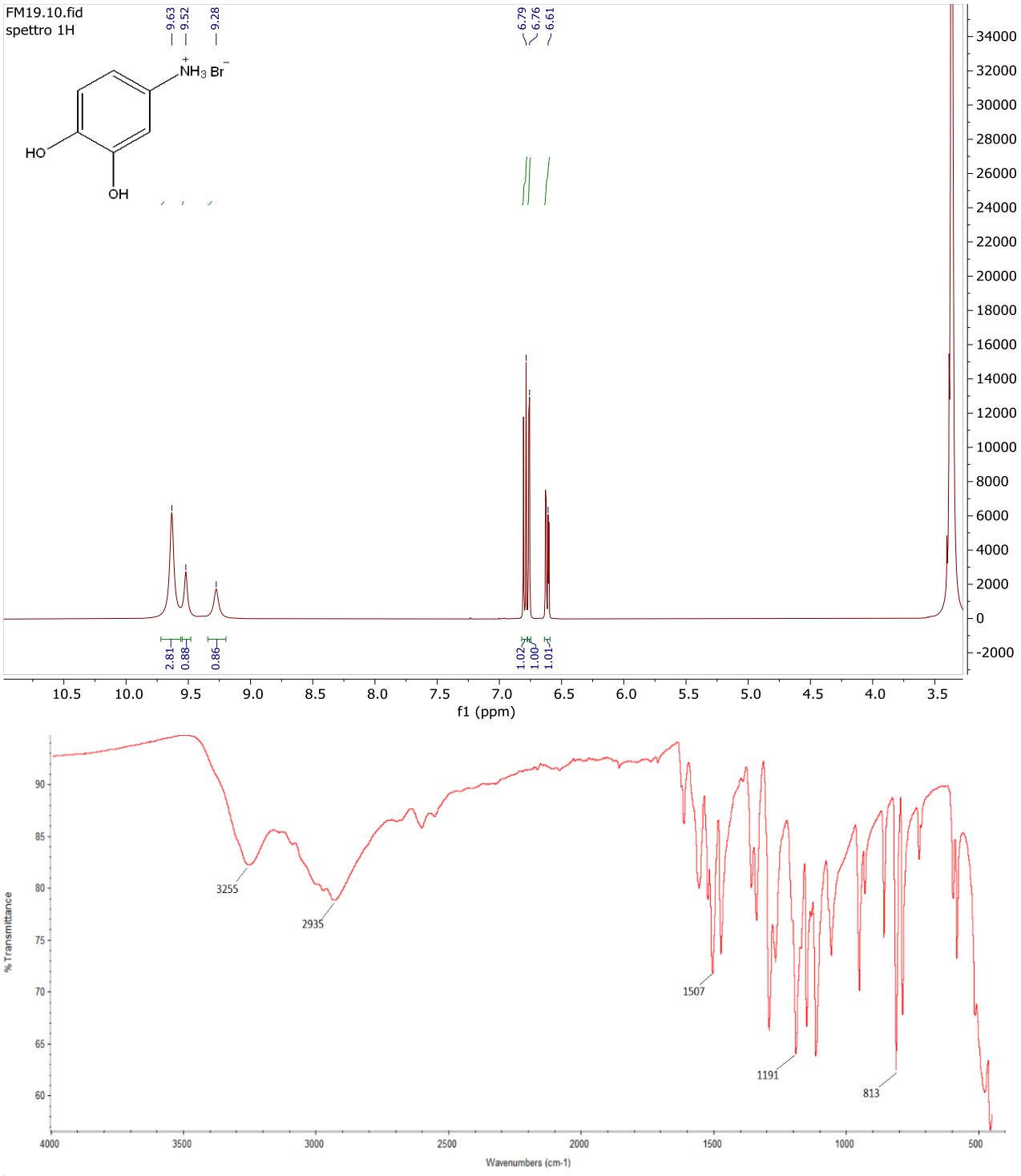


**Figure 5.5** $^{1}$H-NMR spectrum (25°C, 400 MHz, DMSO-$d_6$) (top) and FT-IR spectrum (bottom) of compound **FM19**.

In the $^{1}$H-NMR spectrum of **FM19** the signals between 3.5 and 4.0 ppm are absent, because the methoxy groups have been removed. In the aromatic region there are a doublet of doublets at 6.61 ppm, and two doublets at 6.76 and 6.79 ppm, respectively. Additionally, three broad signals integrating for approximatively five protons are presents between 9.30-9.60 ppm, corresponding to the NH and OH groups.

In the IR spectrum it is possible to see a broad band at 3255 $cm^{-1}$ corresponding to the stretching of O-H and N-H groups and a band at 2935 cm-1 for the aromatic C-H stretching.

Elemental analysis on the powders confirm that these amines were isolated as bromide salts.

Next, the C4 substitution on **FM02** with the amines **FM18**, **FM19**, **FM24** and the commercially available 3,4-dihydroxy benzylamine was performed (**Scheme**).

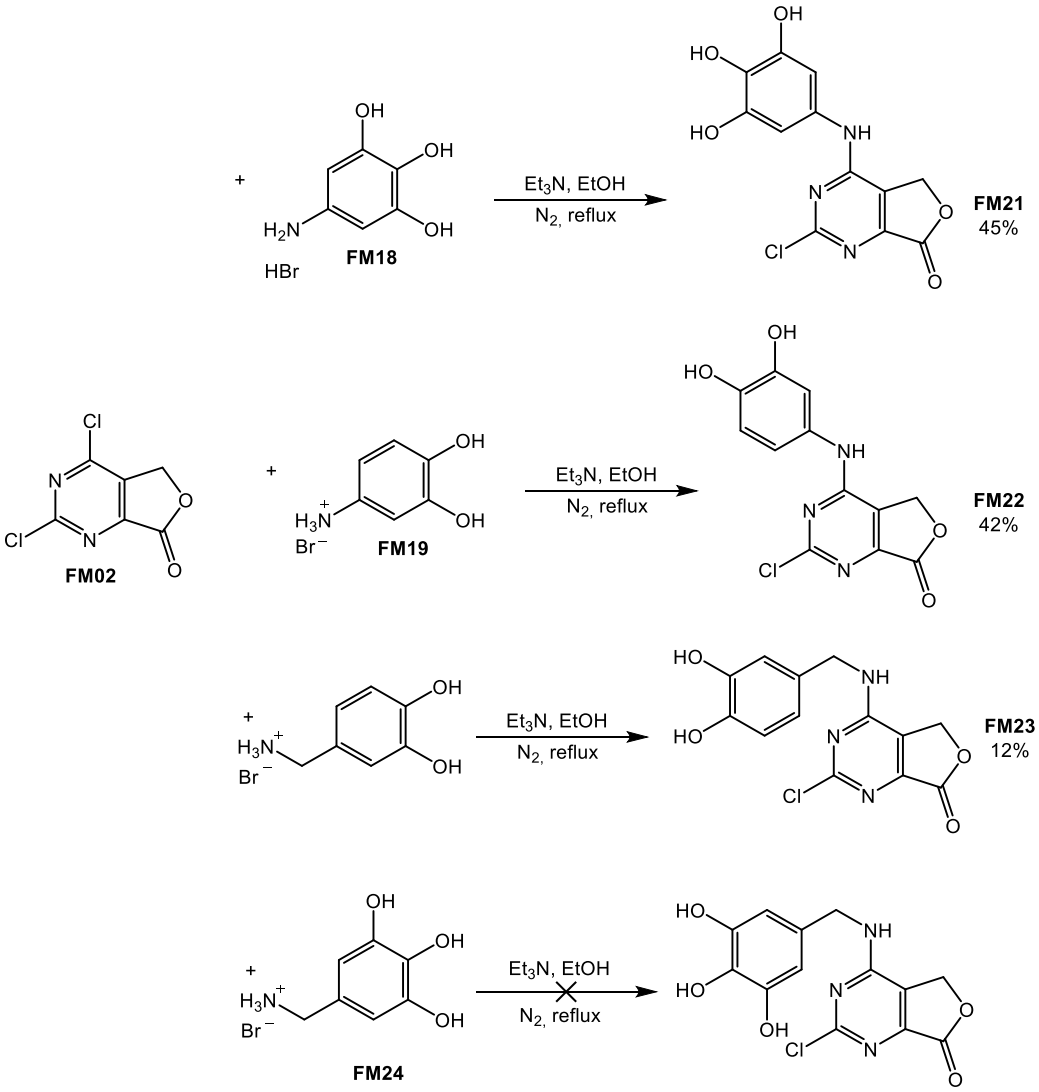


**Scheme 5.6** Substitution on **FM02** with different chelating scaffolds.

The reactions were performed dissolving the appropriate amine (1 eqv) in degassed EtOH and adding 1.5 eqv of triethylamine. After refluxing for 30 minutes, **FM02** (1 eqv) was added and the reaction mixture was stirred at reflux and under $N_2$ overnight. After that time the solvent was removed by vacuum and the crude recrystallized in EtOH/$H_2O$, filtered and washed several times with $H_2O$.

In the case of the benzylamines, these substitutions were particularly challenging due to the formation of many by-products and consequent difficult purification. **FM23** was isolated with a 12% yield, while for the reaction with **FM24** the desired product could not be isolated as a pure compound neither with recrystallization nor chromatographic column.

Compounds **FM21**, **FM22** and **FM23** were characterized by NMR spectroscopy ($^{1}H$ and $^{13}C$), ESI-MS and FT-IR spectroscopy and elemental analysis. In **Figure 5.6** are reported the $^{1}H$ and $^{13}C$ NMR spectra of compound **FM23**.

In the $^{1}H$-NMR spectrum, in addition to the $CH_2$ signal (5.21 ppm) of the furo[3,4-d]pyrimidin-7-one scaffold, the signals of the added amine moiety are present. At 4.25 ppm it is found the benzylic $CH_2$ signal, in the aromatic region a doublet of doublets at 6.63 ppm and two doublets at 6.69 and 6.74 ppm, respectively. Finally, the triplet NH signal is visible at 9.01 ppm and two broad signals of the OH groups are practically overlapped at 8.90-8.89 ppm. The $^{13}C$-NMR spectrum also confirms the formation of the product.

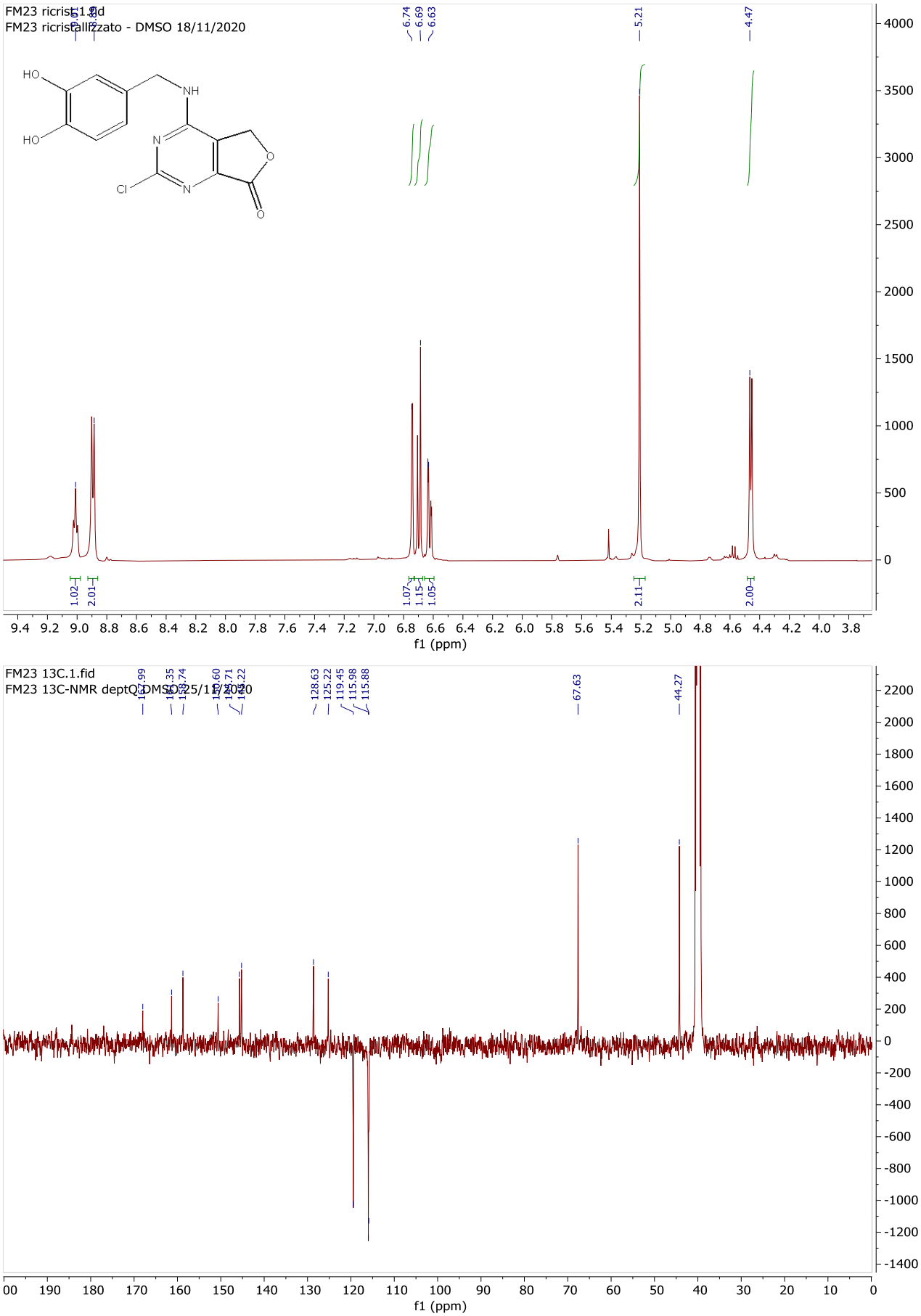


**Figure 5.6** $^{1}$HNMR (25°C, 400 MHz, DMSO-$d_6$) and $^{13}$C deptq (25°C, 101 MHz, DMSO-$d_6$) NMR spectra of **FM23**.

In the $^{1}$H-NMR spectra of compounds **FM21** (**Figure 5.7**) and **FM22** broadened signals are present, as it was observed for **FM03**. For this reason, their $^{13}$C-NMR spectra were acquired at 60°C.

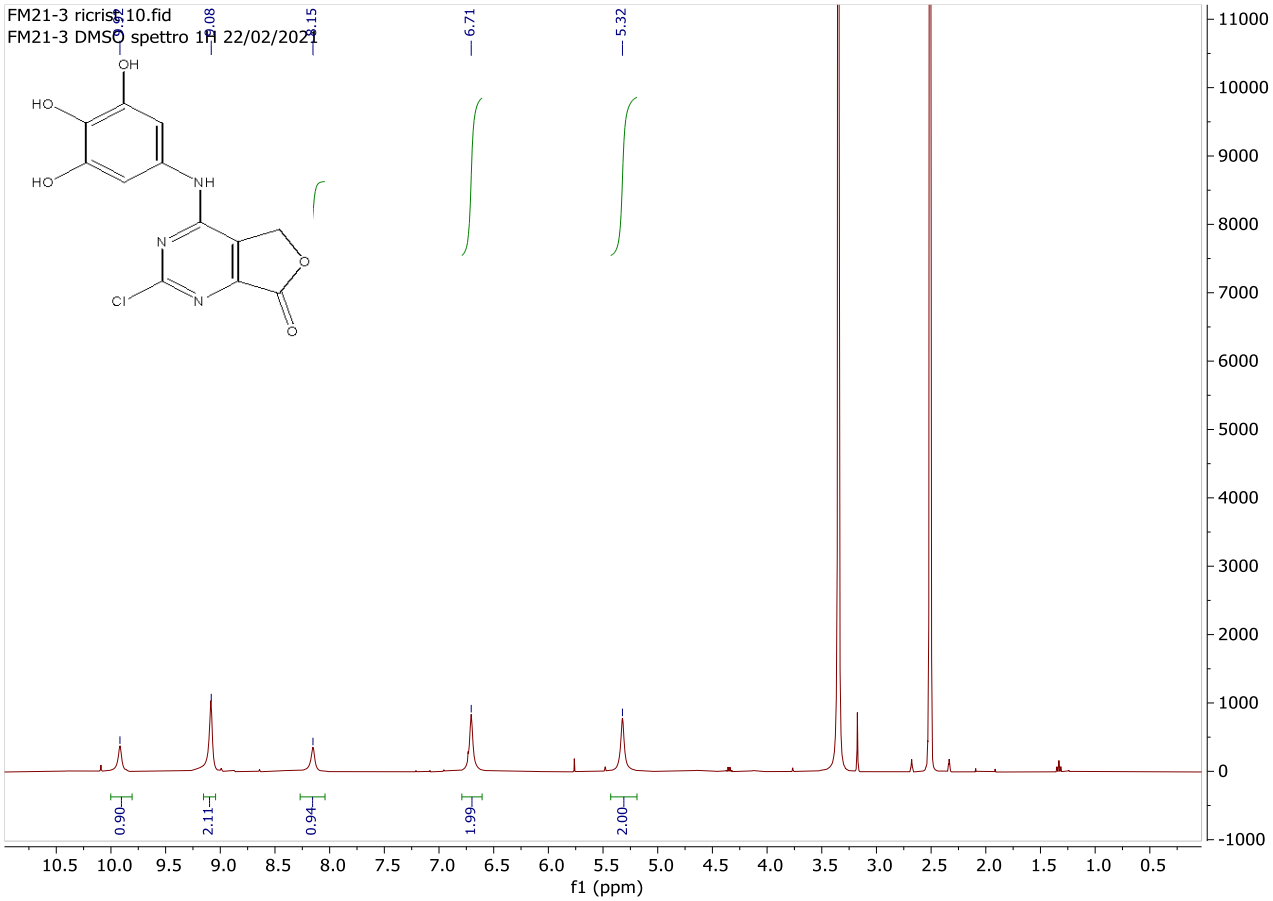


**Figure 5.7.** $^{1}$H NMR (25°C, 400 MHz, DMSO-$d_6$) NMR spectrum of **FM21**.

In the IR spectrum of compound **FM23** (**Figure 5.8**, top) several broad bands corresponding to the N-H and O-H stretching are present between 3550-3100 $cm^{-1}$ and the C=O stretching band is found at 1769 $cm^{-1}$.

In the ESI-MS spectrum of **FM23** (**Figure 5.8**, bottom) there are the peak at 306.3 m/z corresponding to the species $[M\text{-}H^{+}]^{-}$ and the peak at 613.2, corresponding to the dimeric adduct $[2M\text{-}H^{+}]^{-}$.

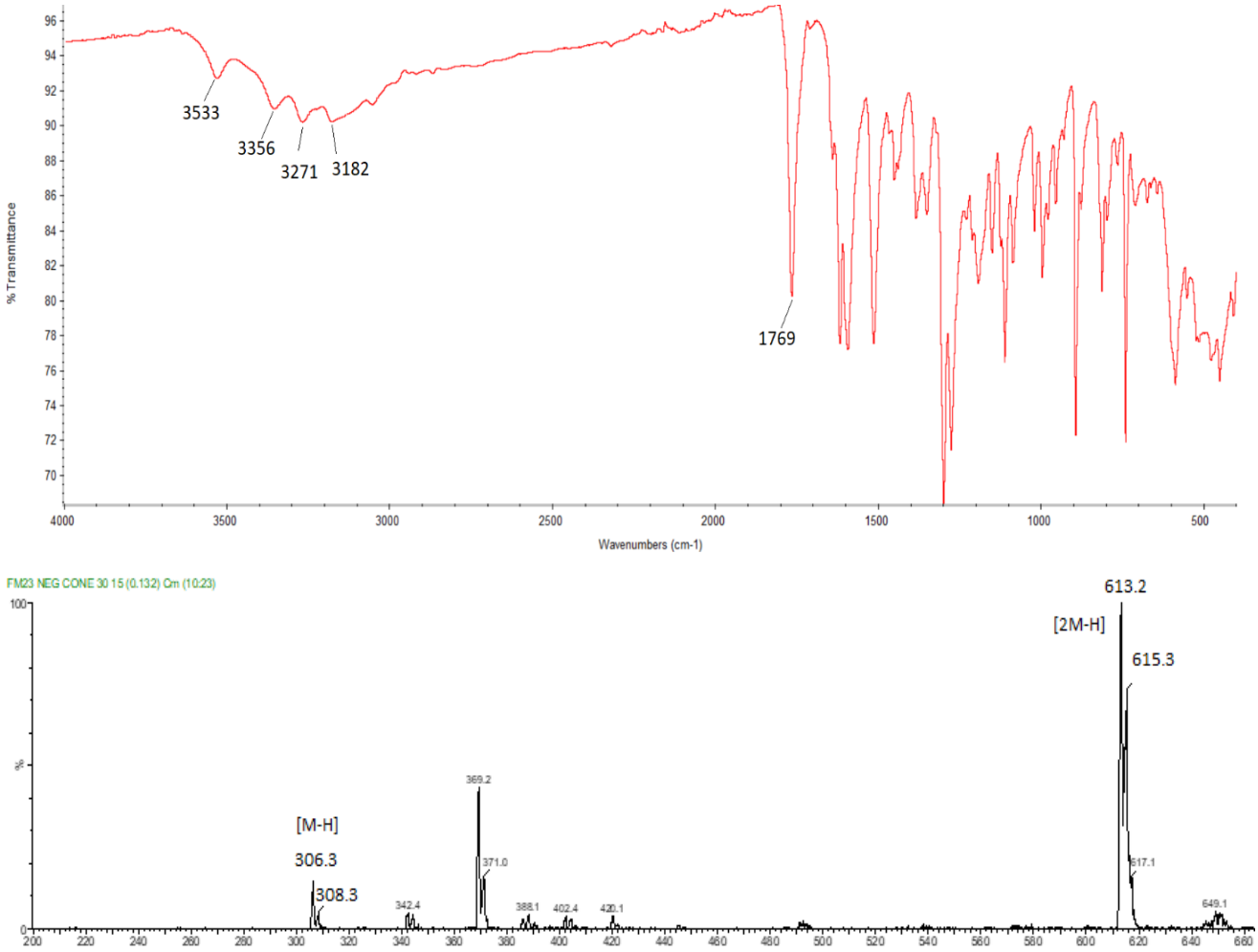


**Figure 5.8** FT-IR spectrum of (top) and ESI-MS spectrum of **FM23** (negative ions, 30 eV) (bottom).

After the isolation and characterization of **FM21**, **FM22** and **FM23**, the substitution at C2 position with morpholine was performed, in order to add a pharmacophoric moiety able to enhance the engagement with the protein (**Scheme 5.7**).[268]

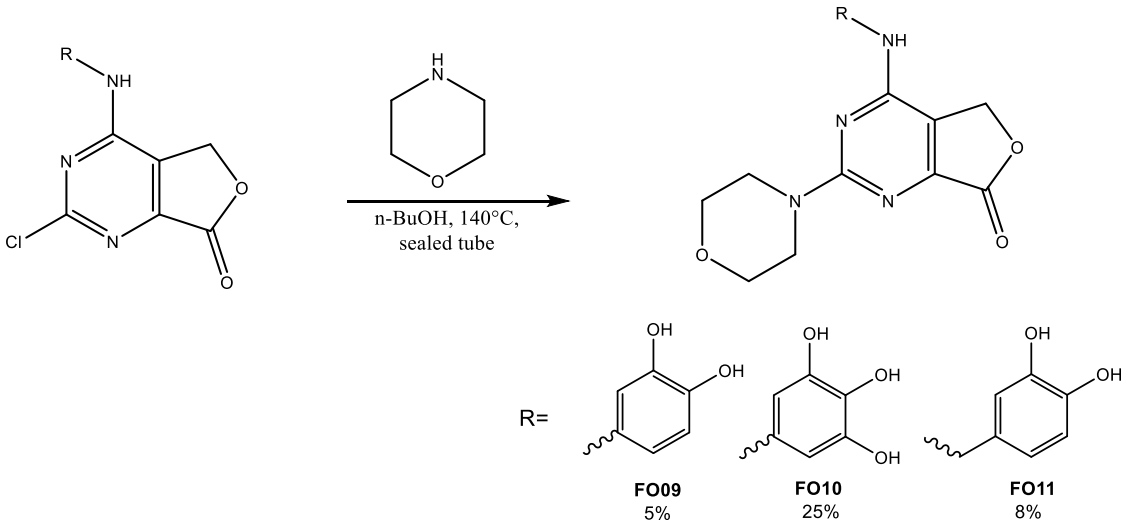


**Scheme 5.7** Substitution reactions at C2 with morpholine.

Briefly, the appropriate mono-substituted compound (**FM21**, **FM22** or **FM23**, 1 eqv) was reacted with morpholine (1.5 eqv), in a sealed tube with n-BuOH at 140°C, for 25°C. After that time, the reaction mixture was left reaching r.t and the solvent was removed by vacuum. The crude was added with acetone and a solid was filtered. The solid was then washed with hot water and with $Et_2O$ several times, obtaining the final products.

These reactions were characterized by the formation of several by-products and a tricky purification, that led to isolate the products **FO09**, **FO10** and **FO11** with very poor yields.

All compounds were characterized by NMR spectroscopy ($^1H$ and $^{13}C$), ESI-MS and IR spectroscopy. The purity of the compounds was verified by elemental analysis. In **Figure 5.9** are reported the $^1H$ and $^{13}C$ NMR spectra of compound **FO10**.

As observed for its precursors, **FO10** presents a $^1H$-NMR spectrum characterized by broad aromatic and cyclic $CH_2$ signals, because of steric constrains. The positive outcome of the reaction is confirmed by the presence of a multiplet integrating for 8 protons at 3.67 ppm, characteristic of the morpholine moiety.

In the $^{13}C$-NMR the two signals corresponding to morpholine $CH_2$ groups (66.6 and 45.1 ppm) are found.

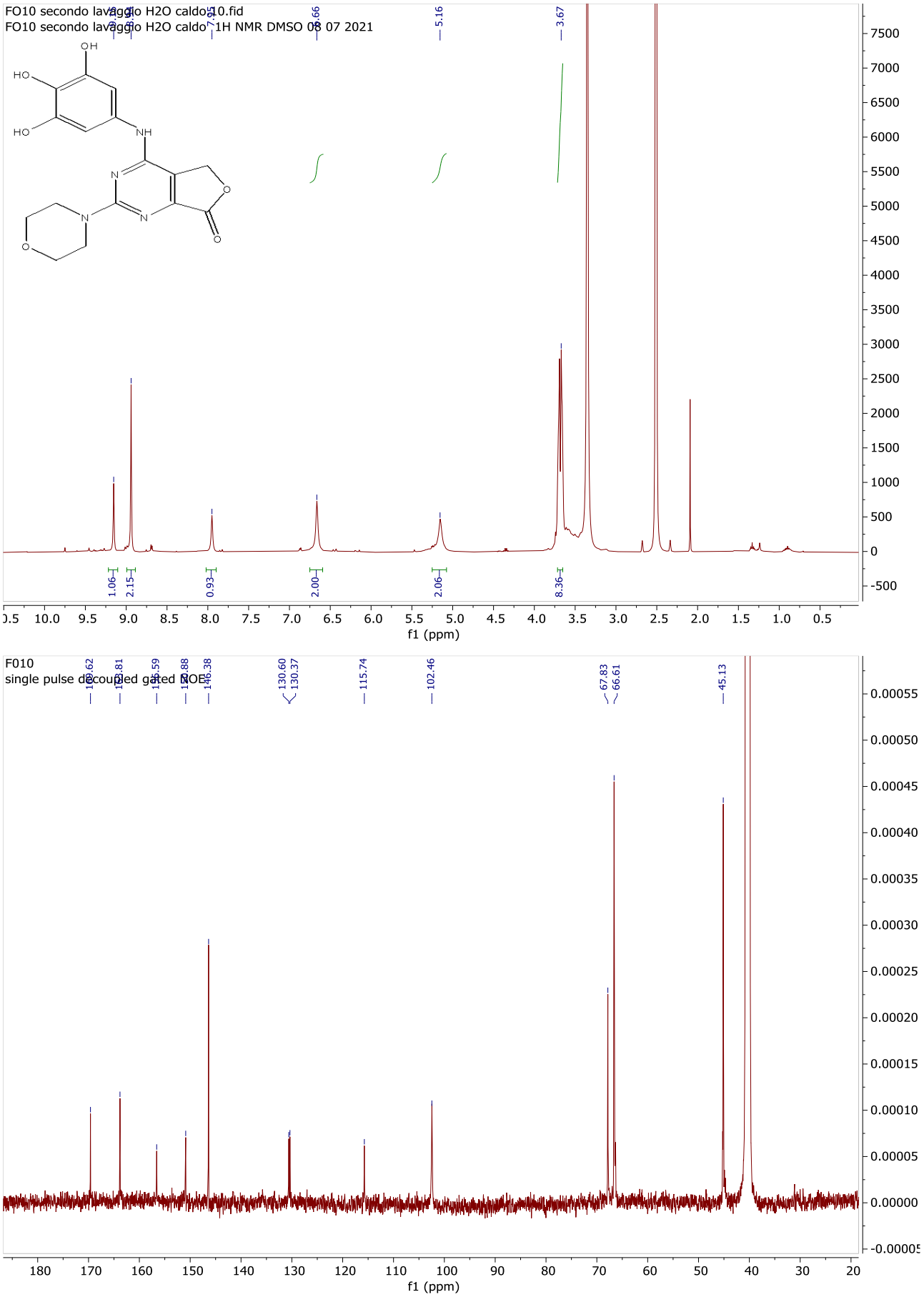


**Figure 5.9** $^{1}$H-NMR (25°C, 400 MHz, DMSO-$d_6$) and $^{13}$C-NMR (60°C, 101 MHz, DMSO-$d_6$) spectra of **F010**.

### 5.2.2 Biological evaluation

All the hydroxylated compounds **FM21**, **FM22**, **FM23**, **FO09**, **FO10**, **F011** and the methoxylated **FM03** were evaluated for their activity against some bunyaviruses.

Prof. Johan Neyts'research group at Rega Institute for Medical Research in Leuven (Belgium) performed some cellular assays on A549 and Vero E6-mCherry cells with different viruses of the *Bunyavirales* order. In particular, activity on Bunyamwera Orthobunyavirus (BUNV-mCherry), La Crosse encephalitis virus (LACV) and Rift Valley fever virus (RVRF) was investigated.

In **Figure 5.10** the graphs related to cell assays with BUNV-mCherry with synthetized compounds are reported.

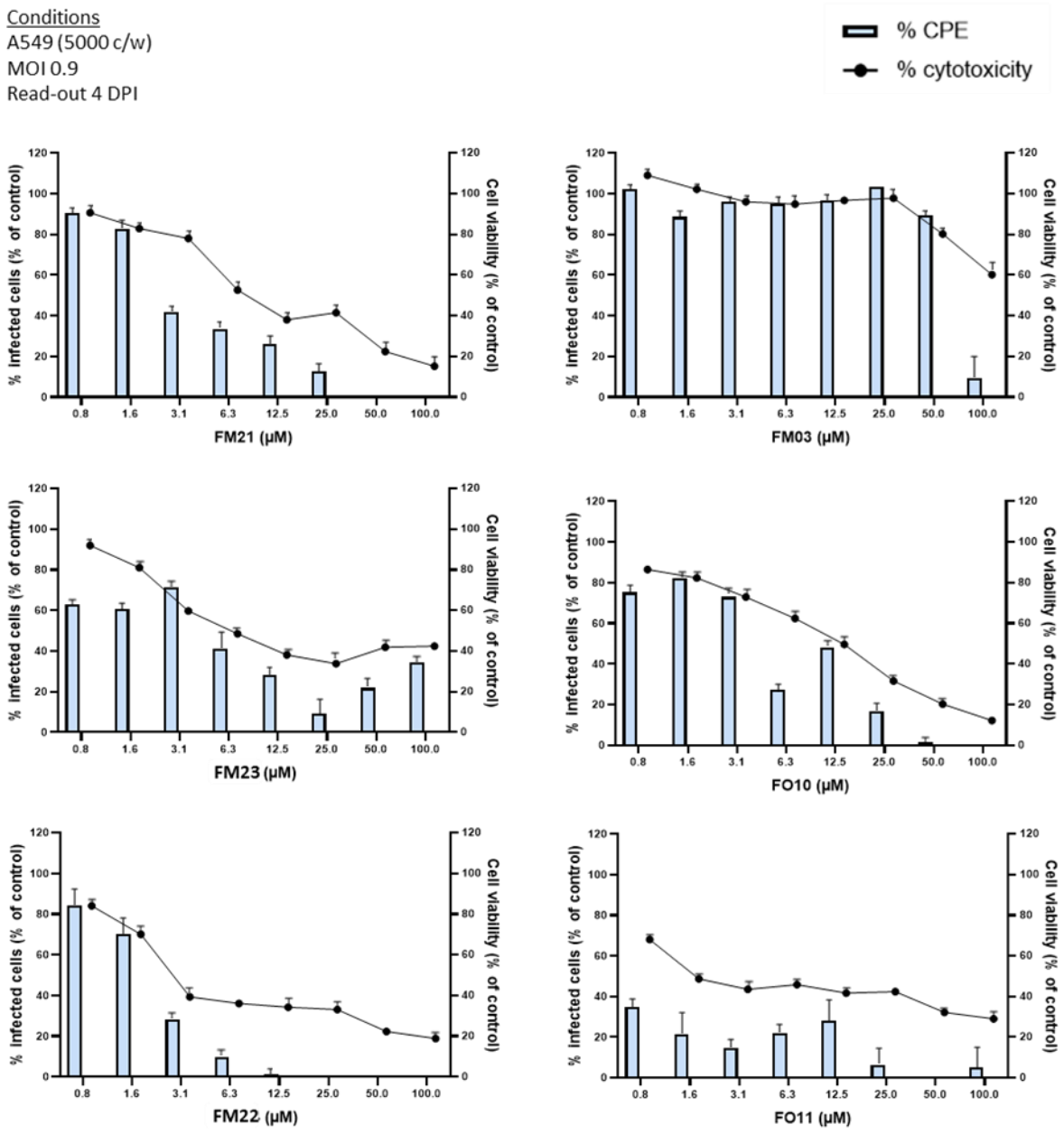


**Figure 5.10** Cellular assays results of the tested compounds on BUNV-m Cherry.

As it can be noted, in most cases the percentage of infected cells is tightly related to the cell viability, suggesting that the observed activity was mainly caused by the cytotoxicity on the tested A549 cells and not by preventing cell infection.

In the case of LACV and RVFV most of the compounds did not show any signs of activity or cytotoxicity under 100 µM towards the tested Vero E6-mCherry cells (results for LACV in **Figure 5.11**).

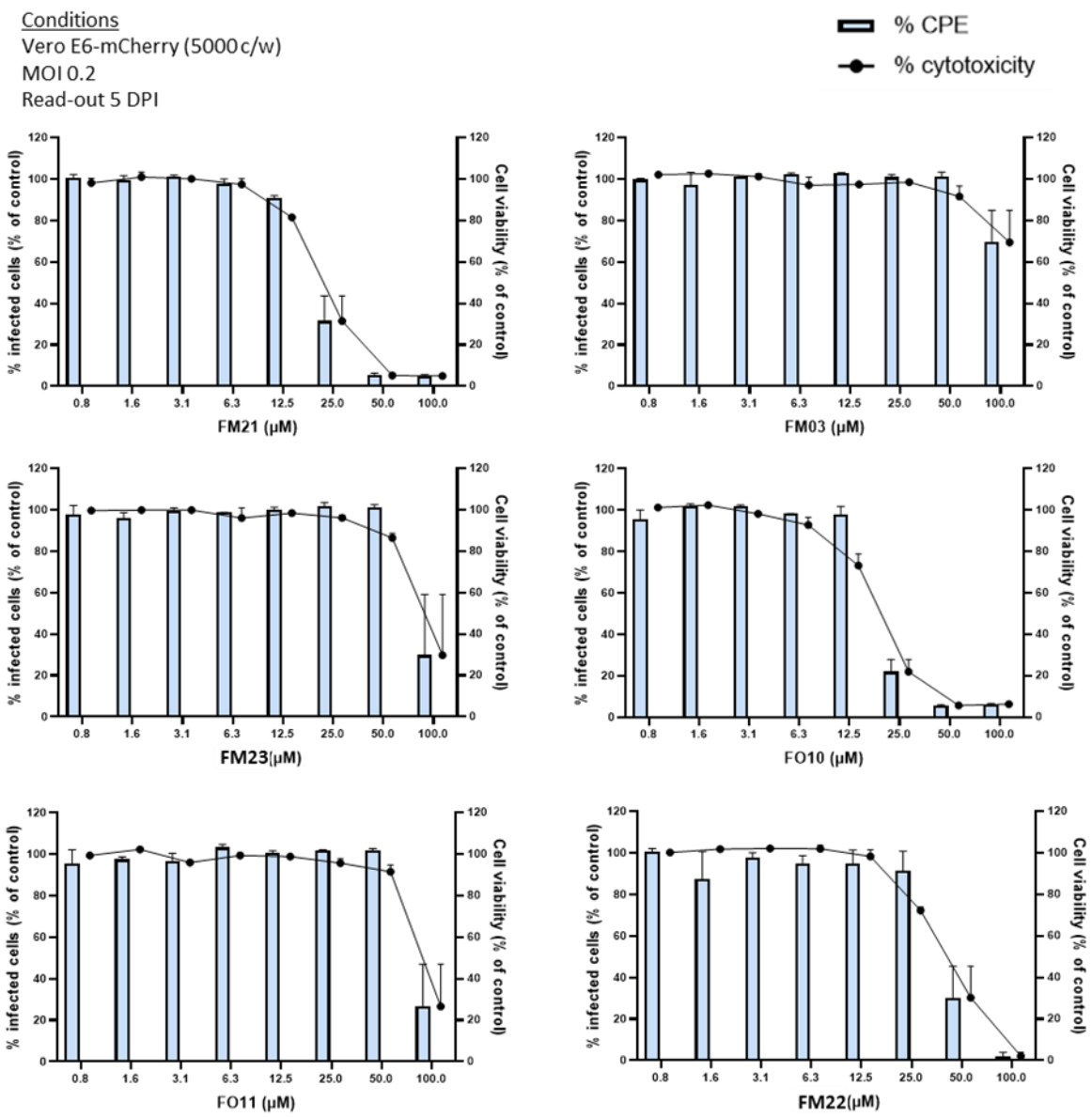


**Figure 5.11** Cellular assays results of the tested compounds on LACV.

Aside from the cellular assays, some thermal shift assays and LCMV cap-Endonuclease, in presence of Mn(II) ions, were conducted by Prof. Stephen Gunther and Dr. Yaiza Fernandez Garcia research group at the Bernhard Nocht Institute for Tropical Medicine, Hamburg.

In these tests the interaction of the compound with the enzyme is estimated measuring the variation of the melting temperature (ΔTm) of the enzyme. The engagement of the compounds should stabilize the protein and result in an increase of the melting temperature of the protein.

Unfortunately, these experiments did not show a stabilizing effect for the protein in presence of the furo[3,4-d]pyrimidin-7-one derivatives, indicating that binding to the LCMV cap-Endonuclease does not occur (**Figure 5.12**).

| LCMV_L1-197_WT | | | |
|---|---|---|---|
| | Tm (°C) | SD | ΔTm (°C) |
| $Mn^{2+}$ | 55.41 | 0.16 | 0 |
| BXA | 61.23 | 0.09 | 5.82 |
| DPBA | 62.89 | 0.34 | 7.48 |
| FM03 | 56.23 | 0.13 | 0.82 |
| FM21 | 53.73 | 0.33 | -1.68 |
| FM22 | 51.89 | 0.08 | -3.52 |
| FM23 | 55.58 | 0.07 | 0.17 |
| FO09 | 51.61 | 0.19 | -3.8 |
| FO10 | 53.35 | 0.14 | -2.06 |
| FO11 | 55.93 | 0.08 | 0.52 |

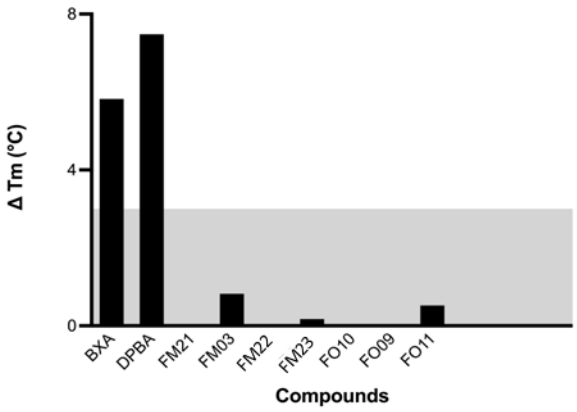


**Figure 5.12** Thermal shift assays results on LCMV cap-endonuclease with standard deviations (SD). ΔTm for each compound is calculated referred to the enzyme in presence of $Mn^{2+}$ ions (10 mM). Baloxavir acid (BXA) and 2,4-dioxo-4-phenylbutanoic acid (DPBA) are used as a control.

The assay results displayed that only BXA and DPBA, known endonuclease inhibitors used as a control, caused considerable ΔTm (5.82 and 7.48 respectively). On the contrary, FM and FO compounds produced just a modest or negative ΔTm.

Unfortunately, these results suggest that these molecules are not effective as Bunyavirus CAP-endo inhibitors and no further biological investigations were considered.

## 5.3 Conclusions

During this project, a panel of new furo[3,4-d]pyrimidin-7-one derivatives, substituted with various aromatic chelating moieties, was synthetized and characterized.

The activity of the synthetized compound towards three different bunyaviruses (BUNV-mCherry, LACV and RVRF) was evaluated in cellular assays. Unfortunately, all the compounds displayed either no activity towards the viruses or high cytotoxicity towards the host cells.

Furthermore, thermal shift assays conducted on LCMV cap-snatching endonuclease suggested that these compounds do not interact with the enzyme. Altogether, these results suggest that the furo[3,4-d]pyrimidin-7-one scaffold substituted with aromatic chelating moieties is not suitable as inhibitor of Bunyaviruses endonucleases.

## 5.4 Experimental

### 5.4.1 Materials and methods

#### 5.4.1.1 Chemistry

All reagents of commercial quality were purchased from Sigma-Aldrich and used without further purification. The purity of the synthesized compounds was determined by elemental analysis and verified to be ≥ 95%.

NMR spectra were recorded on a Bruker Advance spectrometer operating at 400 MHz for the $^{1}H$ and at 101 MHz for $^{13}C$ nuclei, at 25°C. All chemical shifts are expressed in ppm.

The ATR-IR spectra were recorded by means of a Nicolet-Nexus (Thermo Fisher) spectrophotometer by using a diamond crystal plate in the range of 4000-400 $cm^{-1}$.

Elemental analyses were performed by using a FlashEA 1112 series CHNS/O analyzer (Thermo Fisher) with gas-chromatographic separation.

Electrospray mass spectral analyses (ESI-MS) were performed with an electrospray ionization (ESI) time-of-flight Micromass 4LCZ spectrometer. Samples were dissolved in methanol. MS spectra were acquired with a DSQII Thermo Fisher apparatus, equipped with a single quadrupole analyser in positive EI mode, by means of a DEP-probe (Direct Exposure Probe) equipped with a Re-filament.

#### 5.4.1.2 Cell based antiviral activity assays

The antiviral activity of tested compounds was evaluated against BUNV-mCherry.[269] A549 cells (lung carcinoma cell line, ATCC® CCL-185) were seeded in 96-well plates (Greiner Bio-One REF#655090) at a density of 5000 cells/well in DMEM supplemented with 2% FBS and 0.075g/L sodium bicarbonate and incubated overnight at 37 °C and 5% $CO_2$. The next day, serial dilutions of compounds (100 to 0.8 µM) were added followed by infection with 500 $CCID_{50}$ of virus and further incubated for 4 days. At 4 days post infection (dpi) cells were stained with a 2.5 µg/ml Hoechst (Hoechst 33342, Invitrogen) solution. High-content imaging (HCI) analysis was performed on the Arrayscan XTI (Thermofisher) using a custom analysis protocol based on the SpotDetector BioApplication (Cellomics® software). Cell viability was scored based on the number of nuclei-containing objects.

#### 5.4.1.3 Protein expression and purification

In brief, the protein contained an N-terminal His-Tag and was expressed in E. coli strain BL21 Gold (DE3) (Novagen) at 17 °C overnight using LB medium supplemented with 0.5 mM isopropyl-β-D-thiogalactopyranoside for induction. The pelleted cells were resuspended in lysis buffer and disrupted by sonication. Subsequentially, protein purification was performed by an initial nickel affinity chromatography followed by size-exclusion chromatography using a Superdex 200 column. The optimal composition of buffers for each protein has been described previously.[255][270]

### 5.4.1.4 Thermal shift assays

The stability of LCMV_L1-197_WT, produced as previously reported, was measured using a TSA with a protein concentration of 10 µM in 100 mM Tris pH 7.0, 250 mM NaCl, 5% glycerol complemented or not with 25 µM of the tested compounds in the presence of 10 mM EDTA or 10 mM $MnCl_2$ as described.[255][271]

## 5.4.2 Chemistry

**1,5-dihydrofuro[3,4-d]pyrimidine-2,4,7(3H)-trione (FM01)**

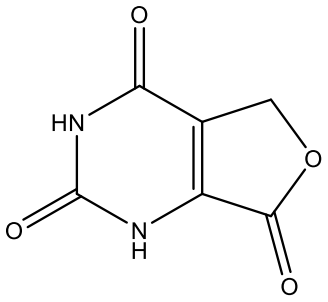

Orotic acid (3g, 17.23 mmol, 1 eqv) and paraformaldehyde (2.07g, 68.92 mmol, 4 eqv) were suspended in 63 mL of HCl 35%. The reaction was stirred at 95°C overnight. The solvent was then evaporated by vacuum. 12 mL of water were added to the crude and it was stirred at 60°C for one hour. The mixture was filtered and washed with water, obtaining **FM01** as a white solid with 45% yield.
$^1$H-NMR (DMSO-$d_6$, 400 MHz, 25°C), ppm: 12.09 (b, 1H, NH); 11.54 (b, 1H, NH); 5.10 (s, 2H, $CH_2$).
$^{13}$C-NMR (DMSO-$d_6$, 100.5 MHz, 25°C), ppm: 164.07 (Cq); 159.6 (Cq); 151.8 (Cq); 137.9 (Cq); 122.5 (Cq); 67.41 ($CH_2$).

**2,4-dichlorofuro[3,4-d]pyrimidin-7(5H)-one (FM02)**

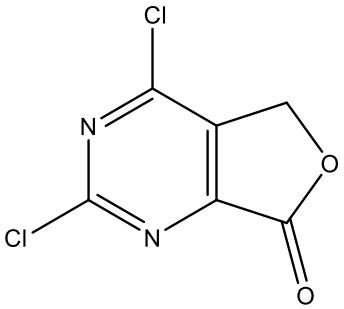

**FM01** (1.424 g, 8.47 mmol) was suspended in 6.5 mL of $CH_2Cl_2$ dry and of 11.5 mL of $POCl_3$ in a round-bottom flask. The suspension was cooled to 0°C and 2.32 mL of $Et_3N$ are added dropwise. The reaction was stirred overnight at 90°C. The solvents were removed by vacuum, iced water was added to the flask and the crude was stirred for 1 hour. The aqueous solution was extracted with $CH_2Cl_2$. The organic phase was washed with brine, dried over $Na_2SO_4$ and concentrated. The crude was purified with a chromatographic column using an EtOAc/Hex 5/1 mixtures as eluent. The fraction with the product was finally recrystallized in $CH_2Cl_2$/Hex obtaining **FM02** as a brown solid with 55% yield.
$^1$H-NMR ($CDCl_3$, 400 MHz, 25°C), ppm: 5.44 (s, 2H, $CH_2$).
$^{13}$C-NMR ($CDCl_3$, 100.5 MHz, 25°C), ppm: 164.4, 163.3, 159.3, 156.2, 135.4, 66.4.

**2-chloro-4-((3,4,5-trimethoxyphenyl)amino)furo[3,4-d]pyrimidin-7(5H)-one (FM03)**

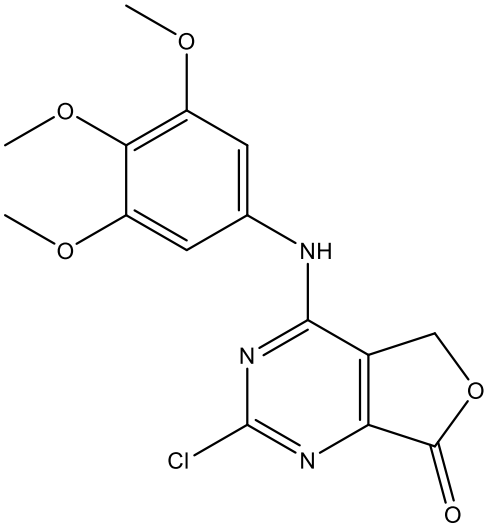

**FM02** (0.250 g, 1.22 mmol, 1 eqv) was dissolved in 12.5 mL of EtOH in a round-bottom flask and 3,4,5-tri methoxy aniline (0.257g, 1.40 mmol, 1.15 eqv) was added, forming a yellow suspension. The reaction was stirred at room temperature for 4 hours. After that, the reaction mixture was filtered and washed with EtOH, obtaining **FM03** as a yellow solid with 75% yield.

$^{1}$H-NMR (DMSO-$d_6$, 600 MHz, 25°C), ppm: 10.36 (b, 1H, NH); 7.15 (b, 2H, $CH_{arom}$); 5.35 (b, 2H, $CH_2$); 3.79 (s, 6H, $OCH_3$); 3.67 (s, 3H, $OCH_3$).

$^{13}$C-NMR (DMSO-$d_6$, 100.5 MHz, 60°C), ppm: 166.8 (Cq); 160.1 (Cq); 156.5 (Cq); 152.6 (Cq); 151.1 (Cq); 135.1 (Cq); 133.1 (Cq); 125.2 (Cq); 100.2 (CH); 67.0 ($CH_2$); 60.0 ($OCH_3$); 55.8 ($OCH_3$).

ESI-MS : m/z= ($M+Na^+$): 373.78

IR (ATR, $cm^{-1}$) ν(NH) = 3337; ν(C=O) = 1770.

E.A. calculated for $C_{15}H_{14}ClN_3O_5 \cdot 0.5\ H_2O$: C 49.94, H 4.19, N 11.65. Found: C 49.95, H 4.15, N 11.32.

**2-chloro-4-((3,4,5-trimethoxybenzyl)amino)furo[3,4-d]pyrimidin-7(5H)-one (FM15)**

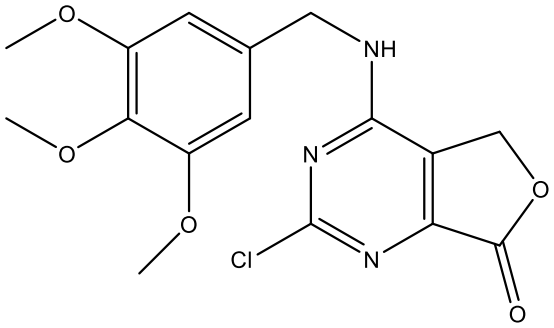

**FM02** (0.400 g, 1.951 mmol, 1 eqv) was dissolved in 20 mL of EtOH and 3,4,5-tri methoxy benzylamine (0.443 g, 2.44 mmol, 384 µL, 1.25 eqv) was added, forming a dark red suspension. The reaction was stirred at room temperature for 4 hours. After that the reaction mixture was filtered and washed with EtOH, obtaining **FM15** as pale pink solid with 47 % yield.

$^{1}$H-NMR (DMSO-$d_6$, 400 MHz, 25°C), ppm: 9.09 (t, *J* = 5.6 Hz, 1H, NH); 6.72 (s, 2H, $CH_{arom}$); 5.23 (s, 2H, $CH_2$); 5.55 (d, *J* = 5.6 Hz, 2H, $CH_2$); 3.76 (s, 6H, $OCH_3$); 3.63 (s, 3H, $OCH_3$).

$^{13}$C-NMR (DMSO-$d_6$, 100.5 MHz, 25°C), ppm: 167.5 (Cq); 160.8 (Cq); 158.4 (Cq); 152.9 (Cq); 150.2 (Cq); 136.8 (Cq); 134.1 (Cq); 133.0 (Cq); 129.5 (Cq); 125.0 (Cq); 105.6 (CH); 67.2 ($CH_2$); 60.0 ($CH_3$); 55.9 ($CH_3$); 44.4 ($CH_2$).

ESI-MS : m/z= ($M+Na^+$): 387.87

IR (ATR, $cm^{-1}$) ν(NH) = 3292; ν($CH_{arom}$) =2946; ν(C=O) = 1790.

E.A. calculated for $C_{16}H_{16}ClN_3O_5$: C 52.54, H 4.41, N 11.49. Found: C 52.31, H 4.53, N 11.03.

**3,4-dihydroxy aniline hydrobromide (FM19):**

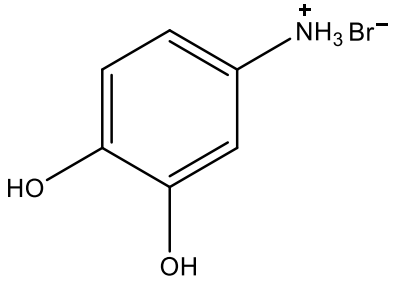


500 mg of 3,4-dimethoxy aniline (3.26 mmol, 1 eqv) was dissolved in 4 mL dry $CH_2Cl_2$ under nitrogen condition and the solution was cooled to -40°C. Then, a solution of $BBr_3$ (3.27 g, 1.20 mL, 4 eqv) in 8 mL of dry $CH_2Cl_2$ was slowly added. The reaction was left reaching room temperature. After 3 hours the reaction mixture was cooled to 0°C and 12 mL of cooled MeOH are slowly added. The solvents were removed by vacuum and the product was recrystallized using MeOH/$Et_2O$, obtaining 3,4-dihydroxy aniline hydrobromide as a purple solid with 84% yield.

$^1$H-NMR (DMSO-$d_6$, 400 MHz, 25°C), ppm: 9.63 (b, 3H, $NH_3$); 9.52 (b, 1H, OH); 9.28 (b, 1H, OH); 6.79 (d, *J* = 8.4 Hz, 1H, H5); 6.76 (d, *J* = 2.5 Hz, 1H, H2); 6.62 (dd, *J* = 8.4, 2.5 Hz, 1H, H6).

$^{13}$C NMR (101 MHz, DMSO-$d_6$, 25°C) δ 146.1, 145.4, 122.2, 115.9, 113.6, 110.6.

ESI-MS: m/z= (M-HBr+$Na^+$): 149.

IR (ATR, $cm^{-1}$) ν(NH)+ ν(OH) =3255; ν($CH_{arom}$) =2935.

E.A. calculated for $C_6H_7NO_2 \cdot HBr$: C 34.97, H 3.91, N 6.80. Found: C 35.09, H 3.97, N 6.51.

**3,4,5-trihydroxy aniline hydrobromide (FM18):**

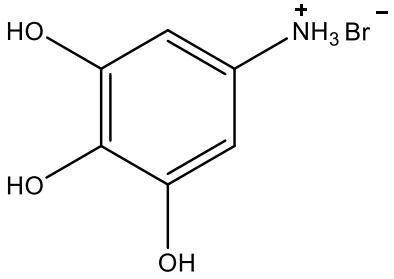


500 mg of 3,4,5-trimethoxy aniline (2.73 mmol, 1 eqv) were dissolved in 4 mL dry $CH_2Cl_2$ under nitrogen condition and the solution is cooled to -40°C. Then, a solution of $BBr_3$ (4.10 g, 1.55 mL, 6 eqv) in 8 mL of dry $CH_2Cl_2$ was slowly added. The reaction was left reaching room temperature and was stirred overnight. The reaction mixture was then cooled to 0°C and 15.5 mL of cooled MeOH are slowly added. The solvents were removed by vacuum and the product was recrystallized by using EtOH/$Et_2O$, obtaining 3,4,5-trihydroxy aniline hydrobromide as a pale orange solid with 80% yield.

$^1$H-NMR (DMSO-$d_6$, 400 MHz, 25°C), ppm: 9.56 (b, 2H); 9.41 (b, 3H); 6.29 (s, 2H, $CH_{arom}$).

$^{13}$C-NMR (DMSO-$d_6$, 100.5 MHz, 25°C), ppm: 144.7; 133.0; 121.5; 102.0.

ESI-MS: m/z= (M-HBr+$H^+$): 141.89.

IR (ATR, $cm^{-1}$) ν(NH)+ ν(OH) =3472, 3165; ν($CH_{arom}$) =3023.

E.A. calculated for $C_6H_7NO_3 \cdot HBr$: C 32.45, H 3.63, N 5.82. Found: C 32.98, H 3.81, N 5.82.

**3,4,5-trihydroxy benzylamine hydrobromide (FM24):**

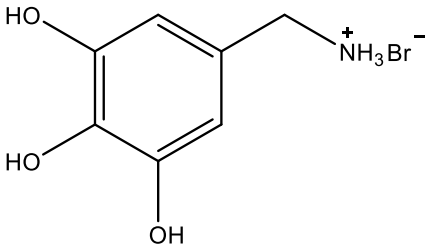


500 mg of 3,4,5-trimethoxy benzylamine (2.53 mmol, 1 eqv) was dissolved in 4 mL dry $CH_2Cl_2$ under nitrogen condition and the solution was cooled to -40°C. Then, a solution of $BBr_3$ (3.80 g, 1.43 mL, 6 eqv) in 8 mL of dry $CH_2Cl_2$ was slowly added. The reaction was left reaching room temperature and was stirred overnight. The reaction mixture was then cooled to 0°C and 14.5 mL of cooled MeOH are slowly added. The solvents were removed by vacuum and the product was recrystallized by using EtOH/$Et_2O$, obtaining 3,4,5-trihydroxy benzylamine hydrobromide as a pale yellow solid with 45% yield.

$^1$H-NMR (DMSO-$d_6$, 400 MHz, 25°C), ppm: 8.82 (s, 2H); 8.11 (s, 1H); 7.96 (b, 3H); 6.35 (s, 2H, $CH_{arom}$); 3.74 (b, 2H, $CH_2$).

$^{13}$C-NMR (DMSO-$d_6$, 100.5 MHz, 25°C), ppm: 146.1; 133.4; 123.8; 108.0; 42.4.

ESI-MS: m/z= (M-HBr+$H^+$): 156.491.

IR (ATR, $cm^{-1}$) ν(NH)+ ν(OH) =3486, 3240, 3085.

E.A. calculated for $C_7H_9NO_3 \cdot HBr$: C 35.62, H 4.27, N 5.93. Found: C 35.66, H 4.33, N 5.79.

***General procedure for the C4 substitution of FM02 with poly-hydroxylated aromatic amines:***

The appropriate amine (1 eqv) was dissolved in degassed EtOH and $Et_3N$ (1.5 eqv) was added. The solution was stirred at reflux for 30 minutes, then **FM02** (1 eqv) was added and the reaction mixture was stirred at reflux and under $N_2$ overnight. After that time the solvent were removed by vacuum and the crude was recrystallized in EtOH/$H_2O$, filtered and washed several times with $H_2O$.

**2-chloro-4-((3,4-dihydroxyphenyl)amino)furo[3,4-d]pyrimidin-7(5H)-one (FM22)**

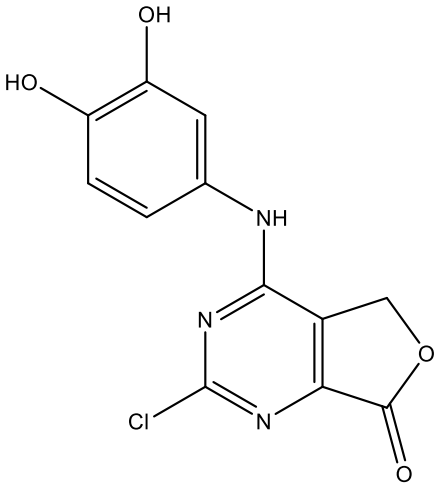


The product was obtained with the general procedure for the C4 substitution. Yield=42%.

$^1$H-NMR (DMSO-$d_6$, 400 MHz, 25°C), ppm: 10.03 (b, 1H); 9.18 (b, 1H); 8.99 (b, 1H); 7.13 (b, 1H, $H_{arom}$); 6.94 (b, 1H, $H_{arom}$); 6.75 (d, $J$ = 8.4 Hz, 1H, $H_{arom}$); 5.32 (b, 1H, $CH_2$).

$^{13}$C-NMR (DMSO-$d_6$, 100.5 MHz, 25°C), ppm: 167.4 (Cq); 160.5 (Cq); 156.3 (Cq); 150.6 (Cq); 145.2 (Cq); 143.0 (Cq); 129.2 (Cq); 125.8 (Cq); 115.8 (CH); 113.6 (CH); 110.6 (CH); 67.4 ($CH_2$). ESI-MS: m/z= (M-$H^+$): 292.3.

ESI-MS : m/z= (M+$Na^+$): 316.

IR (ATR, $cm^{-1}$) ν(NH)+ ν(OH) =3507, 3377; ν(C=O) =1751.

E.A. calculated for $C_{12}H_8O_4N_3Cl \cdot H_2O$: C 46.25, H 3.23, N 13.48. Found: C 45.94, H 3.11, N 13.30.

**2-chloro-4-((3,4-dihydroxybenzyl)amino)furo[3,4-d]pyrimidin-7(5H)-one (FM23)**

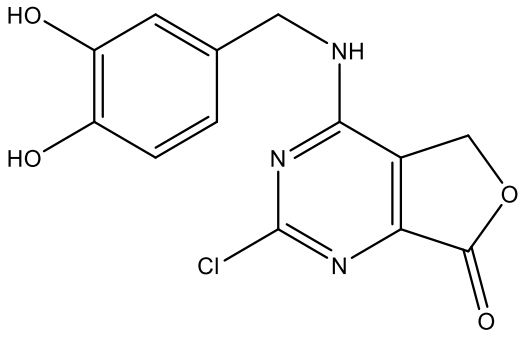


The product was obtained with the general procedure for the C4 substitution as a pink solid (Y=12%).
$^{1}$H-NMR (DMSO-$d_6$, 400 MHz, 25°C), ppm: 9.01 (t, *J* = 5.6 Hz, 1H, NH); 8.90 (b, 1H, OH), 8.89 (b, 1H, OH); 6.74 (d, *J* = 2.1 Hz, 1H, $CH_{arom}$), 6.70 (d, *J* = 8.0 Hz, 1H, $CH_{arom}$); 6.62 (dd, *J* = 8.0, 2.1 Hz, 1H, $CH_{arom}$); 5.21 (s, 2H, $CH_2$); 4.46 (d, *J* = 5.6 Hz, 2H, $CH_2$).
$^{13}$C-NMR (DMSO-$d_6$, 100.5 MHz, 25°C), ppm: 167.5 (Cq); 160.9 (Cq); 158.3 (Cq); 150.1 (Cq); 145.3 (Cq); 144.8 (Cq); 128.2 (Cq); 124.8 (Cq); 119.0 (CH); 115.6 (CH); 115.4 (CH); 67.2 ($CH_2$); 43.8 ($CH_2$).
ESI-MS: m/z= ($M-H^+$): 306.3.
IR (ATR, $cm^{-1}$) ν(NH)+ ν(OH) = 3533, 3356, 3271, 3182; ν(C=O) =1769.
E.A. calculated for $C_{13}H_{10}O_4N_3Cl \cdot H_2O$: C 47.94, H 3.71, N 12.90. Found: C 47.87, H 3.58, N 12.62.

**2-chloro-4-((3,4,5-trihydroxyphenyl)amino)furo[3,4-d]pyrimidin-7(5H)-one (FM21)**

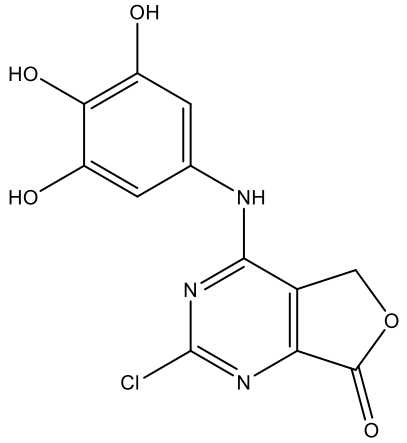


The product is obtained with the general procedure for the C4 substitution. (Y=45%).
$^{1}$H-NMR (DMSO-$d_6$, 400 MHz, 25°C), ppm: 9.92 (b,1H); 9.09 (b, 2H, OH); 8.18 (b, 1H); 6.69 (b, 2H, $CH_{arom}$); 5.31 (b, 2H, $CH_2$).
$^{13}$C-NMR (DMSO-$d_6$, 100.5 MHz, 25°C), ppm: 167.4; 166.0; 160.5; 156.03; 149.9; 145.9; 126.4; 101.5; 67.43; 66.5.
ESI-MS: m/z= ($M-H^+$): 308.
IR (ATR, $cm^{-1}$) ν(NH)+ ν(OH) =3327; ν(C=O) =1766.
E.A. calculated for $C_{12}H_8N_3O_5 \cdot 3/2\ H_2O$: C 42.81, H 2.69, N 12.48. Found: C 43.15, H 2.91, N 12.17.

***General procedure for the C2 substitution with morpholine:***

In a sealed tube 150 mg of the appropriate mono-substituted compound (**FM21**, **FM22** or **FM23**, 1 eqv) were dissolved in 1 mL of n-BuOH and morpholine (1.5 eqv) was added. The reaction was then heated at 140°C for 25 minutes. After that time, the reaction mixture was left reaching r.t and the solvent was removed by vacuum. The crude was added with acetone and a solid was filtered. The solid was then washed with hot water and with $Et_2O$ several times, obtaining the final products.

**2-morpholino-4-((3,4-dihydroxyphenyl)amino)furo[3,4-d]pyrimidin-7(5H)-one (FO09)**

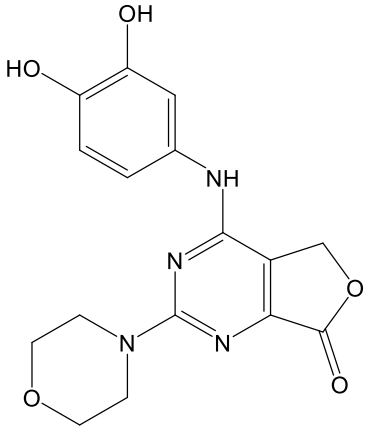


The product was obtained with the general procedure for the C2 substitution with morpholine as a light brown solid (Y=5%).

$^{1}$H-NMR (DMSO-$d_6$, 400 MHz, 25°C), ppm: 9.26 (s, 1H, NH); 9.02 (s, 1H, OH); 8.76 (s, 1H, OH); 7.11 (b, 1H, $CH_{arom}$); 6.89 (b, 1H, $CH_{arom}$); 6.70 (d, *J* = 8.5 Hz, 1H, $CH_{arom}$); 5.14 (b, 2H, $CH_2$), 3.67 (m, 8H, $CH_2$).

$^{13}$C-NMR (DMSO-$d_6$, 100.5 MHz, 25°C), ppm: 169.5, 163.7, 156.5, 150.9, 145.5, 142.7, 130.8, 115.8, 113.8, 111.1, 67.7, 66.5, 45.0.

ESI-MS: m/z = ($M+H^+$): 345.4

**2-morpholino-4-((3,4,5-trihydroxyphenyl)amino)furo[3,4-d]pyrimidin-7(5H)-one (FO10)**

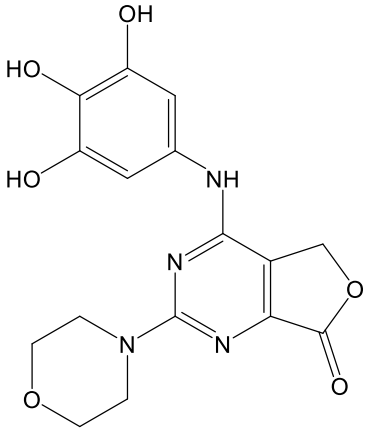


The product was obtained with the general procedure for the C2 substitution with morpholine as a light brown solid (Y=25%).

$^{1}$H-NMR (DMSO-$d_6$, 400 MHz, 25°C), ppm: 9.15 (b, 1H, NH); 8.94 (b, 2H, OH); 7.95 (b, 1H, OH); 6.66 (b, 2H, $H_{arom}$); 5.16 (b, 2H, $CH_2$), 3.68 (m, 8H, $CH_2$).

$^{13}$C-NMR (DMSO-$d_6$, 100.5 MHz, 60°C), ppm: 169.6, 163.8, 156.6, 150.9, 146.4, 130.6, 130.4, 115.7, 102.5, 67.8, 66.6, 45.1.

ESI-MS: m/z= ($M+H^+$): 361.3

E.A. calculated for $C_{16}H_{16}O_6N_4 \cdot 2/3\ H_2O$: C 51.61, H 4.69, N 15.05. Found: C 51.40, H 4.62, N 15.55.

**2-chloro-4-((3,4-dihydroxybenzyl)amino)furo[3,4-d]pyrimidin-7(5H)-one (FO11)**

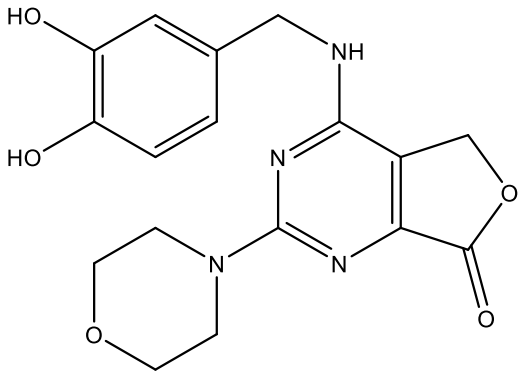


The product was obtained with the general procedure for the C2 substitution with morpholine as a light brown solid (Y=8%).

$^{1}$H NMR (400 MHz, DMSO-$d_6$, 25°C) δ 8.80 (b, 2H, OH), 8.19 (t, *J* = 5.6 Hz, 1H, NH), 6.73 (d, *J* = 2.0 Hz, 1H, $CH_{arom}$), 6.66 (d, *J* = 8.0 Hz, 1H, $CH_{arom}$), 6.60 (dd, *J* = 8.0, 2.0 Hz, 1H, $CH_{arom}$), 5.09 (s, 2H, $CH_2$), 4.42 (d, *J* = 5.6 Hz, 2H, $CH_2$), 3.65 (m, 8H, $CH_2$).

$^{13}$C NMR (101 MHz, DMSO-$d_6$, 25°C) δ 169.5 (Cq), 163.2 (Cq), 157.5 (Cq), 149.6 (Cq), 145.1 (Cq), 144.4 (Cq), 129.8 (Cq), 118.8 (CH), 115.5 (CH), 115.3 (CH), 115.0 (Cq), 67.2 ($CH_2$), 66.0 ($CH_2$), 44.3 ($CH_2$), 43.3 ($CH_2$).

ESI-MS: m/z= ($M+H^+$):

E.A. calculated for $C_{17}H_{18}O_5N_4 \cdot 1/2\ Et_2O$: C 57.73, H 5.09, N 14.17. Found: C 55.70, H 5.10, N 14.16.

# Chapter 6: **Repurposing of the 6,7-dihydroxyisoindolin-1-one scaffold for the inhibition of bunyavirus cap-snatching endonucleases**

## 6.1 Aim of the project

Bunyavirus endonucleases share several structural and functional similarities with influenza $PA_N$ endonuclease.[254] For this reason, various known chelating inhibitors of influenza endonuclease, such as DKAs and BXA, were successfully tested on bunyaviral endonucleases. These results confirmed that $PA_N$ endonuclease inhibitors could represent suitable candidates in the search for bunyaviral endonucleases inhibitors.

A series of 6,7-dihydroxyisoindolin-1-ones were first disclosed by Zao and co-workers[272] as metal-chelating HIV IN inhibitors. Subsequently, this scaffold (**Figure 6.1**) have been studied in this research group for the inhibition of influenza $PA_N$ endonuclease obtaining promising $IC_{50}$ values in the enzymatic assays (between 23.6-193 nM) and good inhibition of virus replication in cellular assays ($EC_{50}$ between 3.6-28 µM).[273]

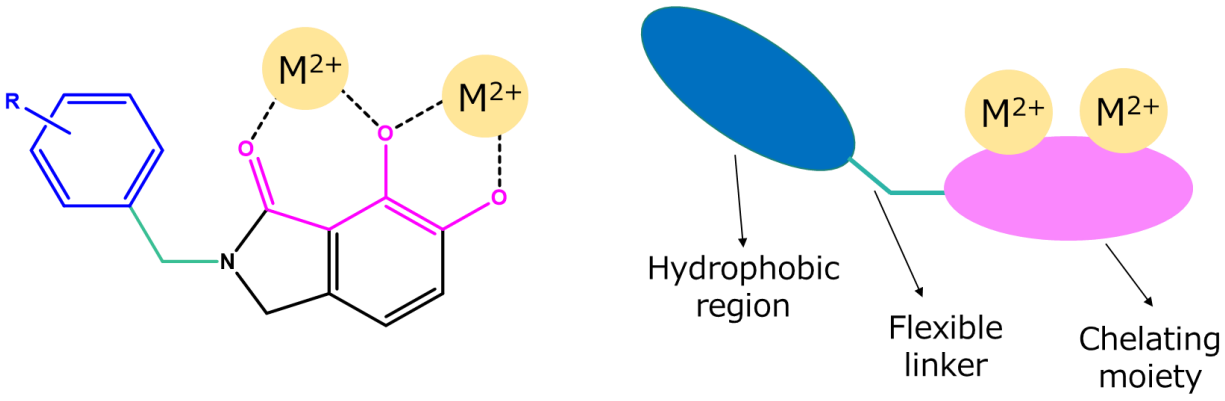


**Figure 6.1**. Structure and functionalities of the 6,7-dihydroxyisoindolin-1-one scaffold.

This pharmacophore bears a metal binding group composed by three coplanar donor oxygen atoms. The chelating moiety has a good affinity for Mg(II) and Mn(II) ions, the two possible metal cofactors of these enzymes. The rigidity and geometry of the chelating motif are functional to coordinate the two metal ions in the active site at the same time. Moreover, this scaffold has a lipophilic benzyl portion that can give further interactions with hydrophobic pockets found in the surroundings of the catalytic endonuclease site, and potentially enhance the inhibition activity. Finally, the flexible linker between the two parts of these molecules can facilitate conformation adjustments in the active sites to achieve more favourable interactions. All these interesting structural features can make this scaffold a suitable inhibitor of cap-snatching endonucleases, as demonstrated by extensive investigation on chelating inhibitors of $PA_N$.[274]

Taking all of this in consideration, the aim of this project is to try the repurposing of the 6,7-dihydroxyisoindolin-1-one scaffold, found active on $PA_N$ endonuclease, for the inhibition of different bunyaviruses endonucleases.

## 6.2 Results and discussion

### 6.2.1 Synthesis and characterization

The synthesis of these compounds was carried out following the procedure reported in the literature,[272] with slight modifications (**scheme 6.1**). In order to investigate the possible relationship between the chemical structures and the activity of these compounds, a panel of variously substituted dihydroxyisoindolin-1-ones were synthetized, expanding the set tested on influenza virus endonuclease.[273]

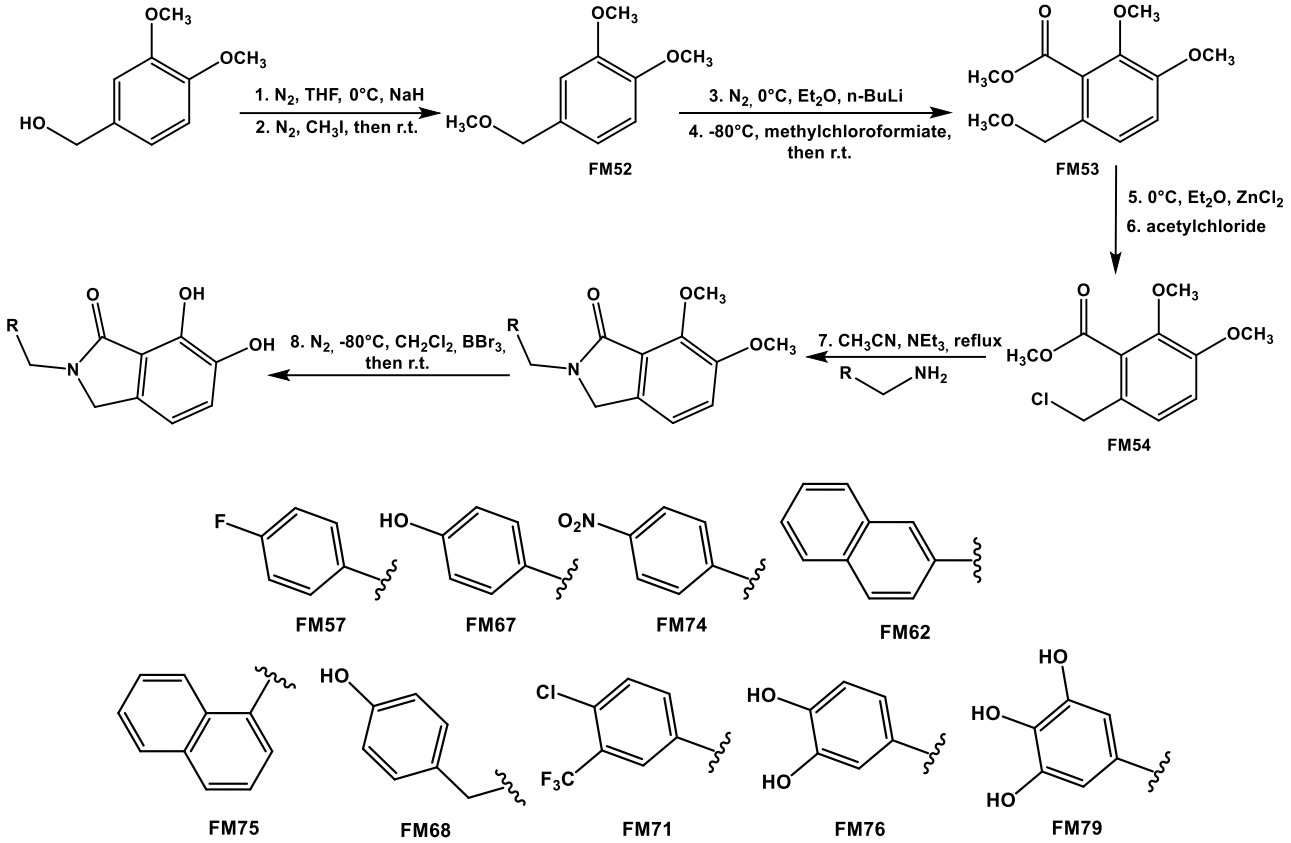


**Scheme 6.1** Synthetic route to the 6,7-dihydroxyisoindolin-1-ones.

First, the hydroxy group of 3,4-dimethoxybenzyl alcohol was converted to a methoxy functionality. The starting material was dissolved in dry THF, under $N_2$ atmosphere, and cooled to 0°C. NaH was added slowly to the solution, followed by iodomethane and the reaction was left at r.t. overnight. The product **FM52** was obtained after a chromatographic purification as colourless oil, with a 96 % yield.

The successful formation of the desired product was confirmed by the $^1$H-NMR spectra in $CDCl_3$, by the presence of the signal at 3.37 ppm relative to the methoxy group (**Figure 6.2**).

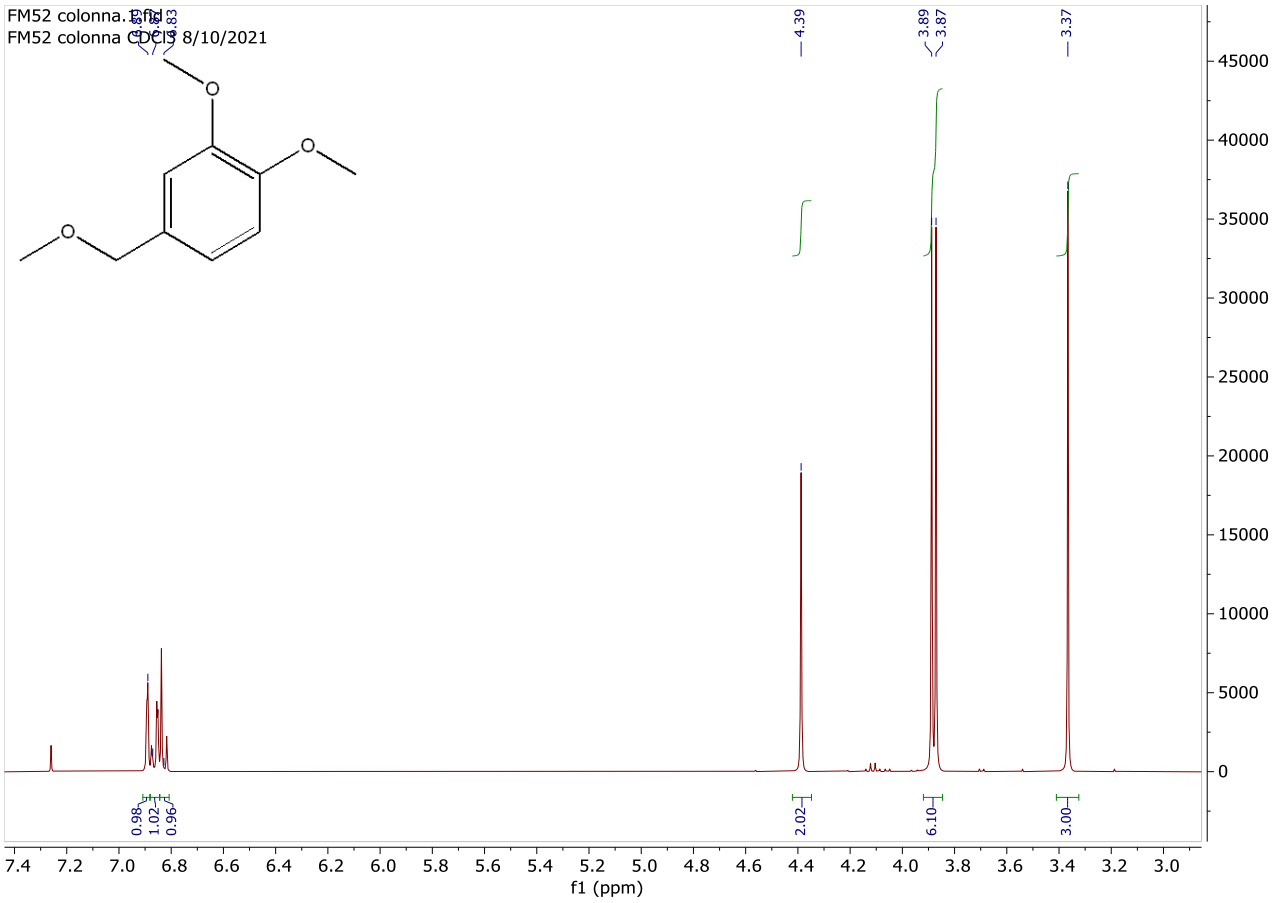


**Figure. 6.2** $^{1}$H NMR spectrum (25°C, 400 MHz, $CDCl_3$) of **FM52**

In the second step, **FM52** in dry $Et_2O$ was cooled to 0°C under $N_2$ atmosphere and n-Butyl lithium added dropwise to the solution. After 1 h, the reaction mixture was cooled to -80°C and methyl chloroformate was added dropwise to the lithiate intermediate. The reaction was left reaching r.t. and stirred overnight. After a water quenching and $Et_2O$ extraction, the crude was purified by a silica chromatographic column obtaining **FM53** as a pale orange oil.

The presence of the methylformate group was confirmed in the $^{1}$H-NMR spectrum of the compound by the disappearance of the signal of one aromatic proton and by the appearance of a signal at 3.92 ppm, corresponding to the newly inserted $OCH_3$. (**Figure 6.3**)

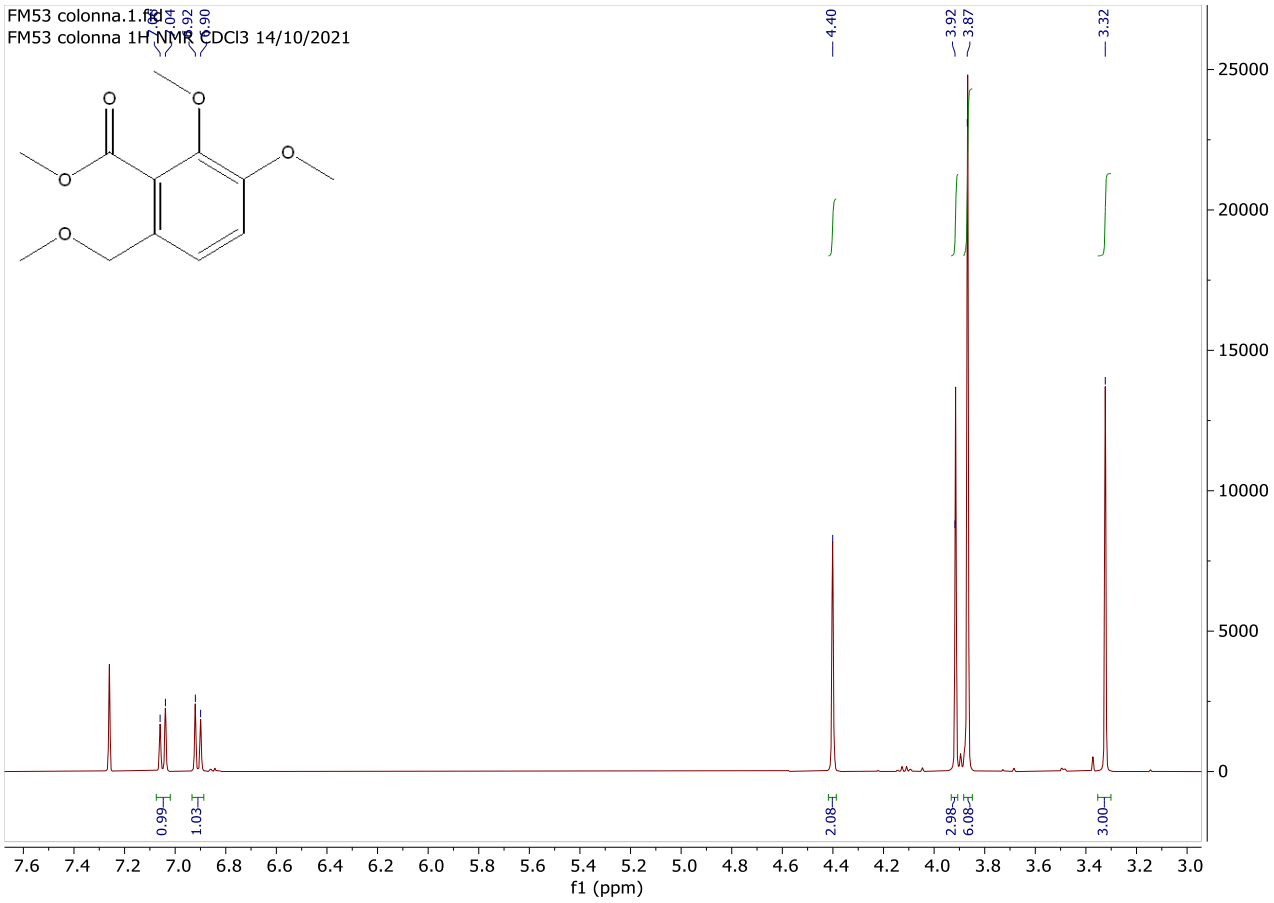


**Figure 6.3** $^{1}$H NMR spectrum (25°C, 400 MHz, $CDCl_3$) of **FM53**.

To obtain the chloride intermediate **FM54**, **FM53** was dissolved in dry $Et_2O$ and 0.15 equivalents of anhydrous $ZnCl_2$ were added. After cooling the mixture to 0°C, acetyl chloride was then added dropwise. After 30 minutes, $Al_2O_3$ was added in the flask and after filtration and chromatographic purification the desired product was obtained as a colourless oil.

As in the previous step, the $^{1}$H-NMR spectrum confirmed the success of the reaction, with the 3.32 ppm $OCH_3$ signal disappearance (**Figure 6.4**). ESI-MS analysis also confirmed the formation of **FM54**.

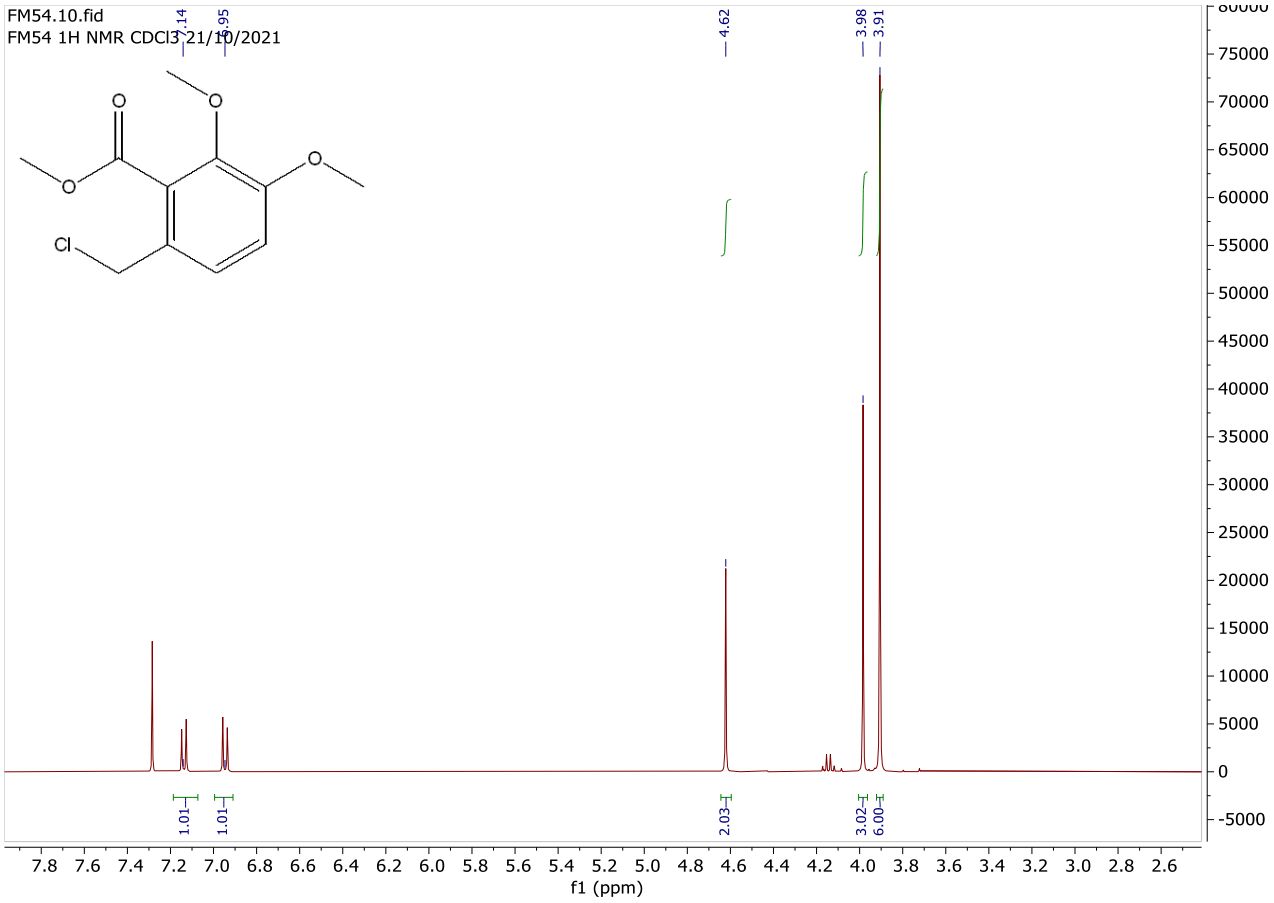


**Figure 6.4** $^{1}$H NMR spectrum (25°C, 400 MHz, $CDCl_3$) of **FM54**.

This compound was used as a common intermediate in the synthesis of all the final 6,7-dihydroxyisoindolin-1-ones. All reactions were conducted with a general procedure for the substitution and cyclization of **FM54** with differently substituted amines obtaining the 6,7-dimethoxyisoindolin-1-ones. To **FM54** in dry acetonitrile, 2 equivalents of $Et_3N$ and one equivalent of the proper amine were added, then the reaction was refluxed overnight. The 6,7-dimethoxy precursors were obtained after DCM/water extraction and chromatography purification, using different solvent mixtures adjusted on the single system.

These compounds were characterized via $^{1}$H and $^{13}$C NMR spectroscopy, AT-IR and ESI-MS. In **Figure 6.5** the $^{1}$H and $^{13}$C deptq NMR spectra of the newly synthetized compound **FM73** are reported as representative of the 6,7-dimethoxyisoindolin-1-ones.

The $^{1}$H spectrum is consistent with this class of compounds. In the aromatic region five proton signals are present, some of them partially overlapped. The signal at 4.62 ppm corresponds to the $CH_2$ within the heterocycle, the signal at 4.18 ppm to the benzylic $CH_2$, the two signals at 3.96 and 3.86 ppm to the methoxy groups.

The $^{13}$C spectrum, acquired through a deptq experiment (shown with Cq and $CH_2$ phased positively, CH and $CH_3$ phased negatively) also confirm the compound structure. The spectrum presents eight quaternary carbon signals, five CH signals between 119-115 ppm, two $OCH_3$ signals (61.8 and 56.4 ppm) and two $CH_2$ signals (47.9, 44.9 ppm).

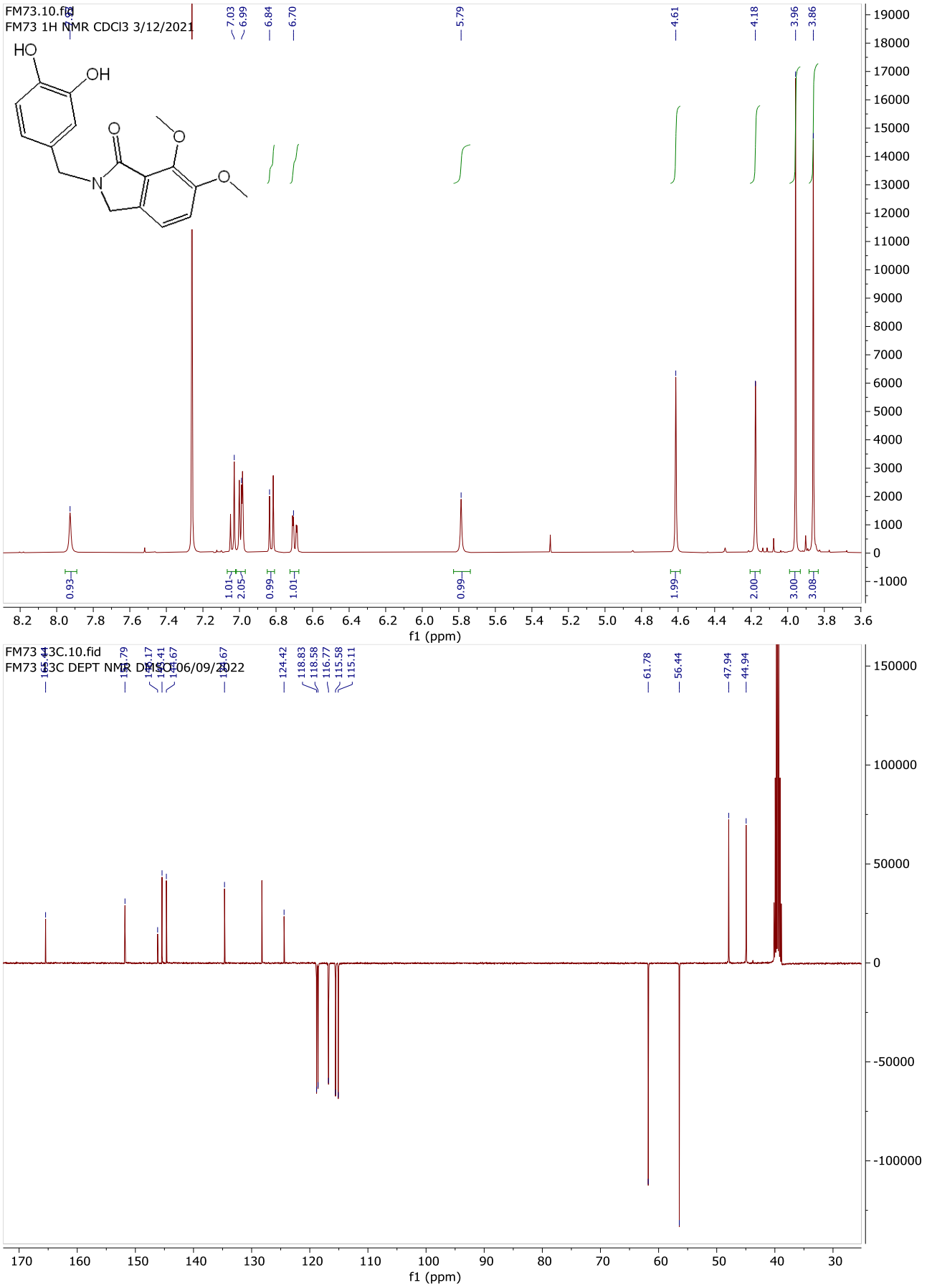


**Figure 6.5** $^{1}$H-NMR (25°C, 400 MHz, $CDCl_3$) and $^{13}$C deptq (25°C, 101 MHz, DMSO-$d_6$) NMR spectra of **FM73**.

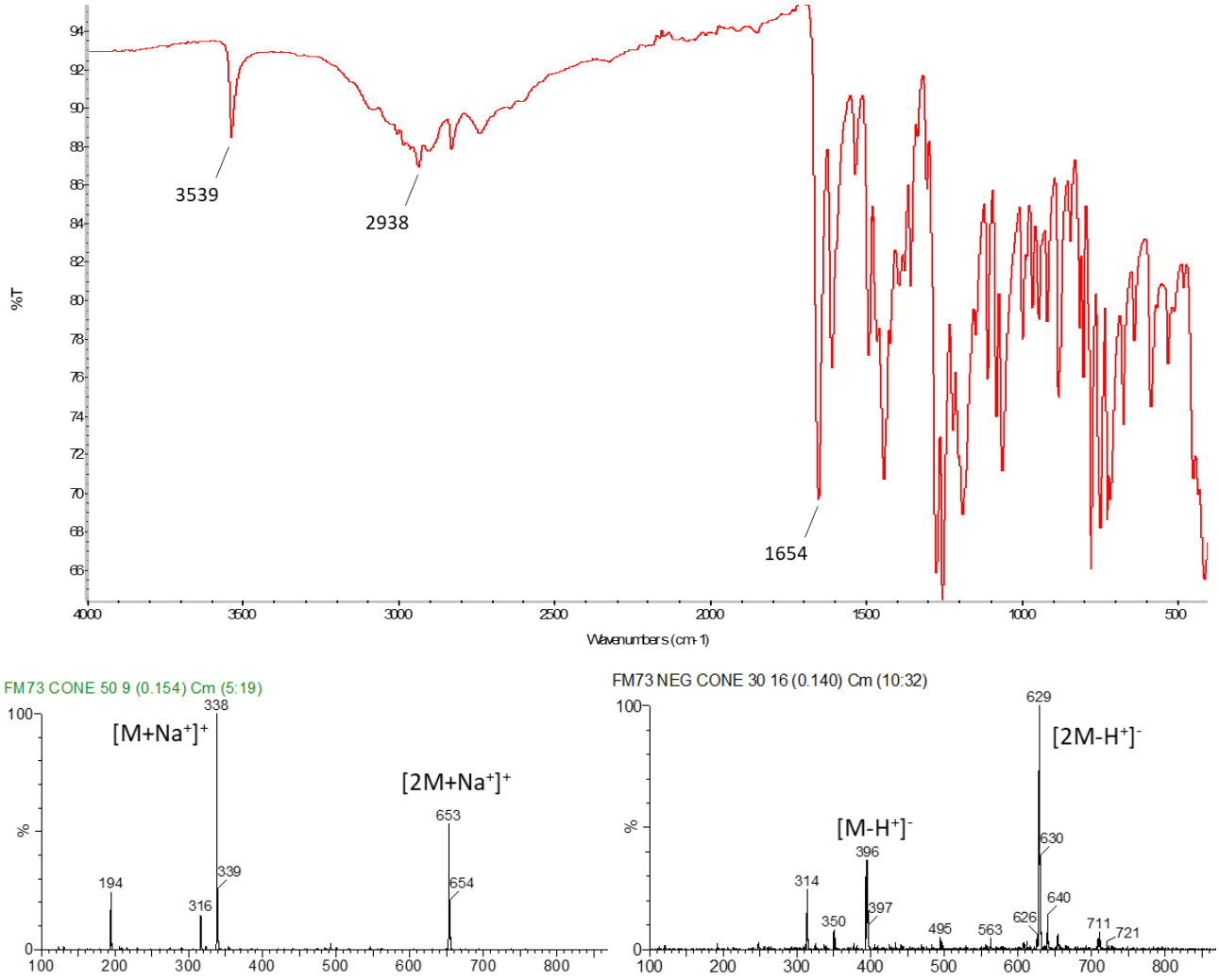


**Figure 6.6** (top) FT-IR and (bottom) ESI-MS spectra for **FM73** (on the right positive ionization 50 eV, on the left negative ionization 30 eV).

In the IR spectrum of **FM73** (**Figure 6.6**, top) it is possible to observe the stretching band relative to the O-H at 3539 $cm^{-1}$, the stretching of aromatic C-Hs between 3000 and 2900 $cm^{-1}$ and the C=O stretching band at 1654 $cm^{-1}$.

In the ESI-MS spectra (**Figure 6.6**, bottom) it is possible to observe peaks of **FM73** molecular ions in both positive (338: $[M+Na^+]^+$) and negative ionization mode (314: $[M-H^+]^-$). In the ESI-MS spectra in both ionization modes are present also peaks related to the dimeric adducts (positive: $[2M+Na^+]^+$ 653 m/z; negative $[2M-H^+]^+$ 629 m/z).

Once these compounds were synthetized and their structure confirmed, demethylation reactions were performed, to obtain the final 6,7-dihydroxyisoindolin-1-ones. To a dry DCM solution of the appropriate 6,7-dimethoxyisoindolin-1-one derivative (1eqv), cooled to -50°C, a solution of $BBr_3$ (8 eqv) in dry DCM was slowly added, then the reaction was left reaching r.t. and stirred overnight under $N_2$. After MeOH quenching and $Et_2O$/water extraction, the final products were recovered without any further purifications.

These compounds, as well for their methoxy forms, were characterized by $^1H$ and $^{13}C$ NMR spectroscopy, AT-IR and ESI-MS. Additionally, elemental analyses were conducted. In **Figure 6.7** and **6.8** are reported, as an example, experimental spectra for the newly synthetized **FM76**, obtained from precursor compound **FM73**.

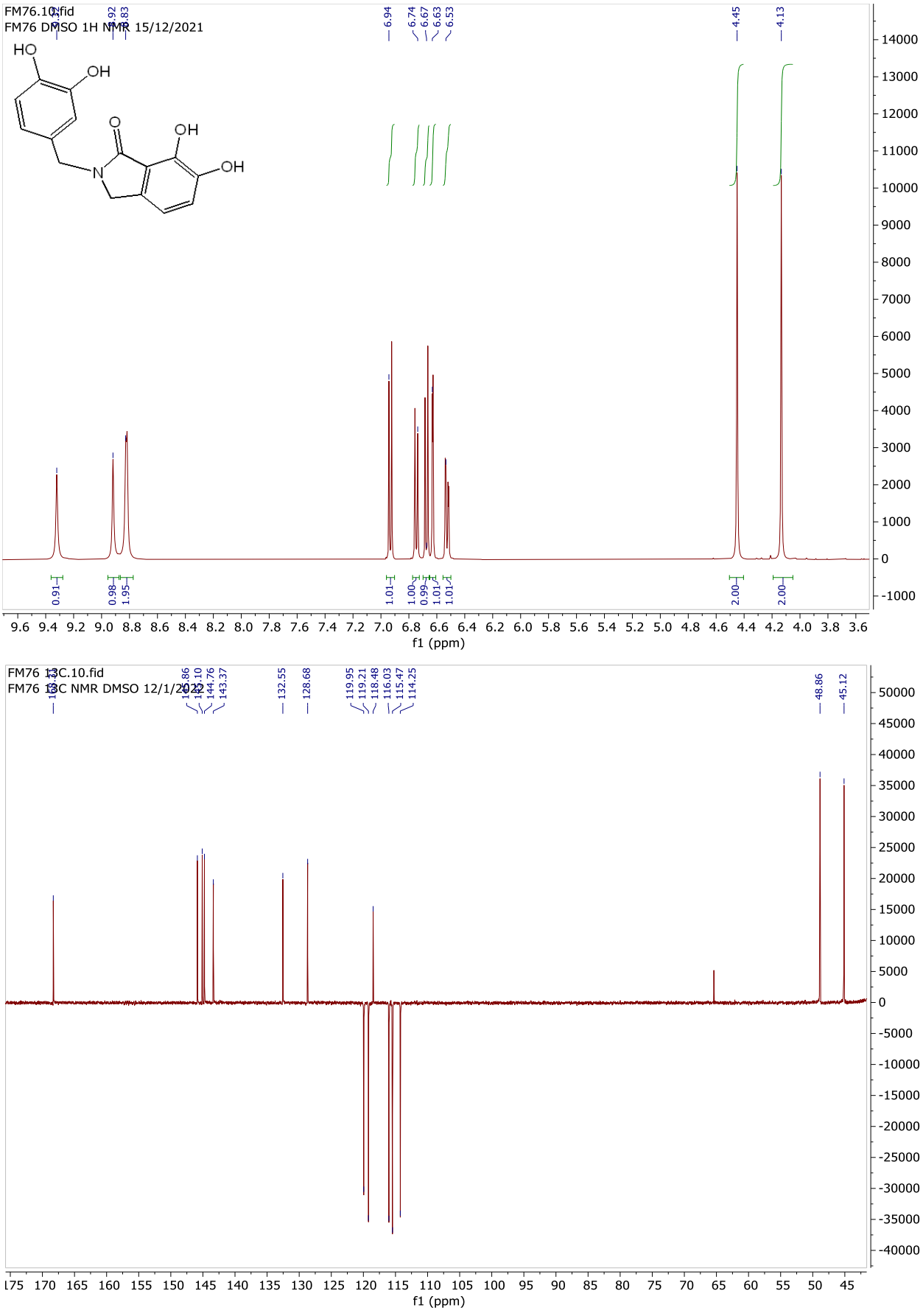


**Figure 6.7** $^{1}$H NMR (25°C, 400 MHz, DMSO-$d_6$) and $^{13}$C deptq (25°C, 101 MHz, DMSO-$d_6$) NMR spectra of **FM76**.

In the $^{1}H$ spectrum of **FM76** (**Figure 6.7**) there are no signals between 3.6 and 4.0 ppm, confirming the successful removal of the methoxy groups. Moreover, the presence of broad signals in the range 8.8-9.4 ppm corroborates the presence of 4 hydroxyl groups in the molecule.

In the $^{13}C$ deptq spectrum of **FM76**, as well, the $OCH_3$ signals between 65 and 75 ppm disappeared, confirming the success of the reaction.

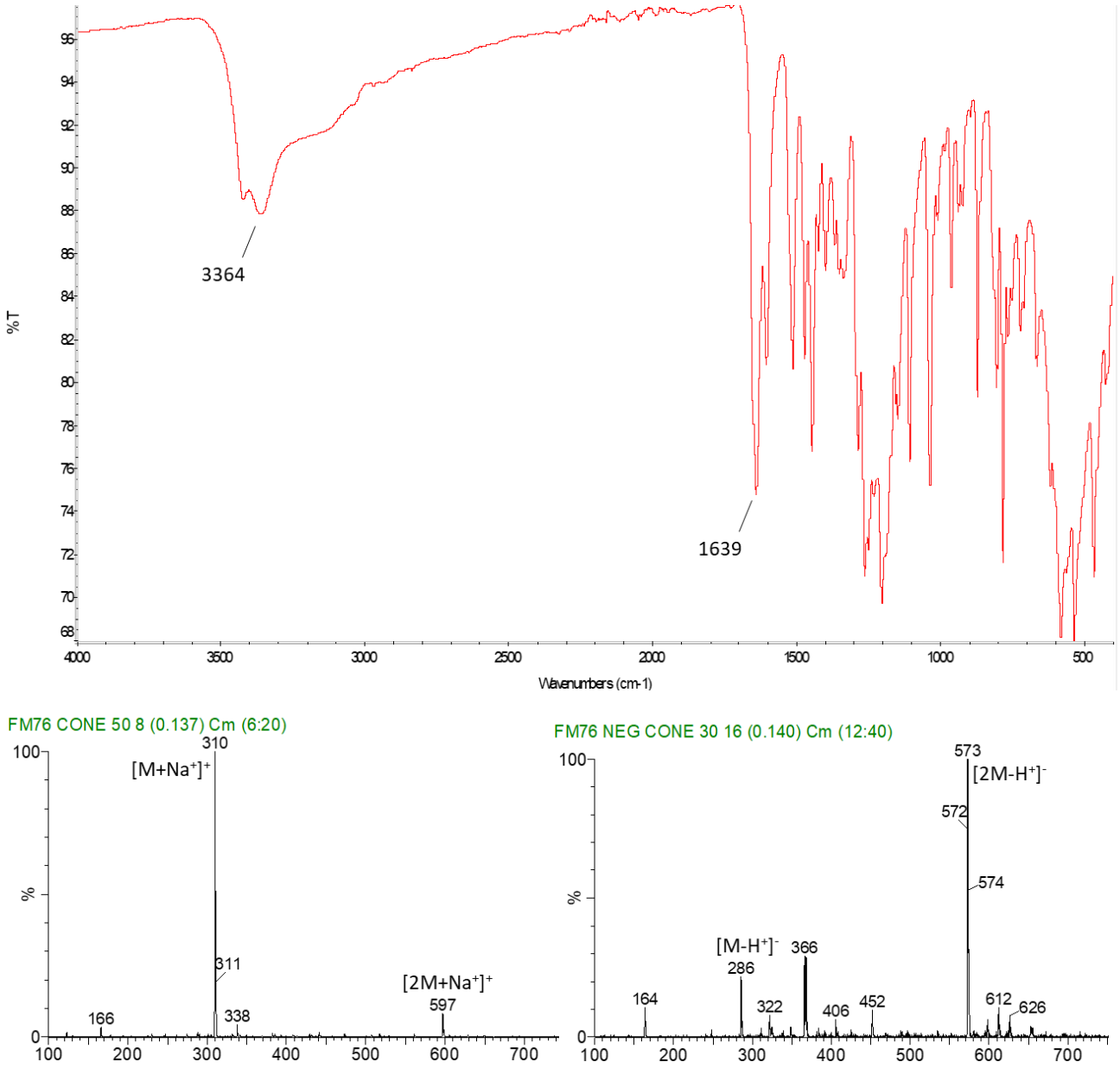


**Figure 6.8** (top) FT-IR and (bottom) ESI-MS spectra for **FM76** (on the right positive ionization 50 eV, on the left negative ionization 30 eV).

In the IR spectrum of **FM76** (**Figure 6.8**) is noticeable another O-H stretching band at 3364 $cm^{-1}$, that was not present in the **FM73** spectrum, suggesting the presence of further OH groups.

In **FM76** ESI-MS spectra (**Figure 6.8**) the molecular ion peak is visible in both positive (310: $[M+Na^+]^+$) and negative ionization mode (286: $[M-H^+]^-$). As in **FM73** and many other compounds of this class, it was possible to observe in both ionization modes also peaks related to the dimeric adducts (positive 597 m/z, negative 573 m/z).

Synthesis of compound **FM79** was not successful, so a slightly different approach was followed (**Scheme 6.2**).

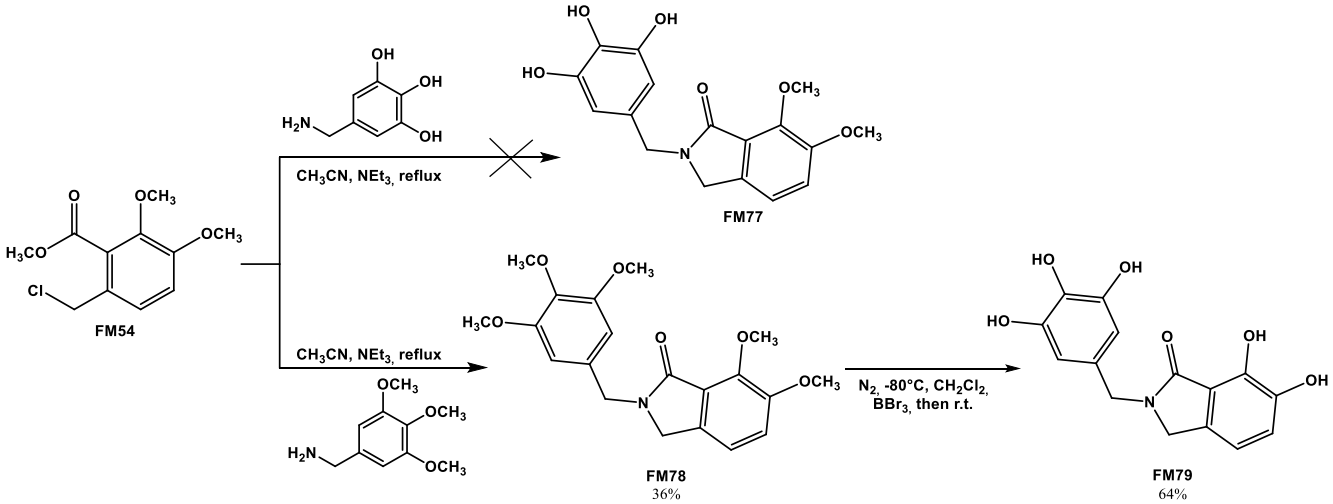


**Scheme 6.2** Synthesis of compound **FM79**

First, 3,4,5-trihydroxybenzylamine · HBr was prepared from the commercially available 3,4,5-trimethoxybenzylamine via demethylation by using $BBr_3$. Then, **FM54** was reacted with this benzylamine, through the general procedure for the synthesis of the dimethoxy isoindolinones. After leaving the reaction overnight, the TLC check of the reaction indicated the presence of many species. A chromatographic column (DCM:MeOH:$NH_4OH_{solution}$ 12:1:0.05 → DCM:MeOH:$NH_4OH_{solution}$ 9:1:0.05) did not succeed in isolating the desired product **FM77**.

It was then decided to synthetized compound **FM78** with 3,4,5-trimethoxybenzylamine and then remove the 5 methyl groups all in once.

**FM78** was synthetized with the general procedure previously disclosed and purified from the crude with a silica column (EtOAc). **FM78** was then treated with 15 eqv of $BBr_3$ in dry DCM. After quenching, during the $Et_2O$/water extraction the precipitation of a white solid was observed in the organic phase. This solid was filtered and dried and after NMR checking it resulted to be compound **FM79**, obtained with 64% yield. Precipitation in $Et_2O$ was observed due to the lower product solubility probably caused by the presence of the five OH groups in this compound.

Compound **FM79** was then completely characterised by usual spectroscopic techniques and $^1$H-NMR spectrum is shown in **Figure 6.9**.

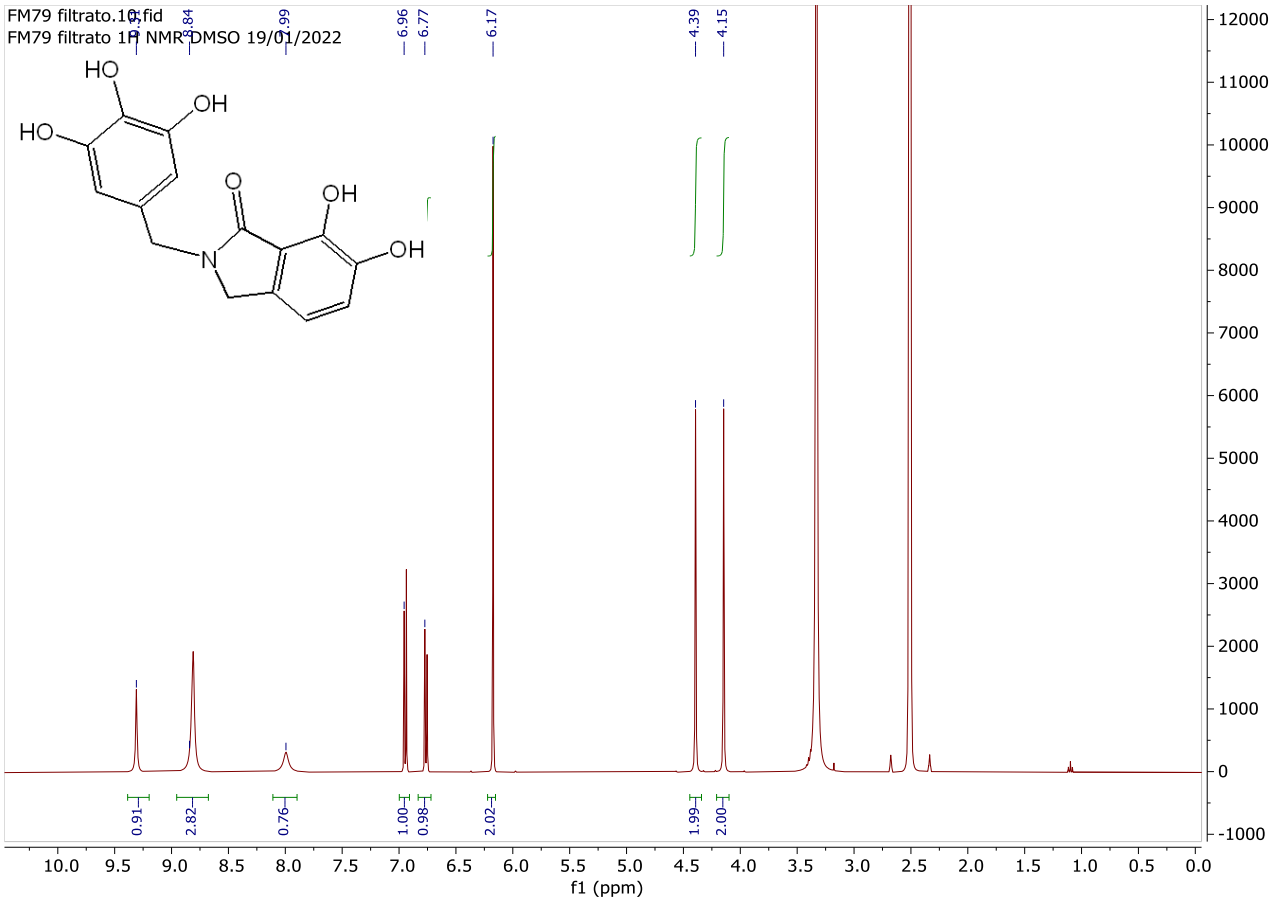


**Figure 6.9** $^{1}$H-NMR spectrum (25°C, 400 MHz, DMSO-$d_6$) of compound **FM79.**

### 6.2.2 Studies in solution

The interaction between the ligand **FM67** and the divalent cations Mg(II) or Mn(II) was studied in solution by means of visible spectrophotometric titrations, in order to determine binding affinities of the 6,7-dihydroxyisoindolin-1-ones scaffold for the two ions, and to verify if there is a binding preference for one of the two ions.

The spectrophotometric titrations of the ligand solutions with solutions of the metal salts were carried out in HEPES buffer and NaCl solution at pH 7.5, in MeOH:$H_2O$ 9:1 (v:v) (see experimental section for details). HEPES has been described to have a weak but competing role in the complexation of the metal ions[275] and therefore the apparent formation constants are expected to be close to the conditional ones.

The UV-visible spectrum of ligand **FM67** revealed two absorption bands at ca. 307 nm and 250 nm (blue line, **Figure 6.10**). Titrations were performed on 80 µM ligand solutions with addition of the metal ion, up to 50:1 metal:ligand ratio. As a general trend, with the addition of the metal ions a band at ca. 340-345 nm appeared with both $Mg^{2+}$ and $Mn^{2+}$, as a consequence of the complex species formation. Upon the addition of the metal, a decreased of the band at 307 nm (associated to the free ligand) was also observed.

Increase of Mn(II) ions concentration was followed by a decrease in the 307 nm band and by the appearance of an absorption at 345 nm, whose value reached a plateau after the addition of 25 equivalents of Mn(II) (**Figure 6.10**).

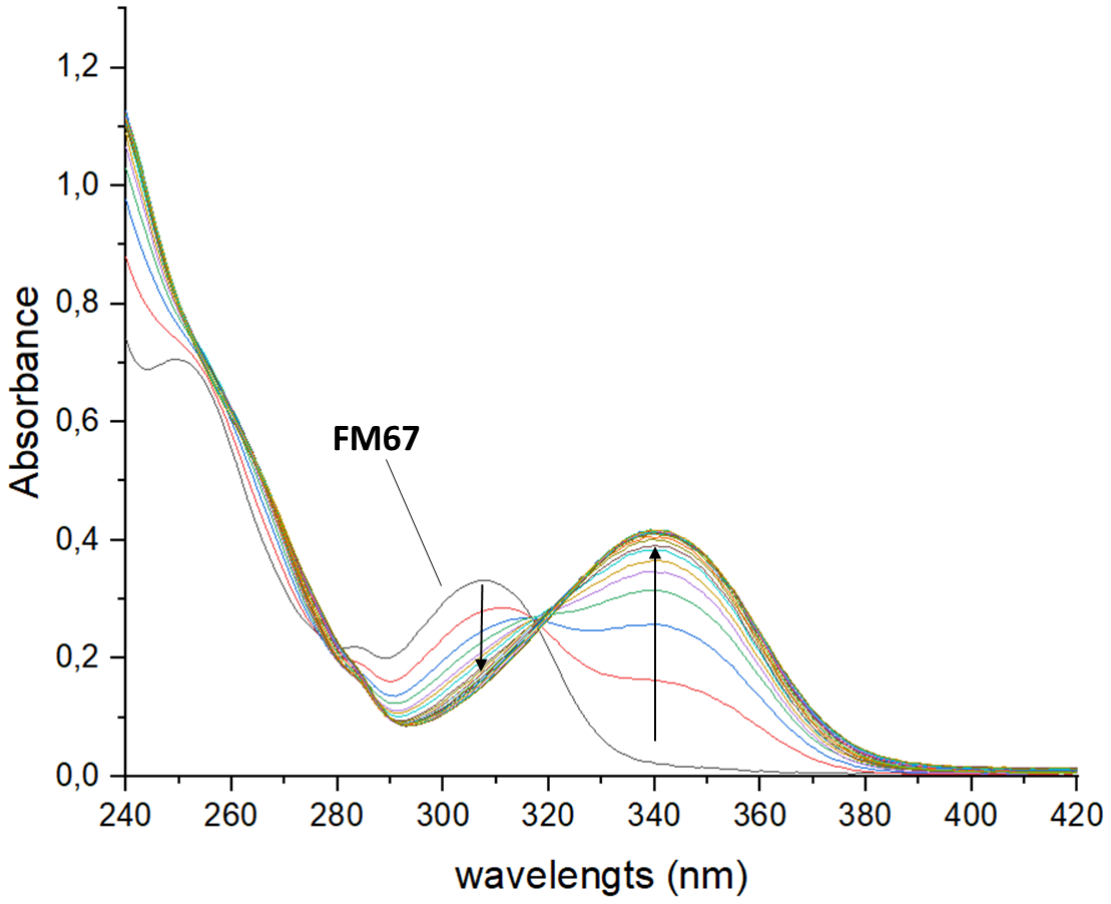


**Figure 6.10.** UV-visible spectra for the titration of **FM67** with $MnCl_2$ in MeOH:$H_2O$ 9:1 (v/v) at pH 7.5 (HEPES 50 mM buffer, NaCl 50 mM. $C_L$ = 80 µM. ligand:metal = 1:0-1:50)

Spectral data treatment suggests a sequential binding with the formation first of a 1:1 [MnL] species, followed by the coordination of a second Mn ion and the formation in solution of a dinuclear [$Mn_2L$] species. The calculated molar absorption UV spectra of the formed MnL and $Mn_2L$ species is reported in **Figure 6.11**. This experimental data set leads to the calculation of the formation constants reported in **Table 6.1**.

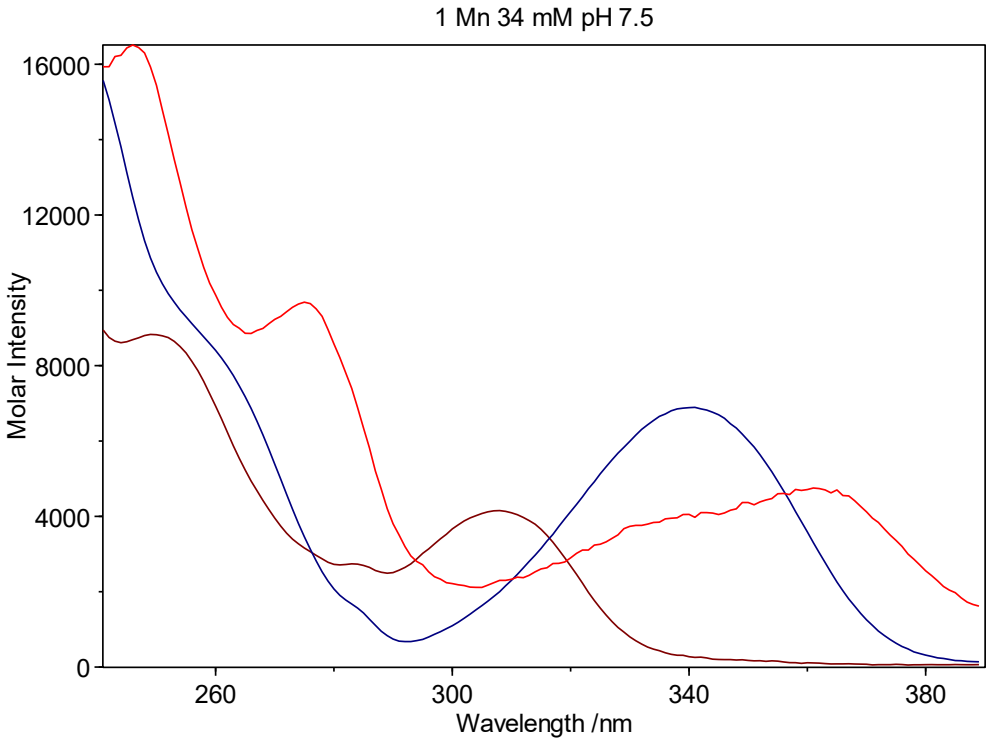


**Figure 6.11** Molar absorption UV spectra of **FM67** (L, dark red), [MnL] (blue, calculated) and [$Mn_2L$] (light red, calculated).

Similarly to what observed for Mn(II), the addition of Mg(II) ions to the ligand resulted into the decrease of the band at 307 nm with appearance of a band at 340 nm. The appearance of this band required the addition of higher amounts of Mg(II), indicating a lower affinity of **FM67** for this metal ion respect to $Mn^{2+}$ (**Figure 6.12**).

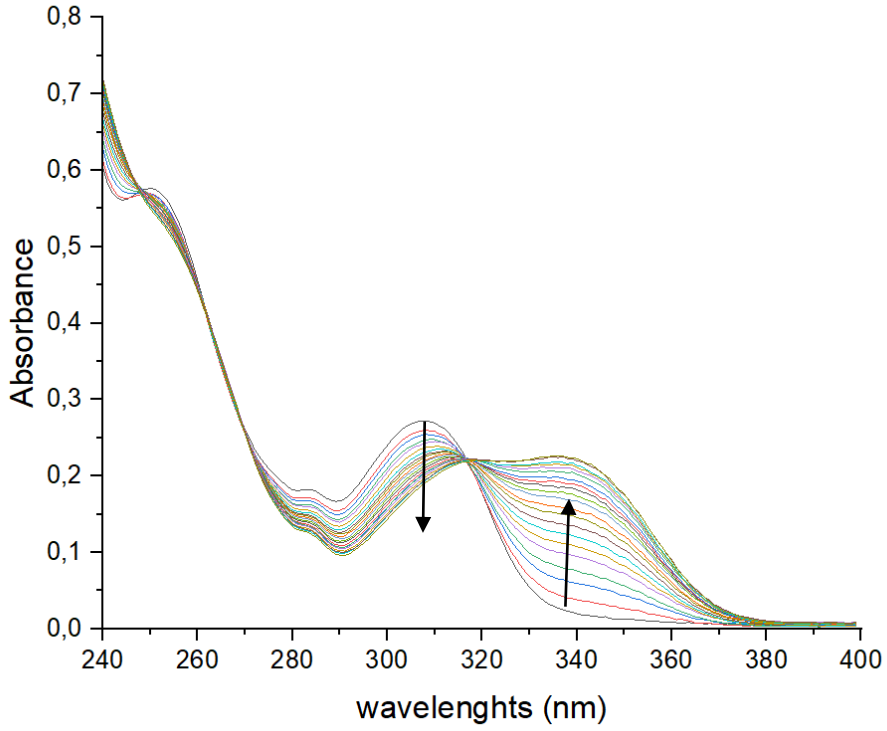


**Figure 6.12** UV-visible spectra for the titration of **FM67** with $MgCl_2$ in MeOH:$H_2O$ 9:1 (v/v) at pH 7.5 (HEPES 50 mM buffer, NaCl 50 mM. $C_L$ = 80 µM. ligand:metal = 1:0-1:50)

Spectral data treatment revealed the formation of a mononuclear 1:1 [MgL] species, but differently from Mn(II), it suggests no formation of a [$Mg_2L$] species. The calculated molar absorption UV spectra of the formed [MgL] species is reported in **Figure**. (**Figure 6.13**).

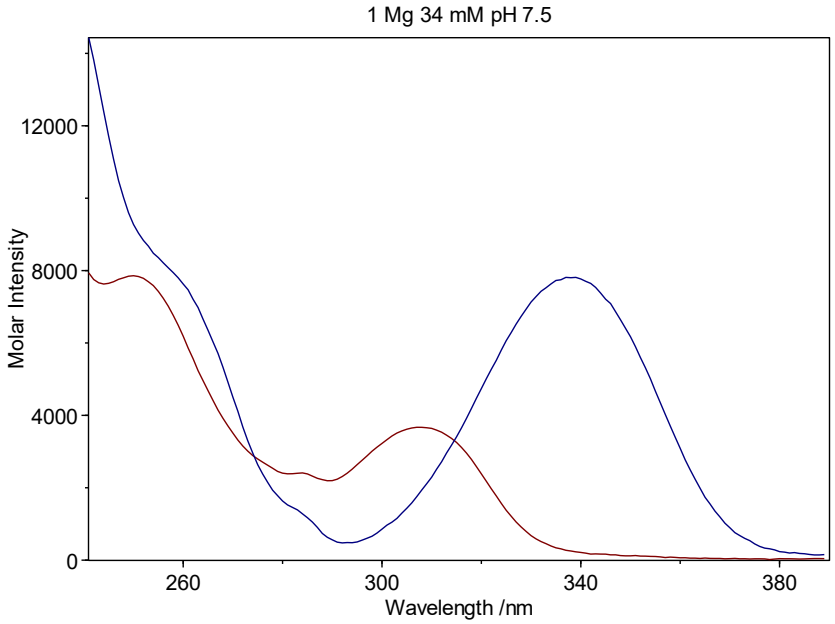


**Figure 6.13** Molar absorption UV spectra of L (red) and [MgL] (blue, calculated)

The fitting between the calculated absorbance value vs the experimental values observed during **FM67** titrations with Mn(II) and Mg(II) was satisfactory, as it can be notice in **Figure 6.14** This indicates that the calculated predictions should effectively describe the experimental behavior in these conditions.

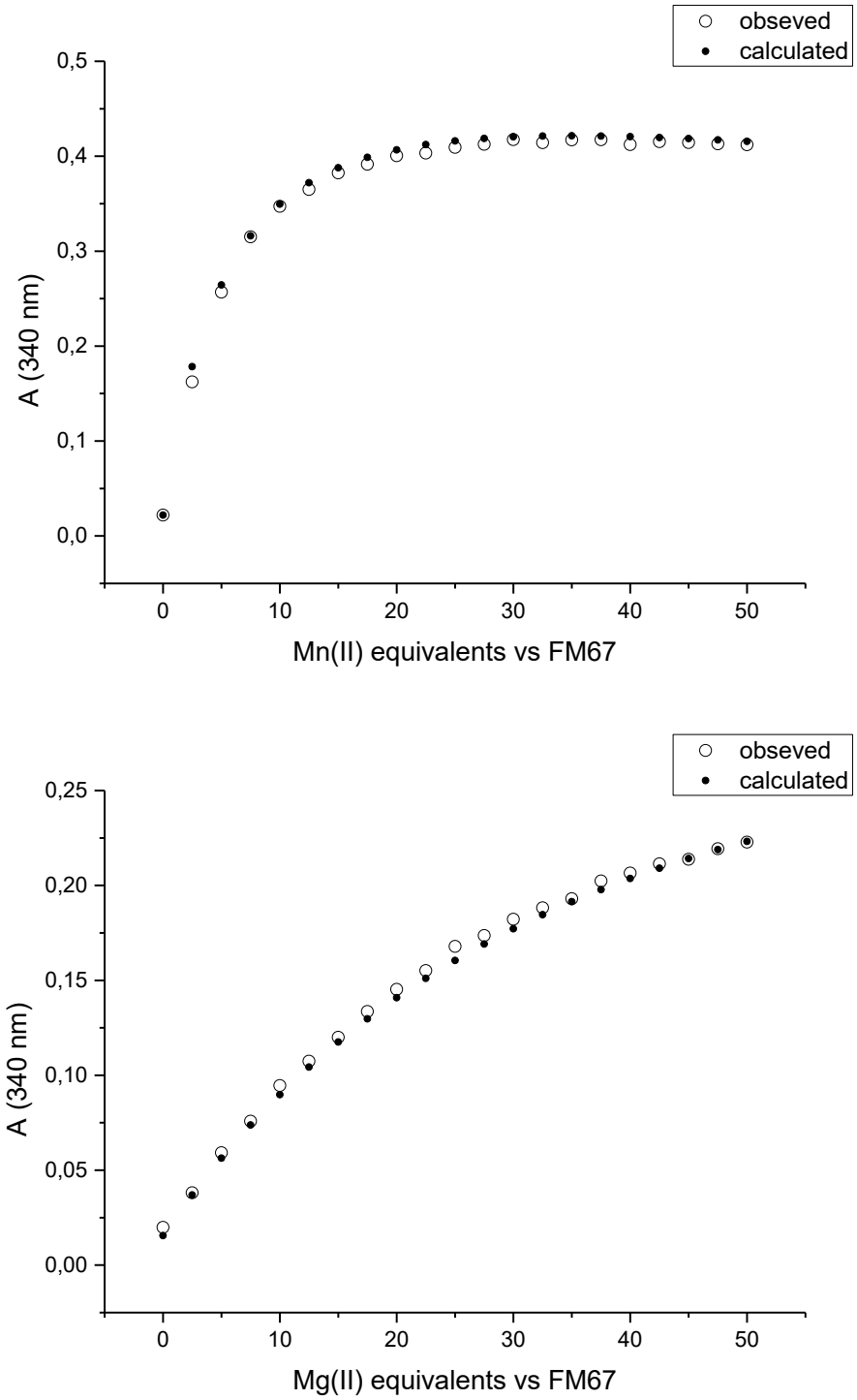


**Figure 6.14** Comparison between experimental A values at 340 nm acquired during **FM67** titration (0 to 50 M:L ratio) and calculated A values at 340 nm for Mn(II) titration (top) and Mg(II) titration (bottom).

The formation constants of [MgL], [MnL] and [$MnL_2$] are reported in **Table 6.1**.

Overall, the equilibrium studies allowed to establish the formation constant values of the complexes of **FM67** with Mg(II) and Mn(II). The results indicate that the formation of the of the Mn(II) complexes is more favorable than the Mg(II) complexes, implying a better affinity of the ligand **FM67** towards Mn(II) ions compared to Mg(II) ions.

| | **Mn(II)** | **Mg(II)** |
|---|---|---|
| **[ML]** | 3.37 ± 0.01 | 2.31 ± 0.01 |
| **[$M_2L$]** | 5.19 ± 0.01 | - |

**Table 6.1.** Logarithms of the complex formation constants of the Mn(II) and Mg(II) complex species with ligand **FM67** in HEPES buffer (50 mM, pH 7.5) and NaCl (50 mM) in MeOH:$H_2O$ 9:1 at 25 °C. Standard deviations are reported in parentheses.

### 6.2.3 Enzymatic activity

Enzymatic activity evaluation was performed by Prof. Stephen Gunther and Dr. Yaiza Fernandez Garcia's research group at the Bernhard Nocht Institute for Tropical Medicine, in Hamburg.

A FRET-based nuclease-monitoring assay was used to calculate the half maximal inhibitory concentration ($IC_{50}$) of the 6,7-dihydroxyisoindolin-1-ones (**Scheme 6.3**) against ANDV (Andes Virus) and TOSV (Toscana Virus) Cap-Endonucleases. All the synthetized dihydroxyisoindolin-1-ones were tested, in addition to compounds **JBSD109**, **JBSD110** and **JBSD113**, previously synthetized for the $PA_N$ influenza screening.

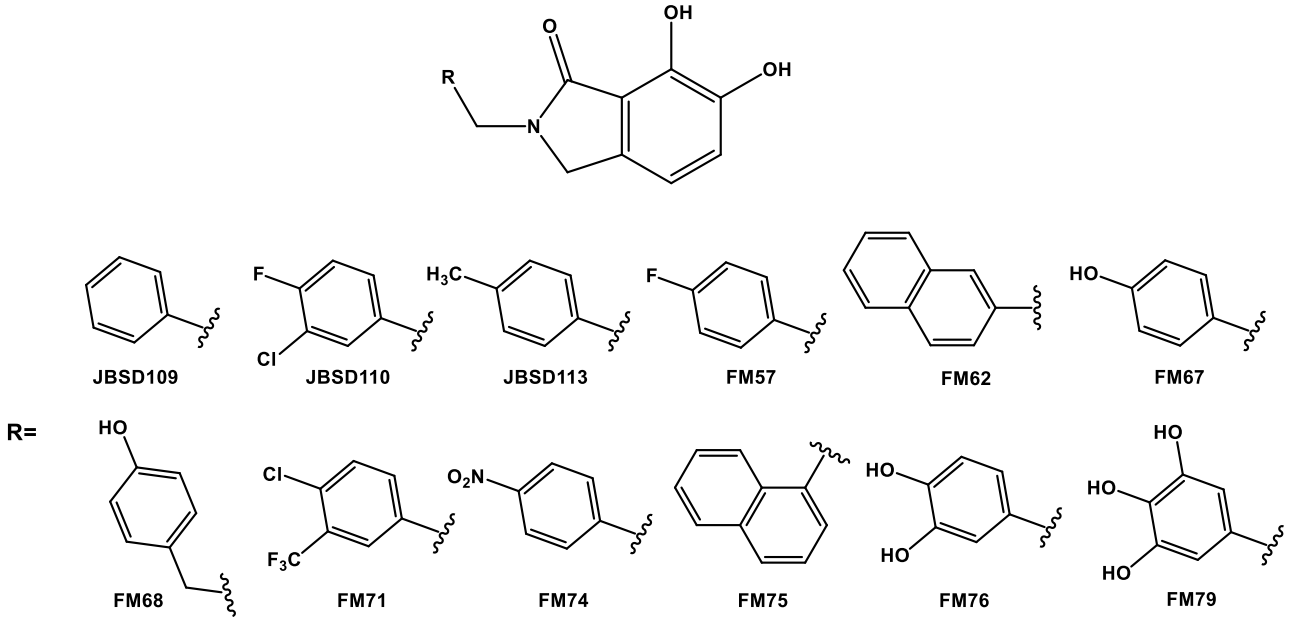


**Scheme 6.3** Chemical structures of the tested 6,7-dihydroxyisoindolin-1-ones compounds.

Serial dilutions of the compounds were preincubated for 15 minutes with the proteins, then the reactions were initiated by the addition of a ssRNA substrate labelled at the 5' end with fluorophore and the 3' end with quencher. The fluorescence signal was measured every 10 seconds for 20 minutes at 490 nm and 515 nm for excitation and emission, respectively.

In **Table 6.2** are reported the $IC_{50}$ values of the compounds.

| | ANDV_L1-200_N167A | | | TOSV_L1-211 | | |
|---|---|---|---|---|---|---|
| | $IC_{50}$ (µM) | 95% CI | $r^2$ | $IC_{50}$ (µM) | 95% CI | $r^2$ |
| **JBSD109** | 0.95 | 0.5 to 1.77 | 0.89 | 5.86 | 3.42 to 10.53 | 0.88 |
| **JBSD110** | 7.64 | 4.95 to 19.83 | 0.87 | 3.86 | 1 to 5.90 | 0.70 |
| **JBSD113** | 6.41 | 3.14 to 13.15 | 0.81 | 1.35 | 0.60 to 3.58 | 0.81 |
| **FM57** | 1.96 | 1.31 to 8.92 | 0.83 | 5.41 | 2.88 to 8.96 | 0.86 |
| **FM62** | 1.93 | 1.17 to 3.14 | 0.91 | 5.09 | 1.69 to 14.12 | 0.71 |
| **FM67** | 1.60 | 1.03 to 2.46 | 0.88 | 1.02 | 0.63 to 1.64 | 0.93 |
| **FM68** | 1.06 | 0.71 to 1.59 | 0.95 | 6.46 | 4.33 to 17.72 | 0.87 |
| **FM71** | 1.25 | 0.94 to 2.01 | 0.93 | 6.95 | 3.41 to 18.15 | 0.83 |
| **FM74** | 6.05 | 4.37 to 12.8 | 0.69 | 4.00 | 2.54 to 15.94 | 0.85 |
| **FM75** | 3.76 | 3.11 to 4.5 | 0.97 | 7.80 | 3.88 to 17.19 | 0.73 |
| **FM76** | 0.46 | 0.37 to 0.58 | 0.98 | 2.37 | 1.48 to 3.76 | 0.92 |
| **FM79** | 1.51 | 1 to 2.24 | 0.94 | 0.91 | 0.63 to 1.33 | 0.95 |

**Table 6.2** $IC_{50}$ values (µM) of the tested compounds on the inhibition of TOSV and ANDV Cap-endonuclease. The half-maximal inhibitory concentration was calculated by fitting the dose-response curves using a four parameters nonlinear regression.

Interestingly, all compounds showed activity in the low micromolar range towards the investigated enzymes. Variation of the $IC_{50}$ values were observed, although in the same order of magnitude, for the different benzylic portions of the isoindolinones. Overall, the best results on the two enzymes were obtained for **FM67**, **FM76** and **FM79**, bearing respectively one, two and three hydroxyl groups on the aromatic moiety. Hence, it is possible to hypothesise a role of the hydroxyl groups on the aromatic portion, that may interact with amino-acidic residues nearby the active site of the enzyme. The other compound of this series bearing a hydroxy group, **FM68**, displayed an interesting $IC_{50}$ value towards ANDV Cap-Endo (1.06 µM); however, its activity towards TOSV Cap-Endo resulted six-fold weaker. These results suggest that the presence of a longer spacer between the isoindolinone scaffold and the aromatic moiety do not guarantee an ideal broad-activity on the tested enzymes. Furthermore, it was detected a general slightly stronger inhibition of the tested compound on ANDV Cap-Endo compared to TOSV Cap-Endo.

The inhibitory activity of the tested compounds on ANDV and TOSV endonucleases, if compared to the inhibition from the screening of the same scaffold on influenza (nanomolar range), results lower.[273] The decreased activity in bunyaviruses compared to influenza could be caused by the less significant scaffold interactions with the surrounding residues of the active site. This can be due to the wider active site pocket present in several bunyaviral endonuclease compared to $PA_N$ endonuclease, especially for TOSV.[258] Thus, the inhibition activity exerted by these compounds (between 0.46-7.80 µM) could be caused primarily by the metal cofactor chelation.

Nonetheless, the 6,7-dihydroxyisoindolin-1-ones panel shows an effective and consistent inhibition towards both ANDV and TOSV Cap-endonuclease, suggesting that the scaffold is suitable for the development of improved candidates.

## 6.3 Conclusions

In this part of the PhD project, a panel of variously substituted 6,7-dihydroxyisoindolin-1-ones was synthetized and characterized. Furthermore, the interaction between the model compound **FM67** and the divalent cations Mg(II) or Mn(II) in solution was studied by means of visible spectrophotometric titrations, in order to determine the binding constants. These data suggest that for **FM67** the formation of Mn(II) complexes is more favorable than the Mg(II) complexes, implying a better affinity of the 6,7-dihydroxyisoindolin-1-ones towards Mn(II) ions compared to Mg(II) ions. These results confirm the idea that this scaffold is suitable for the coordination of the two metal ions that constitute the endonuclease cofactors (*in vivo* and *in vitro*).

Finally, the enzymatic activity of the synthetized compound was tested on two different Cap-Endonucleases of the *Bunyavirales* order (ANDV and TOSV). All the compounds exhibited inhibition activity towards the investigated enzymes, with $IC_{50}$ values in the low micromolar range, therefore demonstrating the successful repurposing of this chemical scaffold for the inhibition of bunyaviral endonucleases.

## 6.4 Experimental

### 6.4.1 Materials and methods

#### 6.4.1.1 Chemistry

All reagents of commercial quality were purchased from Sigma-Aldrich and used without further purification. The purity of the synthesized compounds was determined by elemental analysis and verified to be ≥ 95%.

NMR spectra were recorded on a Bruker Advance spectrometer operating at 400 MHz for the $^{1}H$ and at 101 MHz for $^{13}C$ nuclei, at 25°C. All chemical shifts are expressed in ppm.

The ATR-IR spectra were recorded by means of a Nicolet-Nexus (Thermo Fisher) spectrophotometer by using a diamond crystal plate in the range of 4000-400 $cm^{-1}$.

Elemental analyses were performed by using a FlashEA 1112 series CHNS/O analyser (Thermo Fisher) with gas-chromatographic separation.

Electrospray mass spectral analyses (ESI-MS) were performed with an electrospray ionization (ESI) time-of-flight Micromass 4LCZ spectrometer. Samples were dissolved in methanol. MS spectra were acquired with a DSQII Thermo Fisher apparatus, equipped with a single quadrupole analyser in positive EI mode, by means of a DEP-probe (Direct Exposure Probe) equipped with a Re-filament.

The UV-vis spectra were collected using a Thermo Evolution 260 Bio spectrophotometer provided with a thermostating Peltier device, and quartz cuvettes with 1 cm path length.

#### *6.4.1.2* UV-visible spectrophotometric titrations

The pH was measured using a Thermo Orion 720A pH-meter connected with a Hamilton glass electrode. A 0.1 M KCl solution in $CH_3OH$:$H_2O$ 9:1 (*v/v*) was used to fill the reference compartment of the electrode.[276] Calibration of the glass electrode using buffers in $CH_3OH$:$H_2O$ 9:1 (v/v) solutions was performed immediately before its use.[277] Stock solutions of ligand **FM67** (C = *ca*. 2 mM) have been prepared by weight in $CH_3OH$:$H_2O$ 9:1 (*v/v*) and used within few days. Stock solutions of $MnCl_2 \cdot 4\ H_2O$ and $MgCl_2 \cdot 6\ H_2O$ in $CH_3OH$:$H_2O$ 9:1 (*v/v*) ($C_{Mn}$ *ca.* 0.034 M, $C_{Mg}$ *ca.* 0.034 M) were prepared by weight of the salts. A solution of HEPES 50 mM buffer, NaCl 50 mM in $CH_3OH$:$H_2O$ 9:1 (*v/v*) at pH=7.5 was prepared as follows: HEPES (298 mg) and NaCl (73 mg) were dissolved in 25 mL of a $CH_3OH$:$H_2O$ 9:1 (*v/v*) mixture. Few drops of concentrated aqueous NaOH solution (5 N) was added until pH 7.5 was reached and dissolution of HEPES obtained.

The complex formation equilibria at pH=7.5 for **FM67** with Mn(II) and Mg(II) were studies by direct spectrophotometric titrations of a ligand solution with the metal ions, as follows. Solutions of the ligand ($C_L$ ca. 80 µM) were prepared in the cuvette by diluting 100 µML of ligand stock solution in HEPES 50 mM buffer, NaCl 50 mM, $CH_3OH$:$H_2O$ 9:1 (*v/v*), pH=7.5. Total volume of samples in the cuvette was *ca*. 2.5 mL. The obtained ligand solutions were titrated with $MnCl_2 \cdot 4\ H_2O$ or $MgCl_2 \cdot 6\ H_2O$ solutions up to a metal:ligand ratio of 50:1. For each addition of titrant, the absorption spectrum was collected in the 220-600 nm range. All titrations were performed in duplicate. The logarithms of the stability constants were calculated from the spectral dataset using the HypSpec2014 software.[278][279] For each system, data from

different titrations were treated together. In all other titrations the molar spectrum of the ligand has been used as the only fixed parameter. Speciation diagrams were calculated using the Hyss 2009 software.[280]

#### 6.4.1.3 Protein production

Cap-ENDOs reported in the literature from ANDV[270] and TOSV[258] containing an N-terminal His-tag followed by a TEV protease recognition site (ENLYFQ*S) were expressed in *E. coli* strain BL21 Gold (DE3) at 17°C overnight using LB medium supplemented with 0.5 mM isopropyl-β-D-thiogalactopyranoside for induction. The pelleted cells were resuspended in lysis buffer and disrupted by sonication on ice. Subsequent soluble fractions were incubated with Ni-NTA agarose resin under constant stirring for 30 min at 4°C. Proteins bound to the resin were eluted with 500 mM imidazole concentrations. Next, the eluted proteins were incubated with His-tagged TEV protease overnight at 4°C during dialysis against TEV buffer. The reaction mixtures were then loaded onto HisTrap HP columns, and the flow-throughs containing the untagged proteins were concentrated to inject into a size-exclusion Superdex 200 column.

Proteins: i) ANDV Cap-ENDO in buffer 20 mM NaCit pH 5.5, 500 mM NaCl and 1 % glycerol, ii) TOSV Cap-ENDO in buffer 10 mM HEPES pH 7.5, 150 mM NaCl, 1 % glycerol and 2 mM TCEP.

#### 6.4.1.4 FRET-based nuclease-monitoring enzymatic assays

A fluorescence resonance energy transfer (FRET)-based nuclease monitoring assay was used to examine the ability and potency of compounds to inhibit the RNA hydrolysis catalyzed by *Bunyavirales* biochemically active Cap-ENDOs. Serial dilutions of compounds were pre-incubated for 15 min with 0.25 µM of the corresponding enzymes in a mixture consisting of 50 mM Tris-HCl pH 7.5, 50 mM NaCl, 5% glycerol, 0.05 U/µl RNasin (Promega) and 10 mM $MnCl_2$. The reactions were initiated by the addition of 1 µM of a 12mer poly(A) ssRNA substrate labeled at the 5' end with fluorophore 6-FAM and the 3' end with quencher BHQ-1 (Biomers). The fluorescence signal was measured every 10 s for 20 min in a 96 multiwell plate format at wavelengths 490 nm and 515 nm for excitation and emission, respectively. The initial velocity of the reactions ($V_0$) was determined as the slope of the linear phase of the progress curves, and the percentages of the enzymatic activity were plotted against the concentrations of the compounds on a semilogarithmic graph. The half maximal inhibitory concentration ($IC_{50}$) was calculated using a sigmoidal four-parameter nonlinear regression analysis performed by GraphPad Prism version 9.5.0 for macOS (GraphPad Software, www.graphpad.com). The maximum and minimum values were constrained to be 100 and 0 %, respectively. While the goodness-of-fit of the data points to the nonlinear regression model was defined by the coefficient of determination ($r^2$), the precision of the $IC_{50}$ estimates was determined by the asymmetrical 95% confidence interval (CI).

6.4.2 Chemistry

***1,2-dimethoxy-4-(methoxymethyl)benzene*** **(FM52)**

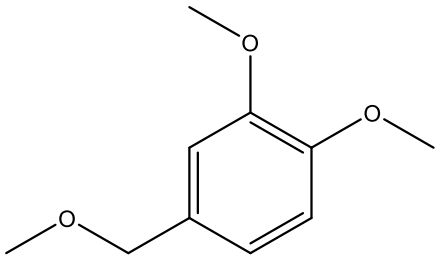

3,4-dimethoxybenzyl alcohol (5 mL, 33.0 mmol, 1 eqv) was dissolved in dry THF (30 mL), under $N_2$ atmosphere, and was cooled to 0°C. NaH 60% (1.718g, 42.9 mmol, 1.3 eqv) was added portion-wise to the solution and was left reacting at 0°C for 30 min. After that time, $CH_3I$ (2.7 mL, 42.9 mmol, 1.3 eqv) was added slowly and the reaction mixture was stirred at r.t. overnight. The reaction was quenched with iced-water and EtOAc was added. The aqueous phase was extracted three times with EtOAc. The combined organic phase was washed with brine, dried over $Na_2SO_4$, filtered and dried by vacuum. The residue was purified by silica column chromatography (AcOEt:Hex 1:1) to give the product as a colorless oil (5.752g, Y=96%).

$^1$H NMR (400 MHz, $CDCl_3$, 25°C) δ 6.89 (d, *J* = 1.8 Hz, 1H, $CH_{arom}$), 6.86 (dd, *J* = 8.0, 1.8 Hz, 1H, $CH_{arom}$), 6.83 (d, *J* = 8.0 Hz, 1H, $CH_{arom}$), 4.39 (s, 2H, $CH_2$), 3.89 (s, 3H, $CH_3$), 3.87 (s, 3H, $CH_3$), 3.37 (s, 3H, $CH_3$).

$^{13}$C NMR (125 MHz, $CDCl_3$, 25°C) δ 149.1, 148.7, 130.8, 120.4, 111.1, 110.9, 74.7, 58.0, 56.0, 55.9.

***Methyl-2,3-dimethoxy-6-(methoxymethyl)benzoate*** **(FM53)**

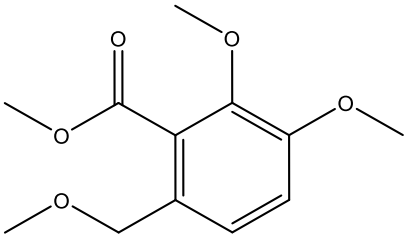

**FM52** (3.9 g, 21.4 mmol, 1 eqv) was dissolved in 50 mL of dry $Et_2O$, under $N_2$ atmosphere, and was cooled to 0°C. n-butyl lithium (2.5 M in hexane solution) (9.8 mL, 24.6 mmol, 1.15 eqv) was added dropwise to the solution. The reaction was left stirring at 0°C for 1 h. After that time, the solution was cooled to -80°C and methyl chloroformate (7.8 mL, 100.6 mmol, 4.7 eqv) was added dropwise. The reaction was left reaching r.t. and stirred overnight. Water was added until the solution appears colourless and the organic phase was separated. The aqueous phase was extracted once with $Et_2O$. The combined organic phase was dried over $Na_2SO_4$, filtered and dried by vacuum. The residual oil was purified by silica column chromatography (Hex:EtOAc 6:4) obtaining the product as a pale orange oil (4.411 g, Y=86%).

$^1$H NMR (400 MHz, $CDCl_3$, 25°C) δ 7.06 (d, *J* = 8.4 Hz, 1H, $CH_{arom}$), 6.91 (d, *J* = 8.4 Hz, 1H, $CH_{arom}$), 4.35 (s, 2H, $CH_2$), 3.92 (s, 3H, $CH_3$), 3.87 (s, 6H, $CH_3$), 3.32 (s, 3H, $CH_3$).

$^{13}$C NMR (125 MHz, $CDCl_3$, 25°C) δ 186.8, 167.9, 152.4, 128.4, 128.1, 124.3, 113.3, 72.2, 61.7, 58.3, 56.0, 52.3.

***Methyl 6-(chloromethyl)-2,3-dimethoxybenzoate* (FM54)**

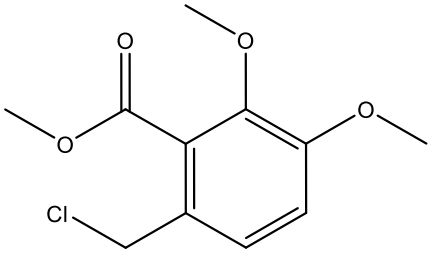

**FM53** (6.160 g, 25.6 mmol, 1 eqv) was dissolved in 25 mL of dry $Et_2O$, under $N_2$ atmosphere, and anhydrous $ZnCl_2$ (0.52 g, 3.85 mmol, 0.15 eqv). The solution was cooled to 0°C and acetyl chloride (6 mL, 25.6 mmol, 3.3 eqv) was added dropwise. The reaction was left stirring for 30 min, then 6 g of $Al_2O_3$ were added in the flask. The mixture was filtered on a small pad of $Al_2O_3$ and the solvent was removed by vacuum. The residue was purified by silica column chromatography (Hex:EtOac 7:3) obtaining the product as a colourless oil (5.573 g, Y=89%).

$^1$H NMR (400 MHz, $CDCl_3$, 25 °C) δ 7.11 (d, *J* = 8.4 Hz, 1H, $CH_{arom}$), 6.92 (d, *J* = 8.4 Hz, 1H, $CH_{arom}$), 4.60 (s, 2H, $CH_2$), 3.96 (s, 3H, $CH_3$), 3.88 (s, 6H, $CH_3$).

$^{13}$C NMR (125 MHz, $CDCl_3$, 25 °C) δ 167.3, 153.2, 146.9, 128.8, 127.5, 125.9, 113.5, 61.7, 56.0, 52.6, 43.8.

***General procedure 1 for the synthesis of 6,7-dimethoxyisoindolin-1-ones*:**

**FM54** (1 eqv) was dissolved in dry acetonitrile, under $N_2$ atmosphere, and $Et_3N$ was added (2 eqv). An equimolar amount of proper amine was added, and the reaction was heated up to reflux overnight. The solvent was then removed by vacuum and the residue was portioned between DCM and water. The aqueous phase was extracted 3 times with DCM and the combined organic phase was dried with $Na_2SO_4$, filtered and dried by vacuum. The residue was purified by silica column chromatography, with different solvent mixtures.

***2-(4-fluorobenzyl)-6,7-dimethoxyisoindolin-1-one* (FM55)**

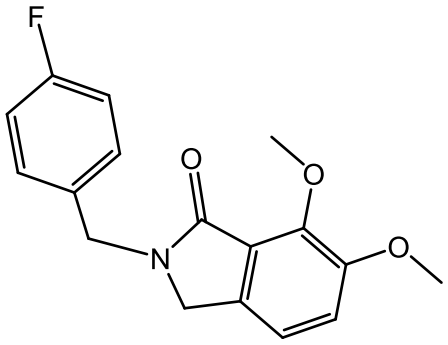

The product was obtained with the general procedure 1 and purified by column chromatography (EtOac:Hex 7:3) as a white powder (Y= 38%).

$^1$H NMR (400 MHz, $CDCl_3$, 25°C) δ 7.28 (m, 2H, $CH_{arom}$), 7.07 (d, *J* = 8.1 Hz, 1H, $CH_{arom}$), 7.00 (m, 3H, $CH_{arom}$), 4.76 (s, 2H, $CH_2$), 4.15 (s, 2H, $CH_2$), 4.11 (s, 3H, $CH_3$), 3.89 (s, 3H, $CH_3$).

$^{13}$C NMR ($CDCl_3$, 125 MHz, 25°C) δ 166.8, 163.3, 161.4, 152.5, 147.4, 134.5, 133.1 (d, J =3.0 Hz), 130.0 (d, J = 8.8 Hz), 124.8, 118.0, 116.6, 115.8, 115.6, 62.6, 56.8, 48.5, 45.7.

HR ESI-MS: m/z= ($M+Na^+$): 324.10

***2-(naphthalen-2-ylmethyl)-6,7-dimethoxy-isoindolin-1-one*** **(FM56)**

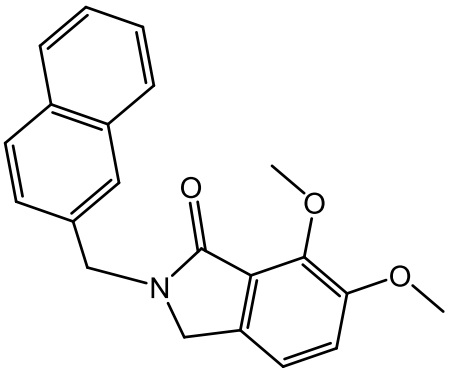

The product was obtained with the general procedure 1 and purified by column chromatography (EtOac:Hex 7:3) as a white powder (Y= 64%).

$^{1}$H NMR (400 MHz, $CDCl_3$, 25°C) δ 7.81 (m, 2H, $CH_{arom}$), 7.75 (s, 1H, $CH_{arom}$), 7.46 (m, 3H, $CH_{arom}$), 7.06 (d, *J* = 8.2 Hz, 1H, $CH_{arom}$), 6.98 (d, *J* = 8.2 Hz, 1H, $CH_{arom}$), 4.91 (s, 2H, $CH_2$), 4.18 (s, 2H, $CH_2$), 4.15 (s, 3H, $CH_3$), 3.89 (s, 3H, $CH_3$).

$^{13}$C NMR ($CDCl_3$, 125 MHz, 25°C) δ 166.9, 152.5, 147.5, 134.7, 134.6, 133.4, 132.9, 128.8, 127.8, 127.1, 126.4, 126.3, 126.1, 125.0, 117.9, 116.6, 62.7, 56.9, 48.6, 46.6.

HR ESI-MS: m/z= ($M+Na^+$): 356.12

***2-(4-hydroxybenzyl)-6,7-dimethoxyisoindolin-1-one*** **(FM64)**

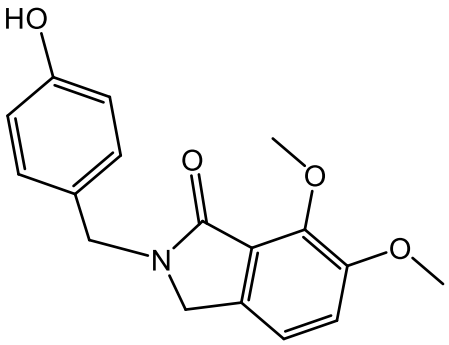

The product was obtained with the general procedure 1 and purified by column chromatography (EtOac:Hex 9:1 → EtOAc) as a white powder (Y= 68%).

$^{1}$H NMR (600 MHz, $CDCl_3$, 25°C) δ 7.15 (m, 2H, $CH_{arom}$), 7.06 (d, *J* = 8.1 Hz, 1H, $CH_{arom}$), 7.00 (d, *J* = 8.1 Hz, 1H, $CH_{arom}$), 6.80 (m, 2H, $CH_{arom}$), 5.85 (b, 1H, OH), 4.66 (s, 2H, $CH_2$), 4.16 (s, 2H, $CH_2$), 4.10 (s, 3H, $CH_3$), 3.88 (s, 3H, $CH_3$).

$^{13}$C NMR (125 MHz, $CDCl_3$, 25°C) δ 167.0, 156.1, 152.4, 147.3, 134.6, 129.6, 128.4, 124.9, 122.5, 118.0, 116.7, 115.9, 62.6, 56.9, 48.7, 46.1.

HR ESI-MS: m/z= ($M+Na^+$): 322.10

***2-(4-hydroxyphenethyl)-6,7-dimethoxyisoindolin-1-one*** **(FM66)**

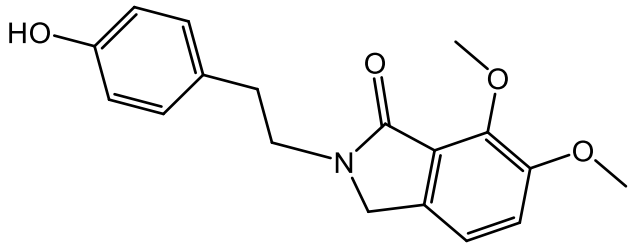


The product was obtained with the general procedure 1 and purified by column chromatography (EtOac:Hex 9:1 → EtOAc) as a white powder (Y= 68%).

$^{1}$H NMR (400 MHz, $CDCl_3$ 25°C) δ 7.06–6.99 (m, 4H, $CH_{arom}$), 6.78 (d, 2H, $CH_{arom}$), 6.29 (s, b, OH), 4.13 (s, 2H, $CH_2$), 4.05 (s, 3H, $OCH_3$), 3.87 (s, 3H, $OCH_3$), 3.76 (t, 2H, $CH_2$), 2.87 (t, 2H, $CH_2$).

$^{13}$C NMR (125 MHz, $CDCl_3$, 25°C) δ 167.1, 155.0, 152.4, 147.4, 134.6, 130.3, 129.8, 125.1, 117.8, 116.6, 115.7, 62.6, 56.9, 49.7, 44.4, 33.9.

**2-(4-chloro-3-(trifluoromethyl)benzyl)-6,7-dimethoxyisoindolin-1-one (FM69)**

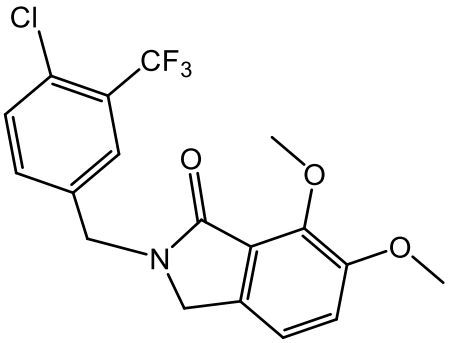


The product was obtained with the general procedure 1 and purified by column chromatography (EtOac:Hex 7:3) as a white powder (Y= 56%).

$^{1}$H NMR (400 MHz, DMSO, 25°C) δ 7.78 (d, *J* = 2.1 Hz, 1H, $CH_{arom}$), 7.70 (d, *J* = 8.3 Hz, 1H, $CH_{arom}$), 7.57 (dd, *J* = 8.3, 2.1 Hz, 1H, $CH_{arom}$), 7.27 (d, d, *J* = 8.2 Hz, 1H, $CH_{arom}$), 7.19 (d, *J* = 8.2 Hz, 1H, $CH_{arom}$), 4.75 (s, 2H, $CH_2$), 4.29 (s, 2H, $CH_2$), 3.88 (s, 3H, $OCH_3$), 3.81 (s, 3H, $OCH_3$).

$^{13}$C NMR (101 MHz, DMSO, 25°C) δ 166.4 (Cq), 152.3 (Cq), 146.7 (Cq), 138.4 (Cq), 135.3 (Cq), 133.9 (CH), 132.5 (CH), 130.0 (Cq), 127.7 (q, $CF_3$, J=5.7 Hz), 124.6 (Cq), 124.4 (Cq), 121.9 (Cq), 119.1 (CH), 117.5 (CH), 62.2 ($CH_3$), 56.9 ($CH_3$), 48.9 ($CH_2$), 44.9 ($CH_2$).

ESI-MS: m/z= ($M+Na^+$): 408

***2-(4-nitrobenzyl)-6,7-dimethoxy-isoindolin-1-one*** **(FM70)**

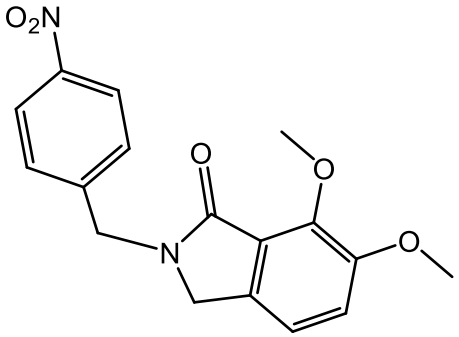

The product was obtained with the general procedure 1 and purified by column chromatography (EtOac:Hex 9:1) as a white powder (Y= 44%).

$^{1}$H NMR (400 MHz, $CDCl_3$, 25°C) δ 8.20 (m, 2H, $CH_{arom}$), 7.48 (m, 2H, $CH_{arom}$), 7.10 (d, *J* = 8.2 Hz, 1H, $CH_{arom}$), 7.05 (d, *J* = 8.2 Hz, 1H, $CH_{arom}$), 4.84 (s, 2H, $CH_2$), 4.21 (s, 2H, $CH_2$), 4.11 (s, 3H, $OCH_3$), 3.90 (s, 3H, $OCH_3$).

$^{13}$C NMR (100 MHz, $CDCl_3$, 25°C) δ 166.9, 152.4, 147.4, 141.4, 134.2, 129.9, 128.5, 125.8, 124.6, 117.6, 115.8, 62.6, 56.9, 48.7, 46.1.

***2-(naphthalen-1-ylmethyl)-6,7-dimethoxy-isoindolin-1-one*** **(FM72)**

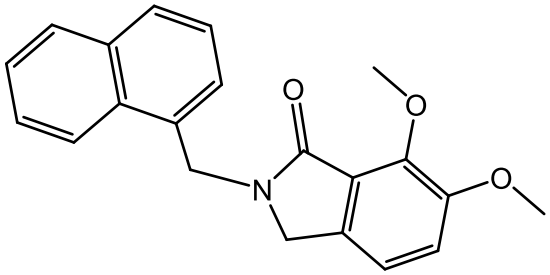

The product was obtained with the general procedure 1 and purified by column chromatography (EtOAc:Hex 7:3 → EtOAc) as a white powder (Y= 57%).

$^{1}$H NMR (400 MHz, $CDCl_3$, 25°C) δ 8.26 (d, *J* = 8.6, 1H, $CH_{arom}$), 7.85 (t, *J* = 7.9, 1H, $CH_{arom}$), 7.49 (m, 4H, $CH_{arom}$), 7.03 (d, *J* = 8.1 Hz, 1H, $CH_{arom}$), 6.91 (d, *J* = 8.1 Hz, 1H, $CH_{arom}$), 5.16 (s, 2H, $CH_2$), 4.14 (s, 3H, $OCH_3$), 4.02 (s, 2H, $CH_2$), 3.87 (s, 3H, $OCH_3$).

$^{13}$C NMR (100 MHz, $CDCl_3$, 25°C) δ 166.38, 153.18, 142.04, 134.02, 132.16, 132.05, 131.52, 129.22, 128.85, 127.51, 127.04, 126.3, 125.3, 123.6, 119.6, 114.5, 62.7, 56.9, 48.7, 46.6.

HR ESI-MS: m/z= ($M+Na^+$): 356.12

**2-(3,4-dihydroxybenzyl)-6,7-dimethoxyisoindolin-1-one (FM73)**

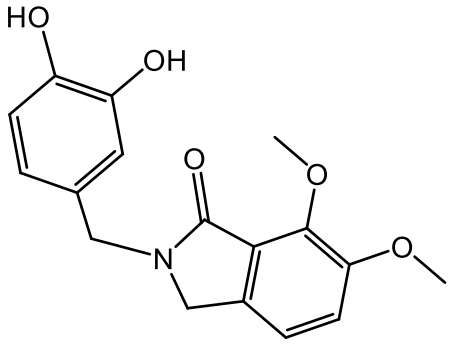

The product was obtained with the general procedure 1 and purified by column chromatography (DCM:MeOH:$NH_4OH_{solution}$ 15:1:0.05) as a white powder (Y= 41%).

$^1$H NMR (400 MHz, $CDCl_3$, 25°C) δ 7.93 (b, 1H, OH), 7.04 (d, *J* = 8.1 Hz, 1H, $CH_{arom}$), 7.00 (m, 2H, $CH_{arom}$), 6.83 (d, *J* = 8.0 Hz, 1H, $CH_{arom}$), 6.70 (dd, *J* = 8.0, 2.0 Hz, 1H, $CH_{arom}$), 5.79 (b, 1H, OH), 4.57 (s, 2H, $CH_2$), 4.18 (s, 2H, $CH_2$), 3.96 (s, 3H, $OCH_3$), 3.86 (s, 3H, $OCH_3$).

$^{13}$C NMR (101 MHz, DMSO, 25°C) δ 165.4 (Cq), 151.8 (Cq), 146.2 (Cq), 145.4 (Cq), 144.7 (Cq), 134.7 (Cq), 128.2 (Cq), 124.4 (Cq), 118.8 (CH), 118.6 (CH), 116.8 (CH), 115.6 (CH), 115.1 (CH), 61.8 ($CH_3$), 56.4 ($CH_3$), 47.9 ($CH_2$), 44.9 ($CH_2$).

ESI-MS: m/z= ($M+H^+$): 316.

**2-(3,4,5-trimethoxybenzyl)- 6,7-dimethoxy isoindolin-1-one (FM78)**

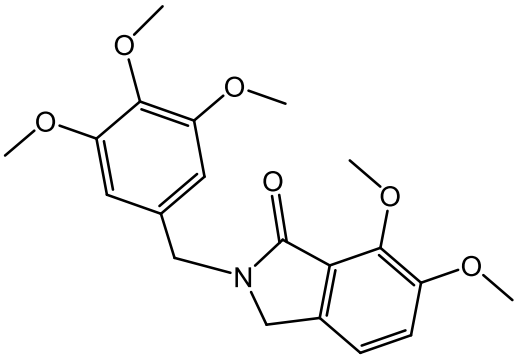

The product was obtained with the general procedure 1 and purified by column chromatography (EtOAc) as a white powder (Y= 36%).

$^1$H NMR (400 MHz, $CDCl_3$) δ 7.08 (d, *J* = 8.2 Hz, 1H, $CH_{arom}$), 7.02 (d, *J* = 8.2 Hz, 1H, $CH_{arom}$), 6.53 (s, 2H, $CH_{arom}$), 4.67 (s, 2H, $CH_2$), 4.17 (s, 2H, $CH_2$), 4.11 (s, 3H, $OCH_3$), 3.89 (s, 3H, $OCH_3$), 3.83 (s, 6H, $OCH_3$), 3.82 (s, 3H, $OCH_3$).

$^{13}$C NMR (101 MHz, $CDCl_3$) δ 166.6 (Cq), 153.5 (Cq), 152.4 (Cq), 147.5 (Cq), 137.5 (Cq), 134.5 (Cq), 132.9 (Cq), 124.9 (Cq), 117.8 ($CH_{arom}$), 116.6 ($CH_{arom}$), 105.4 ($CH_{arom}$), 62.6 ($OCH_3$), 60.5 ($OCH_3$), 56.9 ($OCH_3$), 56.3 ($OCH_3$), 48.5 ($CH_2$), 46.7 ($CH_2$).

ESI-MS: m/z= ($M+H^+$): 374.

***General procedure 2 for the synthesis of 6,7-dihydroxyisoindolin-1-ones:***

The 6,7-dimethoxyisoindolin-1-one derivative (1eqv) was dissolved in dry DMC, under $N_2$ atmosphere, and the solution was cooled to -50°C. A solution of $BBr_3$ in dry DCM was slowly added, the reaction was left reaching r.t. and was left stirring overnight under $N_2$. The mixture was then cooled to 0°C and MeOH was added to quench the reaction. The solvents were removed by vacuum and the residue was partitioned between water and $Et_2O$. The aqueous phase was extracted 3 times with $Et_2O$. The combined organic phase was dried over $Na_2SO_4$, filtered and dried by vacuum obtaining the final compounds without further purification.

***2-(4-fluorobenzyl)-6,7-dihydroxyisoindolin-1-one*** **(FM57)**

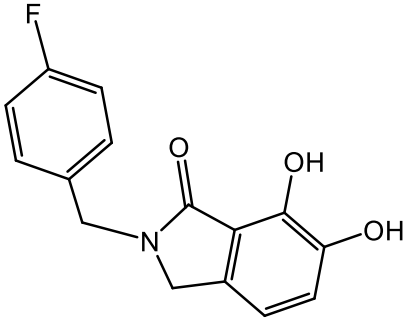


The product was obtained with the general procedure 2, as a pale grey powder (Y=84%).
$^1$H NMR (400 MHz, DMSO-$d_6$, 25°C) δ 9.34 (b, 1H, OH), 8.84 (b, 1H, OH), 7.31 (m, 2H, $CH_{arom}$), 7.17 (t, *J* = 8.8 Hz, 2H, $CH_{arom}$), 6.94 (d, *J* = 7.8 Hz 1H, $CH_{arom}$), 6.76 (d, *J* = 7.8 Hz, 1H, $CH_{arom}$), 4.63 (s, 2H, $CH_2$), 4.19 (s, 2H, $CH_2$).
$^{13}$C NMR (125 MHz, DMSO-$d_6$, 25°C) δ 169.8, 143.3, 142.1, 132.4, 132.0, 129.9 (d, *J* = 7.5 Hz), 119.9, 117.4, 115.9 (d, *J* = 21.2 Hz), 114.5, 49.7, 45.5.
HR ESI-MS : m/z= ($M+H^+$): 274.08
IR (ATR, $cm^{-1}$): ν(OH) = 3336; ν($CH_{arom}$) = 2959, 2923; ν(C=O) = 1661; ν(C–N) = 1270.
E.A. calculated for $C_{15}H_{12}FNO_3$: C 65.93, H 4.43, N 5.13. Found: C 66.08, H 4.77, N 4.93.

***2-(naphthalen-2-ylmethyl)-6,7-dihydroxy-isoindolin-1-one*** **(FM62)**

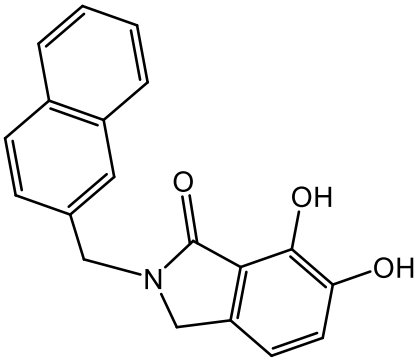


The product was obtained with the general procedure 2, as a pale brown powder (Y=30%).
$^1$H NMR (400 MHz, DMSO-$d_6$, 25°C) δ 9.26 (b, 1H, OH), 8.93 (b, 1H, OH), 7.90 (m, 3H, $CH_{arom}$), 7.79 (s, 1H, $CH_{arom}$), 7.50 (m, 2H, $CH_{arom}$), 7.40 (dd, *J* = 8.5, 1.7 Hz, 1H, $CH_{arom}$), 6.95 (d, *J* = 7.9 Hz, 1H, $CH_{arom}$), 6.75 (d, *J* = 7.9 Hz, 1H, $CH_{arom}$), 4.82 (s, 2H, $CH_2$), 4.24 (s, 2H, $CH_2$).
$^{13}$C NMR (125 MHz, DMSO-$d_6$, 25°C) δ 166.9, 152.5, 147.5, 134.7, 134.6, 132.4, 132.9, 128.8, 127.8, 127.1, 126.4, 126.1, 124.9, 117.9, 116.6, 62.7, 56.9.
HR ESI-MS : m/z= ($M+Na^+$): 306.11
IR (ATR, $cm^{-1}$): ν(OH) = 3383, 3166; ν($CH_{arom}$) = 2921, 2851; ν(C=O) = 1652; ν(C–N) = 1259.
E.A. calculated for $C_{19}H_{15}NO_3 \cdot 0.5\ H_2O$: C 72.60, H 5.13, N 4.46. Found: C 72.96, H 5.09, N 4.38.

***2-(4-hydroxybenzyl)-6,7-dihydroxy-isoindolin-1-one*** **(FM67)**

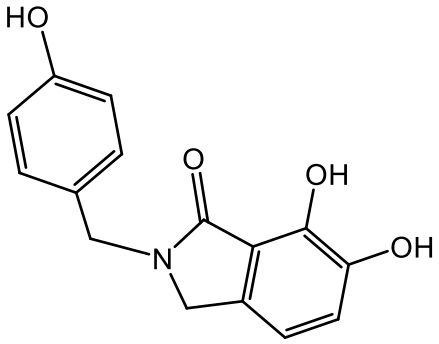


The product was obtained with the general procedure 2, as a pale pink powder (Y=83%).
$^{1}$H NMR (400 MHz, DMSO-$d_6$, 25°C) δ 9.37 (b, 1H, OH), 9.31 (b, 1H, OH), 8.82 (b, 1H, OH), 7.08 (d, *J* = 8.1 Hz, 2H, $CH_{arom}$), 6.93 (d, *J* = 8.1 Hz, 1H, $CH_{arom}$), 6.73 (m, 3H, $CH_{arom}$), 4.51 (s, 2H, $CH_2$), 4.14 (s, 2H, $CH_2$).
$^{13}$C NMR (125 MHz, DMSO-$d_6$, 25°C) δ 168.4, 157.2, 144.8, 143.4, 132.6, 129.7, 128.1, 120.0, 118.5, 115.9, 114.3, 48.9, 45.1.
HR ESI-MS : m/z= ($M+Na^+$): 272.09
IR (ATR, $cm^{-1}$): ν(OH) = 3454; ν($CH_{arom}$) = 2973; ν(C=O) = 1652; ν(C–N) = 1265.
E.A. calculated for $C_{15}H_{13}NO_4 \cdot 0.33\ H_2O$: C 64.97, H 4.97, N 5.05. Found: C 64.92, H 4.91, N 4.95.

***2-(4-hydroxyphenethyl)-6,7-dihydroxy-isoindolin-1-one*** **(FM68)**

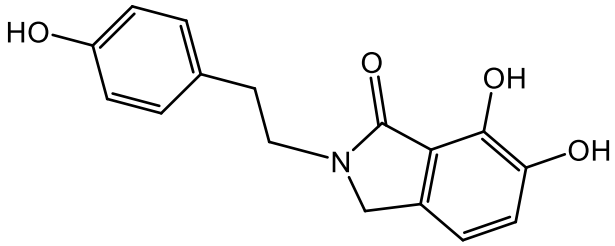


The product was obtained with the general procedure 2, as a pale pink powder (Y=59%).
$^{1}$H NMR (400 MHz, DMSO-$d_6$, 25°C) δ 9.28 (b, 1H, OH), 9.19 (b, 1H, OH), 8.76 (b, 1H, OH), 7.02 (m, 2H, $CH_{arom}$), 6.93 (d, *J* = 7.9 Hz, 1H, $CH_{arom}$), 6.74 (d, *J* = 7.9 Hz, 1H, $CH_{arom}$), 6.66 (m, 2H, $CH_{arom}$), 4.20 (s, 2H, $CH_2$), 3.62 (t, *J* = 7.3 Hz, 2H, $CH_2$), 2.76 (t, *J* = 7.3 Hz, 2H, $CH_2$).
$^{13}$C NMR (125 MHz, DMSO-$d_6$, 25°C) δ 169.8, 155.8, 144.1, 142.9, 132.7, 129.5, 129.4, 129.4, 119.6, 115.1, 113.5, 50.2, 43.9, 33.4.
ESI-MS : m/z= ($M+Na^+$): 308
IR (ATR, $cm^{-1}$): ν(OH) = 3550, 3480, 3322; ν($CH_{arom}$) = 2917, 2848; ν(C=O) = 1645; ν(C–N) = 1224.
E.A. calculated for $C_{16}H_{15}NO_4 \cdot 0.5\ H_2O$: C 65.30, H 5.48, N 4.76. Found: C 65.50, H 5.39, N 4.47.

**2-(4-chloro-3-(trifluoromethyl)benzyl)-6,7-dihydroxyisoindolin-1-one (FM71)**

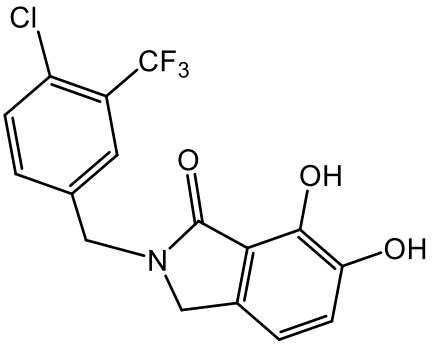


The product was obtained with the general procedure 2, as a white powder (Y=94%).
$^{1}$H NMR (400 MHz, DMSO-$d_6$, 25°C) δ 9.37 (b, 1H, OH), 8.81 (b, 1H, OH), 7.77 (d, *J* = 2.1 Hz, 1H, $CH_{arom}$), 7.71 (d, *J* = 8.3 Hz, 1H, $CH_{arom}$), 7.56 (dd, *J* = 8.3, 2.1 Hz, 1H, $CH_{arom}$), 6.95 (d, *J* = 7.8 Hz, 1H, $CH_{arom}$), 6.75 (d, *J* = 7.8 Hz, 1H, $CH_{arom}$), 4.72 (s, 2H, $CH_2$), 4.24 (s, 2H, $CH_2$).
$^{13}$C NMR (101 MHz, DMSO-$d_6$, 25°C) δ 167.3 (Cq), 145.0 (Cq), 143.5 (Cq), 138.9 (Cq), 133.9 ($CH_{arom}$), 132.9 (Cq), 132.4 ($CH_{arom}$), 130.0 (Cq), 127.6 (q, $CF_3$, J=5.7 Hz), 124.6 (Cq), 121.9 (Cq), 120.0 ($CH_{arom}$), 118.1, 114.2 ($CH_{arom}$), 49.8 ($CH_2$), 45.5 ($CH_2$).
ESI-MS : m/z= (M+$Na^+$): 380
IR (ATR, $cm^{-1}$): ν(OH) = 3242; ν($CH_{arom}$) = 2923; ν(C=O) = 1643; ν(C–N) = 1251; ν(C–F) =784.
E.A. calculated for $C_{16}H_{11}F_3NO_3 \cdot H_2O$: C 51.15, H 3.49, N 3.73. Found: C 51.58, H 3.29, N 3.57.

***2-(4-nitrobenzyl)-6,7-dihydroxy-isoindolin-1-one*** **(FM74)**

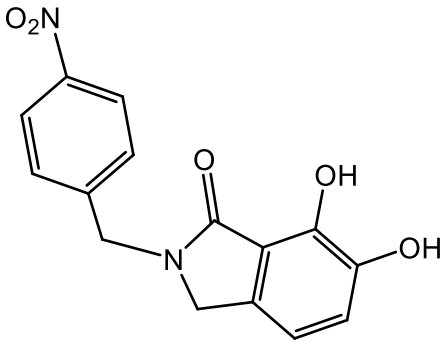


The product was obtained with the general procedure 2, as a pale-yellow powder (Y=49%).
$^{1}$H NMR (400 MHz, DMSO-$d_6$, 25°C) δ 8.21 (m, 2H, $CH_{arom}$), 7.53 (m 2H, $CH_{arom}$), 6.96 (d, *J* = 7.9 Hz, 1H, $CH_{arom}$), 6.78 (d, *J* = 7.9 Hz, 1H, $CH_{arom}$), 4.79 (s, 2H, $CH_2$), 4.25 (s, 2H, $CH_2$).
$^{13}$C NMR (75 MHz, DMSO-$d_6$, 25°C) δ 170.0, 144.1, 143.5, 142.2, 131.8, 128.7, 124.3, 120.1, 117.0, 114.7, 50.0, 45.6.
ESI-MS: *m/z* = (M+$Na^+$): 323
IR (ATR, $cm^{-1}$): ν(OH) = 3363, 3317; ν($CH_{arom}$) = 2913; ν(C=O) = 1660; ν(C–N) = 1270.
E.A. calculated for $C_{15}H_{12}N_2O_5 \cdot H_2O$: C 56.60, H 4.43, N 8.80. Found: C 57.19, H 4.34, N 8.91.

***2-(naphthalen-1-ylmethyl)-6,7-dihydroxy-isoindolin-1-one*** **(FM75)**

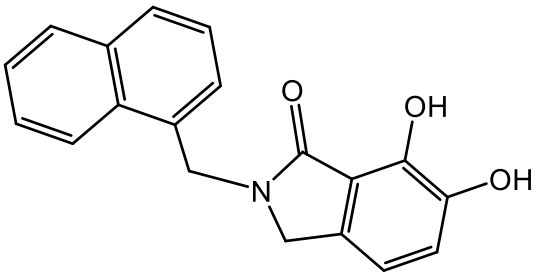


The product was obtained with the general procedure 2, as a pale pink powder (Y=80%).
$^{1}$H NMR (400 MHz, DMSO-$d_6$, 25°C) δ 9.34 (b, 1H, OH), 8.90 (b, 1H, OH), 8.22 (m, 1H, $CH_{arom}$), 7.94 (m, 2H, $CH_{arom}$), 7.51 (m, 4H, $CH_{arom}$), 6.90 (d, *J* = 7.9 Hz 1H, $CH_{arom}$), 6.69 (d, *J* = 7.9 Hz, 1H, $CH_{arom}$), 5.14 (s, 2H, $CH_2$), 4.01 (s, 2H, $CH_2$).
$^{13}$C NMR (75 MHz, DMSO-$d_6$, 25°C) δ 169.4, 143.2, 142.0, 134.0, 132.2, 132.1, 131.5, 129.2, 128.9, 127.5, 127.0, 126.3, 125.3, 123.6, 119.6, 117.5, 114.5, 49.9, 44.4.
IR (ATR, $cm^{-1}$): ν(OH) = 3322; ν($CH_{arom}$) = 2980, 2920, 2850; ν(C=O) = 1652; ν(C–N) = 1259.
ESI-MS: *m/z* = ($M+Na^+$): 327.
E.A. calculated for $C_{19}H_{15}NO_3 \cdot 0.5\ H_2O$: C 72.6, H 5.13, N 4.46. Found: C 72.81, H 5.10, N 4.36.

**2-(3,4-dihydroxybenzyl)-6,7-dihydroxyisoindolin-1-one (FM76)**

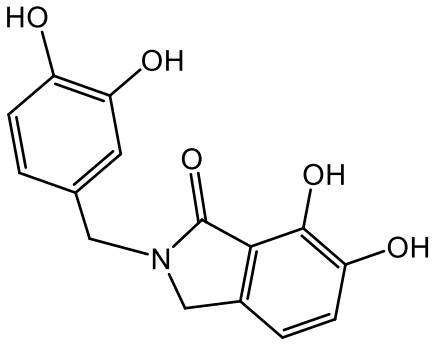


The product was obtained with the general procedure 2, as a white powder (Y=75%).
$^{1}$H NMR (400 MHz, DMSO-$d_6$, 25°C) δ 9.32 (b, 1H, OH), 8.92 (b, 1H, OH), 8.82 (b, 2H, OH), 6.93 (d, *J* = 7.9 Hz, 1H, $CH_{arom}$), 6.75 (d, *J* = 7.9 Hz, 1H, $CH_{arom}$), 6.67 (d, *J* = 8.0 Hz, 1H, $CH_{arom}$), 6.63 (d, *J* = 2.1 Hz 1H, $CH_{arom}$), 6.53 (dd, *J* = 8.0, 2.1 Hz, 1H, $CH_{arom}$), 4.45 (s, 2H, $CH_2$), 4.13 (s, 2H, $CH_2$).
$^{13}$C NMR (101 MHz, DMSO-$d_6$, 25°C) δ 167.9 (Cq), 145.4 (Cq), 144.7 (Cq), 144.3 (Cq), 142.9 (Cq), 132.1 (Cq), 128.2 (Cq), 119.5 ($CH_{arom}$), 118.8 ($CH_{arom}$), 118.0 (Cq), 115.6 ($CH_{arom}$), 115.0 ($CH_{arom}$), 113.8 ($CH_{arom}$), 48.4 ($CH_2$), 44.7 ($CH_2$).
ESI-MS: m/z= ($M+Na^+$): 310.
IR (ATR, $cm^{-1}$) ν(OH) = 3363; ν(C=O) = 1639; ν(C–N) = 1263.
E.A. calculated for $C_{15}H_{13}NO_5$: C 62.71, H 4.56, N 4.88. Found: C 62.53, H 4.66, N 4.75.

**6,7-dihydroxy-2-(3,4,5-trihydroxybenzyl)isoindolin-1-one (FM79)**

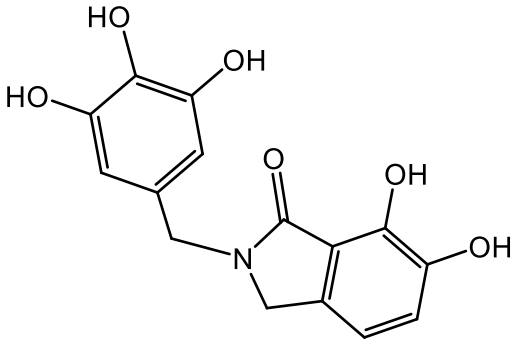


The product was obtained with the general procedure 2 (with 15 eqv of $BBr_3$), after filtration from the organic phase, as a white powder (Y=64%).

$^1$H NMR (400 MHz, DMSO-$d_6$, 25°C) δ 9.30 (b,1H, OH), 8.80 (b, 3H, OH), 7.99 (b, 1H, OH), 6.94 (d, *J* = 7.9 Hz, 1H, $CH_{arom}$), 6.75 (d, *J* = 7.9 Hz, 1H, $CH_{arom}$), 6.16 (s, 2H, $CH_{arom}$), 4.38 (s, 2H, $CH_2$), 4.14 (s, 2H, $CH_2$).

$^{13}$C NMR (101 MHz, DMSO-$d_6$, 25°C) δ 167.9 (Cq), 146.2 (Cq), 144.3 (Cq), 142.9 (Cq), 132.2 (Cq), 132.1 (Cq), 127.4 (Cq), 119.5 ($CH_{arom}$), 118.0 (Cq), 113.8 ($CH_{arom}$), 106.4 ($CH_{arom}$), 48.4 ($CH_2$), 44.8 ($CH_2$).

ESI-MS: m/z= ($M+H^+$): 304.

IR (ATR, $cm^{-1}$) ν(OH) = 3261; ν(C=O) = 1617; ν(C–N) = 1294.

E.A. calculated for $C_{15}H_{13}NO_6 \cdot 1.5\ H_2O$: C 54.54, H 4.88, N 4.17. Found: C 54.19, H 4.67, N 4.17.

# Chapter 7: **Synthesis and characterization of compounds targeting Zn(II) ion in SARS-CoV-2 Papain-Like protease**

## 7.1 Targeting SARS-CoV-2 metal-dependent enzymes

The global COVID-19 pandemics, caused by the severe acute respiratory syndrome coronavirus 2 (SARS-CoV-2) represented one of the major challenge world-wide in the last few years. January 2023 updates from the WHO report more than 660 million of confirmed COVID-19 cases, that led to more than 6.7 million confirmed deaths.

Since the beginning of the pandemics, the research community has put extensive efforts to find effective and rapid solutions to reduce the pressure of this pathology on the public health. Although vaccination was the primary medicinal strategy to mitigate the pandemics, the need of safe and effective antiviral drugs to treat infected patients is of vital importance. To find viable drugs in a very short of time, many drug repurposing attempts have been made for the treatment of COVID-19. Drug repurposing or repositioning represents a valuable strategy, especially in emergency times, since it reduces the timeline for research and development of a new drug. Furthermore, when it involves clinically approved drugs it lowers the risk of adverse effects and unsafe toxicity profiles.[281]

Within the bio-inorganic medicinal chemistry research area, the identification of suitable metal-dependent enzyme targets and of metal chelating or metal-containing anti-SARS-CoV-2 agents became a priority. Starting from the studies conducted on other viruses and SARS-CoV, a wide variety of metal chelating compounds, ionophores and metal complexes were identified as active against SARS-CoV-2.[282]

As for many other viruses, the Mg-dependent RdRP of SARS-CoV-2[283] represents a valuable target for chelating inhibitors, since it is fundamental for the virus life cycle and replication.

It was reported that natural polyphenolic compounds baicalein and baicalin (**Scheme 7.1**), already known inhibitors of influenza and other viruses such as Dengue and Zika, are inhibitors of SARS-CoV-2 RdRP and can inhibit SARS-CoV-2 in cellular assays with $EC_{50}$ values between 1.2 and 9.0 µM.[284]

Additionally, Liu et al. investigated an in-house library containing metal chelating compounds with piperazine scaffold, previously designed as anti-HIV, for their activity towards SARS-CoV-2 RdRP. The hit compound of the screening, DF-47 (**Scheme 7.1**), displayed $IC_{50}$=9.2 µM towards SARS-CoV-2 RdRp.[285]

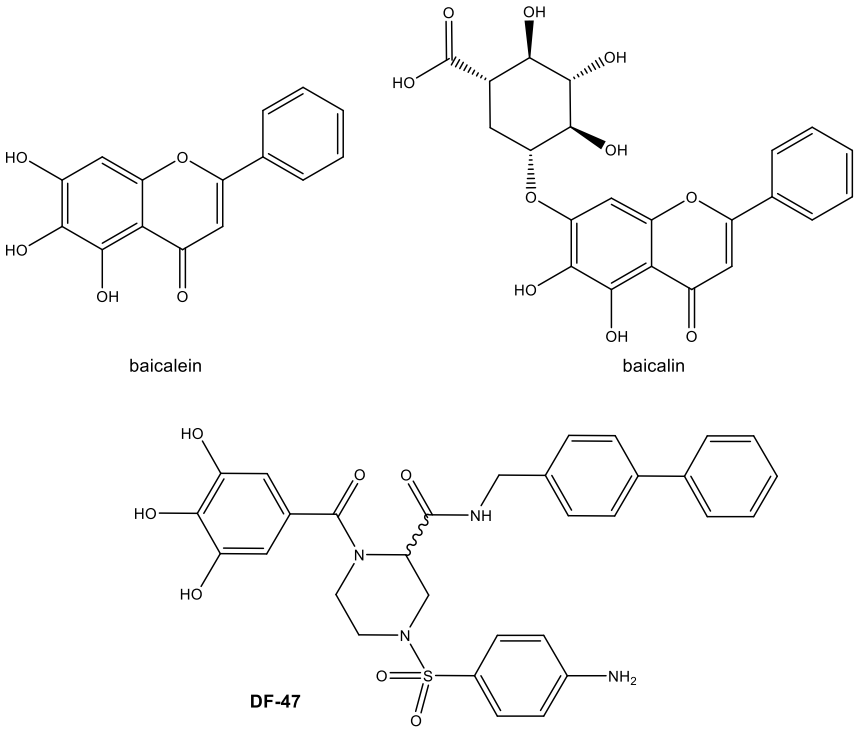


**Scheme 7.1** Structure of the metal-chelating SARS-CoV-2 RdRP inhibitors baicalein, baicalin and DF-47.

In 2009, a panel of aryl DKAs was investigated for its activity towards SARS-CoV NTPase/helicase. This enzyme combines energy from DNP hydrolysis with the unwinding of duplex nucleic acid. SARS-CoV helicase has a zinc binding domain that is essential for enzymatic activity and the virus viability.[286] Some of the tested DKAs (**Scheme 7.2**) revealed inhibition of SARS-CoV helicase duplex DNA-unwinding activity with $IC_{50}$ between 5.4 and 13.6 μM.[287]

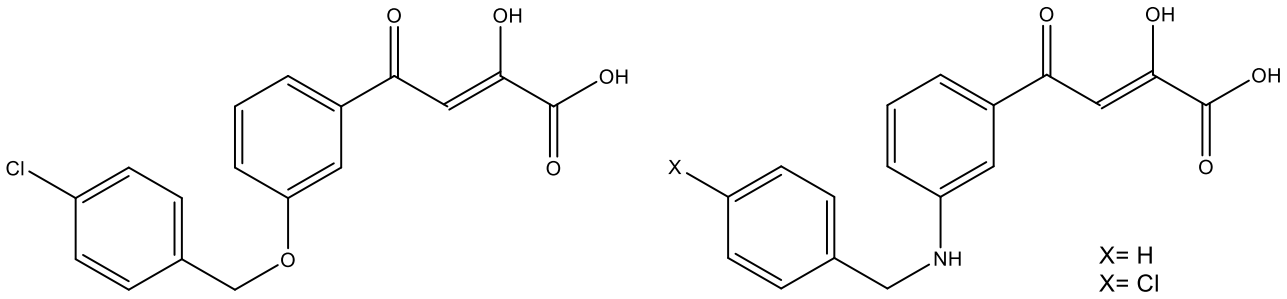


**Scheme 7.2** Structure of the DKA derivatives with SARS-CoV helicase inhibition activity.

Alvarez et al. investigated an in-house library of 113 different metal chelating compounds with different scaffolds (DKAs, polyphenols, *N*-hydroxyisoquinoline-1,3-diones) against SARS-CoV-2 exonuclease.[288] SARS-CoV-2 exonuclease is a Mg-dependent domain within the nsp14 protein, that contributes to the suppression of the host innate immune response.[289] The screening identified four DKAs derivatives causing inhibition of the exonuclease activity in the micromolar range, and $EC_{50}$ value in cellular test between 8 and 38 μM without showing cytotoxicity.

The role of zinc ions has been widely investigated on SARS-CoV-2, since this metal is involved in a great number of cellular processes critical in enzymes folding and activity. Zinc, in fact, has been studied for its antiviral action on numerous viruses.[290]

In 2010 it was described that the use of zinc pyrithione at concentration 2 μM is able to effectively inhibit the SARS-CoV replication in cell cultures, targeting the virus RdRP.[291] Given the tight similarities of the two viruses, the use of $Zn^{2+}$ ions on SARS-CoV-2, was investigated as well. Indeed, it was found that zinc ions in combination with certain ionophores (chelating compounds that transport the ions inside the cellular target) inhibit the replication of SARS-CoV-2 in cellular assays. For instance, it was reported that quercetin in combination with $Zn^{2+}$ inhibits the replication of SARS-CoV-2 in Vero E6 cells more than two-fold efficiently than zinc alone.[292]

The mechanism of action of zinc compounds have been related to the inhibition of polyprotein processing, as a consequence of proteases inhibition.[282] SARS-CoV-2 3C-like protease (3CLpro) and papain-like protease (PLpro) are fundamental for the viral polyproteins processing, generating the functional replicase complex that enables the viral spreading; therefore these proteases represent a suitable drug target.[293][294]

Positive results were obtained by using zinc compounds in inhibiting SARS-CoV 3CLpro,[295] and the synergistic use of a ionophore confirmed to be a suitable strategy to potentially enhance the inhibition activity. The same concept was validated as well for the SARS-CoV-2 3CL protease. For instance, a series of tropolone and thiotropolone, and their Zn(II) complexes (**Scheme 7.3**) revealed very potent inhibition of SARS-CoV-2 3CL pro activity in vitro.[296] The presence of the zinc lowered considerably the $IC_{50}$ values, to a range of 60-100 nM.

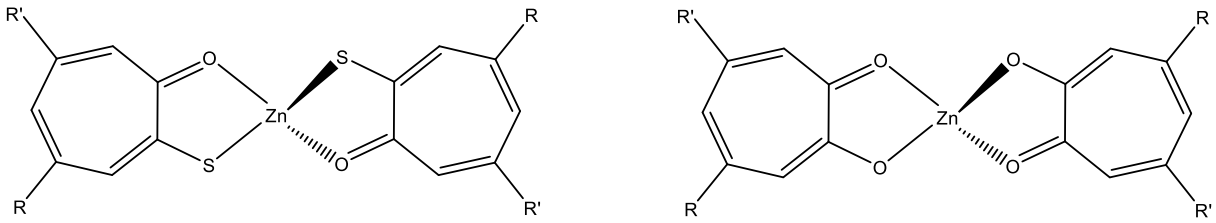


**Scheme 7.3** Structure of the thiotropolones (left) and tropolones (right) Zn(II) complexes with SARS-CoV-2 3CL pro inhibition activity.

The X-ray structure of SARS-CoV-2 3CLpro with zinc pyrithione (PBD 7B83)[297] revealed the zinc atom bound to the catalytic residues His41 and Cys145 and to pyrithione, suggesting that zinc and zinc complexes can bind into the active site pocket of the protease.

Inhibition activity of some zinc complexes was also disclosed for SARS-CoV PLpro, whit N-ethyl-N-phenyldithiocarbamic acid and hydroxypridine-2-thione zinc(II) complexes (**Scheme 7.4**) inhibiting PLpro activity with $IC_{50}$ values of 3.3 and 3.7 μM respectively.[298]

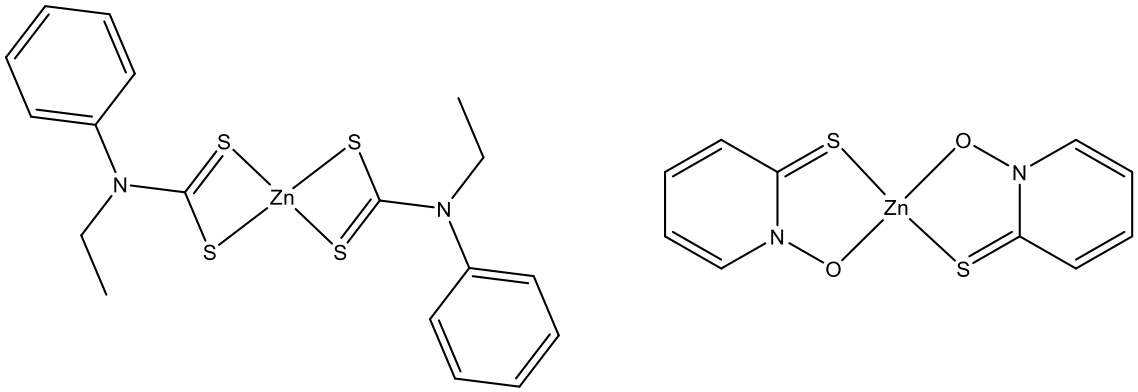


**Scheme 7.4** Structure of the SARS-CoV PLpro inhibitors N-ethyl-N-phenyldithiocarbamic acid (left) and hydroxypridine-2-thione (right) zinc(II) complexes.

Zinc plays as essential role as structural motif in many viral enzymes and the disruption of the zinc finger motif can lead to protein destabilization and impair their functions. For this reason, targeting the zinc-binding domains represents an attractive therapeutic approach for the development of antivirals.[299] As other viral proteases, SARS-CoV PLpro contains a finger motive in which the zinc ion is coordinated tetrahedrally by four cysteines.[300]

Studies on SARS-CoV PLpro with disulfiram (**Scheme 7.5**, A) revealed inhibition of PLpro activity in the micromolar range and that the zinc ions were released from the enzyme by disulfiram binding.[301] Recently, it was disclosed analogously that disulfiram inhibits the activity of SARS-CoV-2 PLpro with $IC_{50}$=7.2 µM, confirming that this compound is able to remove the zinc ion from its finger domain (**Scheme 7.5**, B).[302]

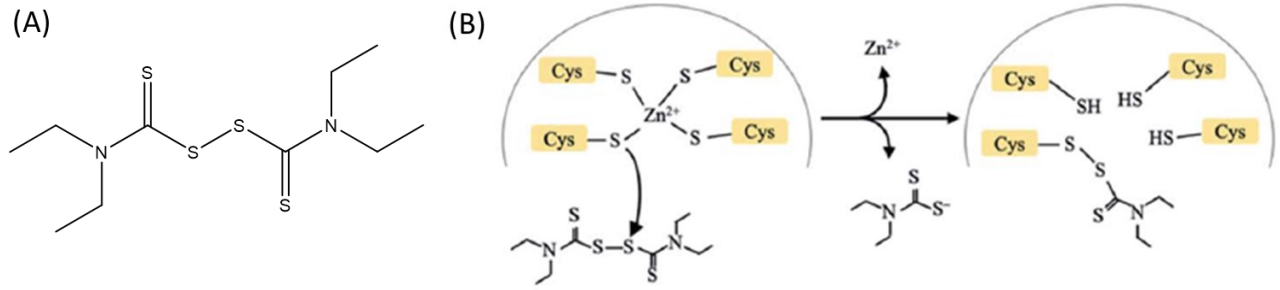


**Scheme 7.5** (A) Chemical structure of disulfiram and (B) schematic representation of the $Zn^{2+}$ release by action of disulfiram. Adapted from ref.[302]

## 7.2 Aim of the project

As discussed previously, metal chelation is a suitable strategy in the search for possible inhibitors of metal-enzymes.[168] Continuing to pursue this idea, it was decided to apply this approach also in the case of SARS-CoV-2, encouraged by the results present in the scientific literature regarding SARS-CoV and SARS-CoV-2, as outlined in the previous paragraphs.

The screening of in-house libraries allows to find some attractive hit in a short period, considering the urgency created by the rapid expansion of the COVID-19 pandemics. For this reason, a library of 40 potential metal-chelating compounds and some metal complexes, previously synthetized and investigated in the research group for the inhibition of other viral metal-dependent enzymes, was put together. The library comprises some metal complexes and different chelating motives (quinolinones, isatin-thiosemicarbazones, hydroxylated thiosemicarbazones and hydrazones, hydroxyquinoline thiosemicarbazone) with the aim to target the Zinc(II) domain of PLpro.

All the compounds composing the in-house chelating library are represented in **Scheme 7.6**.

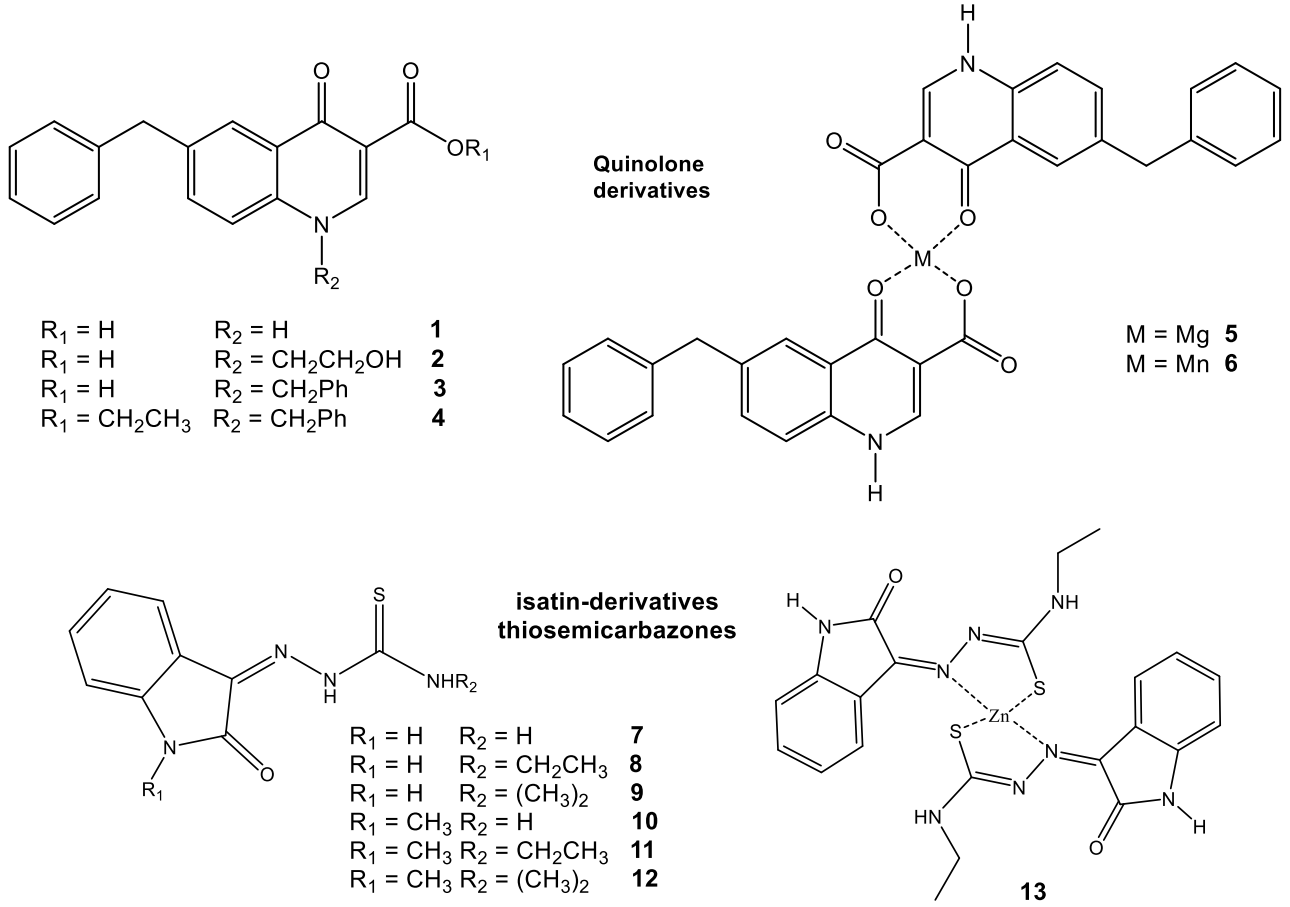

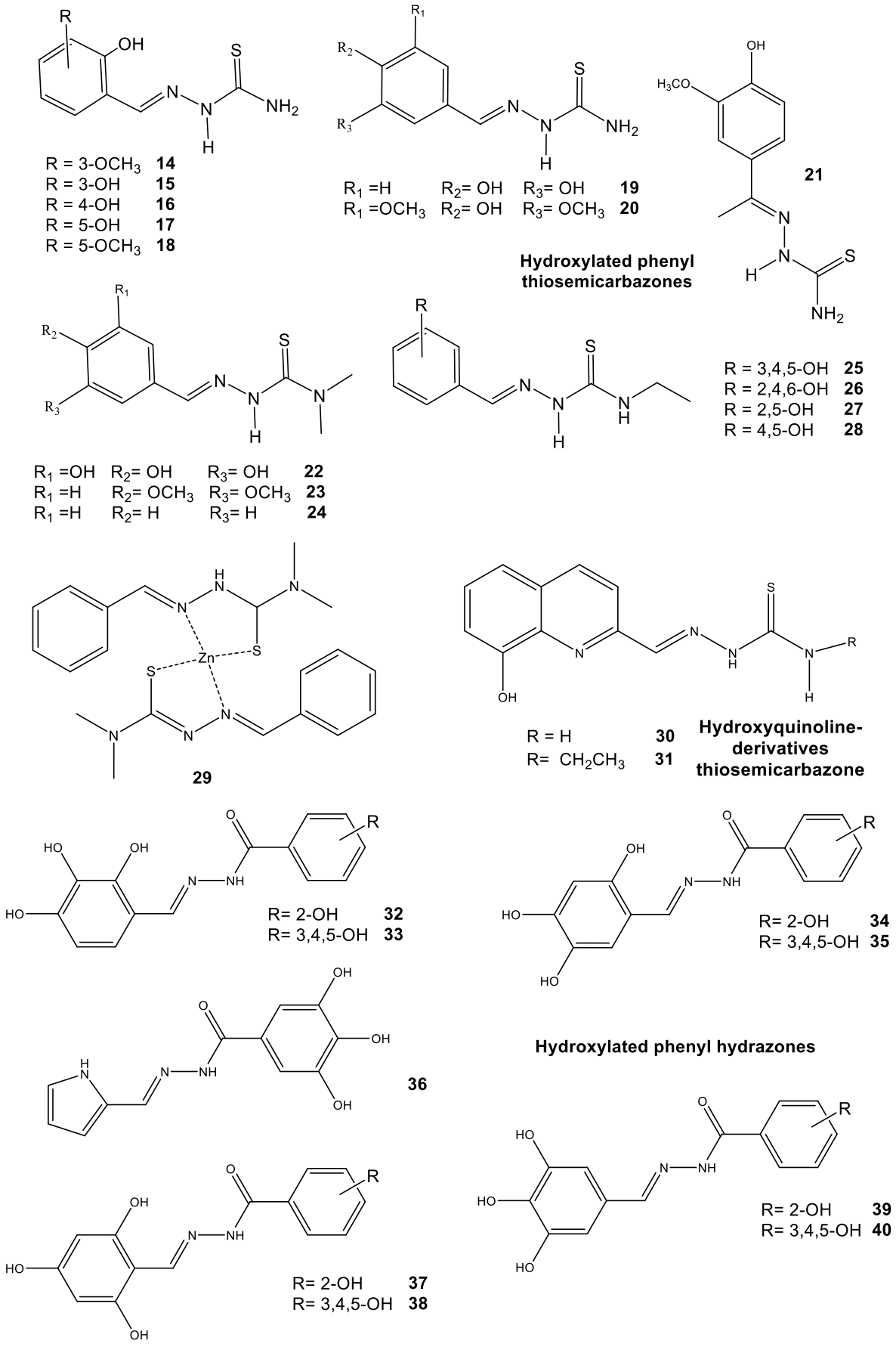


**Scheme 7.6** Library of the screened compounds.

## 7.3 Results and discussion

### 7.3.1 Synthesis and characterization of the metal-chelating library

An in-house library of previously synthetised chelating compounds and some metal complexes with biological activity were composed.[44-49] In particular, quinolinone derivatives **1**-**6** were previously studied as HIV integrase inhibitors;[303] salicylaldehyde thiosemicarbazones **14**-**18** were investigated as $PA_N$ endonuclease inhibitor;[304] hydroxylated hydrazones **32**-**40** were disclosed as influenza $PA_N$ endonuclease inhibitors.[234]

To complete the panel, some new additional compounds (isatin-derivatives thiosemicarbazones **FM05**, **FM06**, **FM07**, **FM08**, **FM09** and hydroxylated phenyl thiosemicarbazones **FM11**) were synthesized (**Scheme 7.7**).

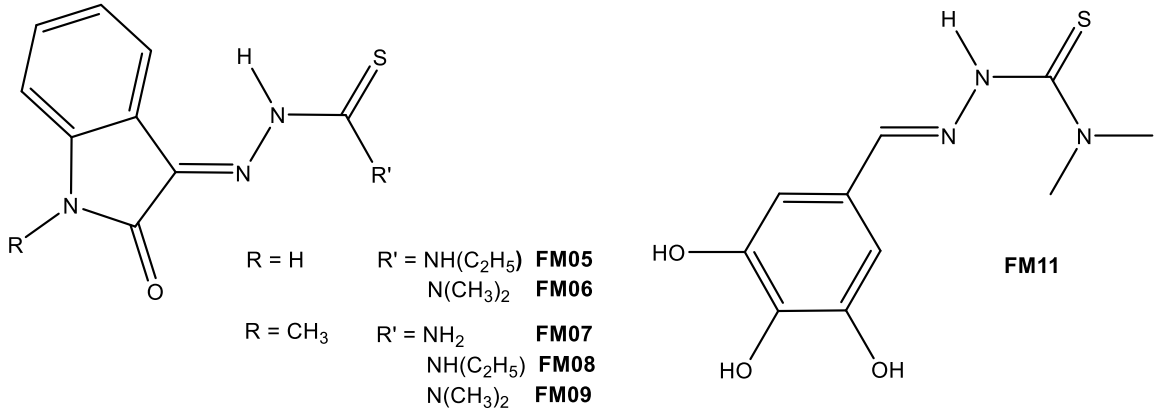


**Scheme 7.7.** Structure of isatin-derivatives thiosemicarbazones (**FM05-9**) and hydroxylated phenyl thiosemicarbazones (**FM11**).

The isatin moiety combined with thiosemicarbazones was chosen since in 2005 some isatin-derivatives were reported to be effective inhibitors of SARS-CoV 3CLpro.[305] Synthesis of the isatin-derivatives thiosemicarbazones and the hydroxylated phenyl thiosemicarbazone were conducted in EtOH at reflux, with equimolar amounts of ketone or aldehyde and the appropriate thiosemicarbazide. The compounds were characterized by NMR spectroscopy ($^1H$ and $^{13}C$), ESI-MS and IR spectroscopy and elemental analysis.

In **Figure 7.1** is reported the $^1H$ NMR and $^{13}C$ spectra of **FM05**, as an example.

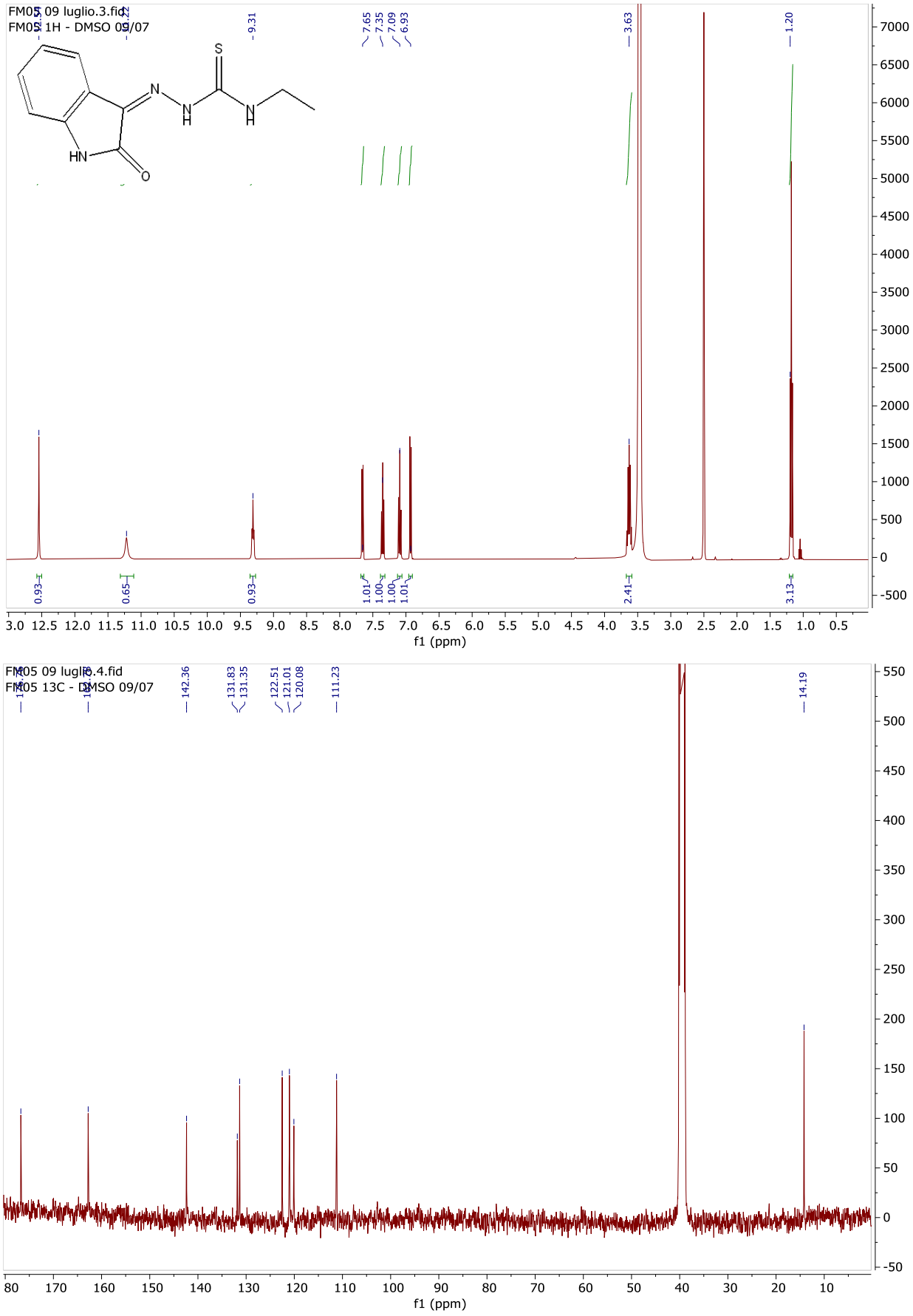


**Figure 7.1** $^{1}$H-NMR (600 MHz, DMSO-$d_6$, 25°C) and $^{13}$C-NMR (101 MHz, DMSO-$d_6$, 25°C) spectra of compound **FM05**.

In the $^{1}H$ spectrum it is possible to observe a broad signal at 11.22 ppm corresponding to the NH of the isatin moiety, while at 12.54 and 9.31 ppm the signals of the thiosemicarbazone NHs (respectively a singlet and a triplet) are present. Between 7.66 and 6.93 ppm are present the 4 aromatic proton signals of the isatin moiety and at 3.63 and 1.18 ppm the $CH_2$ and $CH_3$, respectively.

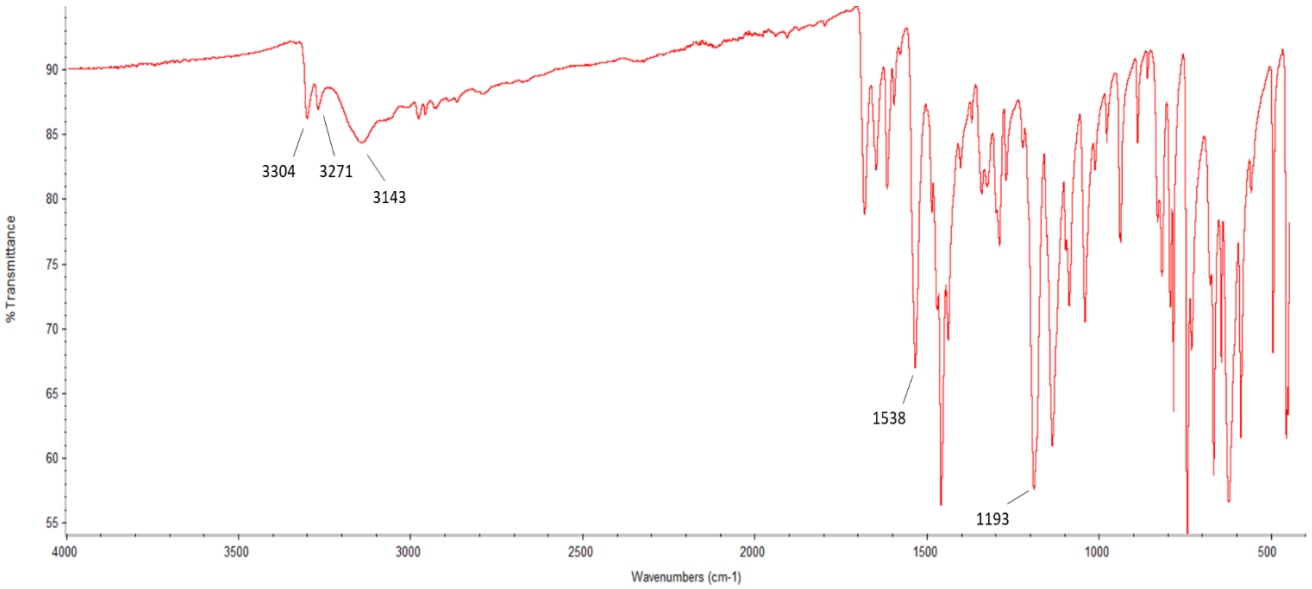


**Figure 7.2**. FT-IR spectrum of **FM05**.

In the IR spectrum of **FM05** (**Figure 7.2**) it is possible to observe the stretching band relative to the N-H at 3304, 3271 and 3143 $cm^{-1}$ and the C=N stretching band at 1538 $cm^{-1}$. The presence of several N-H stretching bands and the absence of a S-H stretching band around 2600 $cm^{-1}$ suggest that **FM05** is in the thione form in the solid state.

The zinc complex $L_2Zn$ **FM13** (**Scheme 7.8**) was synthesized employing **FM05** as ligand (HL).

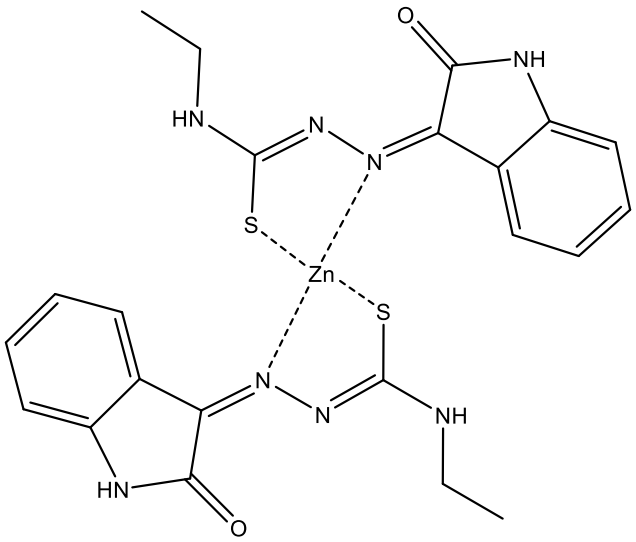


**Scheme 7.8** Structure of zinc(II) complex **FM13.**

Briefly, **FM05** (2 eqv) and $Zn(CH_3COO)_2 \cdot 2H_2O$ (1 eqv) are reacted in methanol, at reflux overnight. A yellow solid is filtrated and washed with methanol and water, obtaining **FM13**. The complex was characterized by $^1H$ NMR spectroscopy, ESI-MS and IR spectroscopy and elemental analysis.

From the comparison between the $^1H$ NMR spectra of the ligand **FM05** and the complex **FM13** (**Figure 7.3**), it is possible to observe the disappearance of the 12.54 ppm NH signal in the complex spectrum, suggesting the ligand is coordinating the zinc atom in the thiol form. Moreover, the ligand signals are doubled, indicating that the complex in DMSO-$d_6$ solution is not symmetric. In particular, the wider ppm difference in the double signals of the complex spectrum is observed for the NH triplet and one of aromatic protons, due to their proximity to the coordination center.

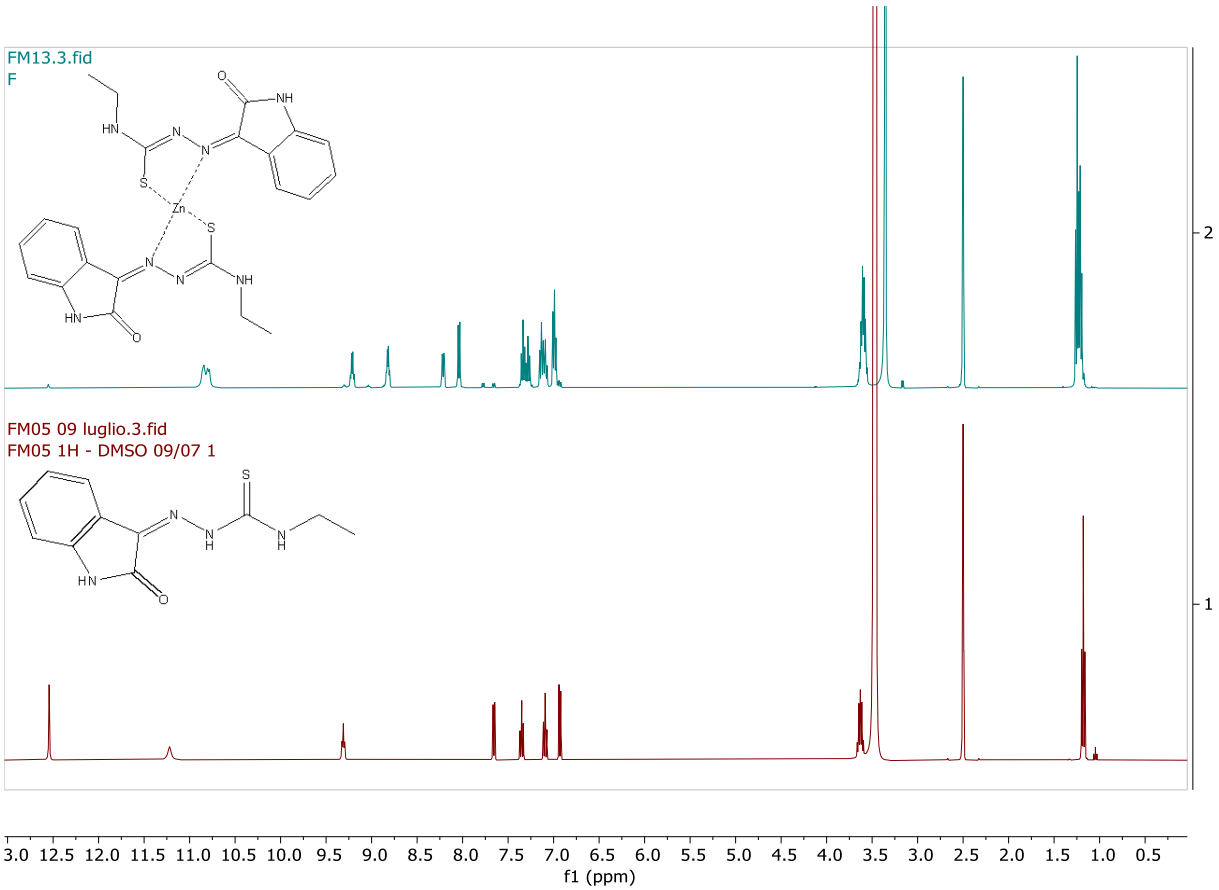


**Figure 7.3** $^1H$-NMR (25°C, 600 MHz, DMSO-$d_6$) spectra of compound **FM13** and **FM05**

The elemental analysis results are as well in line with the proposed stoichiometry.

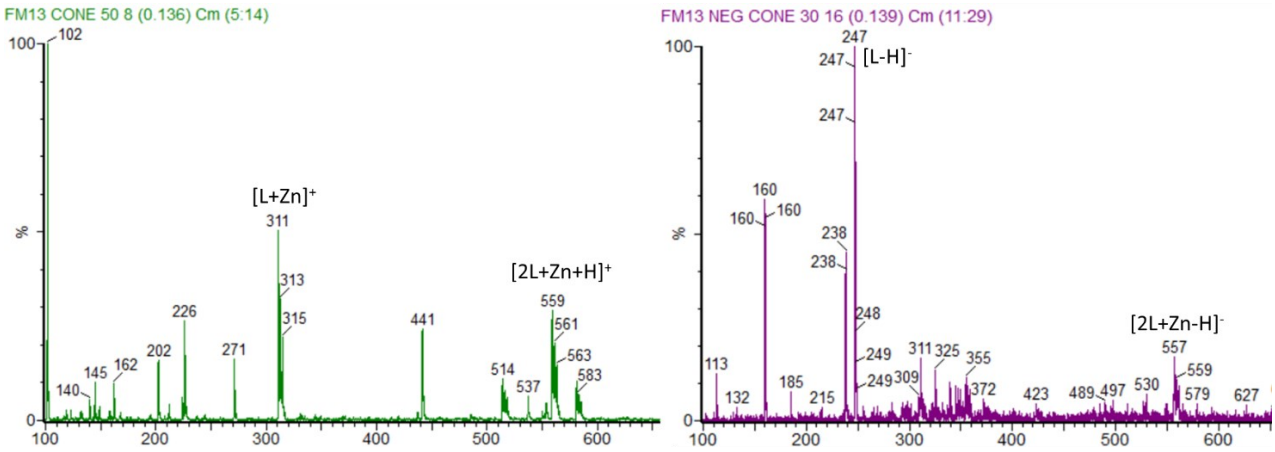


**Figure 7.4** ESI-MS spectra for **FM13**; on the right positive ionization 50 eV, on the left negative ionization 30 eV.

In **FM13** ESI-MS spectra (**Figure 7.4**) the molecular ion peak, with the characteristic Zn isotopic pattern, of the complex is visible in both positive (559: $[2L+Zn+H]^+$) and weakly in the negative ionization mode (557: $[2L+Zn-H]^-$). In positive ionization mode it is also noticeable a peak at 311, corresponding to the Zn species with one ligand $[L+Zn]^+$. In the negative ionization mode, on the other hand, the most prominent peak is the one of the free ligand (247: $[L-H]^-$).

### 7.3.2 X-Ray crystallographic screening against PLpro

The chelating compounds were investigated within an X-ray crystallographic screening against PLpro, conducted by professor A. Ment's group in the Center for Free-Electron Laser Science CFEL, Deutsches Elektronen-Synchrotron DESY, Hamburg, Germany.

PLpro crystallization was reached by mixing 0.2 µL of protein with 0.1 µL of a reservoir buffer solution. After a few days at 4°C some bipyramidal crystals appeared and reach their final size at 100 µM approximatively. The crystals were then soaked for 24 hours with reservoir solutions containing the respective tested compounds up to 5 mM and with a final 5% DMSO concentration. After the soaking, the crystals were harvested and cryo-cooled with liquid-nitrogen and used for the X-ray diffraction data collection. Within this screening, a total of 71 diffraction data sets involving the 40 compounds of the library were collected with high resolution limits between 1.6—3.0 Å.

Surprisingly, none of the putative zinc coordinating ligands were found to bind at the zinc binding site. Instead, six compounds (**Scheme 7.9**) were identified binding to a previously undescribed groove nearby the S1 site (hydrazone **H1**) or in a pocket a pocket between the S2 binding site and Ubl domain (thiosemicarbazones **T1**-**T5**) of PLpro.[306]

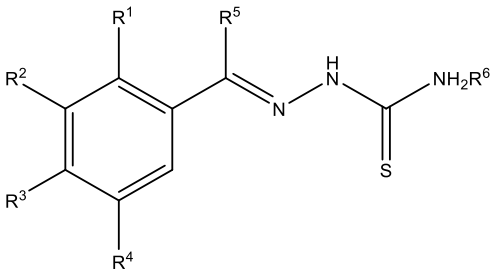


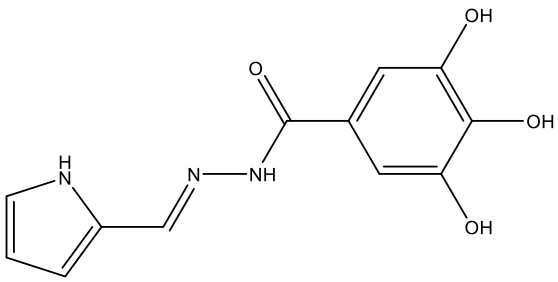


**H1**

$R^1$= OH (**T3**, **T4**) $R^4$= OH (**T3**), MeO (**T1**)
$R^2$= OH (**T2**), MeO (**T1**, **T5**) $R^5$= $CH_3$ (**T5**)
$R^3$= OH (**T1**, **T2**, **T4**, **T5**) $R^6$= $C_2H_5$ (**T2**, **T3**)

**Scheme 7.9** Structure of thiosemicarbazones **T1**-**T5** and hydrazone **H1**.

Sites S1 and S2 are involved in protein-protein interactions, functioning as binding sites for ubiquitin and ISG15 (Interferon-stimulated gene 15) as substrates.

Compound **H1** binding mode (**Figure 7.5**) was particularly interesting, since it interferes with natural substrate binding by sterical hindrance and causes conformational changes in some protein residues that participate in substrate binding. Compounds **T1**-**T5**, on the other hand, could have more of an indirect effect.

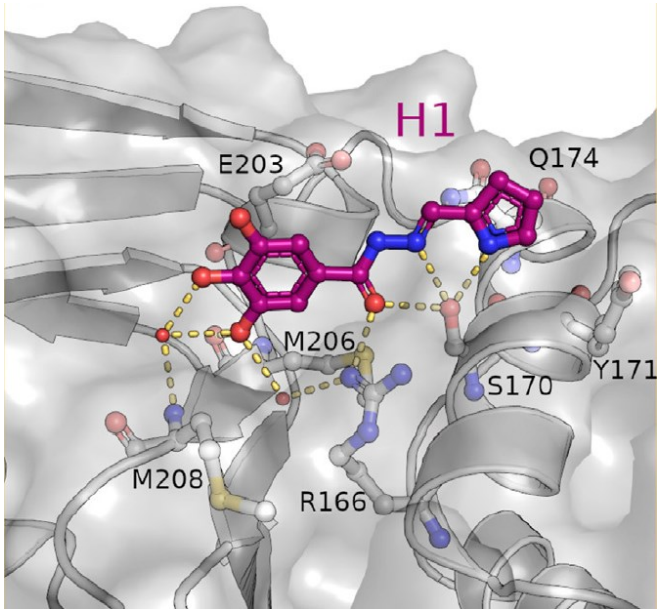


**Figure 7.5** Close-up view on the binding mode of compound **H1. H1** and the interacting residues are indicated as sticks. Interactions with the surrounding residues within hydrogen bonding distance are shown as dashed lines.[306]

Hydrazone **H1** binds near the PLpro S1 site between a β-strand of the palm and a α-helix of the thumb domain. The compound is stabilized within this groove by eight hydrogen bonds.

Residue S170 is observed in a different rotameric state compared to the ligand-free structure. In fact, is moved towards **H1** of 1.7 Å because of the attractive interaction with the compound. Furthermore, residue Q174 also present a side chain rearrangement, in which the carboxamide side chain is shifted to engage in a hydrogen bond with the π-system of hydrazone **H1**.[306]

Fluorescence polarization assay with human ISG15 and ubiquitin as substrates were performed, by the Hamburg research group, in order to evaluate the potential as inhibitors of the six compounds identified by crystallographic the screening (**Figure 7.6**).

Thiosemicarbazones **T1**-**T5** did not show inhibition at the tested concentrations, while **H1** showed a significant inhibition of ubiquitin cleavage at 500 µM. The fivefold reduction in the substrate turnover is coherent with the expected sterical hindrance discussed previously.

Unexpectedly, in presence of **H1** 500 µM the ISG15 is not decreased but rather increased of twofold compared to the ligand-free PLpro.

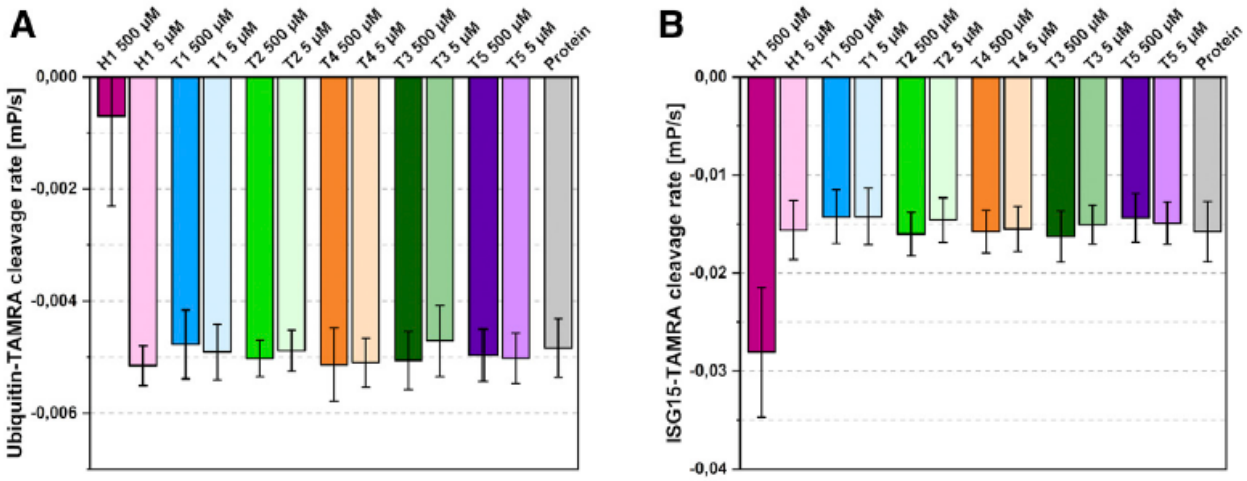


**Figure 7.6** Effects of compounds **H1** and **T1**-**T5** on the substrate cleavage rates of protein PLpro. (A) PLpro Ubiquitin-cleavage rate in presence of 500 µM or 5 µM compound. (B) PLpro ISG15-cleavage rate in presence of 500 µM or 5 µM compound. The average value with standard deviation of four independent experiments is shown.[306]

The found inhibition properties are indicative of the need of compounds optimization, but, also considering their original mode of interaction with the enzyme, these compounds seem interesting candidates in the development of novel lead compounds targeting SARS-CoV-2 PLpro.

### 7.3.3 Structural modification on compound H1

Given the **H1** unique binding mode, a panel of structural derivatives of **H1** (**Scheme 7.10**) was synthesized, in order to evaluate their binding and inhibition activity.

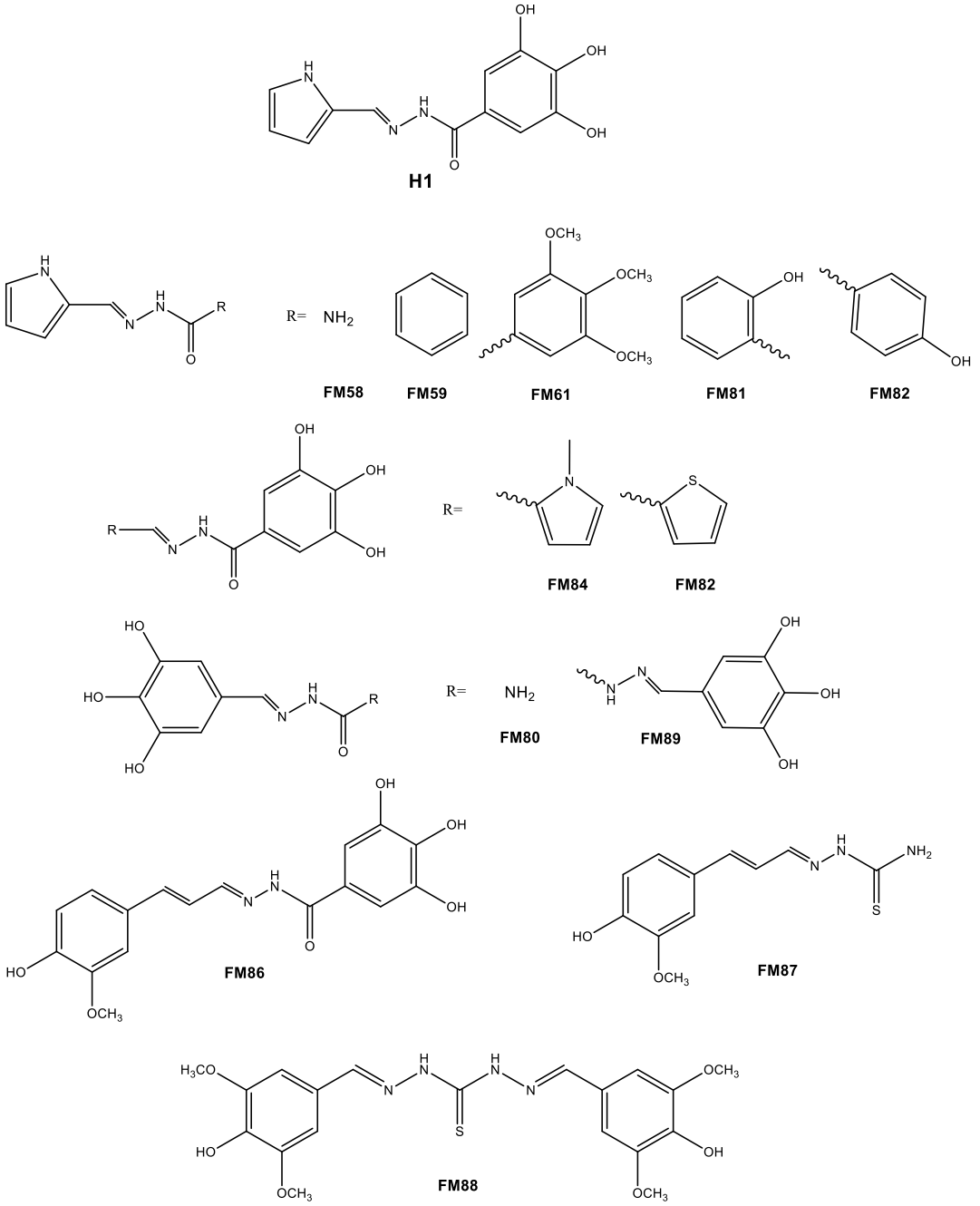


**Scheme 7.10** Structures of **H1** derivatives.

The synthesis of the structurally modified compounds was carried out with the same general procedure previously reported for the other thiosemicarbazones.

3,4,5-hydroxybenzohydrazide and 3,4,5-methoxybenzohydrazide were prepared reacting their respective methylbenzoates in EtOH with 18 eqv of hydrazine, at reflux for 5 hours. After that time the mixture was cooled to 0°C and the product were isolated as powders by filtration.

These structural derivatives were characterized with $^{1}H$ and $^{13}C$ NMR spectroscopy, AT-IR, ESI-MS and elemental analysis. The $^{1}H$-NMR spectra suggest that all the synthetized thiosemicarbazones and hydrazones are in the *E* form in DMSO-$d_6$ solution.

In **Figure 7.7** and **7.8** some spectra for compound **FM85** are reported, as an example. The $^{1}H$-NMR spectrum confirms the success of the condensation reaction, with the absence of the aldehydic proton and with the appearance of a singlet at 8.62 ppm, characteristic of the iminic proton. Moreover, in the aromatic regions two doublets and one doublet of doublets peaks are present, respectively at 7.64, 7.42 and 7.14 ppm, relative to the thiophene moiety. Furthermore, one singlet integrating for two protons, relative to the two chemically equivalent protons of the trihydroxybenzene moiety is found at 6.90 ppm. Finally, at 11.49 and 9.05 ppm (broad) the peaks relatively to the NH and the OH groups are found, respectively. The deptq $^{13}C$-NMR spectrum is also consistent with the structure of the compound.

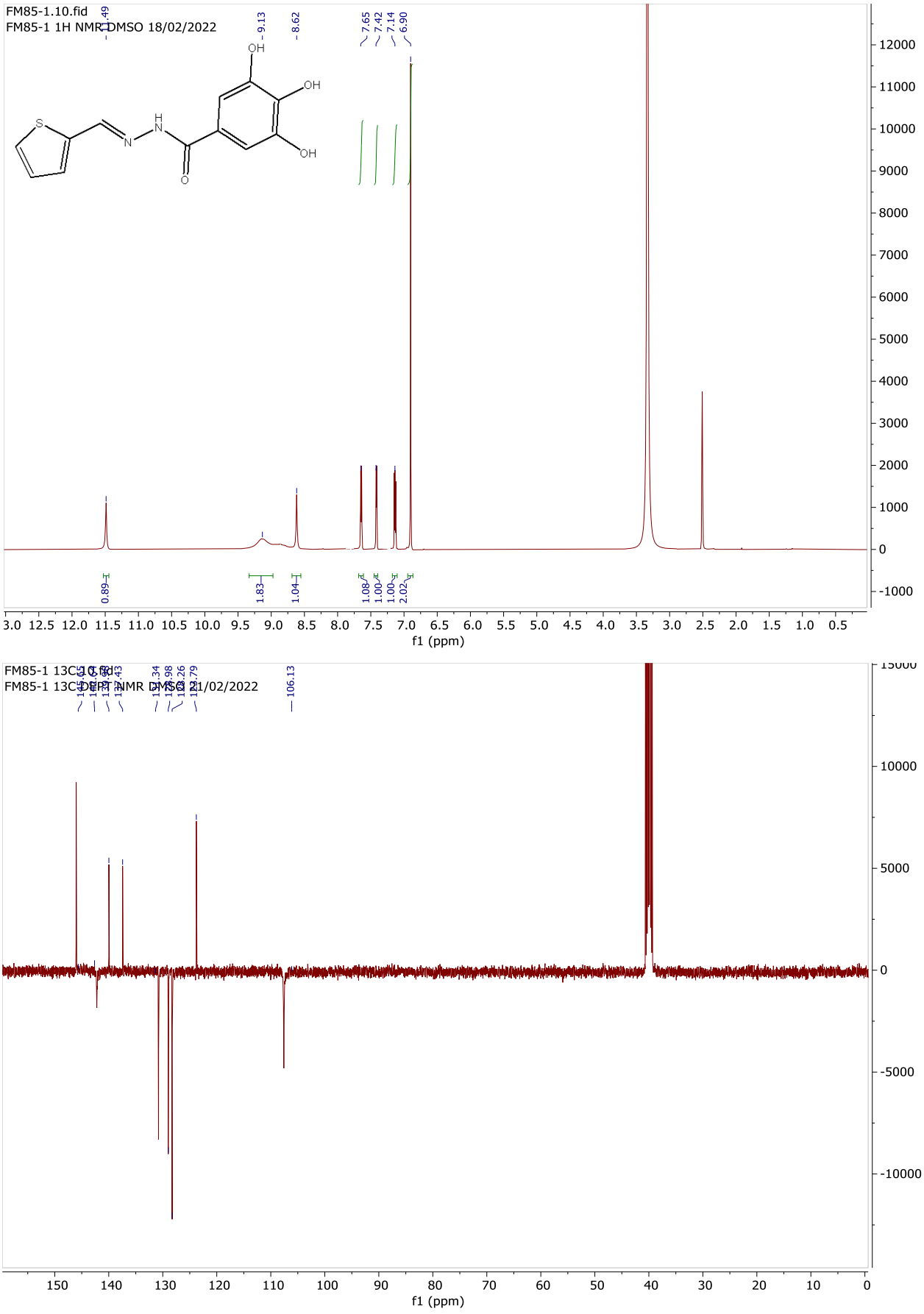


**Figure 7.7** $^{1}$H-NMR (25°C, 400 MHz, DMSO-$d_6$) and $^{13}$C deptq (25°C, 101 MHz, DMSO-$d_6$) NMR spectra of **FM85**.

In the IR spectrum of **FM85** (**Figure 7.8**, top) is possible to observe several stretching bands relative to the O-H and N-H bonds at 3466, 3413, 3333 and 3223 $cm^{-1}$. Furthermore, in the spectrum the C=O and the C=N stretching bands are present respectively at 1575 and 1548 $cm^{-1}$. The absence of a S-H stretching band around 2600 $cm^{-1}$ and the presence of a N-H stretching band indicates that **FM85** in the solid state is found in the thione form.

In the ESI-MS spectra (**Figure 7.8**, bottom), the signal of **FM85** molecular ion is present in both positive (279: $[M+H]^+$ and 301: $[M+Na]^+$) and negative ionization mode (277: $[M-H]^-$). In both ionization modes there also a peaks related to dimeric adducts (positive: $[M+Na]^+$ 579 m/z, negative: $[M-H]^-$ 555 m/z).

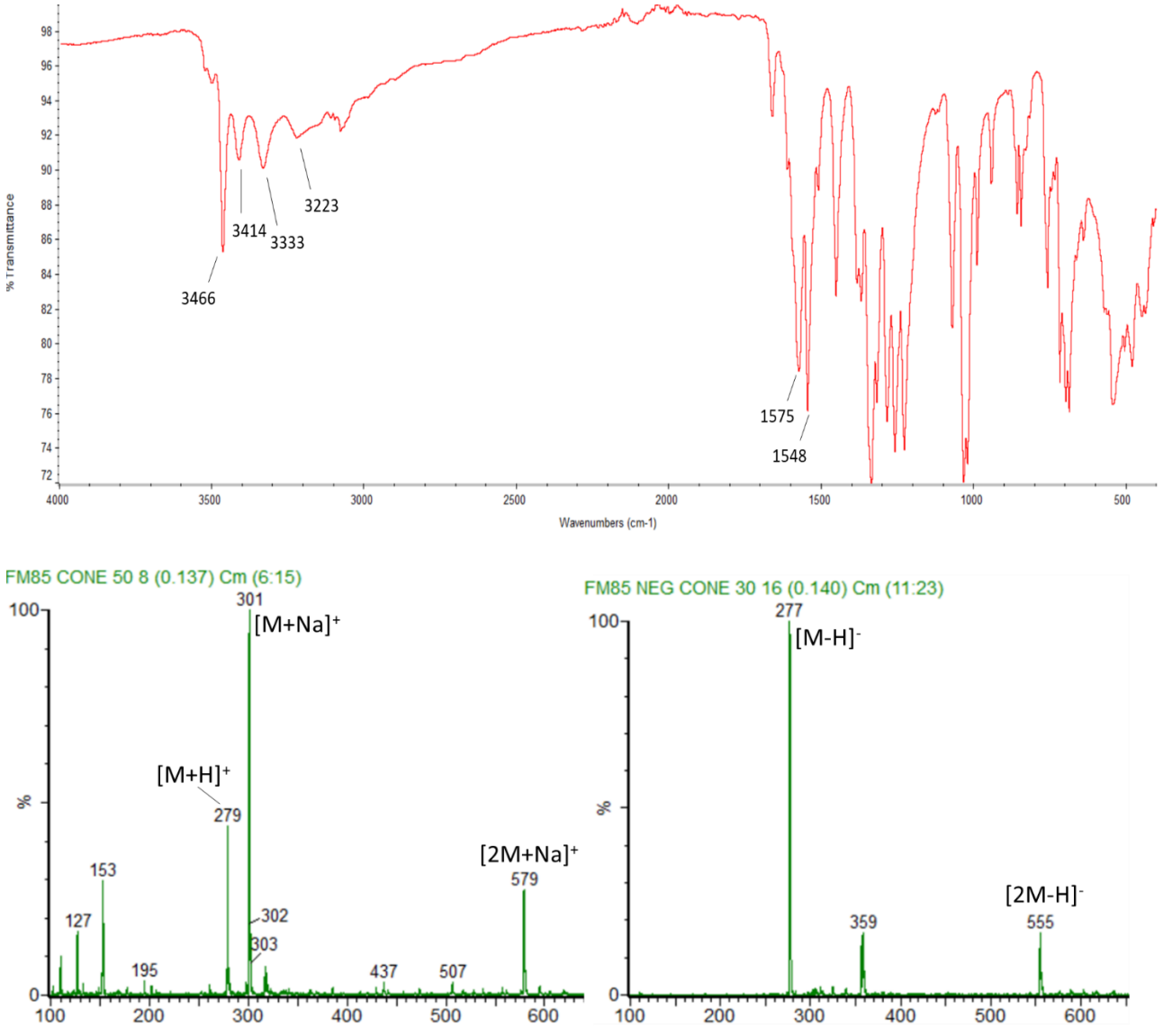


**Figure 7.8** (top) FT-IR spectrum of **FM85**. (bottom) ESI-MS spectra for **FM85**, on the right positive ionization, 50 eV, on the left negative ionization, 30 eV.

The panel of **H1** structural derivatives is under investigation at professor A. Ment's group in the Center for Free-Electron Laser Science CFEL. Preliminary results suggest that compound **FM82** can bind PLpro (**Figure 7.9**) in a highly similar fashion to what observed for **H1**.

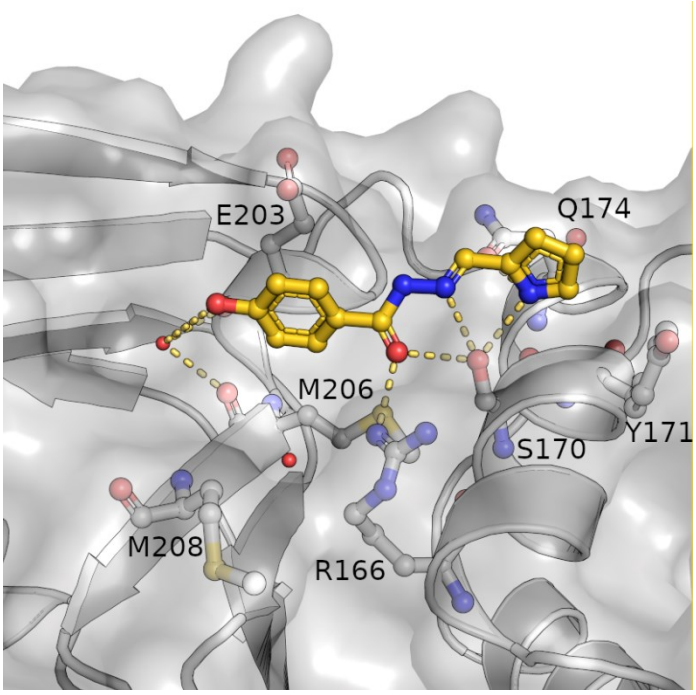


**Figure 7.9** Close-up view on the binding mode of compound **FM82. FM82** and the interacting residues are indicated as sticks. Interactions with the surrounding residues within hydrogen bonding distance are shown as dashed lines.

**FM82**, without two hydroxy groups compared to **H1**, presents its benzene moiety slightly more tilted toward residue E203, likely being stabilized by E203 via π-alkyl interactions. The core interactions appear to be the same as in **H1**, except for residue Q174. To date, the resolution of the structure (2.3 Å) does not allow to tell if the oxygen or the nitrogen of Q174 is pointing towards the ligand.

## 7.4 Conclusions

During this project a panel of 40 chelating compounds and some metal complexes have been tested in an X-ray crystallographic screening against SARS-CoV-2 PLpro, with the aim of targeting the Zn(II) ion essential to the protease activity. Surprisingly, none of the compounds was found to bind the zinc binding site. Instead, six compounds were found binding near sites S1 and S2, that are involved in protein-protein interactions, since they interact with the substrates ubiquitin and ISG15.

The hydrazone derivative **H1** showed a unique and interesting binding mode, impeding the interaction with the natural substrate by sterical hindrance and causing conformational changes in residues involved in the substrate binding. Furthermore, in a fluorescence polarization assay, **H1** proved to give a significant inhibition of ubiquitin cleavage at 500 µM.

Given these promising results, a panel of structural derivatives of compound **H1** was synthesized and characterized. Preliminary results indicate that the hydrazone derivatives **FM82** has a similar binding mode to **H1**. Further investigations on the binding mode will provide useful information on the structure activity relationship of this class of compounds in the inhibition of protein-protein interactions in SARS-CoV-2 PLpro, giving helpful insights for the development of efficient antivirals.

## 7.5 Experimental

### 7.5.1 Materials and methods

#### 7.5.1.1 Chemistry

All reagents of commercial quality were purchased from Sigma-Aldrich and used without further purification. The purity of the synthesized compounds was determined by elemental analysis and verified to be ≥ 95%.

NMR spectra were recorded on a Bruker Advance spectrometer operating at 400 MHz for the $^{1}H$ and at 101 MHz for $^{13}C$ nuclei, at 25°C. All chemical shifts are expressed in ppm.

The ATR-IR spectra were recorded by means of a Nicolet-Nexus (Thermo Fisher) spectrophotometer by using a diamond crystal plate in the range of 4000-400 cm-1.

Elemental analyses were performed by using a FlashEA 1112 series CHNS/O analyser (Thermo Fisher) with gas-chromatographic separation.

Electrospray mass spectral analyses (ESI-MS) were performed with an electrospray ionization (ESI) time-of-flight Micromass 4LCZ spectrometer. Samples were dissolved in methanol. MS spectra were acquired with a DSQII Thermo Fisher apparatus, equipped with a single quadrupole analyser in positive EI mode, by means of a DEP-probe (Direct Exposure Probe) equipped with a Re-filament.

#### 7.5.1.2 Cloning, Expression and Purification of PLpro

The PLpro polypeptide corresponding to amino acid residues 746–1,060 of SARS-CoV-2 nsp3 (YP_009742610.1) was cloned into pETM11 with an additional N-terminal His6-tag and TEVcleavage site. The construct was overexpressed in E. coli Rosetta (DE3) according to a previously published protocol[307] and purified for subsequent crystallization. Lysis was carried out in 50mM NaH2PO4 buffer supplemented with 150mM NaCl and 10mM imidazole at pH 7.2 using ultrasound for cell disruption. After separation of cell fragments and dissolved protein, a subsequent Ni-NTA chromatography step was used to extract the fusion protein. The cleavage of the histidine tag was achieved by TEV protease during an overnight dialysis step at 8°C. After removing the TEV protease and His6- tag via Ni-NTA resin, a final size exclusion chromatography was performed using a HiLoad 16/600 Superdex 75 column attached to an ÄKTA purifier (GE Healthcare) to purify the protein to homogeneity in 50mM Tris-HCl, 150mM NaCl and 1 mM TCEP at pH 7.8.

#### 7.5.1.3 Protein Crystallization

Crystallization of PLpro was achieved by mixing 0.2 µL protein (20mg/ml) with 0.1 µL of reservoir solution consisting of 100mM Tris-HCl buffer pH 8.0, 10% (w/w) glycerol and 0.8M $NaH_2PO_4$/1.2M $K_2HPO_4$. The crystallization drops were prepared using an Oryx6 pipetting robot (Douglas Instruments) and equilibrated by sitting drop vapor diffusion against 40 µL reservoir solution. Bipyramidal crystals appeared within a few days at 4°C and reached a final size of approximately 100 µm. Crystals were soaked with reservoir solution containing up to 5mM of the respective compound with a final DMSO concentration of 5%. After 24 h the soaked crystals were harvested and cryo-cooled in liquid nitrogen for subsequent X-ray diffraction data collection.

#### 7.5.1.4 Data Collection, Processing, Hit Finding and Refinement

Data collection was performed at beamline P11 at the PETRA III storage ring at DESY in Hamburg (Germany). The obtained data sets were processed with DIALS.[308] The results for each data set were subjected to automated structure refinement using phenix[309] followed by pan data set density analysis (PanDDA)[310] using default parameters. The results were manually inspected for hits. Identified hits were further refined by alternating rounds of refinement using phenix.refine[311] and manual model building in COOT.[312]

#### 7.5.1.5 Fluorescence Polarization-Based Activity Assay

Assays were performed using Ub-KG-TAMRA (UbiQ-012, UbiQ bio) and human ISG15-KG-TAMRA (UbiQ-287, UbiQ bio) to determine the inhibitory potential of the selected compounds on PLpro activity following the protocol described by Klemm et al.[313] With substrate concentration kept at 150 nM, PLpro concentration was set to 500 nM for Ub-TAMRA- and to 5 nM for ISG15-TAMRA-cleavage. The protein was preincubated with 500 µM or 5 µM of the selected compounds.

for 20 min at RT before addition of substrate. Reactions were monitored using a Spark 20M plate reader (Tecan) with optical settings for the TAMRA fluorophore (excitation: 540 nm, emission: 590 nm). Data was plotted and analyzed using the software Origin (OriginLab).

7.5.2 Chemistry

**General procedure 1:**

The appropriate aldehyde or ketone (1 eqv) and the appropriate hydrazide (1 eqv) are dissolved in EtOH, then a few drops of $CH_3COOH$ are added and the mixture is left reacted at reflux until the reaction is complete (checked by TLC). In case of chloride salts of hydrazides, an equimolar amount of $Et_3N$ is also added to the mixture. The reaction mixture is cooled to 0°C and, if needed, water is added to promote the precipitation of the product. The solid is then filtered, washed with water and dried, giving the desire products without further purification.

**(Z)-N-ethyl-2-(2-oxoindolin-3-ylidene)hydrazine-1-carbothioamide (FM05** or HL)

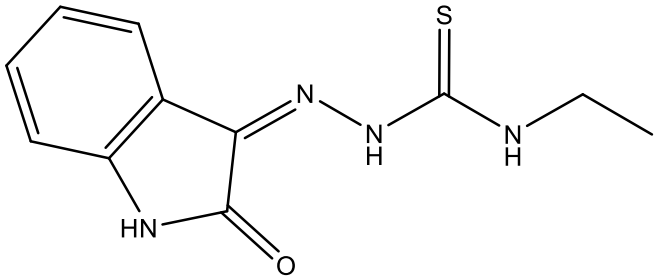


The product was obtained with general procedure 1 as a bright yellow solid. (Y=69%).
$^1$H NMR (600 MHz, DMSO-$d_6$, 25°C) δ 12.54 (s, 1H, NH), 11.22 (b, 1H, NH), 9.31 (t, *J* = 5.9 Hz, 1H, NH), 7.66 (d, *J* = 7.5 Hz, 1H, $CH_{arom}$), 7.35 (t, *J* = 7.6 Hz, 1H, $CH_{arom}$), 7.09 (t, *J* = 7.5 Hz, 1H, $CH_{arom}$), 6.93 (d, *J* = 7.8 Hz, 1H, $CH_{arom}$), 3.63 (p, *J* = 7.0 Hz, 2H, $CH_2$), 1.18 (t, *J* = 7.1 Hz, 3H, $CH_3$).
$^{13}$C NMR (101 MHz, DMSO-$d_6$, 25°C) δ 176.8, 162.8, 142.4, 131.8, 131.4, 122.5, 121.0, 120.1, 111.2, 14.2.
IR (ATR, $cm^{-1}$): ν(NH) = 3304, 3271, 3143; ν(C=N) = 1538.
E.A. calculated for $C_{11}H_{12}N_4OS$: C 53.21, H 4.87, N 22.56, S 12.91. Found: C 53.18, H 4.96, N 22.45, S 12.97.

**(Z)-N,N-dimethyl-2-(2-oxoindolin-3-ylidene)hydrazine-1-carbothioamide (FM06)**

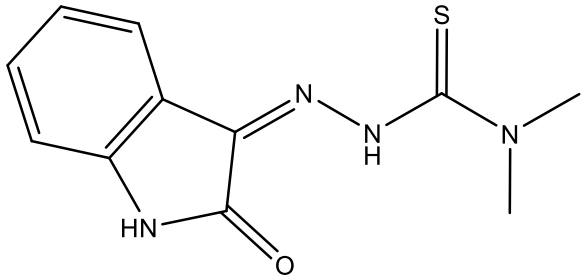


The product was obtained with general procedure 1 as an orange solid. (Y=45%).
$^1$H NMR (600 MHz, DMSO-$d_6$, 25°C) δ 13.43 (s, 1H, NH), 11.29 (s, 1H, NH), 7.55 (d, 1H, *J* = 7.8 Hz, $CH_{arom}$), 7.36 (td, *J* = 7.7, 1.2 Hz, 1H, $CH_{arom}$), 7.10 (td, *J* = 7.6, 0.9 Hz, 1H, $CH_{arom}$), 6.96 (dd, *J* = 7.8, 0.9 Hz, 1H, $CH_{arom}$), 3.37 (s, 6H, $CH_3$).
$^{13}$C NMR (101 MHz, DMSO-$d_6$, 25°C) δ 179.4, 163.3, 142.2, 135.2, 131.4, 123.1, 120.9, 120.6, 111.6.
IR (ATR, $cm^{-1}$): ν(NH) = 3195; ν(C=N) = 1528.
E.A. calculated for $C_{11}H_{12}N_4OS$: C 53.21, H 4.87, N 22.56, S 12.91. Found: C 53.27, H 4.87, N 22.40, S 12.97.

**(Z)-2-(1-methyl-2-oxoindolin-3-ylidene)hydrazine-1-carbothioamide (FM07)**

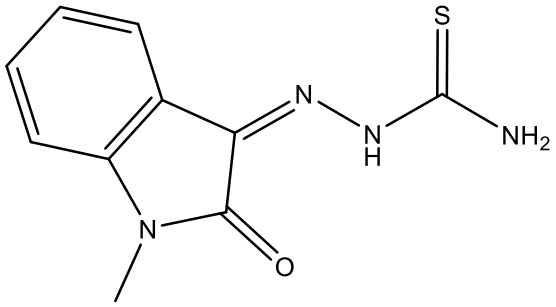

The product was obtained with general procedure 1 as a bright yellow solid. (Y=75%).
$^{1}$H NMR (400 MHz, DMSO-$d_6$, 25°C) δ 12.39 (s, 1H, NH), 9.09 (b, 1H, $NH_2$), 8.74 (b, 1H, $NH_2$), 7.69 (dt, *J* = 7.3, 1.1 Hz, 1H, $CH_{arom}$), 7.45 (td, *J* = 7.7, 1.2 Hz, 1H, $CH_{arom}$), 7.17 (m, 2H, $CH_{arom}$), 3.22 (s, 3H, $NCH_3$).
$^{13}$C NMR (101 MHz, DMSO-$d_6$, 25°C) δ 179.1, 161.3, 144.1, 131.7, 131.7, 123.4, 121.1, 119.7, 110.3, 26.2.
IR (ATR, $cm^{-1}$): ν(NH) = 3424, 3243, 3147; ν(C=N) = 1605.
E.A. calculated for $C_{10}H_{10}N_4OS$: C 51.27, H 4.30, N 23.92, S 13.68. Found: C 51.24, H 4.32, N 23.51, S 14.02.

**(Z)-N-ethyl-2-(1-methyl-2-oxoindolin-3-ylidene)hydrazine-1-carbothioamide (FM08)**

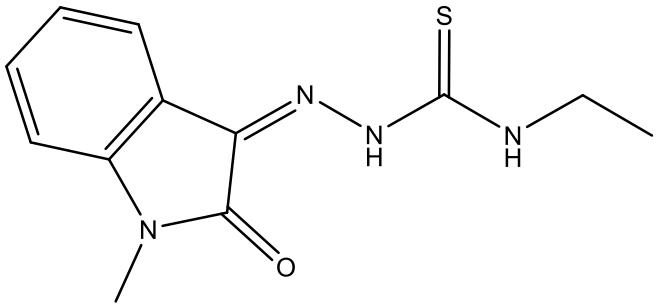

The product was obtained with general procedure 1 as a bright yellow solid. (Y=62%).
$^{1}$H NMR (400 MHz, DMSO-$d_6$, 25°C) δ 12.49 (s, 1H, NH), 9.34 (t, *J* = 5.9 Hz, 1H, NH), 7.70 (m, 1H, $CH_{arom}$), 7.45 (td, *J* = 7.7, 1.2 Hz, 1H, $CH_{arom}$), 7.16 (m, 2H, $CH_{arom}$), 3.65 (qd, *J* = 7.1, 5.9 Hz, 2H, $CH_2$), 3.22 (s, 3H, $NCH_3$), 1.20 (t, *J* = 7.1 Hz, 3H, $CH_3$).
$^{13}$C NMR (101 MHz, DMSO-$d_6$, 25°C) δ 177.1, 161.3, 144.0, 131.6, 131.3, 123.3, 121.0, 119.7, 110.3, 26.2, 14.5.
IR (ATR, $cm^{-1}$): ν(NH) = 3367, 3197; ν(C=N) = 1530.
E.A. calculated for $C_{12}H_{14}N_4OS$: C 54.94, H 5.38, N 21.36, S 12.22. Found: C 54.92, H 5.14, N 21.67, S 12.40.

**(Z)-N,N-dimethyl-2-(1-methyl-2-oxoindolin-3-ylidene)hydrazine-1-carbothioamide (FM09)**

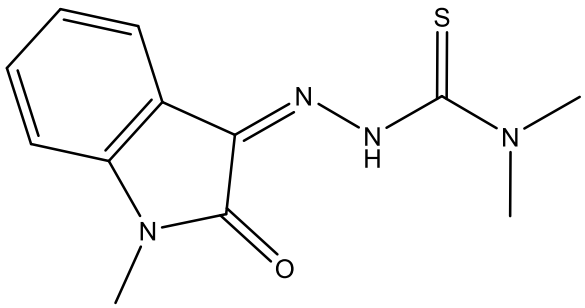

The product was obtained with general procedure 1 as a bright yellow solid. (Y=73%).
$^{1}$H NMR (400 MHz, DMSO-$d_6$, 25°C) δ 13.39 (s, 1H, NH), 7.58 (dd, *J* = 7.2, 1.3 Hz, 1H, $CH_{arom}$), 7.45 (td, *J* = 7.8, 1.3 Hz, 1H, $CH_{arom}$), 7.17 (m, 2H, $CH_{arom}$), 3.38 (s, 6H, $NCH_3$), 3.24 (s, 3H, $NCH_3$).
IR (ATR, $cm^{-1}$): ν(C=N) = 1540.
E.A. calculated for $C_{12}H_{14}N_4OS$: C 54.94, H 5.38, N 21.36, S 12.22. Found: C 54.61, H 5.28, N 21.46, S 12.78.

**(E)-N,N-dimethyl-2-(3,4,5-trihydroxybenzylidene)hydrazine-1-carbothioamide (FM11)**

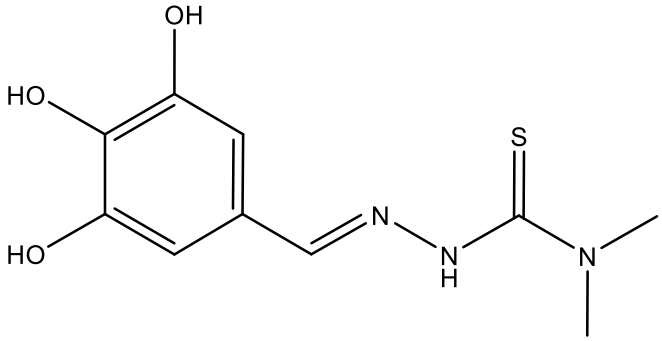


The product was obtained with general procedure 1 as a dark purple solid. (Y=61%)
$^1$H NMR (400 MHz, DMSO-$d_6$, 25°C) δ 10.67 (s, 1H, NH), 7.92 (s, 1H, CH=N), 6.61 (s, 2H, $CH_{arom}$), 3.26 (s, 6H, $NCH_3$).
IR (ATR, $cm^{-1}$): ν(NH+OH) = 3493, 3425, 3359, 3168; ν(C=N) = 1558.
E.A. calculated for $C_{10}H_{13}N_3O_3S$: C 46.68, H 5.88, N 16.33, S 12.46. Found: C 45.04, H 4.91, N 17.25, S 14.22.

**[Zn(II)$L_2$] (FM13)**

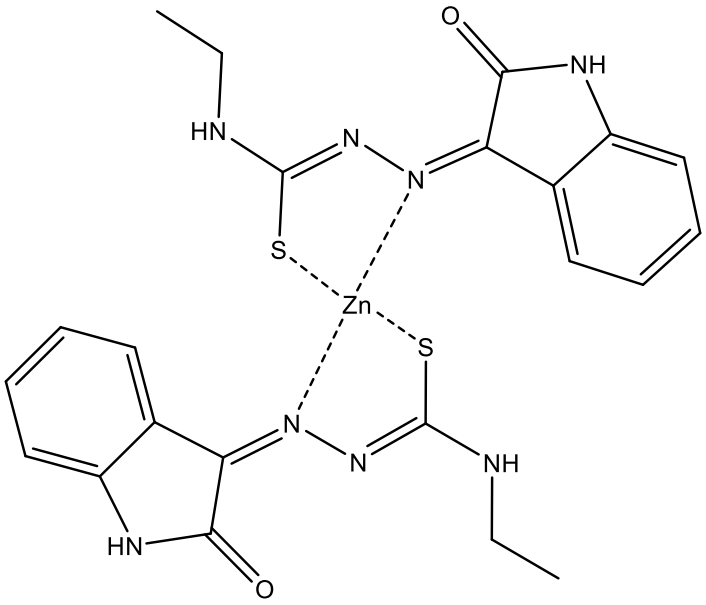


**FM05** (100 mg, 0.403 mmol, 2 eqv) and $Zn(CH_3COO)_2 \cdot 2H_2O$ (44 mg, 0.202 mmol, 1 eqv) are reacted in 25 mL of methanol, at reflux overnight. After that time, a solid is filtrated and washed with methanol and water, obtaining **FM13** as a yellow solid. (Y=33%)
$^1$H NMR (400 MHz, DMSO-$d_6$, 25°C) δ 10.80 (m, 2H, NH), 9.21 (q, *J* = 5.6 Hz, 1H, NH), 8.82 (q, *J* = 5.3 Hz, 1H, NH), 8.21 (dt, *J* = 7.7, 2.1 Hz, 1H, $CH_{arom}$), 8.04 (dd, *J* = 7.5, 1.3 Hz, 1H, $CH_{arom}$), 7.33 (td, *J* = 7.7, 1.3 Hz, 1H, $CH_{arom}$), 7.28 (td, *J* = 7.7, 1.4 Hz, 1H, $CH_{arom}$), 7.11 (m, 2H, $CH_{arom}$), 6.99 (m, 2H, $CH_{arom}$), 3.60 (m, 4H, $CH_2$), 1.23 (m, 6H, $CH_3$).
ESI-MS : m/z= 561 ($M+H^+$).
IR (ATR, $cm^{-1}$): ν(NH) = 3395, 3132, 3057; ν(C=N) = 1613, 1594.
E.A. calculated for $C_{22}H_{22}N_8O_2S_2Zn$: C 47.19, H 3.96, N 20.01, S 11.45. Found: C 47.16, H 3.98, N 20.77, S 11.45.

**2-((1H-pyrrol-2-yl)methylene)hydrazine-1-carboxamide (FM58)**

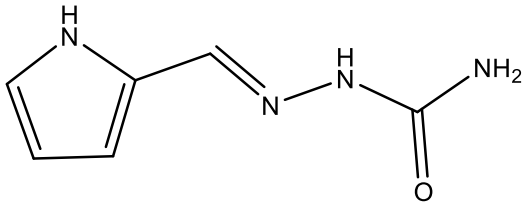

The product was obtained with general procedure 1 as a dark purple solid. (Y=68%)

$^{1}$H NMR (400 MHz, DMSO-$d_6$, 25°C) δ 11.20 (b, 1H, NH), 9.92 (s, 1H, NH), 7.61 (s, 1H, CH=N); 6.87 (td, *J* = 2.5, 1.4 Hz, 1H, $CH_{arom}$); 6.45 (b, 2H, $NH_2$); 6.24 (ddd, *J* = 3.6, 2.5, 1.4 Hz, 1H, $CH_{arom}$); 6.04 (dt, *J* = 3.6, 2.5 Hz, 1H, $CH_{arom}$).

$^{13}$C NMR (101 MHz, DMSO-$d_6$, 25°C) δ 157.1 (Cq), 131.3 (CH), 128.2 (Cq), 120.7 (CH), 110.8 (CH); 108.7 (CH).

ESI-MS : m/z= 153 ($M+H^+$).

IR (ATR, $cm^{-1}$): ν($NH_2$) = 3379; ν(NH) = 3218, 2973; ν(C=O) = 1661; ν(C=N) = 1591.

E.A. calculated for $C_6H_8N_4O \cdot 0.66\ H_2O$: C 43.99, H 5.54, N 34.20. Found: C 44.14, H 5.85, N 33.99.

**N'-((1H-pyrrol-2-yl)methylene)benzohydrazide (FM59)**

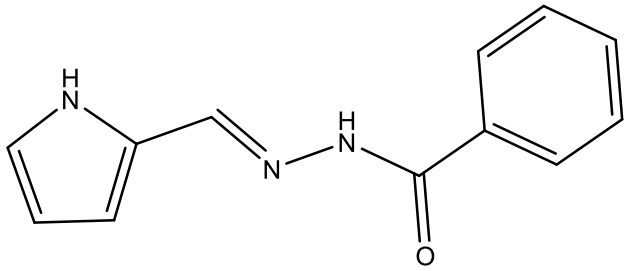

The product was obtained with general procedure 1 as a white solid. (Y=98%)

$^{1}$H NMR (400 MHz, DMSO-$d_6$, 25°C) δ 11.54 (b, 1H, NH), 11.52 (b, 1H, NH), 8.29 (s, 1H, CH=N), 7.90 (m, 2H, $CH_{arom}$), 7.57 (m, 1H, $CH_{arom}$), 7.52 (m, 2H, $CH_{arom}$), 6.92 (m, 1H, $CH_{arom}$), 6.49 (m, 1H, $CH_{arom}$), 6.14 (m, 1H, $CH_{arom}$).

$^{13}$C NMR (101 MHz, DMSO-$d_6$, 25°C) δ 162.7 (Cq), 140.9 (CH), 133.8 (Cq), 131.5 (CH), 128.4 (CH), 127.5 (CH), 127.4 (CH), 127.1 (Cq), 122.6 (CH), 113.4 (CH), 109.3 (CH).

ESI-MS : m/z= 214 ($M+H^+$).

IR (ATR, $cm^{-1}$): ν(NH) = 3225, 2973; ν(C=O) = 1608; ν(C=N) = 1566.

E.A. calculated for $C_{12}H_{11}N_3O \cdot 0.66\ H_2O$: C 63.99, H 5.52, N 18.66. Found: C 63.93, H 5.56, N 18.82.

**3,4,5-trimethoxybenzohydrazide (FM60)**

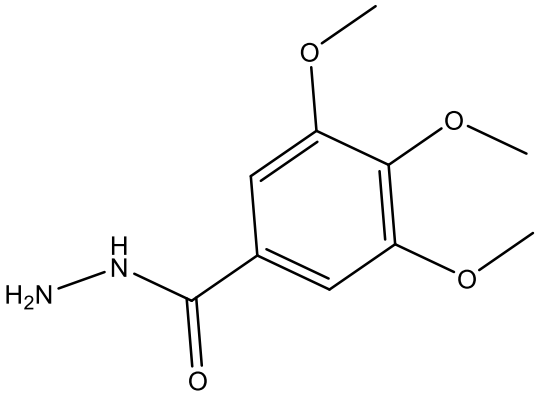

3,4,5-trimethoxy methylbenzoate (450 mg, 1.99 mmol, 1 eqv) is suspended in 4 mL of EtOH, then 1.7 mL of hydrazine (1.754 g, 35 mmol, 17.6 eqv) is added. The mixture is stirred for 30' at r.t. to complete solubilization, then is left reacting at reflux for 5 hours. After that time the reaction mixture is cooled to 0°C, the solid is filtered and washed with $H_2O$, obtaining the product as a white solid (265 mg, Y=59%).
$^1$H NMR (400 MHz, DMSO-$d_6$, 25°C) δ 9.71 (b, 1H, NH), 7.16 (s, 2H, $CH_{arom}$), 4.46 (b, 1H, $NH_2$), 4.45 (b, 1H, $NH_2$), 3.81 (s, 6H, $OCH_3$), 3.69 (s, 3H, $OCH_3$).

**(E)-N'-((1H-pyrrol-2-yl)methylene)-3,4,5-trimethoxybenzohydrazide (FM61)**

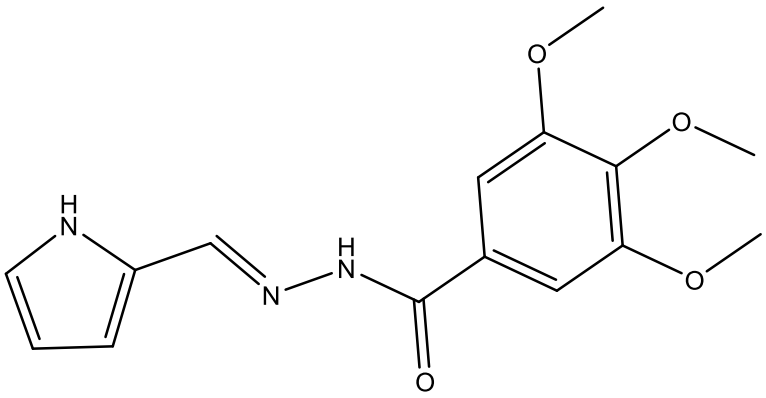

The product was obtained with general procedure 1 as a white solid. (Y=47%)
$^1$H NMR (400 MHz, DMSO-$d_6$, 25°C) δ 11.56 (b, 1H, NH), 11.37 (s, 1H, NH), 8.28 (s, 1H, CH=N), 7.21 (s, 2H, $CH_{arom}$), 6.92 (m, 1H, $CH_{arom}$), 6.49 (m, 1H, $CH_{arom}$), 6.14 (dt, *J* = 3.5, 2.3 Hz, 1H, $CH_{arom}$), 3.86 (s, 6H, $OCH_3$), 3.72 (s, 3H, $OCH_3$).
$^{13}$C NMR (101 MHz, DMSO-$d_6$, 25°C) δ 162.0 (Cq), 152.7 (Cq), 140.9 (CH), 140.2 (Cq), 128.9 (Cq), 127.0 (Cq), 122.6 (CH), 113.5 (CH), 109.3 (CH), 105.1 (CH), 60.1 ($OCH_3$), 56.1 ($OCH_3$).
ESI-MS : m/z= 304 ($M+H^+$).
IR (ATR, $cm^{-1}$): ν(NH) = 3206, 2996; ν(C=O) = 1634; ν(C=N) = 1573.
E.A. calculated for $C_{15}H_{17}N_3O_4$: C 59.40, H 5.65, N 13.85. Found: C 59.83, H 5.73, N 13.81.

**(E)-2-(3,4,5-trihydroxybenzylidene)hydrazine-1-carboxamide (FM80)**

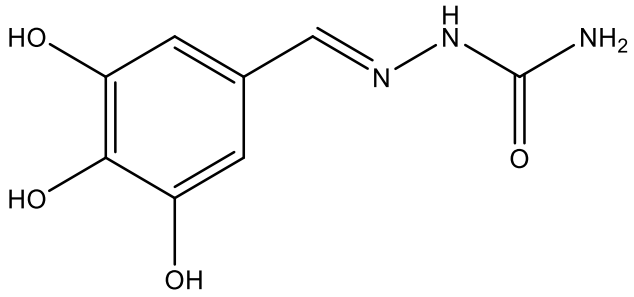


The product was obtained with general procedure 1 as a pale yellow solid. (Y=80%)
$^{1}$H NMR (400 MHz, DMSO-$d_6$, 25°C) δ 9.92 (b, 1H, OH), 8.92 (b, 2H, OH), 8.46 (s, 1H, CH=N), 7.59 (b, 1H, NH), 6.58 (s, 2H, $CH_{arom}$), 6.22 (b, 2H, $NH_2$).
$^{13}$C NMR (101 MHz, DMSO-$d_6$, 25°C) δ 156.7 (Cq), 146.1 (Cq), 140.5 (CH), 134.8 (Cq), 125.1 (Cq), 105.8 (CH).
ESI-MS : m/z= 212 ($M+H^+$).
IR (ATR, $cm^{-1}$): ν($NH_2$)+ ν(OH) = 3494, 3446, 3379; ν(NH) = 3030; ν(C=O) = 1681; ν(C=N) = 1572.
E.A. calculated for $C_8H_9N_3O_4$: C 45.5, H 4.30, N 19.90. Found: C 46.10, H 4.33, N 19.57.

**(E)-N'-((1H-pyrrol-2-yl)methylene)-2-hydroxybenzohydrazide (FM81)**

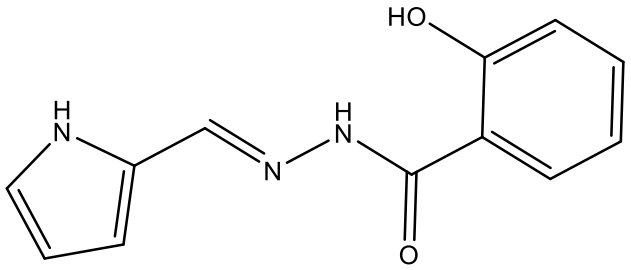


The product was obtained with general procedure 1 as a white solid. (Y=77%)
$^{1}$H NMR (400 MHz, DMSO-$d_6$, 25°C) δ 12.12 (b, 1H, NH), 11.58 (b, 2H, NH+OH), 8.31 (s, 1H, CH=N), 7.90 (dd, *J* = 7.9, 1.7 Hz, 1H, $CH_{arom}$), 7.43 (ddd, *J* = 8.6, 7.2, 1.7 Hz, 1H, $CH_{arom}$), 6.95 (m, 3H, $CH_{arom}$), 6.54 (m, 1H, $CH_{arom}$), 6.17 (q, *J* = 2.5 Hz, 1H, 1H, $CH_{arom}$).
$^{13}$C NMR (101 MHz, DMSO-$d_6$, 25°C) δ 164.5 (Cq), 159.4 (Cq), 142.0 (CH), 133.6 (CH), 128.1 (CH), 126.8 (Cq), 122.9 (CH), 118.8 (CH), 117.3 (CH), 115.5 (Cq), 113.9 (CH), 109.4 (CH).
ESI-MS : m/z= 230 ($M+H^+$).
IR (ATR, $cm^{-1}$): ν(OH) = 3286; ν(NH) = 3105, 2925; ν(C=O) = 1616; ν(C=N) = 1570.
E.A. calculated for $C_6H_8N_4O$: C 62.87, H 4.84, N 18.33. Found: C 62.95, H 4.93, N 18.42.

**(E)-N'-((1H-pyrrol-2-yl)methylene)-4-hydroxybenzohydrazide (FM82)**

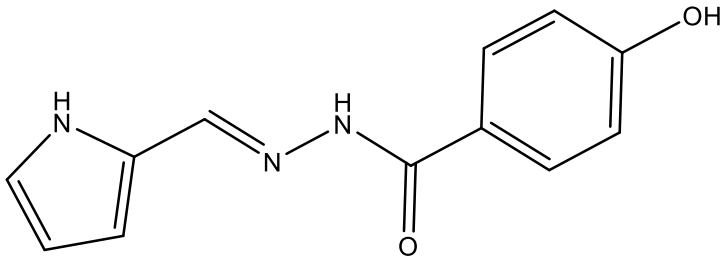


The product was obtained with general procedure 1 as a white solid. (Y=59%)
$^{1}$H NMR (400 MHz, DMSO-$d_6$, 25°C) δ 11.55 (b, 1H), 11.24 (b, 1H), 10.04 (b, 1H), 8.32 (s, 1H, CH=N), 7.78 (d, *J* = 8.3 Hz, 2H, $CH_{arom}$), 6.90 (td, *J* = 2.6, 1.4 Hz, 1H, $CH_{arom}$), 6.85 (m, 2H, $CH_{arom}$), 6.45 (m, 1H, $CH_{arom}$), 6.14 (m, 1H, $CH_{arom}$).
$^{13}$C NMR (101 MHz, DMSO-$d_6$, 25°C) δ 162.3 (Cq), 160.4 (Cq), 140.1 (CH), 129.5 (CH), 127.2 (Cq), 124.27 (cq), 122.2 (CH), 114.9 (CH), 112.9 (CH), 109.1 (CH).
ESI-MS : m/z= 230 ($M+H^+$).
IR (ATR, $cm^{-1}$): ν(OH) = 3361; ν(NH) = 3212; ν(C=O) = 1604; ν(C=N) = 1537.
E.A. calculated for $C_6H_8N_4O$: C 62.87, H 4.84, N 18.33. Found: C 62.21, H 5.02, N 18.75.

**3,4,5-hydroxybenzohydrazide (FM83)**

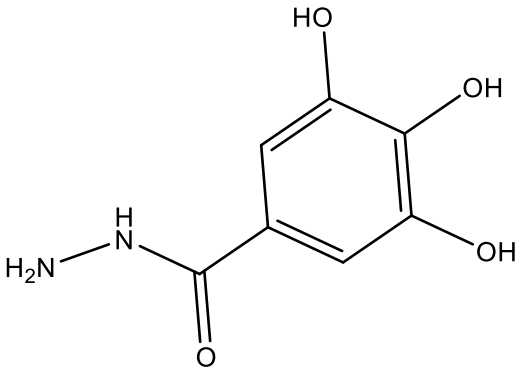


3,4,5-hydroxy methylbenzoate (1.84 g, 9.99 mmol, 1 eqv) is suspended in 4 mL of EtOH, then 9 mL of hydrazine (9.29 g, 185 mmol, 18 eqv) is added. The mixture is stirred for 30' at r.t. to complete solubilization, then is left reacting at reflux for 5 hours. After that time the reaction mixture is cooled to 0°C, the solid is filtered and washed with $H_2O$, obtaining the product as a white solid (1.05 g, Y=57%).
$^{1}$H NMR (600 MHz, DMSO-$d_6$, 25°C) δ 9.27 (b, 1H, NH), 6.74 (s, 2H, $CH_{arom}$), 4.26 (b, 2H, $NH_2$).

**(E)-3,4,5-trihydroxy-N'-((1-methyl-1H-pyrrol-2-yl)methylene)benzohydrazide (FM84)**

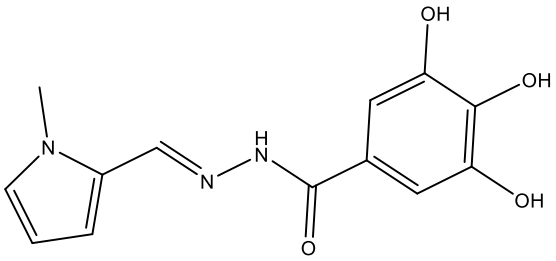


The product was obtained with general procedure 1, with a further DCM wash, as a yellow solid. (Y=34%)
$^{1}$H NMR (400 MHz, DMSO-$d_6$, 25°C) δ 11.18 (b, 1H, NH), 9.03 (b, 2H, OH), 8.34 (s, 1H, CH=N), 6.93 (t, *J* = 2.2 Hz, 1H, $CH_{arom}$), 6.88 (s, 2H, $CH_{arom}$), 6.44 (dd, *J* = 3.8, 1.7 Hz, 1H, $CH_{arom}$), 6.08 (m, 1H, $CH_{arom}$), 3.84 (s, 3H, $NCH_3$).
$^{13}$C NMR (101 MHz, DMSO-$d_6$, 25°C) δ 162.6 (C=O), 145.5 (Cq), 139.9 (CH), 136.7 (Cq), 127.6 (CH), 127.4 (Cq), 123.7 (Cq), 113.7 (CH), 108.2 (CH), 106.9 (CH), 35.8 ($CH_3$).
ESI-MS : m/z= 276 ($M+H^+$).
IR (ATR, $cm^{-1}$): ν(OH) = 3510-3214; ν(NH) = 3063; ν(C=O) = 1590; ν(C=N) = 1542.
E.A. calculated for $C_{13}H_{13}N_3O_4 \cdot 0.5\ CH_3CH_2OH$: C 56.37, H 5.41, N 14.09. Found: C 56.16, H 5.01, N 14.50.

**(E)-3,4,5-trihydroxy-N'-(thiophen-2-ylmethylene)benzohydrazide (FM85)**

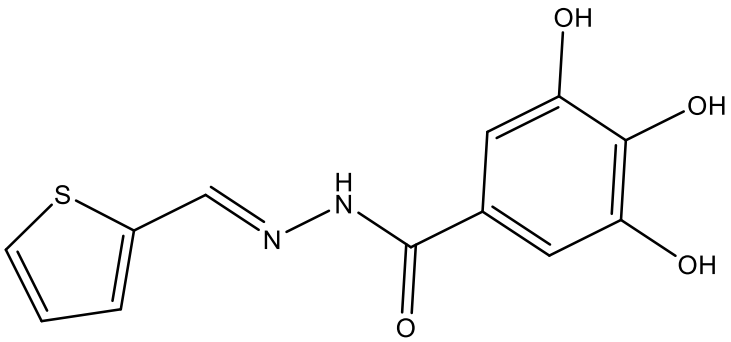


The product was obtained with general procedure 1, with a further DCM wash, as a white solid. (Y=89%)
$^{1}$H NMR (400 MHz, DMSO-$d_6$, 25°C) δ 11.49 (b, 1H, NH), 9.05 (b, 2H, OH), 8.62 (s, 1H, CH=N), 7.64 (d, *J* = 5.0 Hz, 1H, CH), 7.42 (d, *J* = 3.5 Hz, 1H, CH), 7.14 (dd, *J* = 5.0, 3.5 Hz, 1H, CH), 6.90 (s, 2H, $CH_{arom}$).
$^{13}$C NMR (101 MHz, DMSO-$d_6$, 25°C) δ 163.1 (C=O), 145.5 (Cq), 141.7 (CH), 139.5 (Cq), 136.9 (Cq), 130.3 (CH), 128.5 (CH), 127.8 (CH), 123.31 (Cq), 107.1 (CH).
ESI-MS : m/z= 279 ($M+H^+$).
IR (ATR, $cm^{-1}$): ν(OH+NH) = 3466, 3414, 3333, 3223, 3079; ν(C=O) = 1575; ν(C=N) = 1548.
E.A. calculated for $C_{12}H_{10}N_2O_4S$: C 51.79, H 3.62, N 20.07, S 11.52. Found: C 52.40, H 4.26, N 9.89, S 11.72.

**3,4,5-trihydroxy-N'-((1E,2E)-3-(4-hydroxy-3-methoxyphenyl)allylidene)benzohydrazide (FM86)**

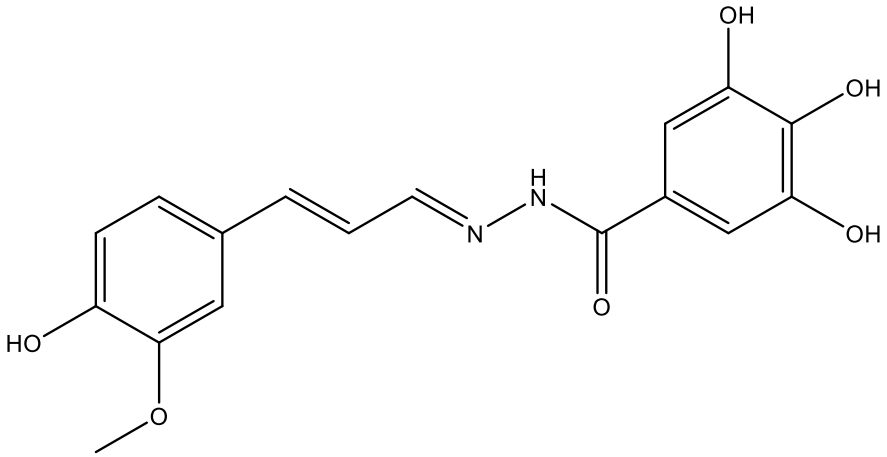


The product was obtained with general procedure 1 as an orange solid. (Y=87%)
$^{1}$H NMR (400 MHz, DMSO-$d_6$, 25°C) δ 11.32 (b, 1H, NH), 9.11 (b, 4H, OH), 8.15 (d, *J* = 7.1 Hz, 1H, CH=N), 7.22 (d, *J* = 2.0 Hz 1H, CH), 7.00 (dd, *J* = 8.2, 1.9 Hz, 1H, CH), 6.88 (m, 4H, CH), 6.78 (d, *J* = 8.1 Hz, 1H, CH), 3.83 (s, 3H, $OCH_3$).
$^{13}$C NMR (101 MHz, DMSO-$d_6$, 25°C) δ 162.9 (Cq), 149.1 (CH), 147.9 (Cq), 147.7 (Cq), 145.5 (Cq), 138.8 (CH), 136.8 (Cq), 127.7 (Cq), 123.5 (Cq), 123.0 (CH), 121.1 (CH), 115.6 (CH), 110.2 (CH), 107.1 (CH), 55.6 ($OCH_3$).
ESI-MS : m/z= 345 ($M+H^+$).
IR (ATR, $cm^{-1}$): ν(OH) = 3483, 3209; ν(NH) = 3060; ν(C=O) = 1598; ν(C=N) = 1513.
E.A. calculated for $C_{17}H_{16}N_2O_6 \cdot CH_3CH_2OH$: C 58.45, H 5.68, N 7.18. Found: C 58.85, H 5.52, N 7.60.

**(E)-2-((E)-3-(4-hydroxy-3-methoxyphenyl)allylidene)hydrazine-1-carbothioamide (FM87)**

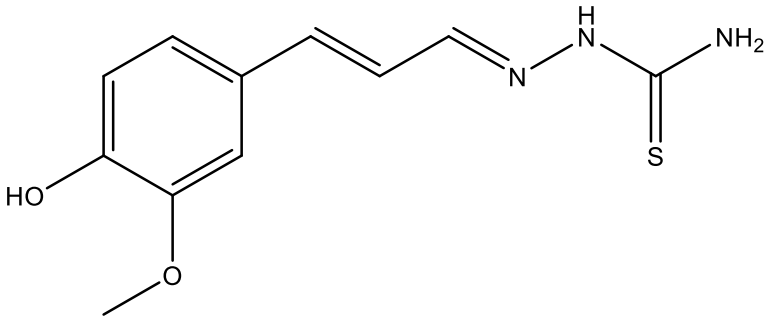


The product was obtained with general procedure 1 as a yellow solid. (Y=70%)
$^{1}$H NMR (400 MHz, DMSO-$d_6$, 25°C) δ 11.28 (s, 1H, NH), 9.36 (s, 1H, OH), 8.08 (b, 1H, $NH_2$), 7.86 (d, *J* = 9.3 Hz, 1H, CH=N), 7.48 (b, 1H, $NH_2$), 7.14 (d, *J* = 2.0 Hz, 1H, $CH_{arom}$), 6.97 (dd, *J* = 8.2, 1.9 Hz, 1H, $CH_{arom}$), 6.89 (d, *J* = 16.0 Hz, 1H, $CH_{arom}$), 6.76 (d, *J* = 8.2 Hz, 1H, $CH_{arom}$), 6.71 (dd, *J* = 16.0, 9.3 Hz, 1H, CH), 3.80 (s, 3H, $OCH_3$).
$^{13}$C NMR (101 MHz, DMSO-$d_6$, 25°C) δ 177.4 (Cq), 147.9 (Cq), 145.4 (CH), 139.6 (CH), 127.5 (Cq), 122.0 (CH), 121.1 (CH), 115.6 (CH), 110.0 (CH), 55.6 ($CH_3$).
ESI-MS : m/z= 252 ($M+H^+$).
IR (ATR, $cm^{-1}$): ν($NH_2$)+ν(OH) = 3444, 3359; ν(NH) = 3172; ν(C=N) = 1587; ν(C=S) = 1226.
E.A. calculated for $C_{11}H_{13}N_3O_2S \cdot 0.66\ H_2O$: C 50.05, H 5.73, N 15.92, S 12.15. Found: C 50.22, H 5.61, N 15.29, S 12.02.

**N',2-bis((E)-4-hydroxy-3,5-dimethoxybenzylidene)hydrazine-1-carbothiohydrazide (FM88)**

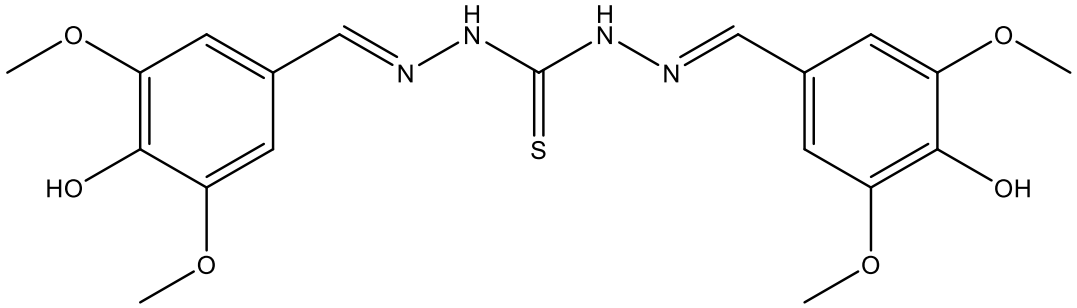

The product was obtained with general procedure 1 (with 2 eqv of aldehyde) as a white solid. (Y=83%)
$^{1}$H NMR (400 MHz, DMSO-$d_6$, 25°C) δ 11.70 (b, 1H, NH), 11.43 (b, 1H, NH), 8.89 (b, 2H, OH), 8.42 (b, 1H, CH=N), 8.03 (b, 1H, CH=N), 7.06 (m, 4H, ArH), 3.83 (s, 12H, $OCH_3$).
$^{13}$C NMR (101 MHz, DMSO-$d_6$, 25°C) δ 173.9 (Cq), 148.1 (Cq), 138.0 (Cq), 124.2 (Cq), 105.5 (CH), 104.8 (CH), 56.1 ($CH_3$).
ESI-MS : m/z= 435 ($M+H^+$).
IR (ATR, $cm^{-1}$): ν(OH) = 3396, 3284; ν(NH) = 3010; ν(C=N) = 1535; ν(C=S) = 1206.
E.A. calculated for $C_{19}H_{22}N_4O_6S$: C 52.53, H 5.10, N 12.90, S 7.38. Found: C 52.23, H 5.11, N 12.67, S 7.47.

**N',2-bis((E)-3,4,5-trihydroxybenzylidene)hydrazine-1-carbohydrazide (FM89)**

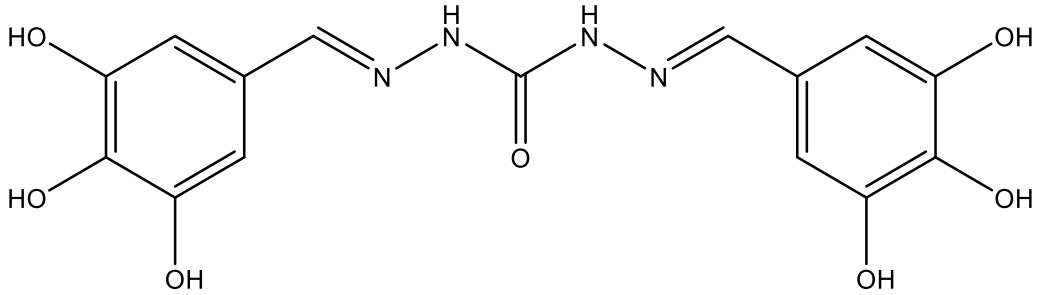

The product was obtained with general procedure 1 (with 2 eqv of aldehyde) as a pale grey solid. (Y=73%)
$^{1}$H NMR (400 MHz, DMSO-$d_6$, 25°C) δ 10.23 (s, 2H, NH), 8.98 (s, 4H, OH), 8.53 (b, 2H, OH), 7.87 (s, 2H, CH=N), 6.66 (s, 4H, ArH).
$^{13}$C NMR (101 MHz, DMSO-$d_6$, 25°C) δ 152.1 (Cq), 146.1 (Cq), 135.0 (Cq), 125.1 (Cq), 106.0 (CH).
ESI-MS : m/z= 363 ($M+H^+$).
IR (ATR, $cm^{-1}$): ν(OH) = 3499, 3447, 3314; ν(NH) = 3128; ν(C=N) = 1598; ν(C=S) = 1290.
E.A. calculated for $C_{15}H_{14}N_4O_7 \cdot H_2O$: C 47.37, H 4.24, N 14.73. Found: C 47.72, H 4.29, N 14.74.

# 8. **Conclusions and perspectives**

The first subject of this PhD project regarded the synthesis of TSC copper(II) complexes as compounds with anticancer activity, being water soluble to improve their pharmacological application. Within this thesis, several water-soluble TSC derivatives and their Cu(II) complexes were synthetized and characterized by FTIR, ESI-MS, NMR spectroscopy, elemental analysis and X-ray diffraction.

A first strategy to improve the water solubility of previously studied TSC Cu(II) complexes with promising anticancer activity consisted in the insertion of a sulfonated group on the TSC scaffold. The sulfonated copper(II) complexes were observed in different solid state stoichiometries, indicating monomeric [Cu(NaHL)Cl] and dimeric $[Cu(HL)(H_2O)]_2$ complexes. The *in vitro* biological evaluation of a panel comprising the copper complexes, the free ligands and a Ni(II) and a Zn(II) complexes gave encouraging results ($IC_{50}$ in the micromolar range for the Cu(II) complexes), implying that the presence of Cu(II) is crucial for the anticancer activity of these water-soluble compounds. 3D *in vitro* assays conducted with the copper complexes also gave excellent $IC_{50}$ values. Altogether, the results suggest that these compounds have an interesting anticancer profile. Considering the 3D *in vitro* assay results, a future *in vivo* assay on the sulfonated TSCs would be the next step in the cytotoxic activity evaluation of these compounds. The increased water-solubility of the copper complexes should facilitate the compounds administration in the *in vivo* tests. The ongoing mechanistic studies performed by professor Gandin's group in the University of Padova will give insight on the targets of these complexes. The analogue non-sulfonated TSCs copper complexes were found to efficiently inhibit protein disulfide isomerase (PDI), an emerging target for copper compounds with anticancer activity; hence the investigation is considering PDI as one of the possible targets of the sulfonated TSC complexes. Additionally, a panel of structurally modified ligands, comprising sulfonated TSC, semicarbazones and hydrazones and their Cu(II) complexes have been synthetised and characterized.

Furthermore, a second strategy to improve the solubility of TSC Cu(II) complexes was explored, with the conjugation of a glucose moiety to the TSC scaffold, that could additionally enhance their selectivity by exploiting the augmented glucose metabolism of cancer cells. A series of glyco-conjugate TSC derivatives and their Cu(II) have been synthetised and characterized. These compounds were obtained with good yields and with a few synthetic steps, overcoming the common drawback of the difficult and tedious sugar chemistry. The ongoing evaluation of the cytotoxic activity of these water-soluble compounds performed by professor Gandin's group in the university of Padova will give information on the activity of these Cu(II) glyco-functionalized derivatives, that have not been extensively investigated in the literature. Furthermore, the internalization of these compounds through glucose transporters will be evaluated to study the mechanisms of cellular uptake of the glyco-TSC complexes.

The second subject of this thesis concerned the synthesis and characterization of chelating compounds as inhibitors of viral metal-dependent enzymes, by using the validated strategy of the metal chelation of the ion cofactors within the active site of the target enzymes. Different chelating compounds targeting the metal-dependent endonuclease domain of RdRP in viruses of the *Bunyavirales* order were synthetised and characterized.

A panel of furo[3,4-d]pyrimidin-7-one derivatives, substituted with various aromatic chelating moieties, was synthetized and characterized. The activity of the compounds was tested on three different bunyaviruses (BUNV-mCherry, LACV and RVRF) in cellular assays by Prof. Johan Neyts'research group at Rega Institute for Medical Research (Leuven, Belgium). Unfortunately, these compounds displayed either no activity towards the viruses or high cytotoxicity towards the host cells. A thermal shift assays conducted on LCMV cap-snatching endonuclease suggested that this scaffold do not interact with the enzyme. Altogether, these results imply that the furo[3,4-d]pyrimidin-7-one scaffold substituted with aromatic

chelating moieties is not suitable as inhibitor of bunyaviruses endonucleases. Additionally, the scaffold repurposing of a panel of variously substituted 6,7-dihydroxyisoindolin-1-ones, known inhibitors of influenza endonuclease, was undertaken. An expanded panel of these molecules was synthetised and characterized with NMR, IR, ESI-MS and elemental analysis. The interaction between a model compound and the divalent cations Mg(II) or Mn(II) in solution was studied by means of visible spectrophotometric titrations, in order to determine the binding constants. The results confirmed that this scaffold can coordinate Mn(II) and Mg(II) ions, hence it can be suitable for the coordination of the endonuclease cofactors (*in vivo* and *in vitro*). Finally, the enzymatic activity of the synthetized compound was tested on two different Cap-Endonucleases of the *Bunyavirales* order (ANDV and TOSV) by Prof. Stephen Gunther and Dr. Yaiza Fernandez Garcia's research group at the Bernhard Nocht Institute for Tropical Medicine, Hamburg. All the compounds exhibited inhibition activity towards the investigated enzymes, with $IC_{50}$ values in the low micromolar range. The micromolar inhibition activity exerted by the compounds could be caused primarily by the metal cofactor chelation. Nonetheless, the 6,7-dihydroxyisoindolin-1-ones panel shows an effective and consistent inhibition towards the tested Cap-endonuclease, suggesting that the scaffold is suitable for the development of improved candidates of broad-spectrum bunyaviruses endonuclease inhibitors.

Finally, due to the arrival of the COVID-19 pandemic, an in-house library of 40 chelating compounds and some metal complexes have been tested in an X-ray crystallographic screening against SARS-CoV-2 PLpro, with the aim of targeting the Zn(II) ion essential to the protease activity. The X-ray screening was performed by professor A. Ment's group in the Center for Free-Electron Laser Science CFEL, Deutsches Elektronen-Synchrotron DESY (Hamburg). Surprisingly, none of the compounds was found to bind the zinc binding site. Instead, six compounds were found binding near sites S1 and S2, that are involved in protein-protein interactions, by interacting with the substrates ubiquitin and ISG15. The hydrazone derivative **H1** showed a unique and interesting binding mode and a significant inhibition of ubiquitin cleavage at 500 µM in a fluorescence polarization assay. Given these promising results, a panel of structural derivatives of compound **H1** was synthesized and characterized. Further investigations on the binding mode of the hydrazones will provide useful information on the structure activity relationship of this class of compounds in the inhibition of protein-protein interactions in SARS-CoV-2 PLpro, giving helpful insights for the development of efficient antivirals.

# Bibliography


[1] W. Maret, *Int. J. Mol. Sci.* **2016**, *17*, 1–8.

[2] R. H. Holm, P. Kennepohl, E. I. Solomon, *Chem. Rev.* **1996**, *96*, 2239–2314.

[3] C. Orvig, M. J. Abrams, *Chem. Rev.* **1999**, *99*, 2201–2203.

[4] P. J. Sadler, *Adv. Inorg. Chem.* **1991**, *36*.

[5] N. C. Lloyd, H. W. Morgan, B. K. Nicholson, R. S. Ronimus, *Angew. Chemie - Int. Ed.* **2005**, *44*, 941–944.

[6] B. Rosenberg, *Platin. Met. Rev* **1971**, 42–51.

[7] C. L. Fox, S. M. Modak, *Antimicrob. Agents Chemother.* **1974**, *5*, 582–588.

[8] C. U. Herborn, E. Honold, M. Wolf, J. Kemper, S. Kinner, G. Adam, J. Barkhausen, *Invest. Radiol.* **2007**, *42*, 58–62.

[9] G. J. Brewer, *J. Cell. Mol. Med.* **2003**, *7*, 11–20.

[10] P. Pace, M. E. Di Francesco, C. Gardelli, S. Harper, E. Muraglia, E. Nizi, F. Orvieto, A. Petrocchi, M. Poma, M. Rowley, et al., *J. Med. Chem.* **2007**, *50*, 2225–2239.

[11] J. Trivedi, D. Mahajan, R. J. Jaffe, A. Acharya, D. Mitra, S. N. Byrareddy, *Curr. HIV/AIDS Rep.* **2020**, *17*, 63–75.

[12] WHO, *World Heal. Organ. Model List Essent. Med.* **2019**.

[13] G. Giaccone, *Drugs* **2000**, *59*, 9–17.

[14] V. Cepeda, M. A. Fuertes, J. Castilla, C. Alonso, C. Quevedo, J. M. Pérez, *Anticancer. Agents Med. Chem.* **2007**, *7*, 3–18.

[15] E. R. Jamieson, S. J. Lippard, *Chem. Rev.* **1999**, *99*, 2467–2498.

[16] D. P. Gately, S. B. Howell, *Br. J. Cancer* **1993**, *67*, 1171–1176.

[17] Y. Jung, S. J. Lippard, *Chem. Rev.* **2007**, *107*.

[18] D. Wang, S. J. Lippard, *Nat. Rev.* **2005**, *4*, 307–320.

[19] M. A. Fuertes, C. Alonso, J. M. Pérez, *Chem. Rev.* **2003**, *103*, 645–662.

[20] W. J. F. van der Vijgh, *Clin. Pharmacokinet.* **1991**, *21*, 242–261.

[21] M. Shimada, H. Itamochi, J. Kigawa, *Cancer Manag. Res.* **2013**, *5*, 67–76.

[22] R. N. Seetharam, A. Sood, S. Goel, *Ecancermedicalscience* **2009**, *3*, 1–8.

[23] K. H. Lee, M. S. Hyun, H.-K. Kim, H. M. Jin, J. Yang, H. S. Song, Y. R. Do, H. M. Ryoo, J. S. Chung, D. Y. Zang, et al., *Cancer Res. Treat.* **2009**, *41*, 12–18.

[24] M. J. McKeage, *Expert Opin. Investig. Drugs* **2001**, *10*, 119–128.

[25] E. Wexselblatt, D. Gibson, *J. Inorg. Biochem.* **2012**, *117*, 220–229.

[26] E. Alessio, L. Messori, *Molecules* **2019**, *24*, 1–20.

[27] M. J. Clarke, S. Bitler, D. Rennert, M. Buchbinder, A. D. Kelman, *J. Inorg. Biochem.* **1980**, *12*, 79–87.

[28] B. K. Keppler, W. Rupp, *J. Cancer Res. Clin. Oncol.* **1986**, *111*, 166–168.

[29] S. Kapitza, M. Pongratz, M. A. Jakupec, P. Heffeter, W. Berger, L. Lackinger, B. K. Keppler, B. Marian, *J. Cancer Res. Clin. Oncol.* **2005**, *131*, 101–110.

[30] R. Trondl, P. Heffeter, C. R. Kowol, M. A. Jakupec, W. Berger, B. K. Keppler, *Chem. Sci.* **2014**, *5*, 2925–2932.

[31] A. Bergamo, R. Gagliardi, V. Scarcia, A. Furlani, E. Alessio, G. Mestroni, G. Sava, *J. Pharmacol. Exp. Ther.* **1999**, *289*, 559–564.

[32] E. Alessio, *Eur. J. Inorg. Chem.* **2017**, 1549–1560.

[33] S. Leijen, S. A. Burgers, P. Baas, D. Pluim, M. Tibben, E. van Werkhoven, E. Alessio, G. Sava, J. H. Beijnen, J. H. M. Schellens, *Invest New Drugs* **2015**, *33*, 201–214.

[34] P. Jia, R. Ouyang, P. Cao, X. Tong, X. Zhou, T. Lei, *J. Coord. Chem.* **2017**, *70*, 2175–2201.

[35] P. M. Gullino, *Anticancer Res.* **1986**, *6*, 153–158.

[36] C. Santini, M. Pellei, V. Gandin, M. Porchia, F. Tisato, C. Marzano, *Chem. Rev.* **2014**, *114*, 815–862.

[37] B. E. Kim, T. Nevitt, D. J. Thiele, *Nat. Chem. Biol.* **2008**, *4*, 176–185.

[38] C. Olivares, F. Solano, *Pigment Cell Melanoma Res.* **2009**, *22*, 750–760.

[39] N. E. Hellman, S. Kono, G. M. Mancini, A. J. Hoogeboom, G. J. De Jong, J. D. Gitlin, *J. Biol. Chem.* **2002**, *277*, 46632–46638.

[40] Y. C. Horng, P. A. Cobine, A. B. Maxfield, H. S. Carr, D. R. Winge, *J. Biol. Chem.* **2004**, *279*, 35334–35340.

[41] C. K. wa. Tsang, Y. Liu, J. Thomas, Y. Zhang, X. F. S. Zheng, *Nat. Commun.* **2014**, *5*, 3446.

[42] D. A. da Silva, A. De Luca, R. Squitti, M. Rongioletti, L. Rossi, C. M. L. Machado, G. Cerchiaro, *J. Inorg. Biochem.* **2022**, *226*, 111634.

[43] M. C. Linder, M. Hazegh-Azam, *Am. J. Clin. Nutr.* **1996**, *63*, DOI 10.1093/ajcn/63.5.797.

[44] I. Bremner, *Am. J. Clin. Nutr.* **1998**, *67*, DOI 10.1093/ajcn/67.5.1069S.

[45] W. H. Koppenol, *Redox Rep.* **2001**, *6*, 229–234.

[46] G. Malgieri, M. Palmieri, L. Russo, R. Fattorusso, P. V. Pedone, C. Isernia, *FEBS J.* **2015**, *282*, 4480–4496.

[47] M. V. Babak, D. Ahn, *Biomedicines* **2021**, *9*, DOI 10.3390/biomedicines9080852.

[48] N. K. Y. Wee, D. C. Weinstein, S. T. Fraser, S. J. Assinder, *Int. J. Biochem. Cell Biol.* **2013**, *45*, 960–963.

[49] R. S. Ohgami, D. R. Campagna, A. McDonald, M. D. Fleming, *Blood* **2006**, *108*, 1388–1394.

[50] R. L. Peterson, S. Kim, K. D. Karlin, *Copper Enzymes*, Elsevier Ltd., **2013**.

[51] M. Deponte, *Biochim. Biophys. Acta - Gen. Subj.* **2013**, *1830*, 3217–3266.

[52] A. Bhattacharjee, K. Chakraborty, A. Shukla, *Metallomics* **2017**, *9*, 1376–1388.

[53] J. H. Freedman, J. Peisach, *Biochem. Biophys. Res. Commun.* **1989**, *164*, 134–140.

[54] P. Ferenci, K. Caca, G. Loudianos, S. Tanner, I. Sternlieb, *Liver Int.* **2003**, 139–142.

[55] A. Ala, A. P. Walker, K. Ashkan, J. S. Dooley, M. L. Schilsky, *Lancet* **2007**, *369*, 397–408.

[56] S. G. Kaler, *Nat. Publ. Gr.* **2011**, *7*, 15–29.

[57] P. De Bie, P. Muller, C. Wijmenga, L. W. J. Klomp, *J. Med. Genet.* **2007**, 673–688.

[58] N. M. Anderson, M. C. Simon, *Curr. Biol.* **2020**, *30*, R921–R925.

[59] D. Yoshida, Y. Ikeda, S. Nakazawa, *J. Neurooncol.* **1993**, *16*, 109–115.

[60] K. Geraki, M. J. Farquharson, D. A. Bradley, *Biol. Phys. Med. Biol* **2002**, *47*, 2327–2339.

[61] M. Diez, M. Arroyo, F. Cerdan, M. Munoz, M. A. Martin, J. L. Balibrea, *Oncology* **1989**, *46*, 230–234.

[62] M. Ebara, H. Fukuda, R. Hatano, H. Saisho, Y. Nagato, K. Suzuki, K. Nakajima, M. Yukawa, F. Kondo, A. Nakayama, et al., *J. Hepatol.* **2000**, *33*, 415–422.

[63] W. I. Mortada, A. Awadalla, S. Khater, A. Ahmed, E. T. Hamam, M. El-zayat, A. A. Shokeir, *Environ. Sci. Pollut. Res.* **2020**, *27*, 15835–15841.

[64] G. D. Kaiafa, Z. Saouli, M. D. Diamantidis, Z. Kontoninas, V. Voulgaridou, M. Raptaki, S. Arampatzi, M. Chatzidimitriou, V. Perifanis, *Eur. J. Intern. Med.* **2012**, *23*, 738–741.

[65] S. Itoh, W. K. Ha, O. Nakagawa, K. Ozumi, S. M. Lessner, H. Aoki, K. Akram, R. D. McKinney, M. Ushio-Fukai, T. Fukai, *J. Biol. Chem.* **2008**, *283*, 9157–9167.

[66] S. Gulec, J. F. Collins, *J. Trace Elem. Med. Biol.* **2014**, *28*, 459–464.

[67] S. Blockhuys, D. C. Brady, P. Wittung-Stafshede, *Breast Cancer* **2020**, *27*, 505–509.

[68] S. Blockhuys, E. Celauro, C. Hildesjö, A. Feizi, O. Stål, J. C. Fierro-González, P. Wittung-Stafshede, *Metallomics* **2017**, *9*, 112–123.

[69] M. L. Turski, D. C. Brady, H. J. Kim, B.-E. Kim, Y. Nose, C. M. Counter, D. R. Winge, D. J. Thiele, *Mol. Cell. Biol.* **2012**, *32*, 1284–1295.

[70] D. C. Brady, M. S. Crowe, M. L. Turski, G. A. Hobbs, X. Yao, A. Chaikuad, S. Knapp, K. Xiao, S. L. Campbell, D. J. Thiele, et al., *Nature* **2014**, *509*, 492–496.

[71] Y. Mizutani, H. Nakanishi, Y. N. Li, H. Matsubara, K. Yamamoto, N. Sato, T. Shiraishi, T. Nakamura, K. Mikami, K. Okihara, et al., *Int. J. Oncol.* **2007**, *30*, 919–925.

[72] S. Li, J. Zhang, H. Yang, C. Wu, X. Dang, Y. Liu, *Sci. Rep.* **2015**, *5*, 1–17.

[73] W. Feng, F. Ye, W. Xue, Z. Zhou, Y. J. Kang, *Mol. Pharmacol.* **2009**, *75*, 174–182.

[74] A. M. Baker, D. Bird, G. Lang, T. R. Cox, J. T. Erler, *Oncogene* **2013**, *32*, 1863–1868.

[75] G. MacDonald, I. Nalvarte, T. Smirnova, M. Vecchi, N. Aceto, A. Dolemeyer, A. Frei, S. Lienhard, J. Wyckoff, D. Hess, et al., *Sci. Signal.* **2014**, *7*, 1–13.

[76] E. D. Harris, D. Ph, *Nutr. Rev.* **2004**, *62*, 60–64.

[77] F. Soncin, J. D. Guitton, T. Cartwright, J. Badet, *Biochem. Biophys. Res. Commun.* **1997**, *236*, 604–610.

[78] S. Brem, S. A. Grossman, K. A. Carson, P. New, J. B. Alavi, T. Mikkelsen, J. D. Fisher, N. Approaches, *Neuro. Oncol.* **2005**, *7*, 246–253.

[79] J. Lu, *Mol. Cancer Ther.* **2010**, *9*, 2458–2467.

[80] Y. Huang, M. T. Kuo, Y. Liu, Y. Cheng, P. Wu, *Front. Oncol.* **2019**, *9*, 1–11.

[81] G. J. Brewer, S. D. Merajver, *Integr. Cancer Ther.* **2002**, *1*, 327–337.

[82] D. Denoyer, S. Masaldan, S. La Fontaine, M. A. Cater, *Metallomics* **2015**, *7*, 1459–1476.

[83] C. Trejo-solís, D. Jimenez-farfan, S. Rodriguez-enriquez, F. Fernandez-valverde, A. Cruz-salgado, L. Ruiz-azuara, J. Sotelo, *BMC Cancer* **2012**, *12*.

[84] A. De Vizcaya-Ruiz, A. Rivero-Muller, L. Ruiz-Ramirez, G. E. N. Kass, L. R. Kelland, R. M. Orr, M. Dobrota, *Toxicol. Vitr.* **2000**, *14*, 1–5.

[85] Z. Aguilar-Jiménez, M. González-Ballesteros, S. G. Dávila-Manzanilla, A. Espinoza-Guillén, L. Ruiz-Azuara, *Int. J. Mol. Sci.* **2022**, *23*, 12756.

[86] C. Marzano, V. Gandin, M. Pellei, D. Colavito, G. Papini, G. G. Lobbia, E. Del Giudice, M. Porchia, F. Tisato, C. Santini, *J. Med. Chem.* **2008**, *51*, 798–808.

[87] L. W. Oberley, *Antioxid. Redox Signal.* **2001**, *3*, 461–472.

[88] C. Muscoli, S. Cuzzocrea, D. P. Riley, J. L. Zweier, Z. Wang, D. Salvemini, *Br. J. Pharmacol.* **2003**, *140*, 445–460.

[89] J. M. Matés, *Toxicology* **2000**, *153*, 83–104.

[90] C. R. Kowol, B. K. Keppler, C. G. Hartinger, U. Jungwirth, *Antioxid. Redox Signal.* **2011**, *15*, DOI 10.1089/ars.2010.3663.

[91] M. Devereux, D. O'Shea, M. O'Connor, H. Grehan, G. Connor, M. McCann, G. Rosair, F. Lyng, A. Kellett, M. Walsh, et al., *Polyhedron* **2007**, *26*, 4073–4084.

[92] M. Devereux, M. Mccann, D. O. Shea, M. O. Connor, E. Kiely, V. Mckee, D. Naughton, A. Fisher, A. Kellett, M. Walsh, et al., *Bioinorg. Chem. Appl.* **2006**, 1–11.

[93] B. Coyle, P. Kinsella, M. Mccann, M. Devereux, R. O. Connor, M. Clynes, K. Kavanagh, *Toxicol. Vitr.* **2004**, *18*, 63–70.

[94] S. Tardito, O. Bussolati, F. Gaccioli, R. Gatti, S. Guizzardi, J. Uggeri, L. Marchiò, M. Lanfranchi, R. Franchi-Gazzola, *Histochem. Cell Biol.* **2006**, *126*, 473–482.

[95] V. Gandin, M. Pellei, F. Tisato, M. Porchia, C. Santini, C. Marzano, *J. Cell. Mol. Med.* **2012**, *16*, 142–151.

[96] S. E. Bryanf, E. Frieden, *Biochemistry* **1967**, *6*.

[97] T. F. Kagawa, B. H. Geierstanger, A. H. J. Wang, P. S. Ho, *J. Biol. Chem.* **1991**, *266*, 20175–20184.

[98] D. S. Sigman, D. R. Graham, V. D'Aurora, A. M. Stern, *J. Biol. Chem.* **1979**, *254*, 12269–12272.

[99] R. Buchtík, Z. Trávníček, J. Vančo, *J. Inorg. Biochem.* **2012**, *116*, 163–171.

[100] L. J. Tang, X. Chen, Y. N. Sun, J. Ye, J. Lu, Y. Han, X. Jiang, C. C. Cheng, C. C. He, P. H. Qiu, et al., *J. Inorg. Biochem.* **2011**, *105*, 1623–1629.

[101] S. Gama, I. Santos, F. Mendes, F. Marques, I. C. Santos, M. F. Carvalho, I. Correia, J. C. Pessoa, A. Paulo, *J. Inorg. Biochem.* **2011**, *105*, 637–644.

[102] J. C. Wang, *Annu. Rev. Biochem.* **1996**, *65*, 635–692.

[103] D. Jayaraju, A. K. Kondapi, *Curr. Sci.* **2001**, *81*, 787–792.

[104] J. Chen, Y. Huang, G. Liu, Z. Afrasiabi, E. Sinn, S. Padhye, Y. Ma, *Toxicol. Appl. Pharmacol.* **2004**, *197*, 40–48.

[105] O. F. Ikotun, E. M. Higbee, W. Ouellette, R. P. Doyle, *J. Inorg. Biochem.* **2009**, *103*, 1254–1264.

[106] Q. P. Dou, D. M. Smith, K. G. Daniel, A. Kazi, *Prog. Cell Cycle Res.* **2003**, *5*, 441–446.

[107] H. C. A. Drexler, *Proc. Natl. Acad. Sci. U. S. A.* **1997**, *94*, 855–860.

[108] K. G. Daniel, P. Gupta, R. H. Harbach, W. C. Guida, Q. P. Dou, *Biochem. Pharmacol.* **2004**, *67*, 1139–1151.

[109] S. S. Hindo, M. Frezza, D. Tomco, M. J. Heeg, L. Hryhorczuk, B. R. McGarvey, Q. P. Dou, C. N. Verani, *Eur. J. Med. Chem.* **2009**, *44*, 4353–4361.

[110] Y. Xiao, D. Chen, X. Zhang, Q. Cui, Y. Fan, C. Bi, Q. P. Dou, *Int. J. Oncol.* **2010**, *37*, 81–87.

[111] H. A. Khan, B. Mutus, *Front. Chem.* **2014**, *2*, 1–9.

[112] S. Narindrasorasak, P. Yao, B. Sarkar, *Biochem. Biophys. Res. Commun.* **2003**, *311*, 405–414.

[113] A. M. Benham, *Antioxidants Redox Signal.* **2012**, *16*, 781–789.

[114] S. Hager, V. F. S. Pape, V. Pósa, B. Montsch, L. Uhlik, G. Szakács, S. Tóth, N. Jabronka, B. K. Keppler, C. R. Kowol, et al., *Antioxidants Redox Signal.* **2020**, *33*, 395–414.

[115] S. Hager, K. Korbula, B. Bielec, M. Grusch, C. Pirker, M. Schosserer, L. Liendl, M. Lang, J. Grillari, K. Nowikovsky, et al., *Cell Death Dis.* **2018**, *9*, 1052.

[116] M. Carcelli, M. Tegoni, J. Bartoli, C. Marzano, G. Pelosi, M. Salvalaio, D. Rogolino, V. Gandin, *Eur. J. Med. Chem.* **2020**, *194*, 112266.

[117] H. Beraldo, D. Gambino, *Mini-Reviews Med. Chem.* **2004**, *4*, 31–39.

[118] T. S. Lobana, R. Sharma, G. Bawa, S. Khanna, *Coord. Chem. Rev.* **2009**, *253*, 977–1055.

[119] M. E. Helsel, K. J. Franz, *Dalt. Trans.* **2015**, *44*, 8760–8770.

[120] P. Heffeter, V. F. S. Pape, É. A. Enyedy, B. K. Keppler, G. Szakacs, C. R. Kowol, *Antioxidants Redox Signal.* **2019**, *30*, 1062–1082.

[121] R. C. Deconti, B. R. Toftness, K. C. Agrawal, R. Tomchick, J. A. R. Mead, J. R. Joseph, B. Bertino, A. C. Sartorelli, W. A. Creasey, *Cancer Res.* **1972**, *32*, 1455–1462.

[122] L. Feun, M. Modiano, K. Lee, J. Mao, A. Marini, N. Savaraj, P. Plezia, B. Almassian, E. Colacino, J. Fischer, et al., *Cancer Chemother. Pharmacol.* **2002**, *50*, 223–229.

[123] J. Chao, T. W. Synold, R. J. Morgan, C. Kunos, J. Longmate, H. J. Lenz, D. Lim, S. Shibata, V. Chung, R. G. Stoller, et al., *Cancer Chemother. Pharmacol.* **2012**, *69*, 835–843.

[124] M. J. Mackenzie, D. Saltman, H. Hirte, J. Low, C. Johnson, G. Pond, M. J. Moore, *Invest. New Drugs* **2007**, *25*, 553–558.

[125] S. Attia, J. Kolesar, M. R. Mahoney, H. C. Pitot, D. Laheru, J. Heun, W. Huang, J. Eickhoff, C. Erlichman, K. D. Holen, *Invest. New Drugs* **2008**, *26*, 369–379.

[126] K. Y. Salim, S. M. Vareki, W. R. Danter, S. San-marina, *Oncotarget* **2016**, *7*.

[127] N. C. Synnott, D. O'Connell, J. Crown, M. J. Duffy, *Breast Cancer Res. Treat.* **2020**, *179*, 47–56.

[128] Z. Kovacevic, S. Chikhani, D. B. Lovejoy, D. R. Richardson, *Mol. Pharmacol.* **2011**, *80*, 598–609.

[129] Z. Guo, D. R. Richardson, D. S. Kalinowski, Z. Kovacevic, K. C. Tan-un, G. C. Chan, *J. Hematol. Oncol.* **2016**, *9*, 1–16.

[130] P. J. Jansson, P. C. Sharpe, P. V Bernhardt, D. R. Richardson, *J. Med. Chem.* **2010**, *53*, 5759–5769.

[131] S. Gu, P. Yu, J. Hu, Y. Liu, Z. Li, Y. Qian, Y. Wang, Y. Gou, F. Yang, *Eur. J. Med. Chem.* **2019**, *164*, 654–664.

[132] Y. Huang, E. Kong, J. Zhan, S. Chen, C. Gan, Z. Liu, L. Pang, J. Cui, *Bioinorg. Chem. Appl.* **2017**, *2017*.

[133] P. S. Donnelly, J. R. Liddell, S. Lim, B. M. Paterson, M. A. Cater, M. S. Savva, A. I. Mot, J. L. James, I. A. Trounce, A. R. White, et al., *PNAS* **2012**, *109*, 47–52.

[134] F. G. Parsa, M. A. H. Feizi, R. Safaralizadeh, S. A. Hosseini-Yazdi, M. Mahdavi, *J. Biol. Inorg. Chem.* **2020**, *25*, 383–394.

[135] A. Sîrbu, O. Palamarciuc, M. V. Babak, J. M. Lim, K. Ohui, E. A. Enyedy, S. Shova, D. Darvasiová, P. Rapta, W. H. Ang, et al., *Dalt. Trans.* **2017**, *46*, 3833–3847.

[136] S. A. Hosseini-Yazdi, A. Mirzaahmadi, A. A. Khandar, V. Eigner, M. Dušek, F. Lotfipour, M. Mahdavi, S. Soltani, G. Dehghan, *Inorganica Chim. Acta* **2017**, *458*, 171–180.

[137] E. B. Hager, B. C. E. Makhubela, G. S. Smith, *Dalt. Trans.* **2012**, *41*, 13927–13935.

[138] D. Rogolino, A. Gatti, M. Carcelli, G. Pelosi, F. Bisceglie, F. M. Restivo, F. Degola, A. Buschini, S. Montalbano, D. Feretti, et al., *Sci. Rep.* **2017**, *7*, 11214.

[139] T. V. Petrasheuskaya, M. A. Kiss, O. Dömötör, T. Holczbauer, N. V. May, G. Spengler, A. Kincses, A. Čipak Gašparović, É. Frank, É. A. Enyedy, *New J. Chem.* **2020**, *44*, 12154.

[140] M. Ranjani, P. Kalaivani, F. Dallemer, S. Selvakumar, T. Kalpana, R. Prabhakaran, *Inorganica Chim. Acta* **2022**, *530*, 120683.

[141] S. I. Orysyk, G. G. Repich, V. V. Bon, V. V. Dyakonenko, V. V. Orysyk, Y. L. Zborovskii, O. V. Shishkin, V. I. Pekhnyo, M. V. Vovk, *Inorganica Chim. Acta* **2014**, *423*, 496–503.

[142] S. A. Hosseini-Yazdi, A. Mirzaahmadi, A. A. Khandar, V. Eigner, M. Dušek, M. Mahdavi, S. Soltani, F. Lotfipour, J. White, *Polyhedron* **2017**, *124*, 156–165.

[143] S. A. Hosseini-Yazdi, A. Mirzaahmadi, A. A. Khandar, V. Eigner, M. Dušek, F. Lotfipour, M. Mahdavi, S. Soltani, G. Dehghan, E. B. Hager, et al., *Dalt. Trans.* **2017**, *67*, 13927–13935.

[144] *SAINT SAX, Area Detect. Integr. Siemens Anal. Instruments Inc., Madison, Wisconsin, USA* **n.d.**

[145] *Sheldrick G. SADABS Siemens Area Detect. Absorpt. Correct. Software, Univ. Goettingen, Ger. 1996.* **n.d.**

[146] A. Altomare, M. C. Burla, M. Camalli, G. L. Cascarano, C. Giacovazzo, A. Guagliardi, A. G. G. Moliterni, G. Polidori, R. Spagna, *J. Appl. Crystallogr.* **1999**, *32*, 115–119.

[147] G. M. Sheldrick, *Acta Crystallogr.* **2008**, *A64*, 112–122.

[148] L. J. Farrugia, *J. Appl. Crystallogr.* **1999**, *32*, 837–838.

[149] M. C. Alley, D. A. Scudiere, A. Monks, M. L. Hursey, M. J. Czerwinski, D. L. Fine, B. J. Abbott, J. G. Mayo, R. H. Shoemaker, M. R. Boyd, *Cancer Res.* **1988**, *48*, 589–601.

[150] V. Gandin, C. Ceresa, G. Esposito, S. Indraccolo, M. Porchia, F. Tisato, C. Santini, M. Pellei, C. Marzano, *Sci. Rep.* **2017**, *7*, 1–12.

[151] O. Warburg, *Science (80-. ).* **1956**, *123*, 309–314.

[152] S. H. Kim, K. H. Baek, *Int. J. Mol. Sci.* **2021**, *22*, 6173.

[153] M. G. V. Heiden, L. C. Cantley, C. B. Thompson, *Science (80-. ).* **2009**, *324*, 1029–1033.

[154] M. L. Macheda, S. Rogers, J. D. Best, *J. Cell. phisiology* **2005**, *202*, 654–662.

[155] C. Granchi, F. Minutolo, *ChemMedChem* **2012**, *7*, 1318–1350.

[156] M. Jang, S. S. Kim, J. Lee, *Exp. Mol. Med.* **2013**, *45*, 1–8.

[157] A. Pettenuzzo, R. Pigot, L. Ronconi, *Metallodrugs* **2016**, *1*, 36–61.

[158] E. Briasoulis, I. Judson, N. Pavlidis, P. Beale, J. Wanders, Y. Groot, G. Veerman, M. Schuessler, G. Niebch, K. Siamopoulos, et al., *J. Clin. Oncol.* **2000**, *18*, 3535–3544.

[159] T. Halmos, M. Santarromana, K. Antonakis, D. Scherman, *Eur. J. Pharmacol.* **1996**, *318*, 477–484.

[160] G. Bononi, D. Iacopini, G. Cicio, D. Pietro, *ChemMedChem* **2021**, *16*, 30–64.

[161] N. D. Thanh, N. T. K. Giang, T. H. Quyen, D. T. Huong, V. N. Toan, *Eur. J. Med. Chem.* **2016**, *123*, 532–543.

[162] E. A. Akam, E. Tomat, *Bioconjug. Chem.* **2016**, *27*, 1807–1812.

[163] C. Bonaccorso, G. Grasso, N. Musso, V. Barresi, D. F. Condorelli, D. La Mendola, E. Rizzarelli, *J. Inorg. Biochem.* **2018**, *182*, 92–102.

[164] H. El Hajji, O. Dangles, P. Figueiredo, R. Brouillard, *Helv. Chim. Acta* **1997**, *80*, 398–413.

[165] N. Mora-Soumille, S. Al Bittar, M. Rosa, O. Dangles, *Dye. Pigment.* **2013**, *96*, 7–15.

[166] M. H. Assaleh, A. R. Božić, S. Bjelogrlić, M. Milošević, M. Simić, A. D. Marinković, I. N. Cvijetić, *Struct. Chem.* **2019**, *30*, 2447–2457.

[167] J. H. Laity, B. M. Lee, P. E. Wright, *Curr. Opin. Struct. Biol.* **2001**, *11*, 39–46.

[168] A. Y. Chen, R. N. Adamek, B. L. Dick, C. V Credille, C. N. Morrison, S. M. Cohen, *Chem. Rev.* **2019**, *119*, 1323–1455.

[169] C. Andreini, I. Bertini, G. Cavallaro, G. L. Holliday, J. M. Thornton, *J. Biol. Inorg. Chem.* **2008**, *13*, 1205–1218.

[170] K. J. Waldron, J. C. Rutherford, D. Ford, N. J. Robinson, *Nature* **2009**, *460*, 823–830.

[171] S. M. Cohen, *Acc. Chem. Res.* **2017**, *50*, 2007–2016.

[172] M. Ondetti, B. Rubin, D. W. Cushman, *Science (80-. ).* **1977**, *325*, 441–444.

[173] D. Coates, *Int. J. Biochem. Cell Biol.* **2003**, *35*, 769–773.

[174] E. W. Petrillo, M. A. Ondetti, *Med. Res. Rev.* **1982**, *2*, 1–41.

[175] I. P. Kaur, R. Smitha, D. Aggarwal, M. Kapil, *Int. J. Pharm.* **2002**, *248*, 1–14.

[176] V. M. Krishnamurthy, G. K. Kaufman, A. R. Urbach, I. Gitlin, K. L. Gudiksen, D. B. Weibel, G. M. Whitesides, *Chem. Rev.* **2008**, *108*, 946–1051.

[177] K. H. Sippel, A. H. Robbins, J. Domsic, C. Genis, M. Agbandje-Mckenna, R. McKenna, *Acta Crystallogr. Sect. F Struct. Biol. Cryst. Commun.* **2009**, *65*, 992–995.

[178] M. Zervos, F. Meunier, *Int. J. Antimicrob. Agents* **1993**, *3*, 147–170.

[179] R. G. Kranz, C. Richard-Fogal, J.-S. Taylor, E. R. Frawley, *Microbiol. Mol. Biol. Rev.* **2009**, *73*, 510–528.

[180] L. M. Podust, T. L. Poulos, M. R. Waterman, *Proc. Natl. Acad. Sci. U. S. A.* **2001**, *98*, 3068–3073.

[181] B. Mann, J. R. Jhonson, M. Cohen, R. Justice, R. Pazdur, *Oncologist* **2007**, *12*, 1247–1252.

[182] M. Paris, M. Porcelloni, M. Binaschi, D. Fattori, *J. Med. Chem.* **2008**, *51*, 1505–1529.

[183] T. Kouzarides, *Curr. Opin. Genet. Dev.* **1999**, *9*, 40–48.

[184] M. S. Finnin, J. R. Donigian, A. Cohen, V. M. Richon, R. A. Rifkind, P. A. Marks, R. Breslow, N. P. Pavletich, *Nature* **1999**, *401*, 188–193.

[185] D. Rogolino, M. Carcelli, M. Sechi, N. Neamati, *Coord. Chem. Rev.* **2012**, *256*, 3063–3086.

[186] W. Yang, J. Y. Lee, M. Nowotny, *Mol. Cell* **2006**, *22*, 5–13.

[187] J. A. Cowan, *BioMetals* **2002**, *15*, 225–235.

[188] T. Kirschberg, J. Parrish, *Curr. Opin. Drug Discov. Devel.* **2007**, *10*, 460–472.

[189] E. Zakharova, J. Wang, W. Konigsberg, *Biochemistry* **2004**, *43*, 6587–6595.

[190] L. S. Beese, T. A. Steitz, *EMBO J.* **1991**, *10*, 25–33.

[191] G. Palermo, A. Cavalli, M. L. Klein, M. Alfonso-Prieto, M. Dal Peraro, M. De Vivo, *Acc. Chem. Res.* **2015**, *48*, 220–228.

[192] T. A. Steitz, J. A. Steitz, *Proc. Natl. Acad. Sci. U. S. A.* **1993**, *90*, 6498–6502.

[193] T. A. Steitz, *Nature* **1998**, *391*, 231–232.

[194] H. Jaffe, *Science (80-. ).* **2004**, *305*, 1243–1244.

[195] J. Cohen, *Science (80-. ).* **2002**, *296*, 2320–2324.

[196] Y. Pommier, A. A. Johnson, C. Marchand, *Nat. Rev. Drug Discov.* **2005**, *4*, 236–248.

[197] D. Esposito, R. Craigie, *Adv. Virus Res.* **1999**, *52*, 319–333.

[198] A. Engelman, K. Mizuuchi, R. Craigie, *Cell* **1991**, *67*, 1211–1221.

[199] E. Asante-Appiah, A. M. Skalka, *Adv. Virus Res.* **1999**, *52*, 351–369.

[200] F. Dyda, A. B. Hickman, T. M. Jenkins, A. Engelman, R. Craigie, D. R. Davies, *Science (80-. ).* **1994**, *266*, 1981–1986.

[201] D. C. Van Gent, A. A. M. O. Groeneger, R. H. A. Plasterk, *Proc. Natl. Acad. Sci. U. S. A.* **1992**, *89*, 9598–9602.

[202] S. Hare, S. S. Gupta, E. Valkov, A. Engelman, P. Cherepanov, *Nature* **2010**, *464*, 232–236.

[203] G. C. G. Pais, T. R. Burke, *Drugs Future* **2002**, *27*, 1101–1111.

[204] N. Anthony, *Curr. Top. Med. Chem.* **2005**, *4*, 979–990.

[205] N. Neamati, H. Hong, J. M. Owen, S. Sunder, H. E. Winslow, J. L. Christensen, H. Zhao, T. R. Burke, G. W. A. Milne, Y. Pommier, *J. Med. Chem.* **1998**, *41*, 3202–3209.

[206] X. Z. Zhao, K. Maddali, B. C. Vu, C. Marchand, S. H. Hughes, Y. Pommier, T. R. Burke, *Bioorganic Med. Chem. Lett.* **2009**, *19*, 2714–2717.

[207] N. Mahmood, C. Pizza, R. Aquino, N. De Tommasi, S. Piacente, S. Colman, A. Burke, A. J. Hay, *Antiviral Res.* **1993**, *22*, 189–199.

[208] Z. Lin, N. Neamati, H. Zhao, Y. Kiryu, J. A. Turpin, C. Aberham, K. Strebel, K. Kohn, M. Witvrouw, C. Pannecouque, et al., *J. Med. Chem.* **1999**, *42*, 1401–1414.

[209] E. Serrao, S. Odde, K. Ramkumar, N. Neamati, *Retrovirology* **2009**, *6*, 1–14.

[210] M. Kobayashi, T. Yoshinaga, T. Seki, C. Wakasa-Morimoto, K. W. Brown, R. Ferris, S. A. Foster, R. J. Hazen, S. Miki, A. Suyama-Kagitani, et al., *Antimicrob. Agents Chemother.* **2011**, *55*, 813–821.

[211] S. Hare, S. J. Smith, M. Me, A. Jaxa-chamiec, Y. Pommier, S. H. Hughes, P. Cherepanov, *Mol. Pharmacol.* **2011**, *80*, 565–572.

[212] S. A. Hassounah, A. Alikhani, M. Oliveira, S. Bharaj, R. Ibanescu, N. Osman, H. Xu, B. G. Brenner, T. Mesplède, M. a Wainberg, *Antimicrob. Agents Chemother.* **2017**, *61*, 1–9.

[213] M. Tsiang, G. S. Jones, J. Goldsmith, A. Mulato, D. Hansen, E. Kan, L. Tsai, R. A. Bam, G. Stepan, K. M. Stray, et al., *Antimicrob. Agents Chemother.* **2016**, *60*, 7086–7097.

[214] A. H. Reid, J. K. Taubenberger, T. G. Fanning, *Microbes Infect.* **2001**, *3*, 81–87.

[215] N. M. Ferguson, C. Fraser, C. A. Donnelly, A. C. Ghani, R. M. Anderson, *Science (80-. ).* **2004**, *304*, 968–969.

[216] G. Chowell, S. M. Bertozzi, M. A. Colchero, H. Lopez-Gatell, C. Alpuche-Aranda, M. Hernandez, M. A. Miller, *N. Engl. J. Med.* **2009**, *361*, 674–679.

[217] T. C. M. Li, M. C. W. Chan, N. Lee, **2015**, *7*, 4929–4944.

[218] T. Huang, P. Palese, M. Krystal, *J. Virol.* **1990**, *64*, 5669–5673.

[219] A. Pflug, M. Lukarska, P. Resa-Infante, S. Reich, S. Cusack, *Virus Res.* **2017**, *234*, 103–117.

[220] S. J. Plotch, M. Bouloy, I. Ulmanen, R. M. Krug, *Cell* **1981**, *23*, 847–858.

[221] A. Dias, D. Bouvier, T. Crépin, A. A. McCarthy, D. J. Hart, F. Baudin, S. Cusack, R. W. H. Ruigrok, *Nature* **2009**, *458*, 914–918.

[222] P. Yuan, M. Bartlam, Z. Lou, S. Chen, J. Zhou, X. He, Z. Lv, R. Ge, X. Li, T. Deng, et al., *Nature* **2009**, *458*, 909–913.

[223] A. Stevaert, L. Naesens, *Med. Res. Rev.* **2016**, *36*, 1127–1173.

[224] I. Giacchello, F. Musumeci, I. D'Agostino, C. Greco, G. Grossi, S. Schenone, *Curr. Med. Chem.* **2020**, *27*, 1–23.

[225] J. C. Hastings, H. Selnick, B. Wolanski, J. E. Tomassini, *Antimicrob. Agents Chemother.* **1996**, *40*, 1304–1307.

[226] J. Tomassini, H. Selnick, M. E. Davies, M. E. Armstrong, J. Baldwin, M. Bourgeois, J. Hastings, D. Hazuda, J. Lewis, W. McClements, et al., *Antimicrob. Agents Chemother.* **1994**, *38*, 2827–2837.

[227] M. S. Song, G. Kumar, W. R. Shadrick, W. Zhou, T. Jeevan, Z. Li, P. J. Slavish, T. P. Fabrizio, S. W. Yoon, T. R. Webb, et al., *Proc. Natl. Acad. Sci. U. S. A.* **2016**, *113*, 3669–3674.

[228] J. M. Song, K. H. Lee, B. L. Seong, *Antiviral Res.* **2005**, *68*, 66–74.

[229] T. Kuzuhara, Y. Iwai, H. Takahashi, D. Hatakeyama, N. Echigo, *PLoS Curr.* **2009**, *1*, RRN1052.

[230] E. Kowalinski, C. Zubieta, A. Wolkerstorfer, O. H. J. Szolar, R. W. H. Ruigrok, S. Cusack, *PLoS Pathog.* **2012**, *8*, DOI 10.1371/journal.ppat.1002831.

[231] J. D. Bauman, D. Patel, S. F. Baker, R. S. K. Vijayan, A. Xiang, A. K. Parhi, L. Martínez-Sobrido, E. J. Lavoie, K. Das, E. Arnold, *ACS Chem. Biol.* **2013**, *8*, 2501–2508.

[232] A. K. Parhi, A. Xiang, J. D. Bauman, D. Patel, R. S. K. Vijayan, K. Das, E. Arnold, E. J. Lavoie, *Bioorganic Med. Chem.* **2013**, *21*, 6435–6446.

[233] E. Chen, R. V. Swift, N. Alderson, V. A. Feher, G. S. Feng, R. E. Amaro, *ACS Med. Chem. Lett.* **2014**, *5*, 61–64.

[234] M. Carcelli, D. Rogolino, A. Gatti, L. De Luca, M. Sechi, G. Kumar, S. W. White, A. Stevaert, L.

Naesens, *Sci. Rep.* **2016**, *6*, 31500.

[235] Y. Heo, *Drugs* **2018**, *78*, 693–697.

[236] T. Noshi, M. Kitano, K. Taniguchi, A. Yamamoto, S. Omoto, K. Baba, T. Hashimoto, K. Ishida, Y. Kushima, K. Hattori, et al., *Antiviral Res.* **2018**, *160*, 109–117.

[237] S. Omoto, V. Speranzini, T. Hashimoto, T. Noshi, H. Yamaguchi, M. Kawai, K. Kawaguchi, T. Uehara, T. Shishido, A. Naito, et al., *Sci. Rep.* **2018**, *8*, 9633.

[238] B. Todd, E. P. Tchesnokov, M. Götte, *J. Biol. Chem.* **2021**, *296*, 100486.

[239] B. J. Blitvich, B. J. Beaty, C. D. Blair, A. C. Brault, G. Dobler, M. A. Drebot, A. D. Haddow, L. D. Kramer, A. D. LaBeaud, T. P. Monath, et al., *Am. J. Trop. Med. Hyg.* **2018**, *99*, 11–16.

[240] P. Maes, S. Adkins, S. V. Alkhovsky, T. Avšič-Županc, M. J. Ballinger, D. A. Bente, M. Beer, É. Bergeron, C. D. Blair, T. Briese, et al., *Arch. Virol.* **2019**, *164*, 927–941.

[241] A. Abudurexiti, S. Adkins, D. Alioto, S. V. Alkhovsky, T. Avšič-Županc, M. J. Ballinger, D. A. Bente, M. Beer, É. Bergeron, C. D. Blair, et al., *Arch. Virol.* **2019**, *164*, 1949–1965.

[242] S. S. Leventhal, D. Wilson, H. Feldmann, D. W. Hawman, *Viruses* **2021**, *13*, 1–21.

[243] P. Léger, P.-Y. Lozach, *Future Virol.* **2015**, *10*, 859–881.

[244] M. Mardani, M. Keshtkar-jahromi, B. Ataie, P. Adibi, *Am. J. Trop. Med. Hyg.* **2009**, *81*, 675–678.

[245] M. S. Mehand, F. Al-Shorbaji, P. Millett, B. Murgue, *Antiviral Res.* **2018**, *159*, 63–67.

[246] W. B. Parker, *Virus Res.* **2005**, *107*, 165–171.

[247] G. J. Mertz, L. Miedzinski, D. Goade, A. T. Pavia, B. Hjelle, C. O. Hansbarger, H. Levy, F. T. Koster, K. Baum, A. Lindemulder, et al., *Clin. Infect. Dis.* **2004**, *39*, 1307–1313.

[248] S. B. Ozbey, Ç. Kader, A. Erbay, Ö. Ergönül, *Vector-Borne Zoonotic Dis.* **2014**, *14*, 300–302.

[249] C. T. Walter, J. N. Barr, *J. Gen. Virol.* **2011**, *92*, 2467–2484.

[250] J. Reguera, F. Weber, S. Cusack, *PLoS Pathog.* **2010**, *6*, DOI 10.1371/journal.ppat.1001101.

[251] A. Amroun, S. Priet, X. de Lamballerie, G. Quérat, *Crit. Rev. Microbiol.* **2017**, *43*, 753–778.

[252] S. Olschewski, S. Cusack, M. Rosenthal, *Trends Microbiol.* **2020**, *28*, 293–303.

[253] F. Ferron, F. Weber, J. C. de la Torre, J. Reguera, *Virus Res.* **2017**, *234*, 118–134.

[254] J. Reguera, P. Gerlach, M. Rosenthal, S. Gaudon, F. Coscia, S. Günther, S. Cusack, *PLoS Pathog.* **2016**, *12*, 1–24.

[255] T. Holm, J. D. Kopicki, C. Busch, S. Olschewski, M. Rosenthal, C. Uetrecht, S. Günther, S. Reindl, *J. Biol. Chem.* **2018**, *293*, 19686–19698.

[256] R. Raju, L. Raju, D. Hacker, D. Garcin, R. Compans, D. Kolakofsky, *Virology* **1990**, *174*, 53–59.

[257] M. Saez-Ayala, E. Laban Yekwa, C. Mondielli, L. Roux, S. Hernández, F. Bailly, P. Cotelle, D. Rogolino, B. Canard, F. Ferron, et al., *Antiviral Res.* **2019**, *162*, 79–89.

[258] R. Jones, S. Lessoued, K. Meier, S. Devignot, S. Barata-García, M. Mate, G. Bragagnolo, F. Weber, M. Rosenthal, J. Reguera, *Nucleic Acids Res.* **2019**, *47*, 10914–10930.

[259] M. Saez-Ayala, E. L. Yekwa, M. Carcelli, B. Canard, K. Alvareza, F. Ferron, *IUCrJ* **2018**, *5*, 223–235.

[260] Y. Fernandez-García, S. ter Horst, M. Bassetto, A. Brancale, Y. Fern, J. Neyts, D. Rogolino, M. Sechi,

M. Carcelli, S. Günther, et al., *Antiviral Res.* **2020**, *183*, 104947.

[261] C. Ye, D. Wang, H. Liu, H. Ma, Y. Dong, M. Yao, Y. Wang, H. Zhang, L. Zhang, L. Cheng, et al., *Front. Pharmacol.* **2019**, *10*, 1–8.

[262] W. Wang, W. J. Shin, B. Zhang, Y. Choi, J. S. Yoo, M. I. Zimmerman, T. E. Frederick, G. R. Bowman, M. L. Gross, D. W. Leung, et al., *Cell Rep.* **2020**, *30*, 153-163.e5.

[263] J. E. Tavis, G. Zoidis, A. Pinto, J. Brien, R. Murelli, *Inhibitors of Bunyavirales and Uses Thereof*, **2021**, US 2021/0393548 A1.

[264] P. Vincetti, F. Caporuscio, S. Kaptein, A. Gioiello, V. Mancino, Y. Suzuki, N. Yamamoto, E. Crespan, A. Lossani, G. Maga, et al., *J. Med. Chem.* **2015**, *58*, 4964−4975.

[265] P. Vincetti, S. J. F. Kaptein, G. Costantino, J. Neyts, M. Radi, *ACS Med. Chem. Lett.* **2019**, *10*, 558–563.

[266] S. J. F. Kaptein, P. Vincetti, E. Crespan, I. A. Rivera, G. Costantino, G. Maga, J. Neyts, M. Radi, *ChemMedChem* **2018**, *13*, 1371–1376.

[267] P. Vincetti, G. Costantino, M. G. Martina, M. Radi, *Synlett* **2019**, *30*, 2010–2014.

[268] L. D. Cantin, M. Bayrakdarian, C. Buon, E. Grazzini, Y. J. Hu, J. Labrecque, C. Leung, X. Luo, G. Martino, M. Paré, et al., *Bioorganic Med. Chem. Lett.* **2012**, *22*, 2565–2571.

[269] X. Shi, T. Van Mierlo, A. French, R. M. Elliott, *J. Virol.* **2010**, *84*, 8460–8469.

[270] Y. Fernández-García, J. Reguera, C. Busch, G. Witte, O. Sánchez-Ramos, C. Betzel, S. Cusack, S. Günther, S. Reindl, *PLoS Pathog.* **2016**, *12*, 1–18.

[271] U. B. Ericsson, B. M. Hallberg, G. T. DeTitta, N. Dekker, P. Nordlund, *Anal. Biochem.* **2006**, *357*, 289–298.

[272] X. Z. Zhao, K. Maddali, S. J. Smith, M. Métifiot, B. C. Johnson, C. Marchand, S. H. Hughes, Y. Pommier, T. R. Burke, *Bioorganic Med. Chem. Lett.* **2012**, *22*, 7309–7313.

[273] D. Rogolino, L. Naesens, J. Bartoli, M. Carcelli, L. De Luca, G. Pelosi, R. W. Stokes, R. Van Berwaer, S. Vittorio, A. Stevaert, et al., *Bioorg. Chem.* **2021**, *116*, 1–36.

[274] A. Stevaert, S. Nurra, N. Pala, M. Carcelli, D. Rogolino, C. Shepard, R. A. Domaoal, B. Kim, M. Alfonso-Prieto, S. A. E. Marras, et al., *Mol. Pharmacol.* **2015**, *87*, 323–337.

[275] H. M. V. M. S. C. M. H. Ferreira, I. S. S. Pinto, E. V. Soares, *RCS Adv.* **2015**, *5*, 30989–31003.

[276] E. Fisicaro, A. Braibanti, *Talanta* **1988**, *35*, 769–774.

[277] M. Tegoni, M. Furlotti, M. Tropiano, C. S. Lim, V. L. Pecoraro, *Inorg. Chem.* **2010**, *49*, 5190–5201.

[278] P. Gans, A. Sabatini, A. Vacca, *Ann. Chim.* **1999**, *89*, 45–49.

[279] P. Gans, A. Sabatini, A. Vacca, *Talanta* **1996**, *43*, 1739–1753.

[280] L. Alderighi, P. Gans, A. Ienco, D. Peters, A. Sabatini, A. Vacca, *Coord. Chem. Rev.* **1999**, *184*, 311–318.

[281] T. T. Ashburn, K. B. Thor, *Nat. Rev. Drug Discov.* **2004**, *3*, 673–683.

[282] H. Li, S. Yuan, X. Wei, H. Sun, *Chem. Commun.* **2022**, *58*, 7466–7482.

[283] H. S. Hillen, G. Kokic, L. Farnung, C. Dienemann, D. Tegunov, P. Cramer, *Nature* **2020**, *584*, 154–156.

[284] K. Zandi, K. Musall, A. Oo, D. Cao, B. Liang, P. Hassandarvish, S. Lan, R. L. Slack, K. A. Kirby, L. Bassit, et al., *Microorganisms* **2021**, *9*, 893.

[285] S. Gao, L. Song, H. Xu, A. Fikatas, M. Oeyen, S. De Jonghe, F. Zhao, L. Jing, D. Jochmans, L. Vangeel, et al., *Molecules* **2023**, *28*, 160.

[286] A. Seybert, C. C. Posthuma, L. C. van Dinten, E. J. Snijder, A. E. Gorbalenya, J. Ziebuhr, *J. Virol.* **2005**, *79*, 696–704.

[287] C. Lee, J. M. Lee, N. R. Lee, B. S. Jin, K. J. Jang, D. E. Kim, Y. J. Jeong, Y. Chong, *Bioorganic Med. Chem. Lett.* **2009**, *19*, 1636–1638.

[288] S. Hernández, M. Feracci, C. T. De Jesus, P. El Kazzi, R. Kaci, L. Garlatti, C. Mondielli, F. Bailly, P. Cotelle, F. Touret, et al., *Antiviral Res.* **2022**, *204*, DOI 10.1016/j.antiviral.2022.105364.

[289] X. Lei, X. Dong, R. Ma, W. Wang, X. Xiao, Z. Tian, C. Wang, Y. Wang, L. Li, L. Ren, et al., *Nat. Commun.* **2020**, *11*, DOI 10.1038/s41467-020-17665-9.

[290] A. S. Prasad, *J. Am. Coll. Nutr.* **2009**, *28*, 257–265.

[291] A. J. W. te Velthuis, S. H. E. van den Worml, A. C. Sims, R. S. Baric, E. J. Snijder, M. J. van Hemert, *PLoS Pathog.* **2010**, *6*, e1001176.

[292] L. Panchariya, W. A. Khan, S. Kuila, K. Sonkar, S. Sahoo, A. Ghoshal, A. Kumar, D. K. Verma, A. Hasan, M. A. Khan, et al., *Chem. Commun.* **2021**, *57*, 10083–10086.

[293] Z. Jin, X. Du, Y. Xu, Y. Deng, M. Liu, Y. Zhao, B. Zhang, X. Li, L. Zhang, C. Peng, et al., *Nature* **2020**, *582*, 289–293.

[294] K. Sanachai, P. Mahalapbutr, V. Sanghiran Lee, T. Rungrotmongkol, S. Hannongbua, *J. Phys. Chem. B* **2021**, *125*, 13644–13656.

[295] J. T. A. Hsu, C. J. Kuo, H. P. Hsieh, Y. C. Wang, K. K. Huang, C. P. C. Lin, P. F. Huang, X. Chen, P. H. Liang, *FEBS Lett.* **2004**, *574*, 116–120.

[296] C. DeLaney, Y. Sheng, D. C. Pectol, E. Vantansever, H. Zhang, N. Bhuvanesh, I. Salas, W. R. Liu, C. F. Fierke, M. Y. Darensbourg, *Dalt. Trans.* **2021**, *50*, 12226–12233.

[297] S. Günther, P. Y. A. Reinke, Y. Fernández-Garciá, J. Lieske, T. J. Lane, H. M. Ginn, F. H. M. Koua, C. Ehrt, W. Ewert, D. Oberthuer, et al., *Science (80-. ).* **2021**, *372*, 642–646.

[298] Y. S. Han, G. G. Chang, C. G. Juo, H. J. Lee, S. H. Yen, J. T. A. Hsu, X. Chen, *Biochemistry* **2005**, *44*, 10349–10359.

[299] C. Abbehausen, *Metallomics* **2019**, *11*, 15–28.

[300] C. L. Shetler, J. C. Ferreira, T. H. S. Cardoso, E. M. A. Silva, N. K. Saksena, W. M. Rabeh, *Biochem. J.* **2022**, *479*, 2175–2193.

[301] M. H. Lin, D. C. Moses, C. H. Hsieh, S. C. Cheng, Y. H. Chen, C. Y. Sun, C. Y. Chou, *Antiviral Res.* **2018**, *150*, 155–163.

[302] K. Sargsyan, C. C. Lin, T. Chen, C. Grauffel, Y. P. Chen, W. Z. Yang, H. S. Yuan, C. Lim, *Chem. Sci.* **2020**, *11*, 9904–9909.

[303] A. Bacchi, M. Carcelli, C. Compari, E. Fisicaro, N. Pala, G. Rispoli, D. Rogolino, T. W. Sanchez, M. Sechi, V. Sinisi, et al., *J. Med. Chem.* **2011**, *54*, 8407−842.

[304] D. Rogolino, A. Bacchi, L. De Luca, G. Rispoli, M. Sechi, A. Stevaert, L. Naesens, M. Carcelli, *J. Biol. Inorg. Chem.* **2015**, *20*, 1109–1121.

[305] L. R. Chen, Y. C. Wang, W. L. Yi, S. Y. Chou, S. F. Chen, T. L. Lee, Y. T. Wu, C. J. Kuo, T. S. S. Chen, S. H. Juang, *Bioorganic Med. Chem. Lett.* **2005**, *15*, 3058–3062.

[306] W. Ewert, S. Günther, F. Miglioli, S. Falke, P. Y. A. Reinke, S. Niebling, C. Günther, H. Han, V. Srinivasan, H. Brognaro, et al., *Front. Chem.* **2022**, *10*, 1–13.

[307] F. W. Studier, *Protein Expr. Purif.* **2005**, *41*, 207–234.

[308] G. Winter, D. G. Waterman, J. M. Parkhurst, A. S. Brewster, R. J. Gildea, M. Gerstel, L. Fuentes-Montero, M. Vollmar, T. Michels-Clark, I. D. Young, et al., *Acta Crystallogr. Sect. D Struct. Biol.* **2018**, *74*, 85–97.

[309] D. Liebschner, P. V. Afonine, M. L. Baker, G. Bunkoczi, V. B. Chen, T. I. Croll, B. Hintze, L. W. Hung, S. Jain, A. J. McCoy, et al., *Acta Crystallogr. Sect. D Struct. Biol.* **2019**, *75*, 861–877.

[310] N. M. Pearce, T. Krojer, A. R. Bradley, P. Collins, R. P. Nowak, R. Talon, B. D. Marsden, S. Kelm, J. Shi, C. M. Deane, et al., *Nat. Commun.* **2017**, *8*, 15123.

[311] P. V Alfonine, B. K. Poon, R. J. Read, O. V. Sobolev, T. C. Terwilliger, A. G. Urzhumtsev, P. D. Adams, *Acta Crystallogr.* **2018**, *74*, 531–544.

[312] P. Emsley, K. Cowtan, *Acta Crystallogr. Sect. D Struct. Biol.* **2004**, *60*, 2126–2132.

[313] T. Klemm, G. Ebert, D. J. Calleja, C. C. Allison, L. W. Richardson, J. P. Bernardini, B. G. Lu, N. W. Kuchel, C. Grohmann, Y. Shibata, et al., *EMBO J.* **2020**, *39*, 1–17.